DEPARTMENT OF
AEROSPACE ENGINEERING
INDIAN INSTITUTE OF
TECHNOLOGY
MADRAS
CHENNAI-600 036

STATISTICS AND DYNAMICS OF TURBULENT PREMIXED FLAMES

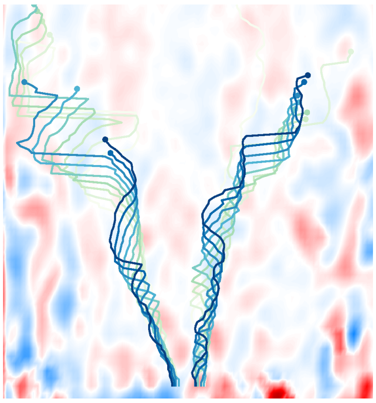

A thesis

Submitted by

AMITESH ROY

For the award of the degree

Of

DOCTOR OF PHILOSOPHY

February, 2022

DEPARTMENT OF
AEROSPACE ENGINEERING
INDIAN INSTITUTE OF
TECHNOLOGY
MADRAS
CHENNAI-600 036

STATISTICS AND DYNAMICS OF TURBULENT PREMIXED FLAMES

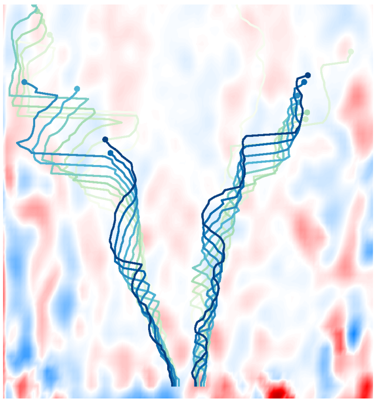

A thesis

Submitted by

AMITESH ROY

For the award of the degree

Of

DOCTOR OF PHILOSOPHY

February, 2022

© 2022 Indian Institute of Technology Madras

I shall be telling this with a sigh
Somewhere ages and ages hence:
Two roads diverged in a wood, and I –
I took the one less traveled by,
And that has made all the difference.

– The Road Not Taken
Robert Frost (1915)

To my grandparents who enrich me through their blessings

THESIS CERTIFICATE

This is to undertake that the thesis titled, **STATISTICS AND DYNAMICS OF TURBULENT PREMIXED FLAMES** submitted by **Amitesh Roy**, to the Indian Institute of Technology Madras, for the award of Doctor of Philosophy, is a bonafide record of the research work done by me under the supervision of Prof. R I Sujith. The contents of this thesis, in full or in parts, have not been submitted to any other Institute or University for the award of any degree or diploma.

Chennai 600 036 **Research Scholar**

Date: 11th February 2021

Research Guide

Prof. R I Sujith
Professor
Dept. of Aerospace Engineering
IIT-Madras, 600 036

LIST OF PUBLICATIONS

I. REFEREED JOURNALS BASED ON THESIS

1. Small-scale intermittency of premixed turbulent flames
   A. Roy, J. R. Picardo, T. C. Lieuwen & R. I. Sujith
   arXiv:2202.12066 (2022)
2. Fractal dimension of premixed flames in intermittent turbulence
   A. Roy, R. I. Sujith
   Combustion and Flame, **226**, 412-418 (2021)
3. Critical region in the spatiotemporal dynamics of a turbulent thermoacoustic system and smart passive control
   A. Roy, C. Premchand, M. Raghunathan, A. Krishnan, V. Nair & R. I. Sujith
   Combustion and Flame, **226**, 274-284 (2021)
4. Nonlinear flame response dependencies of a V-flame subjected to harmonic forcing and turbulence
   A. Roy, R I Sujith
   Combustion and Flame., **207**, 101-119 (2019)

II. PATENT

Systems and methods for suppressing thermo-acoustic instabilities in a combustor
R. I. Sujith, K. Manoj, S. A. Pawar, A. Krishnan, M. P. Midhun, Reeja K. V., M. Raghunathan, **A. Roy**
U.S. Patent No. - 20210095848 (2021).

III. REFEREED JOURNALS (OTHERS)

1. On the mechanism of open-loop control of thermoacoustic instability in a laminar premixed combustor
   A. Roy, S. Mondal, S. Pawar & R. I. Sujith
   Journal of Fluid Mechanics, **884**, A2 (2020)
2. Flame dynamics during intermittency and secondary bifurcation to longitudinal thermoacoustic instability in a swirl-stabilized annular combustor
   A. Roy, S. Singh, A. Nair, S. Chaudhuri & R. I. Sujith
   Proceedings of the Combustion Institute, **38** (4), 6221-6230 (2020)
3. Nonlinear dynamics of coupled thermoacoustic oscillators under asymmetric forcing
   A. Sahay, **A. Roy**, S. Pawar & R. I. Sujith
   Physical Review Applied, **15**, 044011 (2021)
4. Intermittency, secondary bifurcation and mixed mode oscillations in a swirl-stabilized annular combustor: Experiments and modeling

S. Singh, **A. Roy**, K. V. Reeja, A. Nair, S. Chaudhuri & R. I. Sujith
Journal of Engineering for Gas Turbine and Power, **143** (5), 051028 (2021)

5. Mean-field synchronization model for open-loop, swirl controlled thermoacoustic systems
S. Singh, A. K. Dutta, J. Dhadphale, **A. Roy**, S. Chaudhuri & R. I. Sujith
arXiv:2201.01764 (2022)

IV. PRESENTATIONS IN CONFERENCES

1. Fluttering flames, intermittency, and the KPZ equation
J. R. Picardo, **A. Roy**, B. Emerson, T. C. Lieuwen & R. I. Sujith
Stochastic Approaches to Turbulence in Hydrodynamical Equations: New Challenges at the Mathematics-Physics Interface, 27 February - 4 March, Banff International Research Station (Online)
2. Coupled behavior of oscillators under asymmetric forcing
A. Sahay, **A. Roy**, S. A. Pawar & R. I. Sujith
Dynamics Days Europe, 23-27 August (Online)
3. Flame dynamics during intermittency and secondary bifurcation to longitudinal thermoacoustic instability in a swirl-stabilized annular combustor
A. Roy, S. Singh, A. Nair, S. Chaudhuri & Sujith R I
38th International Symposium on Combustion, 24-29 January 2021, Adelaide, Australia (Online).
4. Intermittency, secondary bifurcation and mixed mode oscillations in a swirl-stabilized annular combustor: Experiments and modeling
S. Singh, **A. Roy**, K. V. Reeja, A. Nair, S. Chaudhuri & R. I. Sujith
ASME Turbo Expo, 22-26 June 2020, London, UK (Online).
5. Open-loop control of thermoacoustic instability in a laminar combustor: Forced synchronization and physical mechanism
A. Roy, S. Mondal, S. A. Pawar & R. I. Sujith
12th Conference on Nonlinear Systems and Dynamics, IIT Kanpur, 12-15 December 2019, Kanpur, UP, India.
6. Forced synchronization and the mechanism of open-loop control of thermoacoustic instability in a laminar combustor
A. Roy, S. Mondal, S. A. Pawar & R. I. Sujith
Workshop on Data Analysis and Machine Learning, IISER Tirupati, May 2019, Tirupati, AP, India.

ACKNOWLEDGEMENTS

This thesis is a result of hard work, advice and support of a lot of people without whom this work would not have come to fruition. Foremost, I wish to express heartfelt gratitude to Prof. R. I. Sujith for agreeing to be my thesis advisor. He is meticulous in planning, relentless in execution and tenacious under inclement situations. It is indeed this philosophy which I have truly learned during the course of my Ph. D. He has taught me to be an open-minded researcher and enthusiastically prompted me to probe various research directions. I have learnt a lot from him, and will continue to look up to him for the rest of my life.

I am indebted to Prof. K. Bhaskar, Prof. P. Sriram and Prof. H. S. N. Murthy for their guidance and encouragement during various stages of my Ph. D. I wish to also thank Prof. P. A. Ramakrishna, Prof. Sunetra Sarkar and Prof. Niket Kaisare for motivating me and critically reviewing my research work as a part of my Doctorol Committee. I am especially thankful to Prof. N. R. Panchapakesan for introducing me to turbulence research. In hindsight, Chapter 5 is a direct result of his course.

I am extremely grateful to Prof. Tim Lieuwen (Georgia Tech) for his generosity in sharing the experimental dataset on premixed V-flames. I am also thankful to Dr. Luke Humphrey and Sukruth Somappa (Georgia Tech) for performing the experiments and promptly clarifying any questions I had on the dataset. I am extremely fortunate to have found two exceptional mentors in Prof. Swetaprovo Chaudhuri (UTIAS, Toronto) and Dr. Jason Picardo (IIT Bombday). They patiently helped me through many hours of discussion on various aspects of combustion and turbulence. An hour of discussion with them was worth more than several days of me breaking my head over various concepts. I gained a lot of motivation and confidence following each of our conversations. I am also grateful to Dr. Vineeth Nair (IIT Bombay) for patiently reviewing and revising my paper which is discussed in Chapter 7. I further acknowledge the support received from Office of Naval Research Global (ONRG), Siemens Corporate Technology India, and JC Bose fellowship for Dr. R I Sujith from Department of Science and Technology (DST), India.

I am grateful to Dr. Sirshendu Mondal (NIT Durgapur) and Dr. Samadhan Pawar, who quite literally held my hand through experiments and rounds of corrections of my papers in the first two years of my Ph. D. I am also thankful to Dr. Vishnu Unni (Princeton), Dr. Abin Krishnan and to soon be Dr. S Manikandan (DRDO) for many insightful discussions over the last few years. I also hold dearly the camaraderie with my labmates Praveen, Vedasri, Induja, Manikandan and Krishna. We had a lot of fun designing experiments and discussing various academic and non-academic issues. I am also thankful to all my juniors who through their exuberance would keep the spirit at the lab buoyed. I am extremely thankful to Thilagaraj and Anand for patiently designing and manufacturing the various setups on which I worked throughout the duration of my PhD. I am especially grateful to Jabasteena for tending to my innumerous administrative requests and help in keeping the lab running smoothly. I wish to express my gratitude to Priyanshu, Pankaj and Varun for their friendship and company. Finally, I want to thank Poojit, Sushobhan, Abhinav and Utkarsh for being there through thick and thin since our days in VIT.

I am immeasurably grateful to my sister Amita and brother-in-law Saptarshi for supporting me over the past 5 years and looking over me. Little Ayaansh has truly been a joy to behold and has constantly been a reason for me to smile. Finally, I am eternally indebted to my parents for their love and affection, and for supporting my education through many difficult situations. They continue to be patient and steadfast anchor of my life.

ABSTRACT

KEYWORDS: Combustion; Premixed Flames; Turbulence; Statistics; Dynamics; Harmonic Flame Response; Intermittency; Fractals; Multifractals; Thermoacoustic Instability; Passive Control; Critical Region

In the present thesis, we discuss the statistics and dynamics of premixed flames in turbulent flows. We begin by experimentally studying the dynamics of a premixed CH_4-air flame evolving in a turbulent background. We discern nonlinear interference effects from convecting disturbances on the flame surface and quantify their impact on the large-scale harmonic flame response. We also determine the local and global heat release rate response and explain its dependence on the local structure of the flame response. We measure the scale-dependent statistics of the fluctuating flame surface. We show that the large-scale statistics are significantly different from the small-scale statistics. In particular, we estimate the effect of small-scale turbulence on the statistics of flame fluctuations. We observe that power-spectrum and the moments of the increments of flame fluctuations depict well-defined power-laws, implying self-similarity in the fluctuations over an intermediate range of scales not affected by viscosity and the restorative effect of the flame propagating normal to itself, termed as kinematic restoration. Further, we observe that scaling exponents of the structure-function are anomalous as they do not grow linearly with the order of the structure-functions, indicating the presence of small-scale intermittency in the power-law range. The presence of such small-scale intermittency has important implications in the

modeling of turbulent premixed flames.

We then analytically determine the effect of turbulence on the flame surface. For turbulent premixed flames, the fractal dimension is argued to be $\mathbb{D} = 7/3$ for flamelet combustion and $\mathbb{D} = 8/3$ for thickened flames ($Da \sim \mathcal{O}(1)$) based on heuristic scaling arguments. However, such scaling arguments do not consider the effect of the intermittent nature of turbulent kinetic energy dissipation on the flame surface. We account for the effects of intermittent dissipation on the fractal dimension of thickened flames. Intermittent dissipation leads to variability in the inner cut-off, which then affects the scalar flux and total interface area. We account for these variabilities through two approaches: Coarse-grained approach based on the moments of the dissipation and fine-scale analysis by adopting the multifractal formalism. We derive two corrections to the upper-limit of fractal dimension – $\mathbb{D} = 8/3+3/4(1-D_{1/4})$ and $\mathbb{D} = 8/3 + 2/3(3 - D_{1/3})$. We further show that the second correction leads to an explicit dependence of the fractal dimension ($\mathbb{D}$) on the scaling exponent (ζ_p) of the velocity structure function through the relation: $\mathbb{D} = 7/3 + \zeta_p$. Thus, we explicitly quantify the effect of the intermittent nature of turbulence upon low Da premixed combustion.

In the final part of this thesis, we develop a novel strategy based on the statistics of turbulent flows in practical combustors for the passive control of thermoacoustic instability. When the equivalence ratio is varied, there is a transition from combustion noise to thermoacoustic instability via intermittency in the combustor. We determine the spatial distribution of the Hurst exponent measured from the turbulent velocity field. We

show that the Hurst exponent is able to determine the so-called “critical region” of the flow field, perturbing which leads to optimal control of thermoacoustic oscillations.

TABLE OF CONTENTS

Page

LIST OF PUBLICATION i

ACKNOWLEDGEMENTS iii

ABSTRACT vi

LIST OF TABLES xiv

LIST OF FIGURES xxi

GLOSSARY xxii

ABBREVIATIONS xxiii

NOTATION xxiv

1 INTRODUCTION 1

1.1 Historical overview 1

1.1.1 Mankind and fire 1

1.1.2 Environmental concerns and global warming 3

1.1.3 The way forward: Alternative and low-emission technologies 5

1.2 Gas turbines: Turbulent, lean premixed combustion technology 7

1.2.1 Pollutant Emissions 7

1.2.2 NO_x generation pathways 9

1.2.3 Emission mitigation strategies 11

1.2.4 Lean, premixed combustion 13

1.2.5 The challenge of lean, premixed turbulent combustion 15

1.2.6 The problem of thermoacoustic instability 16

1.3 Motivation 17

1.4 Objectives 18

1.5 Overview of the thesis 19

2 BACKGROUND **22**

2.1 Turbulent flows 23

2.1.1 Governing equations of turbulent flows 23

2.1.2 Scales of turbulent motion 26

2.1.3 Universal equilibrium theory of turbulence 29

2.1.4 Higher-order statistics of turbulent flows 31

2.1.5 Small-scale intermittency in turbulent flows 37

2.1.6 Intermittent fields and multiplicative processes 39

2.1.7 The multifractal formalism 40

2.1.8 Scalar fields in turbulent flows 43

2.2 Turbulent combustion 48

2.2.1 Regimes of turbulent premixed flames 48

2.2.2 Premixed flame formulation 51

2.2.3 Large-scale flame response 63

2.3 Thermoacoustic instability 67

2.3.1 Wave equation and acoustic energy balance in reacting flows . 67

2.3.2 The Rayleigh criteria and its extensions 69

2.3.3 Mechanisms of thermoacoustic instability 70

2.3.4 Bifurcations and transition to thermoacoustic instability . . . 73

2.3.5 Spatiotemporal behavior during intermittency route to thermoacoustic instability 77

2.3.6 Control of thermoacoustic instability 78

2.4 Interim summary 82

3 EXPERIMENTAL FACILITIES AND DIAGNOSTICS 84

3.1 Turbulent V-flame facility 84

3.1.1 Optical diagnostics 86

3.1.2 Flame edge identification and post-processing 89

3.2 Bluff-body stabilized combustor 93

4 LARGE-SCALE HARMONIC RESPONSE OF TURBULENT PREMIXED FLAMES 97

4.1 Harmonic response of flame surface fluctuations 97

4.1.1 Ensemble averaged flame response 97

4.1.2 Amplitude spectrum of flame fluctuations 98

4.1.3 Effect of turbulence on harmonic flame response 99

4.1.4 Interference of non-identical disturbances 103

4.1.5 Frequency dependence of flame sheet response at comparable flow conditions 107

4.2 Heat release rate response 108

4.2.1 Flame asymmetry and cross-correlation 110

4.2.2 Local Heat Release Response 113

4.2.3 Global heat release rate response 117

4.3 Interim summary 119

5 SELF-SIMILARITY AND SMALL-SCALE INTERMITTENCY IN TURBULENT PREMIXED FLAMES 121

5.1 Spectral scaling of flame surface fluctuations 122

5.1.1 Temporal power spectrum of flame fluctuations 122

5.1.2 Kolmogorov's limit for temporal power spectrum 126

5.2 Statistics of large-scale flame fluctuations 130

5.3 Small-Scale intermittency in flame fluctuations 133

5.3.1 Non-Gaussian statistics of increments in flame fluctuations . . 133

5.3.2 Power-law scaling of structure functions 136

5.3.3 Kolmogorov's limit for structure-function scaling 137

5.3.4 Anomalous scaling exponents 139

5.4 Multifractal behavior of turbulent flames 141

5.4.1 Generalized dimension of flame fluctuations 142

5.4.2 Singularities and the multifractal spectrum 145

5.5 Interim Summary 152

6 FRACTAL DIMENSION OF PREMIXED FLAMES IN INTERMITTENT TURBULENCE 153

6.1 Fractals, measures and dimensions 153

6.2 Fractals in classical turbulent flows 156

6.3 Fractals in premixed turbulent flames 158

6.4 Estimate of fractal dimension of thickened flames 161

6.5 Influence of intermittency on the fractal dimension of the flame 166

6.5.1 A coarse-grained estimate based on the moments of the intermittent dissipation field 166

6.5.2 A fine-scaled estimate based on the multifractal formalism . . 169

6.6 Discussion 174

6.7 Interim Summary 177

7 CRITICAL REGION AND SMART PASSIVE CONTROL IN A TURBULENT THERMOACOUSTIC SYSTEM 178

7.1 Characterizing the turbulent combustor 179

7.2 Nonlinear time series analysis: the Hurst exponent 181

7.3 Spatiotemporal behavior during the transition to thermoacoustic instability 185

7.4 Passive control of thermoacoustic instability 190

7.4.1 Suppression of thermoacoustic instability 190

7.4.2 Spatiotemporal behavior during suppression 192

7.4.3 Mechanism of suppression 195

7.5 Optimized passive control using Hurst exponent 196

7.6 Interim Summary 200

8 CONCLUSION AND OUTLOOK 203

8.1 Future directions 205

REFERENCES 207

LIST OF TABLES

Table **Title** **Page**

4.1 The range of Strouhal numbers, St_d, based on the flame holder diameter (d), considered in our study. The italicized values of Strouhal number corresponds to the cases for which we expect vortex shedding by the flame holder due to BVK instability. 104

4.2 Comparison of the interference length scale $\lambda_{\text{int},1}$ calculated from Eqn. (4.1) and $\lambda_{\text{int},2}$ calculated from the harmonic flame response as $\lambda_{\text{int},2} = \Delta y_{\text{peak}}/\cos\theta$ (see Fig. 4.3e). Also tabulated are the convective (λ_c) and flame wrinkle (λ_t) length scales. 106

5.1 Relevant properties of the two turbulent premixed flames considered in this chapter. The convective wavelength is calculated as $\lambda_c = \bar{u}_y/f_f$. The quantities s_L and δ_F were obtained using CHEMKIN PREMIX calculation (see Humphrey, 2017). 123

5.2 Generalized dimension of the fluctuations ξ' for flame F1 measured at the three locations. 145

5.3 Comparison of the properties of the multifractal $f(\alpha) - \alpha$ spectrum for flame F1 at two locations. 150

5.4 Comparison of the properties of the multifractal $f(\alpha) - \alpha$ spectrum measured at $y/\lambda_c = 2$ for flames F1 and F2. 151

LIST OF FIGURES

1.1 (a) Historic trend of CO_2 levels (NASA, 2021) and the (b) global temperature anomaly measured by EPICA from Antarctica Vostok ice core (Augustin *et al.*, 2004). Reproduced with permission from (a) NASA and (b) Springer Nature. 4

1.2 Pronounced global temperature anomaly observed in 2020 in comparison to that during industrial age in 1884 (Courtesy: NASA, 2021). 5

1.3 Sector based share of power output from various sources of electricity generation over the last four decades. Adapted from (IEA, 2021). . . . 6

1.4 (a) NO_x and CO emission as a function of the air-to-fuel ratio and combustion temperature for different levels of premixedness indicated by PB. (b) Computational result showing the relative contribution of different NO_x producing pathways at different equivalence ratios. (a) Reproduced with permission from (Maghon *et al.*, 1988) and (b) from (Gokulakrishnan and Klassen, 2013). 10

2.1 (Left) Transition to fully-developed turbulence in a jet flow. Turbulent large-scale motion arises from mean flow instabilities and breaks down into finer scales. (Right) Schematic depicting the cascade through which finer scales are generated. It is evident that after a few generations of the cascade process, effects of mean flow inhomogeneity and anisotropy become negligible. Adapted from (a) Bradshaw *et al.* (1964) and (b) Frisch (1995) with permission from Cambridge University Press. 28

2.2 (a) Kolmogorov's $5/3^{\text{rd}}$ law observed empirically in a variety of turbulent flow datasets compiled by Saddoughi and Veeravalli (1994). The range over which $k^{-5/3}$ scaling is observed increases with an increase in Re. (b) Scaling of structure-function compensated with 'guessed' power-law exponents ζ_p for different values of p for wind tunnel data reported in Anselmet *et al.* (1984). Figures have been adapted with permission from Cambridge University Press. 32

2.3 Typical time trace and properties of turbulent velocity fluctuations. Subfigure (a) shows $u'(t)$ for a turbulent jet and (b) shows the same signal after high-pass filtering (denoted as $u'(t)_>$) to highlight extreme fluctuations associated with small-scales (Gagne, 1980). (c) Time series of turbulent kinetic energy dissipation $\varepsilon \sim (du'/dt)^2$ obtained from atmospheric surface layer (Meneveau and Sreenivasan, 1991). (d) The PDF of velocity increments $\delta u'$ for different values of separation r/η (Anselmet *et al.*, 1984). Figures (c,d) have been adapted with permission from Cambridge University Press. 33

2.4 Anomalous scaling exponent ζ_p associated with structure-function based on (a) velocity increments ($\delta u'(r)$) and (b) scalar increments ($\delta c'(r)$). Various model predictions are shown in (a). Note the departure from $\zeta_p = p/3$ as predicted by K41 theory. Adapted from (a) Frisch (1995) with permission from Cambridge University Press and (b) Sreenivasan and Antonia (1997) with permission from Annual Reviews. 36

2.5 Regimes of turbulent combustion. Adapted from Law (2010) with permission from Cambridge University Press. 49

2.6 Schematic of the compensated spectrum function $k^{5/3}\Gamma(k)$ associated with flame fluctuations ξ' as a function of the non-dimensional wavenumber. We note that the spectrum decays exponentially through the additional term in Eqn. (5.5). The pertinent length scales are marked for clarity, where ℓ is the integral scale, ℓ_g is the Gibson scale, η_c the Corrsin scale and η_M the Markstein length. 59

2.7 Effect of harmonic forcing and turbulence on the large-scale flame dynamics. (a) Flame sheet anchored on an oscillating bluff-body ensemble-averaged at different time instances. (b) Increase in the mean flame position, $\bar{\xi}(y,t)$, and decrease in the flame flame wrinkle amplitude $|\langle\hat{\xi}(y,f_0)\rangle|$, with downstream distance. (c) Cartoon depicting the effect of wavelength of harmonic disturbances on the mean flame response. (d) Typical response of a bluff-body stabilized flame. Adapted from (a, b) Shin and Lieuwen (2012), (c) Hemchandra *et al.* (2011) and (d) Shanbhogue *et al.* (2009*a*) with permission from Elsevier. 66

2.8 Normal form of (a) Supercritical and (b) subcritical Hopf bifurcation for a Van der Pol oscillators depicting the change in the amplitude of oscillations with a change in control parameter μ. Adapted from Ananthkrishnan *et al.* (1998) with permission from Elsevier. 75

2.9 Typical bifurcation diagram showing amplitude p'_{rms} as a function of the equivalence ratio ϕ as observed in a bluff-body stabilized combustor. State (i) corresponds to the state of combustion noise, (ii-v) intermittency and (vi) thermoacoustic instability. Figure is adapted from George *et al.* (2018) with permission Cambridge University Press. 76

3.1 Turbulent V-flame facility in Ben T Zinn lab in Georgia Tech. The large-scale and small-scale statistics of flame fluctuations measurement from this setup is reported in Chapter 4 and 5. Adapted from Humphrey *et al.* (2018) with permission from Cambridge University Press. . . . 85

3.2 Arrangement of the optical diagnostic setup for measuring the flame surface and velocity field using TiO_2 Mie scattering and PIV. Adapted from Humphrey *et al.* (2018) with permission from Cambridge University Press. 87

3.3 The turbulence intensity profile measured at a downstream distance of $y = 1.5$ mm above the flame holder for $f_f = 200$ Hz and for four different turbulence levels at a nominal velocity of (a) 5 m/s and (b) 8 m/s. Here r is the radius of the nozzle exit. 88

3.4 (a) Instantaneous Mie scattering image at at $\bar{u}_y = 4.2$ m/s, $u'/\bar{u}_y = 26.5$ and $f_0 = 750$ Hz. (b) The resulting binarized flame edge with the flame front identified in green. (c) Instantaneous flame edge, $\xi(x, y, t)$, indicated in color, and the mean flame edge, $\langle\xi(y)\rangle$, calculated using Eq. (3.1) and indicated in black for $\bar{u}_y = 4.87$ m/s, $u'/\bar{u}_y = 8.9\%$ and $f_0 = 200$ Hz. All dimensions are in mm. Reproduced from (a) (Humphrey *et al.*, 2018) with permission from Cambridge University Press. 90

3.5 (a) Exaggerated pictorial depiction of converting multi-valued flame front into a locally averaged, leading and trailing flame edge, all of which are single-valued. (b) Representative left flame edge illustrating the difference between the leading, trailing and locally averaged flame edge. (c) Flame response of (-) locally averaged, (- -) trailing, (-.) leading flame edge as a function of the downstream distance. The difference between the response of leading and trailing edge (•) is plotted on the right axis. (b) and (c) are plotted for $f_f = 750$ Hz, $\bar{u}_y = 4.87$ m/s and $u'/\bar{u}_y = 8.9\%$. 92

3.6 (a) The bluff-body stabilized turbulent combustor used for studying passive control of thermoacoustic instability in Chapter 7. (b) Schematic of the combustor cross-section indicating the PIV and CH* field of view. Secondary air injection ports (P1-P5) are present on either side of the centerline for the passive control study. PT indicates the location of the pressure transducer. All dimensions are in mm. 95

4.1 Ensemble-averaged flame fluctuations $\langle\xi'\rangle$ of the left flame edge plotted at different phases of the forcing cycle indicated by the legend. The experimental condition are: (a) $f_0 = 200$ Hz, $\bar{u}_y = 4.83$ m/s, $u'/\bar{u}_y = 8.4\%$, (b) $f_0 = 750$ Hz, $\bar{u}_y = 4.87$ m/s, $u'/\bar{u}_y = 8.9\%$, and (c) $f_0 = 1250$ Hz, $\bar{u}_y = 4.69$ m/s, $u'/\bar{u}_y = 7.6\%$. 98

4.2 Amplitude spectrum of flame fluctuations $\hat{\xi}(y, f)$ plotted for different turbulence levels $(u'/\bar{u}_y)$. Left column corresponds to a nominal velocity of 5 m/s and right to 8 m/s. The forcing frequency is (a,b) $f_f = 200$ Hz, (c,d) $f_f = 750$ Hz and (e,f) $f_f = 1250$ Hz. The fluctuations are measured at $y = 0.5\lambda_c$. The insets in each figure shows the variation in the strength of the peak at the forcing frequency as a function of the turbulence level. 100

4.3 Amplitude of harmonic flame response $\hat{\xi}(y, f_f)$ as a function of downstream distance measured at (a,b) $f_f = 200$ Hz, (c,d) $f_f = 750$ Hz and (e,f) $f_f = 1250$ Hz. Each subfigure compares the harmonic flame response with increasing turbulence levels $u'/\bar{u}_y$. The response is measured for a nominal velocity of (left row) $\bar{U} = 5$ m/s and (right row) $\bar{U} = 8$ m/s. 102

4.4 Flame sheet response, $\hat{\xi}(y, f_f)$, for increasing forcing frequencies at nominal velocity of $\bar{U} = 5$ m/s and comparable flow conditions. The mean velocity $\langle\bar{u}_y\rangle$ and turbulent intensity $\langle u'/\bar{u}_y\rangle$ are: (a) 4.8 m/s, 10.4%, (b) 4.7 m/s, 15.5%, (c) 4.1 m/s, 29.2%, and (d) 3.7 m/s, 33.2%, respectively. Here $\langle.\rangle$ indicates the average of the flow condition indicated in the legend of each sub-figure. The arrow in (a) and (b) indicates the shift in peak with increasing frequency. 108

4.5 Flame sheet response, $\widehat{L}(y, f_0)$, for increasing forcing frequencies at nominal velocity of $\bar{U} = 8$ m/s and comparable flow conditions. The mean flow velocity $\langle\bar{u}_y\rangle$ and turbulence levels $\langle u'/\bar{u}_y\rangle$ are:(a) 8.0 m/s, 8.7%, (b) 7.8 m/s, 14.7%, (c) 7.0 m/s, 27.5% and (d) 6.1 m/s, 35.1%, respectively. Here $\langle.\rangle$ indicates the average of the flow condition indicated in the legend of each sub-figure. The arrow in (a)-(c) shows the shift in peak with increasing forcing frequency. 109

4.6 (a-c) Comparison of harmonic response of the left and right flame edge for representative forcing conditions for $\bar{U} = 5$ m/s. (d-f) Axial dependence of the phase difference, $\Delta\phi$ between the response of the two flame edges. The experimental conditions are: (a, d) $f_f = 200$ Hz; $\langle u'/\bar{u}_y\rangle \sim 8.5\%$; (b, e) $f_f = 750$ Hz; $\langle u'/\bar{u}_y\rangle \sim 9.1\%$; and (c, f) $f_f = 1250$ Hz, $\langle u'/\bar{u}_y\rangle \sim 12.7\%$. 111

4.7 The correlation coefficient between left and right flame edge for: $\bar{U} =$ (a-c) 5 m/s and (d-f) 8 m/s, and (a,d) $f_f = 200$ Hz, (b,e) $f_f = 750$ Hz and (c,f) $f_f = 1250$ Hz for increasing turbulence levels. The markers are consistent with those in Figs 4.3. 111

4.8 Flame peak correlation between the left and the right edge measured at the location of maxima in flame sheet response at nominal velocity (a) $\bar{U} = 5$ m/s and (b) $\bar{U} = 8$ m/s for different forcing frequencies. 113

4.9 Normalized heat release response, $|\hat{Q}(y, f_f)|/\bar{Q}$ measured from the flame sheet response plotted as a function of the normalized downstream distance y/λ_c for (a) $\bar{U} = 5$ m/s and (b) $\bar{U} = 8$ m/s at $f_f = 200$ Hz. The markers are consistent with those used in Fig. 4.3. . 116

4.10 Spatially integrated heat release response measured from the harmonic flame response as a function of the (a) turbulence level, $u'/\bar{u}_y$, for different forcing frequencies and nominal velocities, and (b) forcing frequency, f_f, at different turbulence levels. The $1/f_f$ roll-off in the global heat release rate response with increase in forcing frequency has been indicated in (b) 117

5.1 Temporal power spectral density $E(\tilde{\omega})$ measured at various axial locations y/λ_c, for flame F1. The power spectra varies as $E(\tilde{\omega}) \sim \tilde{\omega}^{-\alpha}$ over an intermediate range of frequencies. The estimated values of the exponent $-\alpha$ at various y/λ_c are shown in the inset for both flames F1 and F2. In both cases, the exponent is close to -2; the corresponding scaling behavior is depicted by the solid line in the main panel. The frequency corresponding to Gibson ($\tilde{\omega}_g$), Corrsin ($\tilde{\omega}_c$) and Kolmogorov ($\tilde{\omega}_\eta$) scales have been indicated by dashed lines. 124

5.2 (a) Probability density function (PDF) of flame position fluctuations normalized by the standard deviation (σ_ξ) for increasing downstream distance from the flame holder ($y/\lambda_c = 0.2, 1, 2, 5, 8$). (b) Flatness factor ($\langle \xi'^4 \rangle / \sigma_\xi^4$) and skewness ($\langle \xi'^3 \rangle / \sigma_\xi^3$) of the PDF of $\xi'(t)$ as a function of the downstream distance. The data corresponds to flame F1. The PDFs have been shifted vertically for clarity. 132

5.3 PDF of the normalized flame position increment ($\delta\xi'(\tau)/\sigma_\xi$) function for different values of normalized time lag τ/τ_η measured from $\xi'(t)$ at $y/\lambda_c = 0.5$ for flame F1. Each curve has been vertically shifted for clarity. 134

5.4 Flatness factor S_4/S_2^2 (■) and the skewness $S_3/S_2^{3/2}$ (▼) measured at $y = 2\lambda_c$ for flame F1. Note that the left axis for the flatness factor is in logarithms while right axis for the skewness is linear. 136

5.5 Structure function S_p with generalized order p is plotted as a function of the normalized time lag for flame position increments at $y/\lambda_c = 0.5$ for flame F1. Curves have been shifted vertically for clarity. 137

5.6 The variation of the scaling exponents ζ_p with the order p of the structure function, for both flames at $y/\lambda_c = 2$. The dashed line indicates the non-intermittent limit of $\zeta_p = p/2$. The strong deviation of ζ_p from this limit for $p > 2$, implies that the exponents scale anomalously and that the flame fluctuations are strongly intermittent. The error bars represent the standard deviation of the measured values obtained from different time series. 140

5.7 The moment order exponent ζ_p plotted as a function of the normalized downstream distance y/λ_c and order p. 141

5.8 Scaling of the generalized moment (Eqn. 5.19) with time scales τ for various order q. The linear fits are also indicated for each case. The slope of the qth order moment with τ gives the mass exponent $\mu(q)$ and the generalized dimension D_q. The fluctuations $\xi'(t)$ corresponds to $y = 0.5\lambda$ for flame F1. 143

5.9 The variation of (a) the generalized dimension D_q, and (b) the mass exponent $\mu(q) = (q-1)D_q$ as a function of the generalized moment order q measured from ξ' at the indicated y/λ_c values for flame F1. . . 144

5.10 Multifractal spectrum $f(\alpha)$ as a function of the singularity spectrum (α) obtained from the Legendre transform of D_q and q. 149

5.11 Comparison of multifractal spectrum $f(\alpha)$ as a function of the singularity spectrum (α) obtained from the Legendre transform of D_q and q for flame F1 and F2. 151

7.1 Intermittency route to thermoacoustic instability observed in the turbulent combustor. Variation of (a) p'_{rms} and (b) the frequency corresponding to the acoustic (f_a) and hydrodynamic mode (f_h) as a function of nominal velocity of air v_a (bottom axis) and equivalence ratio ϕ (top axis). Adapted from (a) (George *et al.*, 2018) with permission from Cambridge Unversity Press, and (b) (Premchand *et al.*, 2019*b*) with permission from AIP Publishing. 180

7.2 (a-c) Time series of turbulent velocity fluctuations (u'_T) during combustion noise, intermittency and thermoacoustic instability at a representative point inside the combustor shown in the inset in (b). The three states correspond to point A, B and C indicated in Fig. 7.1. (d) The variation of the second-order structure function $F_2(s)$ measured from u'_T with the scale s for the three states. 183

7.3 Comparison of the Fourier amplitude of turbulent velocity fluctuations $|\hat{u}_T(f_a)|$ (m/s), time-averaged vorticity $\bar{\omega}_z$ ($\times 10^3$, s^{-1}), time-averaged heat release field $\bar{q}$ (a.u.) and time-average Rayleigh index $\overline{RI}$ (a.u.) during the states of (a-d) combustion noise, (e-h) intermittency and (i-l) thermoacoustic instability. The flow conditions are indicated in Fig. 7.1. The span of the ordinate and abcissa are indicated in Fig. 3.6b. The gray region indicates the position of the bluff-body. 186

7.4 Phase-averaged heat release rate field at the indicated phases of the acoustic cycle during the state of thermoacoustic instability. The gray mask indicates the position of the bluff-body. 188

7.5 Illustration of control of thermoacoustic instability through secondary air injection targeting different regions of the combustor. (a) Amplitude of pressure fluctuations, p'_{rms}, as functions of the momentum ratio, $(\upsilon_{inj}/\upsilon_a)^2$, and mass flow ratio, $\dot{m}_{inj}/\dot{m}_a$. Representative (b) time series and (c) sound pressure level (SPL) observed during thermoacoustic instability, point I in (a), and subsequent control, point II in (a). Subfigure (a) adapted from (Krishnan *et al.*, 2019*b*) with permission from IOP Publishing. 191

7.6 (a) Amplitude of velocity fluctuations $|\hat{u}_T(f_a)|$, (b) time-averaged vorticity $\bar{\omega}_z$, (c) time-averaged HRR $\bar{q}$ and (d) Rayligh index $\overline{RI}$ during suppressed state corresponding to point II in Fig. 7.5(a) attained after inject secondary air from port P1. 193

7.7 Heat release rate field during the state of suppression of thermoacoustic instability for point II indicated in Fig. 7.5a. (a) Intermittent acoustic pressure fluctuations during suppression and (b) an enlarged portion showing alternate cycles of periodic and aperiodic fluctuations. (c) Points i-iv correspond to $\dot{q}'(x,y)$ at four points of the periodic cycle indicated in (b). Points v-viii correspond to $\dot{q}'(x,y)$ at the indicated points during aperiodic oscillations as indicated in (b). 194

7.8 Field of Hurst exponent (H) calculated from the intensity of velocity fluctuations during (a) combustion noise, (b) intermittency and (c) thermoacoustic instability. The experimental conditions for (a-c) correspond to the points A, B and C in Fig. 7.1, and (d) corresponds to point II in Fig. 7.5. 197

7.9 Histogram showing the distribution of the Hurst exponent (H) during the states of combustion noise (CN), intermittency (INT), and thermoacoustic instability (TAI). 199

GLOSSARY

The following are some of the commonly used terms in the thesis:

Fractal dimension	Typically used to characterize geometrically complex objects. It is defined as the ratio of change of statistical measure such as length, area, volume, etc., of the complex object with a change in the scale of measurement.
Harmonic flame response	Refers to the response of flame when subjected to harmonic fluctuations. The response is typically measured by determining the amplitude and phase of the flame fluctuations measured at the forcing frequency using Fourier transform.
Intermittency	Refers to the property of processes and variables to depict extreme value fluctuations with a higher probability than observed for random Gaussian processes. The probability density function of these fluctuations typically posses wide and significant tails.
Kinematic restoration	The kinematic process through which fluctuations on flame surface are smoothed on account of the flame propagation along its local normal.
Lean combustion	Combustion of fuel in the presence of air/oxidizer in excess of the amount or air/oxidizer required for a stoichiometric reaction to take place.
Premixed combustion	Combustion of a mixture of fuel and air/oxidizer after they have been thoroughly mixed.
Thermoacoustic instability	A phenomenon arising in confined combustion environment where a feedback between pressure fluctuations and heat release rate fluctuations arising from laminar or turbulent flames, causing a growth in acoustic energy and leading to a state of large amplitude pressure oscillations. Thermoacoustic instability leads to catastrophic damage in gas turbines.

ABBREVIATIONS

BVK	Bénard-von Kármán
CN	Combustion Noise
DNS	Direct Numerical Simulation
HRR	Heat Release Rate
INT	Thermoacoustic Intermittency
K41	Statistical theory of turbulence by Kolmogorov (1941*b*,*a*)
KOC	Kolmogorov-Oboukhov-Corrsin phenomenology for scalar turbulence
LCO	Limit Cycle Oscillations
LES	Large Eddy Simulation
LPG	Liquefied Petroleum Gas
LPP	Lean Premixed Prevaporized
NO_x	Oxides of NO and NO_2
ORZ	Outer Reaction Zone
PDF	Probability Density Function
PIV	Particle Image Velocimetry
PM	Particulate Matter
SL	Shear Layer
TAI	Thermoacoustic Instability
UHC	Unburned Hydrocarbons

NOTATION

Upper-case Latin alphabets

A, A_0, A_T	Flame area
B	Amplitude of oscillations of the flame holder
C	Scalar field
C_s	Universal constant for scalar spectrum
C_k	Kolmogorov's constant
Da	Damköhler number
D_q	Generalized dimension of order q
E	Power spectral density
F	Arbitrary function, Flatness factor
G	Scalar level-set function
H	Hurst exponent
Ka	Karlovitz number
L	Mean flow length scale, m
Le	Lewis number
$\bar{L}_f$	Mean flame length, m
Pe	Peclet number
Q_{ij}	Second-order velocity correlation tensor, m^{2}s^{-2}
R	Two-point correlation
Re	Reynolds number based on the indicated scale
RI	Rayleigh index
Sc	Schmidt number
S_{ij}	Strain-rate tensor, s^{-1}
S_p	Structure-function of order p
St	Strouhal number
T	Time duration for statistical averaging, s; Time period, $T = 1/f$
$\bar{U}$	Nominal flow velocity, ms^{-1}
V	Control volume
$\bar{W}_f$	Half-width of mean flame, m
X, Y	Constants

Lower-case Latin alphabets

c_0	Speed of sound, ms^{-1}
c_p, c_v	Heat capacity
d	Diameter of flame holder, m
d_i	Inlet diameter, m
f, f_a, f_h, f_s	Frequency, Hz
f_f	Forcing frequency, Hz

f, g	Longitudinal and lateral velocity correlation
$\boldsymbol{k}$	Wavenumber, m^{-1}
k_c	Phase speed parameter
ℓ	Integral length scale, m
ℓ_g	Gibson length scale, m
$\dot{m}$	Mass flow rate, mass burning rate of fuel, kg s^{-1}
$\boldsymbol{n}$	Local flame normal
p	Fluid or acoustic pressure, Pa
$\dot{q}$	Heat release rate
r	Scale separation, m
s_c	Flame consumption speed, ms^{-1}
s_L	Laminar flame speed, ms^{-1}
u'	Turbulent root mean square velocity, m^{-1}
u_η	Characteristic velocity of Kolmogorov size eddy, ms^{-1}
$\bar{u}_y$	Mean flow velocity, ms^{-1}
$\boldsymbol{u}$	Velocity vector, ms^{-1}
x, y, z	Rectangular Coordinate system, m

Greek

α	Power spectrum scaling exponent, Multifractal singularity exponent
β_p, β'_p	Empirical constant for p^{th} order structure-function
γ	Ration of specific heat capacity
Γ	Spectrum function of flame fluctuations
δ_F	Laminar flame thickness, m
ε	Rate of turbulent kinetic energy dissipation per unit mass, m^2 s^{-3}
ζ_p	Scaling exponent of p^{th} order structure-function
η	Kolmogorov length scale, m
η_b	Batchelor length scale, m
η_c	Corrsin length scale, m
η_M	Markstein length, m
θ	V-Flame half-angle, deg
κ	Flame curvature
λ	Thermal conductivity
λ_c	Wavelength of coherent disturbances, m
λ_{int}	Wavelength of interference of disturbances, m
μ	Dynamic viscosity, Kg(ms)$^{-1}$
ν	Kinematic viscosity, m^{2}s^{-1}
ξ	Instantaneous flame fluctuations
ρ	Density, kg m^{-3}
σ_ξ	Standard deviation of flame fluctuations
τ_c	Turn-over time scale of Oboukhov-Corrsin scale eddy, s
τ_g	Turn-over time scale of Gibson scale eddy, s
τ_η	Turn-over time scale of Kolmogorov sized eddy, s

τ_{ij}	Shear stress tensor, Kg $\mathrm{m}^{-1}\mathrm{s}^{-2}$
ϕ	Equivalence ratio
χ	Rate of scalar dissipation
ω	Vorticity, Angular frequency, s^{-1}

Script

$\mathcal{D}$	Scalar diffusion coefficient
$\mathbb{D}$	Fractal dimension of turbulent flames
$\mathscr{D}$	Fractal dimension of intersection of set $\mathcal{S}_1$ and $\mathcal{S}_2$
$\mathcal{H}$	Heaviside function
$\Im$	Imaginary part of a complex quantity
$\mathcal{J}_\alpha$	Set containing scaling exponents α
$\mathcal{N}$	Gaussian process
$\mathcal{O}()$	Of the order
$\Re$	Real part of a complex quantity, set of real numbers
$\mathbb{R}$, $\mathbb{R}^d$	Real number space, Euclidean space of $d-$dimensions
$\mathcal{S}_{1,2}$	Sets containing fractal objects

Subscripts

a	Associated with acoustics
F	Associated with laminar flame
η	Associated with Kolmogororov scale
ij	Index notation for tensors
ξ	Related to flame fluctuations
L, R	Related to left or right edge of the flame
r	Related to separation r
R	Associated with reaction zone of a flame
t	Tangential component
τ	Related to time delay τ
u	Related to velocity field $\boldsymbol{u}$
x, y, z	Along rectangular coordinates

Other symbols

$(\cdot)_{\mathrm{rms}}$	Root mean square
$(\cdot)'$	Fluctuating above mean

$\bar{(\cdot)}$	Mean
$\hat{(\cdot)}$	Fourier transformed quantity
$\langle\cdot\rangle$	Ensemble or time average

Operators

δ	Differential increment in a quantity
∇	Differential operator
$\|\| \cdot \|\|$	Norm
$\angle(\cdot)$	Phase of the quantity
$\subset$	Subset
$\sim$	Relates quantities to their leading order
$\forall$	For all

CHAPTER 1

INTRODUCTION

1.1 HISTORICAL OVERVIEW

1.1.1 Mankind and fire

Humans have always been fascinated by fire and flames. One of mankind's biggest achievements has been the ability to harness the power of fire and flames. Indeed, it is this ability to control fire for a better part of the last $300,000$ years that have fulfilled our energy requirements, kept us safe from natural elements, and have led to unremitting evolutionary and technological progress (Harari, 2014). The power of combustion led us through the bronze and metal ages where metallurgy became the driver (Tylecote, 1977; Choi, 2012). Metallurgy ushered in the study and development of metals and alloys and served as one of the foundations of modern society (Brinley, 1993). It was, however, only since the beginning of the industrial revolution in the late sixteenth century did we truly realise the potential of energetic fuels and developed means of converting their latent energy into efficient work.

The advent of the industrial revolution started with the widespread use of coal combustion in smelters and thermal power plants. The development of steam engines by James Watts in 1776 revolutionized transportation. Typically, coal combustion was used to convert water into steam, which then was used as the prime mover for generating power in transport ships, trains, and power plants. By the late 1800s, steam engines were complemented by the development of internal combustion devices operating on a variety of thermodynamic principles such as Rankine, Brayton, Otto, Diesel, etc. While these reciprocating engines have since then remained widespread in commercial transport vehicles, it was soon realized that they provided a very low power-to-weight ratio. This was especially problematic for operations that required a high power-to-weight ratio, such as naval propulsion and aviation. These drawbacks motivated the development of gas turbine engines operating on an open Brayton cycle (Turns, 1996).

The first patent of the gas turbine was granted to John Barber, a British inventor, in 1791 (Cook, 2003). Although the gas turbine was technically and conceptually sound, it was not physically viable because of the limitations in the metallurgical quality and fabrication techniques of the time. It was only a century later that the first practically viable gas turbine was independently developed by Frank Whittle in England and Hans von Ohain in Germany around 1930s. In 1939, the first gas turbine power plant with a capacity of 4 MW was established in Neuchâtel, Switzerland, and remarkably remained operational for 63 years till 2002 (ASME, 2007). Since then, gas turbines have become integral to the naval and aviation propulsion and power generation industry.

Today, the aviation industry is a crucial cog of the global transportation network and has a global market share of US\$170 billion[1]. Further, global aviation is one of the fastest-growing economic sectors, boasting a compound annual growth rate of greater than 7.6% and is tipped to grow to US\$303 billion by 2026, despite recent setbacks due to COVID-19 pandemic[1]. The multi-billion industry relies solely on high-performing gas turbine engines. In the energy sector, gas turbine power plants are responsible for 23% of all electrical energy produced throughout the world and generating revenue of around US$20 billion (IEA, 2021). Gas turbines have become a key technology on which the entire world depends directly or indirectly.

---

[1] Source: https://www.mordorintelligence.com/industry-reports/aviation-market

1.1.2 Environmental concerns and global warming

The drive towards modernization has come at a price to humanity. The rush towards ever-increasing mechanization, particularly since the industrial revolution, has led to a gradual increase in pollution levels across the globe. High levels of particulates, oxides of sulphur, nitrogen, and carbon have led to several health emergencies. The great smog of London remains one such instance when unchecked pollution from industries exacerbated by cold weather and anticyclonic conditions led to around $10,000 - 12,000$ deaths by modern estimates (Stone, 2002). Estimates show that around $8 - 10.2$ million excess deaths every year are caused by air pollution, with around 62% of them in China and India (Vohra *et al.*, 2021; Burnett *et al.*, 2018). The picture is all too familiar given that Indian cities regularly feature top of the list of cities with the worst air quality index (WHO, 2018).

The world has seen a persistent and gradual increase in the concentration of CO_2 levels in the atmosphere since the industrial revolution (inset in figure 1.1). Today, the global CO_2 concentration levels stand at 416 ppm (NASA, 2021), and have grown by 48% above the pre-industrial levels. The increase over the last 300 years is much larger than what happened naturally over $20,000$ years since the last glacial maximum (figure 1.1). CO_2 is a potent greenhouse gas, and the persistent increase in its concentration has led to an increase in global temperatures. The positive or negative departure from the average

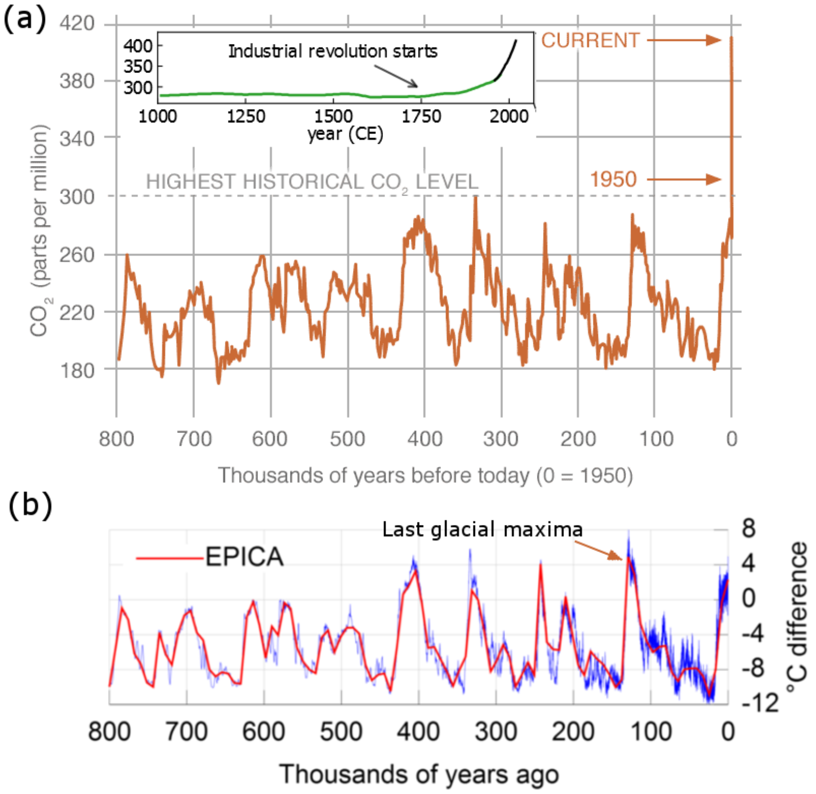

Figure 1.1: (a) Historic trend of CO_2 levels (NASA, 2021) and the (b) global temperature anomaly measured by EPICA from Antarctica Vostok ice core (Augustin *et al.*, 2004). Reproduced with permission from (a) NASA and (b) Springer Nature.

temperature over a period of time is referred to as temperature anomaly. The global temperature anomaly measured from the Antarctica Vostok ice core (figure 1.1b) shows a correlated behavior with the historical variation in CO_2 levels. There has been a sharp increase in global temperatures, driven by anthropogenic emission of greenhouse gases, similar to levels observed during the last glacial maximum. The correlation is indicative of the feedback loop between the global temperature and the atmospheric levels of CO_2 and other greenhouse gases (Al-Ghussain, 2019; Hansen *et al.*, 2006). Other measures such as the global sea surface temperature and the land-ocean temperature also corroborate the striking picture of significantly larger temperature anomalies (Hansen *et al.*, 2006). The increase is clearly evident when we compare the global temperature

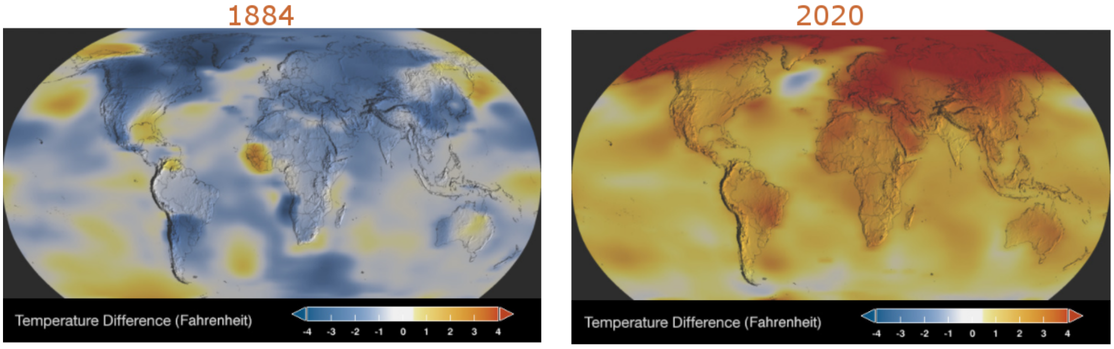
1884
2020
Temperature Difference (Fahrenheit)
-4 -3 -2 -1 0 1 2 3 4
Temperature Difference (Fahrenheit)
-4 -3 -2 -1 0 1 2 3 4

Figure 1.2: Pronounced global temperature anomaly observed in 2020 in comparison to that during industrial age in 1884 (Courtesy: NASA, 2021).

anomaly during the industrial age in 1884 with the contemporary levels (figure 1.2).

Anthropogenic emission-driven global warming and climate change are perhaps the biggest challenges that mankind has faced till now. Extreme weathers, loss of polar ice caps, irreparable loss of flora and fauna in what is coming to be known as the sixth mass extinction (McKinney and Lockwood, 1999; Wake and Vredenburg, 2008), and inundation of several island nations due to rising sea levels have become our reality. There is an alarming urgency with which mankind needs to fight the biggest existential threat it has ever faced. The recent Paris Agreement was a step in that direction which 196 countries ratified in 2016 in order to keep the rise in global average temperature to well below 2°C by reducing the emission of greenhouse gases (UNCC, 2016).

1.1.3 The way forward: Alternative and low-emission technologies

While there is a requirement for global cooperation and informed policy-making by governments of countries the world over, a key solution in this existential fight for survival is the development of low emission technologies. Global energy review of 2021 suggests that global energy demands are set to increase above pre-COVID pandemic

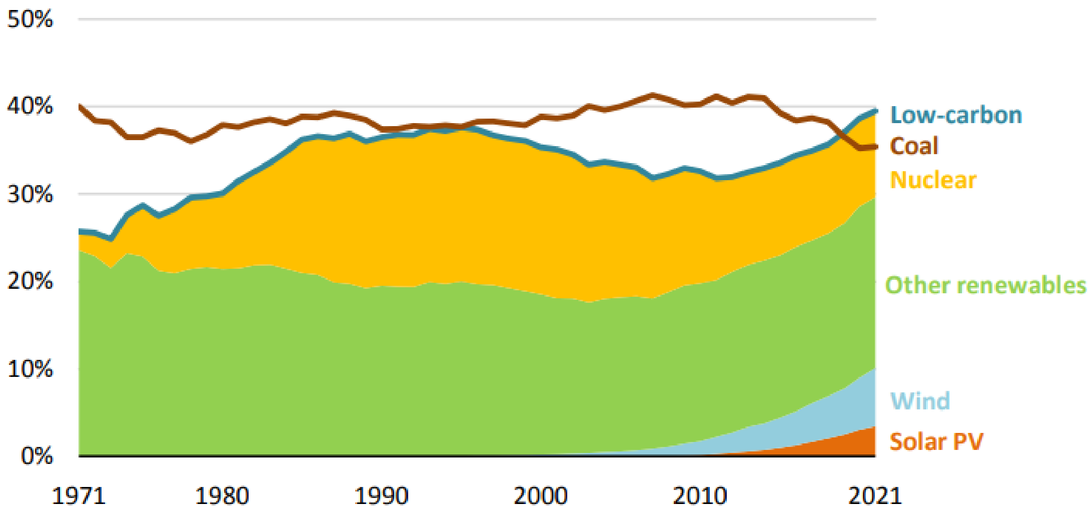

Figure 1.3: Sector based share of power output from various sources of electricity generation over the last four decades. Adapted from (IEA, 2021).

levels (IEA, 2021). The increase in electricity, oil, coal, and gas would be driven by the contributions from emerging markets such as south-east Asian countries. Along with the demand for power, the global energy-related CO_2, CO and NO_x emissions are expected to be heading towards their second-largest annual increase ever. Similarly, the market forecasts growth of over 7.6%[1] in global aviation. The net CO_2 emission from aviation is around 2.5% of all CO_2 emissions (Ritchie, 2020). However, a recent review suggests that aviation emission such as NO_x, CO and aerosols are exacerbating global warming three times as fast as those associated with CO_2 emission from aviation alone (Lee *et al.*, 2021). Thus, by all estimates, global emissions of greenhouse gases are bound to increase in the coming decades.

Burgeoning new technologies capable of harnessing renewable energy resources have been revitalized by the Paris agreement. The dependence on coal as the primary fuel for power generation has increasingly been disincentivized and disinvested over the years.

---

[1] Source: https://www.mordorintelligence.com/industry-reports/aviation-market

In fact, the share of power generated through coal power plants has fallen below the combined output of low-carbon and renewable technologies for the first time in history (figure 1.3). A significant contributor to the fall in demand for power generated from coal power plants has been the rise of low-carbon gas turbine power plants, which are responsible for the production of 23% of all electrical energy produced (IEA, 2021). The share of alternate energy resources such as solar, wind, and nuclear have bucked the trend and emerged as the sectors with the largest growth (IEA, 2021). In the future, with greater investment through further policy changes, the share of electricity produced by these renewable technologies will no doubt increase. At present, however, low-emission gas turbine power plants remain a crucial cog in our fight towards lowering global greenhouse gases.

1.2 GAS TURBINES: TURBULENT, LEAN PREMIXED COMBUSTION TECHNOLOGY

1.2.1 Pollutant Emissions

Gas turbines primarily rely on the combustion of fuels such as methane or natural gas, ethane, ethylene, propane, and butane (Lieuwen and Yang, 2005). The combustion of these fuels lead to the emission of carbon monoxide (CO), carbon dioxide (CO_2), oxides of nitrogen (NO_x), unburned hydrocarbons (UHC) and particulate matter (PM). As discussed in the previous sections, CO_2 and NO_x emissions are direct contributors to global warming. The level of gas turbine emission of these pollutants is a direct consequence of their applications. For instance, aircraft gas turbines are constrained by the necessity to maintain combustion at different power levels throughout different stages of flight. They should also be capable of mid-air re-ignition in the case of a flame blow-out. Similarly, ground-based gas turbines used in power plants must be capable of ramping up power based on the demand for energy. These demands constrain the choice of operating parameters such as air-fuel ratio, pressure, temperature, etc., and result in increased emission of various pollutants at various stages of operation.

The emission of NO_x and PM increases at high-power conditions during aircraft take-off or power ramp-up in power plants. On the other hand, low power operation leads to an increased emission of UHC and CO (Gokulakrishnan and Klassen, 2013). Thus, there is always a trade-off in the operability requirements based on the allowable emission levels. While, the control and mitigation of emission of CO, CO_2, UHCs, PMs and NO_x are important, the present thesis is directly motivated from efforts of reducing NO_x emission levels in gas turbine engines.

Generally, NO and NO_2 are referred to as NO_x. These NO_x compounds are both primary pollutants in that they directly affect human health and the environment and also act as secondary pollutants by reacting with other gases to produce other pollutants (Skalska *et al.*, 2010). NO_x emissions are highly toxic, and prolonged exposure is known to increase the risk of respiratory and cardiovascular diseases (Chaloulakou *et al.*, 2008) and cause acute lung injury through pneumonitis and fulminant pulmonary edema (Woodrow, 1997). Further, NO_x emissions also promote tropospheric ozone (O_3) production, which is very toxic to human health.

Apart from severe health concerns, NO_x emissions also contribute to environmental problems such as acid rains, photochemical smog, greenhouse effect, and ozone layer depletion. Nitrous oxide N_2O, produced from NO_x emissions, is a potent greenhouse gas and is capable of absorbing infra-red radiation with 300-times higher intensity than CO_2 and has an atmospheric lifetime of around 120 years (Tian *et al.*, 2020). Further, N_2O leads to the depletion of stratospheric ozone depletion (Prather *et al.*, 2015). NO_x emissions are severely concerning and have led to increasingly stringent regulations on their emission over the years throughout the world.

1.2.2 NO_x generation pathways

There are a number of different pathways through which NO_x emissions are produced, as reviewed in Skalska *et al.* (2010) and Gokulakrishnan and Klassen (2013). For the present purposes, we briefly discuss the mechanisms responsible for the generation of NO_x in gas turbine relevant conditions. The formation of NO_x is most affected by the temperature of combustion. NO_x emission is enhanced if the temperature of combustion exceeds 1800 K. The production of NO_x at elevated temperatures is known as the thermal pathway. However, for flames with peak temperatures less than 1800 K and low residence times, as in gas turbines, this is not the leading pathway for NO_x production. The second is known as the N_2O pathway in which reaction is initiated between atomic oxygen and molecular nitrogen leading to the formation of N_2O. The N_2O then reacts with atomic oxygen or hydrogen to produce NO_x. The third pathway is known as the prompt NO pathway, where there is a reaction between hydrocarbon radicals such as CH and N_2 leading to the formation of NCN radicals. The NCN radicals then react with atomic O and H to form NO_x. Finally, the fourth pathway is known as the NNH

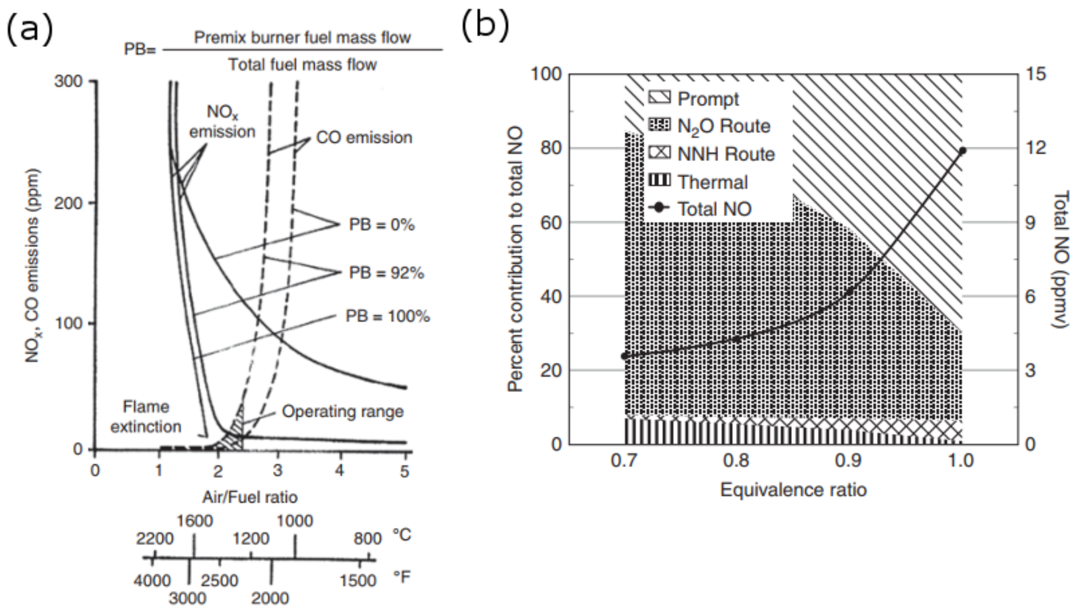

Figure 1.4: (a) NO$_x$ and CO emission as a function of the air-to-fuel ratio and combustion temperature for different levels of premixedness indicated by PB. (b) Computational result showing the relative contribution of different NO$_x$ producing pathways at different equivalence ratios. (a) Reproduced with permission from (Maghon *et al.*, 1988) and (b) from (Gokulakrishnan and Klassen, 2013).

pathway where the radical NNH is formed through the reaction of N_2 and H, which then reacts with atomic O to form NO$_x$.

Figure 1.4(a) shows the NO$_x$ and CO emission as a function of the air-to-fuel ratio along with the temperature of combustion for various degrees of fuel premixedness indicated by PB. Fuel premixedness indicates the degree of fuel and air mixing before combustion takes place. We can clearly observe the exponential increase in NO$_x$ emission as the temperature of combustion is increased, and the air-to-fuel ratio is decreased. In figure 1.4(b), we observe the relative contribution of different pathways of NO$_x$ production, as discussed previously, for different equivalence ratios. The equivalence ratio indicates the air-to-fuel ratio of the combustion relative to the stoichiometric air-to-fuel ratio. The stoichiometric air-to-fuel ratio implies a balanced chemical reaction between air and fuel such that there is no excess air or fuel left after the reaction. We note that NO_x is produced predominantly through the prompt NO route and N_2O routes for gas turbine engine relevant equivalence ratios (Gokulakrishnan and Klassen, 2013).

1.2.3 Emission mitigation strategies

Strategies for limiting and mitigating emissions can broadly be classified into two classes. The first includes methods which are employed for removing NO_x from the combustion by-products, and the second includes methods capable of reducing the production of NO_x during combustion.

The first of these methods involve the removal of NO_x through the use of fuel reburning, where additional fuel is used to burn the by-products of primary combustion in order to convert NO_x into N_2 (Myerson, 1975). Other methods involve the catalytic and non-catalytic reduction of NO_x into N_2 using catalytic agent (Pt/Al_2O_3, V, etc.) or reacting reagents such as urea or ammonia (Skalska *et al.*, 2010). Yet another method is the use of ozone in oxidizing NO_x into N_2O_5, which can then be removed as dry deposition (Skalska *et al.*, 2010). Alternatively, combustion in the presence of pure oxygen or other nitrogen-free oxidizers can be used for reducing NO_x emission. However, combustion in pure oxygen leads to very high temperatures, which requires additional cooling mechanisms. If air is used as a coolant, NO_x may still be formed. Finally, NO_x can also be sequestered from the combustion products through the use of chemical adsorbents such as activated carbon or scrubbing in absorbents such as H_2O_2 and other alkaline solutions (Skalska *et al.*, 2010).

The second strategy is to limit the formation of NO_x during the process of combustion. The formation of NO_x strongly depends on the temperature of combustion, as shown in figure 1.4. Thus, a simple strategy is to reduce the temperature through various means. These include the injection of energy diluting agents such as water, steam, or exhaust gas recirculation (EGR). However, injecting water and EGR often leads to reduced efficiency, enhanced CO emission, and local quenching (Mcdonell and Klein, 2013; Amato *et al.*, 2013). Combustion staging is another commonly used method for reducing the temperature of combustion and NO_x emissions. Combustion staging involves manipulating the amount of air and fuel injected at various locations to prevent peak temperature in the combustion zone (Davis and Black, 1995; Winkler *et al.*, 2017; Bothien *et al.*, 2019).

The above-mentioned methods are effective in reducing NO_x emissions. However, they suffer from many drawbacks. Treating combustion by-products rely on catalytic and adsorption agents, which are often very expensive and have low durability (Skalska *et al.*, 2010). Other relatively inexpensive methods such as non-catalytic reduction and scrubbing often require heavy installments, making them unsuitable for aircraft applications and are only used in land-based gas turbine power plants. Similarly, the concept of combustion staging requires a sequence of combustion chambers, leading to an increase in length and weight of the combustor, making them unsuitable for aircraft applications. One of the most widely used approaches which do not have the above drawbacks is the use of lean, premixed, and sometimes pre-vaporized combustion.

1.2.4 Lean, premixed combustion

In lean, premixed combustion, the fuel is thoroughly mixed with excess air before combustion (Lefebvre, 1977; Lieuwen and McManus, 2003). Since air is used in excess during combustion, the equivalence ratio (ϕ) is less than unity and is referred to as lean combustion. If the fuel is gaseous, then it is directly mixed with air, and if the fuel is liquid such as ethanol, Jet-A, heptane, kerosene, etc., then the liquid fuel is first pre-vaporized before mixing it with air (Gokulakrishnan *et al.*, 2008; Temme *et al.*, 2014). There are multiple advantages of lean, premixed combustion. First, as the fuel is burned in excess air (i.e., $\phi < 1$), the temperature of combustion is much lower in comparison to combustion at stoichiometric ($\phi = 1$) or rich conditions ($\phi > 1$). The lowered temperature of combustion automatically limits the amount of NO_x produced during the reaction (figure 1.4). Consequently, combustion by-products no longer need to be treated to reduce emission levels. Second, since excess air is used, fuel is completely burned, leading to a significant reduction in the emission of UHCs and PMs. Third, as the fuel is fully premixed, the chances of near stoichiometric conditions inside the combustion zone are completely eliminated. Finally, fully premixed combustion leads to a more homogeneous temperature distribution at the combustor outlet, leading to higher efficiency in turbine operation.

Despite manifest advantages of lean, premixed combustion, no aircraft to date has utilized fully premixed combustion. Gas turbine combustors used in aviation generally operate at fuel-rich ($\phi > 1$) conditions and continue to be a major source of NO_x emissions (Freeman *et al.*, 2018). Fully and partially premixed combustion is used almost exclusively in land-based gas turbines. The lack of implementation of fully-premixed combustion in aircraft stems from a number of issues. The first difference is the use of liquid fuels in aero engines as opposed to the use of gaseous fuels in industrial gas turbines. The fuel and control system for premixing and pre-vaporizing liquid fuels scale non-trivially with engine size, leading to difficulty in implementation in aircrafts. Second, the efficiency of premixed combustion under take-off, cruise, and landing have been found to be lacking (Ralph *et al.*, 2009; Hassa, 2013).

However, the biggest hurdle in the use of lean, premixed combustion is the issue of stability of the combustor. Fully premixed flames are difficult to stabilize and quite often are prone to lift-off at the flame holder and flashbacks upstream of the combustion chamber along the air-fuel lines. This is only exacerbated by the greater risk of autoignition of the air-fuel mixture before they reach the combustion zone (Lieuwen *et al.*, 2008). Further, premixed flames are prone to extinction and blow-out, threatening complete power outage in the combustor (Shanbhogue *et al.*, 2009*b*). Finally, fully-premixed combustors are prone to the problem of combustion or thermoacoustic instability. Thermoacoustic instability (TAI) refers to the phenomenon of large amplitude pressure oscillations arising from the non-trivial coupling between heat release rate fluctuations from the flame and the acoustic pressure fluctuations inside the combustor. These oscillations severely limit the operability limits of gas turbines, increase maintenance expenses, enhance the thermal loading on combustor walls and turbine blades, and in some cases lead to a complete failure of the combustion system (Lieuwen and McManus, 2003).

1.2.5 The challenge of lean, premixed turbulent combustion

Thus, lean, premixed turbulent combustion is a topic of immense practical interest and has led to a large volume of analytical, experimental, and computational studies (see Peters, 2001; Poinsot and Veynante, 2005; Law, 2010, for review). Despite being a field of active research interest, the study of lean, premixed turbulent combustion is replete with many fundamental complications. The problem essentially arises from the interaction of a large range of scales of turbulent motion with heat and mass transport processes that underlie the process of combustion. This is compounded by the lack of isotropy on account of flow dilation due to non-isothermal effects, which promote flame instabilities (Law, 2010; Chaudhuri *et al.*, 2011). Further, there are significant scatter in experimental measurements of quantities of practical interest in turbulent premixed combustions such as turbulent flame speed, flame stretch, etc. These quantities have been known to depend crucially on the burner configuration (Driscoll, 2008). These problems have refuted efforts towards the development of a self-consistent and universal theory of turbulent combustion.

More specifically, the loss of stability of lean, premixed turbulent flames discussed earlier arise from statistics of quantities that depend on the gradient of turbulent quantities. For instance, high local strain-rate and curvature are well-known to lead to local flame extinctions in premixed flames (Chaudhuri *et al.*, 2010; Morales *et al.*, 2019; Shanbhogue *et al.*, 2009*b*). Flame strain-rate and curvature depend on the gradient of flame surface fluctuations and turbulent velocity fluctuations. Thus, the practical concerns of flame extinction and blow-out are necessarily coupled with the small-scale phenomenology of turbulent flows. Thus, the study of small-scale phenomenology of turbulent premixed flames is of immense practical relevance.

1.2.6 The problem of thermoacoustic instability

The other aspect of stability in turbulent premixed combustion concerns the coupling between heat release rate fluctuations from the turbulent flame and the acoustic pressure fluctuations arising inside a combustion chamber. The feedback coupling leads to a growth in the acoustic energy of the combustion chamber and leads to the state of limit cycle oscillations known as combustion or thermoacoustic instability (Lieuwen and Yang, 2005; Juniper and Sujith, 2018). The large-amplitude pressure and heat release rate oscillations are detrimental to combustor operation and cause the failure of gas turbine engines through extreme thermal loading and pressure-induced structural vibrations. Thermoacoustic instability continues to severely affect the operational capabilities of liquid-fuelled rocket engines (Oefelein and Yang, 1993; Culick and Kuentzmann, 2006) and gas turbines (Lieuwen and Yang, 2005).

The mechanism of thermoacoustic instability was first proposed in the seminal exposition by Rayleigh (1878) and continues to be used to the present day. The essential idea is that the acoustic waves inside a combustion chamber perturb the flame surface, as well as compress and expand the gas around the flame. If the heat released by the perturbed flame is higher on average during the local pressure maxima, more work is done by the gas during the acoustic expansion phase than the work done on it during the acoustic compression phase. If the excess work is not dissipated, acoustic energy inside the combustor grows, leading to a growth in the amplitude of pressure oscillations (Rayleigh, 1878; Chu, 1965).

The mechanism of coupling between the heat release rate and acoustic pressure fluctuations strongly depends on a number of different factors such as combustion mechanisms, acoustic modes of the combustor, presence of hydrodynamic instabilities, and turbulence levels (see Lieuwen, 2003; Poinsot, 2017; Juniper and Sujith, 2018; Sujith and Unni, 2020, for a review). Thus, delineating the nonlinear contributions from these mechanisms is essential for devising control strategies capable of breaking the coupling between heat release rate and acoustic pressure fluctuations.

1.3 MOTIVATION

All current estimates indicate that gas turbines will continue to operate in power generation, naval, and aviation industries, despite the growing emission concerns. The key to reducing emission then is through the development of reliable lean, premixed combustion technology.

Developing a comprehensive understanding of the dynamics of premixed flames is challenging because of the complex interactions taking place inside combustion chambers. As discussed above, the stability of lean, premixed turbulent flame remains an elusive and unsolved problem. These stability issues arise from kinematic balances at play at small-scales in turbulent flows, as well as from nonlinear coupling of the overall heat release rate with broadband turbulence fluctuations and narrowband acoustic pressure fluctuations arising at large scales. Thus, one needs to carefully consider the problem as a multiscale phenomena and analyse the large-scale harmonic flame response when dealing with coupling with acoustic fluctuations, and quantify the small-scale statistics of flame fluctuations, where the effect of turbulence on the dynamics of turbulent flames are concerned.

The present thesis is, therefore, motivated directly by the requirement of developing a scale-dependent understanding of the dynamics of turbulent premixed flames.

1.4 OBJECTIVES

The objectives of the present thesis are to recognize the multiscale nature of the problem of turbulent premixed combustion and perform a scale-dependent quantification of large and small-scale dynamics. More precisely, large-scale characteristics of the flame response such as flow instabilities, global heat release response and flame-acoustic coupling lead to thermoacoustic instability Lieuwen (2012). In contrast, small-scale dynamics of turbulent flows fundamentally affect the physical balances on which the flame relies upon for stability (Peters, 2001; Law, 2010). Consequently, the dynamics of small-scale flame fluctuations are expected to be drastically different from their large-scale counterpart and would play a dominant role in effects such as local flame quenching and flame blow-out.

In cognizance of the above, the objectives of the thesis are:

1. To explain the large-scale response of flame surface fluctuations when simultaneously subjected to narrowband and broadband turbulent fluctuations.

2. To understand the various mechanisms which affect the local flame behavior and explain its role in determining the global flame behavior.
3. To characterize and quantify the scale-dependent statistics of turbulent flame fluctuations.
4. To establish the range of scales over which turbulent flame fluctuations display self-similarity and are neither affected by large scale flow anisotropies nor by small scale dissipation effects, along with the development of supporting theory.
5. To establish the phenomenon of small-scale intermittency in turbulent flames and quantify its anomalous scaling behavior.
6. To quantify the effect of small-scale intermittency of turbulent flows on the phenomenology of premixed flames. In particular, obtain the correction to the estimate of fractal dimension of premixed flames as a result of the intermittent nature of turbulent dissipation.
7. To utilize the statistics of turbulent velocity fluctuations and develop a smart method of passive control in practical turbulent combustion systems prone to thermoacoustic instability.

1.5 OVERVIEW OF THE THESIS

The thesis is organized as follows. In Chapter 2, we provide an overview of turbulent flows and the statistical theory due to Kolmogorov (1941*b*,*a*) which was a step towards developing a universal theory of turbulence. We then introduce the phenomenon of small-scale intermittency arising due to coupling between large and small scales of the flow and due to the multiplicative nature of cascade processes in turbulence. We also discuss the phenomenology of scalar fields in turbulent flows, which has historically followed the developments in classical turbulence. Following this, we introduce the modes of turbulent combustion and develop the statistical theory of premixed turbulent flames due to Peters (1992). We explain some of the limitations of the theory of turbulent premixed flames and explain the requirement for understanding the small-scale intermittency in turbulent premixed flames, a subject that has received scant attention till now. We also expound on the large-scale flame response and its dependencies. Understanding the large-scale flame response is crucial in developing a better understanding of thermoacoustic instability. We conclude the chapter with a brief discussion of the genesis and mechanisms of thermoacoustic instability in reacting flows. We then discuss some of the control strategies commonly used in combating thermoacoustic instability. We conclude the chapter by arguing the requirement of developing spatio-temporal statistical measures for enhancing the capabilities of control strategies currently used in practical gas turbine combustors.

In Chapter 3, we provide details of the turbulent V-flame facility and the bluff-body stabilized combustor, which have been used for experiments. We explain the experimental procedure and the various diagnostic techniques used for measuring system variables such as velocity field, flame surface, heat release rate, and acoustic pressure. We also discuss the processing techniques used to obtain flame fluctuations.

In Chapter 4, we consider the large-scale response of the turbulent V-flame. We depict the nonlinear harmonic flame response arising due to effects of interference among dissimilar convecting disturbances imposed on the V-flame. We further depict how these local effects of interfering disturbances, flame asymmetry, and kinematic restoration affect local and global flame behavior. In particular, we depict the contribution of local effects on the global heat release rate response.

In Chapter 5, we discuss the small-scale phenomenology of the V-flame in response to high turbulence levels. We show that the flame fluctuations depict statistical self-similarity with well-defined power-law behavior. We develop heuristic arguments based on Kolmogorov's theory for explaining the exponent of the power-law over an intermediate-range of scales. Most importantly, we clearly demarcate small-scale and large-scale intermittency in premixed turbulent flames, something which has not been done till now. We show that the scaling exponents in the power-law range do not grow linearly with the order of the structure-function, and hence, cannot be predicted by dimensional analysis. We then invoke multifractal formalism to quantify the singularities of the multiplicative process underlying the small-scale phenomenology of turbulent flames.

In Chapter 6, we analytically derive closed-form expressions for the effect of the intermittent nature of turbulent kinetic energy dissipation on the fractal dimension ($\mathbb{D}$) of premixed flames with finite thickness.

In Chapter 7, we analyze the statistics of turbulent velocity fluctuations. We show that the scaling of moments of turbulent velocity fluctuations obtained from a practical combustor can be used to develop a smart passive control strategy. With the help of these scaling exponents, we identify the so-called critical regions of the velocity field, which can be detected in the flow field much before thermoacoustic instability sets in the combustor. When the critical region is selectively targeted, large amplitude pressure oscillations are suppressed.

We conclude our discussion in Chapter 8, where we highlight the key findings, discuss the context of these findings and their practical implications. We close our discussion by summarizing many exciting research directions arising out of the present thesis.

CHAPTER 2

BACKGROUND

In this chapter, we introduce various concepts which would be useful when discussing the results related to the statistics and dynamics of turbulent premixed combustion in the chapters to follow. Turbulent combustion is a multi-scale problem wherein many different interactions take place over a large range of scales. These interactions underlie the observed dynamics of turbulent combustion.

We begin by introducing the statistical theory of turbulence introduced by Kolmogorov (1941*a*) in §2.1 and build our understanding of the nature of small-scale and large-scale interactions in turbulent flows. We further propound the concept of intermittent fields depicting extreme-value fluctuations. We then provide the theoretical background of the tools required for studying such intermittent fields. We then introduce the theory of turbulent combustion in §2.2 and discuss the modes of turbulent combustion. We also emphasize the statistical theory of premixed turbulent combustion as introduced by Peters (1992). We further discuss the typical large-scale response of flames in the presence of turbulence and acoustic disturbances. In §2.3, we review the problem of thermoacoustic instability arising due to complex interaction between combustion, turbulence, and acoustics in practical gas turbine engines. Finally, we close our discussion with an account of various mitigation strategies used for combating thermoacoustic instability.

2.1 TURBULENT FLOWS

Turbulence has been and continues to be one of the most important problems in physics. Despite the many long-standing difficulties, the study of turbulence has fostered the development of important concepts such as anomalous diffusion, power-law scaling, universality, chaos, correlated structures, etc., all of which were posed concretely in the context of turbulence. These ideas have not only led to great insights into the nature of turbulence but also influenced neighboring areas of physics and mathematics. In this section, we review some of the key statistical ideas and discuss their implications for reacting turbulent flows.

2.1.1 Governing equations of turbulent flows

The starting point is the Navier-Stokes equations which arise from the mass and momentum conservation. Thus, for a freely evolving velocity field $\boldsymbol{u}(\boldsymbol{x}, t)$, the governing equations in the absence of effects such as compressibility and reaction, are given by:

$$\frac{\partial \rho}{\partial t} + \boldsymbol{\nabla} \cdot (\rho \boldsymbol{u}) = 0 \tag{2.1}$$

$$\frac{\partial \boldsymbol{u}}{\partial t} + (\boldsymbol{u} \cdot \boldsymbol{\nabla})\, \boldsymbol{u} = -\frac{1}{\rho} \nabla p + \nu \nabla^2 \boldsymbol{u} \tag{2.2}$$

Here, p is the normal pressure, $\nabla^2 \boldsymbol{u}$ arises from viscous effects on the fluid element, ρ is the density (kg/m^3) and ν is the kinematic viscosity (m^2/s). Much of the flow dynamics arises through a balance between the inertial and the viscous effects. The inertial force per unit mass $\boldsymbol{u} \cdot \boldsymbol{\nabla} \boldsymbol{u} = u_j \partial u_i / \partial x_j$ can be estimated as $\sim U^2/L$, where U and L are some characteristic velocity and length, while the viscous force per unit mass is $\nu \boldsymbol{\nabla}^2 \boldsymbol{u} \sim \nu \partial^2 u_i / \partial x_j \partial x_j$ and can be estimated as $\sim \nu U / L^2$. The ratio of these terms is referred to as Reynolds number $Re_L \equiv UL/\nu$, which characterizes the flow. For small Re_L, viscous effects arrest any fluctuations and result in a laminar flow. For large values of Re_L, viscous effects are negligible and inertial effects dominate the dynamics leading to turbulence, and is the focus of the present discussion.

The central quantity of interest in turbulent flows is the kinetic energy ($u^2/2$) and its distribution through the turbulent flow field. The evolution equation of kinetic energy is derived from Eqn. (2.2) by taking its dot product with $\boldsymbol{u}(\boldsymbol{x}, t)$, which, in index notation ($i, j = 1, 2, 3$), is written as,

$$\frac{\partial (u^2/2)}{\partial t} = -\frac{\partial}{\partial x_j} \left((u^2/2) u_j \right) - \frac{1}{\rho} \frac{\partial}{\partial x_j} (p u_j) + \frac{1}{\rho} \frac{\partial}{\partial x_j} (u_i \tau_{ij}) - 2\nu S_{ij} S_{ij}. \qquad (2.3)$$

Here, $S_{ij} = \partial u_i / \partial x_j$ is the strain-rate tensor and the shear stress $\tau_{ij} = 2\rho\nu S_{ij}$ follows from Newton's law of viscosity. Equation (2.3) describes the conservation of kinetic energy in a turbulent flow. The first three terms on the right-hand side of the equation imply the convection of kinetic energy across a control volume, the rate at which work is done by pressure forces on the boundary, and the rate at which work is done by the viscous forces on the boundary, respectively. The final term indicates the rate at which kinetic energy per unit mass is lost to heat and is referred to as kinetic energy dissipation:

$$\varepsilon \equiv 2\nu S_{ij} S_{ij}. \qquad (2.4)$$

The rate of kinetic energy dissipation is a conserved scalar in turbulent flows.

Before moving forward, it is instructive to introduce some statistical tools useful in the analysis of turbulent flows. It is helpful to split statistical quantities in terms of their mean and fluctuating components, a concept referred to as Reynolds decomposition in turbulence. The time-average is determined as:

$$\langle \boldsymbol{u}(\boldsymbol{x}) \rangle = \frac{1}{T} \int_0^T \boldsymbol{u}(\boldsymbol{x}, t) dt, \tag{2.5}$$

where, T is time duration over which the average converges statistically. The fluctuations in the velocity field are then obtained as: $\boldsymbol{u}'(\boldsymbol{x}, t) = \boldsymbol{u}(\boldsymbol{x}, t) - \langle \boldsymbol{u}(\boldsymbol{x}) \rangle$.

The other important statistical quantity is the second-order velocity correlation tensor, defined as:

$$Q_{ij}(\boldsymbol{r}, \boldsymbol{x}, t) \equiv \langle u_i(\boldsymbol{x}) u_j(\boldsymbol{x} + \boldsymbol{r}) \rangle. \tag{2.6}$$

The velocity correlation tensor allows one to probe the properties of the turbulent flow in a scale dependent manner defined by $r = ||\boldsymbol{r}||$. Quantities are termed as homogeneous and isotropic if their statistical properties remain invariant under translation and rotation, respectively. Thus, for homogeneous turbulence, the velocity correlation tensor is only a function of $\boldsymbol{r}$ such that $Q_{ij}(\boldsymbol{r}, \boldsymbol{x}, t) = Q_{ij}(\boldsymbol{r})$. The tensor Q_{ij} is related to the kinetic energy of the velocity through the relation $Q_{ij}(0) = 1/2 \langle \boldsymbol{u}^2 \rangle$. The longitudinal ($f$) and lateral ($g$) velocity correlations are expressed as:

$$u'^2 f(r) = Q_{ii}(r), \qquad u'^2 g(r) = Q_{jj}(r), \tag{2.7}$$

where the non-dimensionalization is done using the root mean square velocity fluctuations, which defined as,

$$u' = \langle {u'_x}^2 \rangle^{1/2} = \langle {u'_y}^2 \rangle^{1/2} = \langle {u'_z}^2 \rangle^{1/2} = \left(1/3 \langle \boldsymbol{u} \cdot \boldsymbol{u} \rangle\right)^{1/2}, \tag{2.8}$$

and represents the characteristic velocity of large-scale flow. Thus, the integral length scale of turbulent flows is defined as:

$$\ell = \int_0^\infty f(r) dr. \tag{2.9}$$

The integral scale is the characteristic length scale of large-scale turbulent flows and implies the length over which the velocity field is correlated.

2.1.2 Scales of turbulent motion

Turbulent flows are characterized by a wide range of scales. Large scales eddies are of the order of the domain (L) of observation. These large-scale eddies can be easily demarcated as the large-scale structures observed in turbulent flows. For example, the boundary of turbulent rain clouds or the vortices shed past an obstruction in a flow are representative of the large scales of turbulent motion. These large-scale eddies are responsible for most of the transport of heat, momentum, and contaminants. These large-scale motions are generated as a result of non-homogeneous effects such as through the presence of mean shear or density gradients.

In contrast, the small scales are the scales at which the turbulent kinetic energy is dissipated through viscous and heat loss due to molecular diffusion. At these small scales, fluid viscosity becomes effective in smoothing out velocity fluctuations. These small scales are generated by the nonlinear term in Eqn. (2.2). For large Re values, the large scales are unaffected by the effects of viscosity. The nonlinear term counteracts the inertial forces by generating scales small enough to be affected by viscosity.

The small scales evolve at shorter time and length scales with lower velocities as compared to large scales, which evolve at a much larger time, and length scales with large velocities. Hence, one can approximate that at small scales, the statistics are independent of the large-scale turbulence of the mean flow (Fig. 2.1). Thus, the dynamics of small scales should depend entirely on the rate of kinetic energy supplied to these scales, an assumption which forms the basis of Kolmogorov's *universal equilibrium theory*. Thus, the small-scale motion is controlled by the average rate of turbulence kinetic energy dissipation $\langle \varepsilon \rangle$ (m^2/s^3) and kinematic viscosity ν (m^2/s). Here, $\langle \varepsilon \rangle$ implies a volume-averaged value of turbulent kinetic energy dissipation ε. Thus, using $\langle \varepsilon \rangle$ and ν we can define the characteristic scales of small-scale motion as follows (Tennekes and Lumley, 2018):

$$\eta \equiv (\nu^3/\langle \varepsilon \rangle)^{1/4}, \qquad \tau_\eta \equiv (\nu/\langle \varepsilon \rangle)^{1/2}, \qquad u'_\eta \equiv (\nu \varepsilon)^{1/4}. \tag{2.10}$$

These scales are referred to as Kolmogorov's microscales. The Reynolds number at these scales is $Re_\eta = u'_\eta \eta / \nu = 1$, implying the dominant role viscosity plays at these small-scales.

As kinetic energy is transferred from large-scales to small-scales, we can relate the

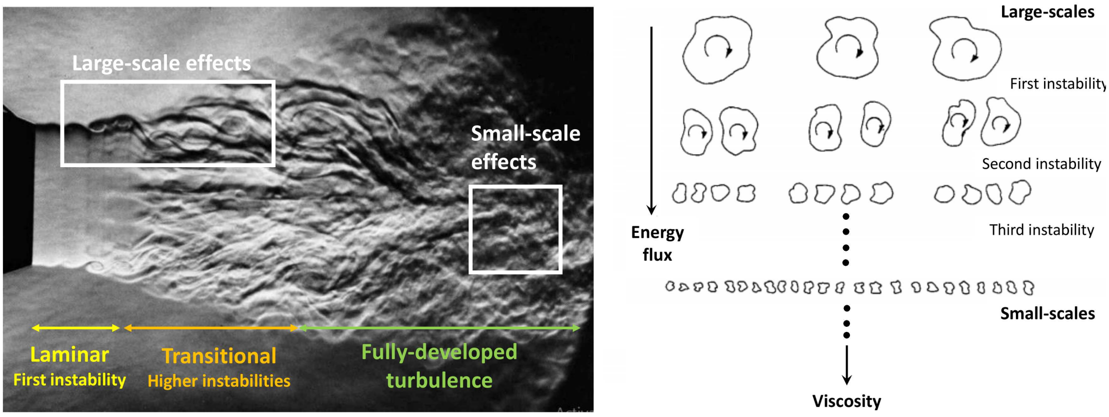
Large-scale effects
Small-scale effects
Laminar
First instability
Transitional
Higher instabilities
Fully-developed turbulence
Large-scales
First instability
Second instability
Third instability
Energy flux
Small-scales
Viscosity

Figure 2.1: (Left) Transition to fully-developed turbulence in a jet flow. Turbulent large-scale motion arises from mean flow instabilities and breaks down into finer scales. (Right) Schematic depicting the cascade through which finer scales are generated. It is evident that after a few generations of the cascade process, effects of mean flow inhomogeneity and anisotropy become negligible. Adapted from (a) Bradshaw *et al.* (1964) and (b) Frisch (1995) with permission from Cambridge University Press.

large-scales with the small-scales of turbulent motion. The characteristic length ℓ and velocity u' of large-scales were introduced above. Large eddies lose a fraction of their kinetic energy $1/2u'^2$ over one eddy turnover time t_ℓ. Thus, the average rate of kinetic energy per unit mass is estimated, to the leading order, as

$$\langle \varepsilon \rangle \sim \frac{u'^2}{t_\ell} \sim \frac{u'^3}{\ell}. \tag{2.11}$$

Note that only a very small-fraction of the total kinetic energy is lost through viscous effects. The energy lost to viscous effects can be estimated as $u'^2/(\ell^2/\nu)$, where the time scale of energy loss is ℓ^2/ν. The energy dissipation is thus $\nu u'^2/\ell^2$, which is much smaller as compared to u'^3/ℓ for large Reynolds number ($Re = u'\ell/\nu$). Thus, using Eqn. (2.11) in Eqn. (2.10), we obtain:

$$\frac{\eta}{\ell} \sim Re^{-3/4}, \qquad \frac{\tau_\eta}{t_\ell} \sim Re^{-1/2}, \qquad \frac{u'_\eta}{u'} \sim Re^{-1/4}. \tag{2.12}$$

The above relations imply that the range of scales in a turbulent flow depends on the Reynolds number (Re). The large Re is, the larger is the separation of scales of turbulent motion between η and ℓ.

2.1.3 Universal equilibrium theory of turbulence

We now introduce the statistical theory of Kolmogorov (1941*a*,*b*), which is designated as K41. We begin by considering the longitudinal velocity-structure function,

$$\left\langle [\delta u'(r)]^2 \right\rangle \equiv \left\langle [u'_x(x+r) - u'_x(x)]^2 \right\rangle . \tag{2.13}$$

The structure function relates to the longitudinal velocity correlation f through the relation $\langle (\delta u'(r))^2 \rangle = 2{u'}^2(1-f)$ for homogenous isotropic turbulence (Batchelor, 1953). The exact form of Eqn. (2.13) is not obvious. However, it should depend on a variety of flow properties, such that

$$\left\langle [\delta u'(r)]^2 \right\rangle = F(u', \ell, r, t_\ell, \nu). \tag{2.14}$$

The variables u', ℓ and t_ℓ are dependent on the average rate through which kinetic energy is transferred across smaller scales, to be eventually dissipated, as given according to the relation ${u'}^3/\ell \sim \langle \varepsilon \rangle \sim \nu {u'_\eta}^2/\eta^2$. Thus, the dependence on u', ℓ and τ_ℓ can replaced by $\langle \varepsilon \rangle$.

Kolmogorov's *First Similarity Hypothesis* suggests that for large enough Re and $r <<$ ℓ, the statistical properties of $\delta u'(r)$ depend only on $\langle \varepsilon \rangle$, r and ν. In other words, at small scales, the statistics remain unaffected by large-scale anisotropies, and only depend on the average rate of kinetic energy injection onto smaller scales and the kinematic viscosity. Thus, the first hypothesis implies a return to *local isotropy* in the state of the turbulent flow at smaller scales. Thus, we can re-write Eqn. (2.14) as:

$$\left\langle [\delta u'(r)]^2 \right\rangle = F(\langle \varepsilon \rangle, r, \nu), \qquad \forall \ r << \ell. \tag{2.15}$$

Kolmogorov's *Second Similarity Hypothesis* suggests that for large Re and in the range $\eta << r << \ell$, the statistical properties of $\delta u'(r)$ are uniquely determined by r and $\langle \varepsilon \rangle$, alone. Thus, the second hypothesis introduces a lower cut-off above which viscous effects are negligible. Thus, for this *inertial sub-range*, Eqn. (2.15) can be re-written as:

$$\left\langle [\delta u'(r)]^2 \right\rangle = F(\langle \varepsilon \rangle, r), \qquad \forall \eta << r << \ell. \tag{2.16}$$

A quick perusal based on dimensional consistency implies that the function F should follow,

$$\left\langle [\delta u'(r)]^2 \right\rangle = \beta_2 \langle \varepsilon \rangle^{2/3} r^{2/3}, \qquad \forall \ \eta << r << \ell, \tag{2.17}$$

where, β_2 is a universal constant, which have been empirically estimated to be $\beta_2 \sim 2$ (Davidson, 2015). This is known as Kolmogorov's *two-third* law. A reformulation in spectral space leads to

$$E_u(k) = C_k \langle \varepsilon \rangle^{2/3} k^{-5/3}. \tag{2.18}$$

C_k is referred to as Kolmogorov's constant and is found to be universal with a value of $C_k = 0.52 \pm 0.04$ (Sreenivasan, 1995). Equation (2.18) is referred to as Kolmogorov's *five-third* law and has been shown in Fig. 2.2(a). Alternatively, the five-third law can be obtained from the two-third law by noting that the following relation holds: $\langle[\delta u'(r)]^2\rangle \sim \int_{\pi/r}^{\infty} E(k)dk$.

Another important universal law for turbulent flows is known. In *globally isotropic* turbulent flows, the third-order velocity structure function $\langle[\delta u'(r)]^3\rangle$ has been shown to exactly follow (Kolmogorov, 1941*a*),

$$\left\langle[\delta u'(r)]^3\right\rangle = -\frac{4}{5}\langle\varepsilon\rangle r, \tag{2.19}$$

where, β_3 takes the value of $-4/5$ in the equation above. This is known as Kolmogorov's *four-fifths* law. Note that the four-fifths law is an exact law derived from the Karman-Howarth equation (Karman and Howarth, 1938), unlike the five-third law which is obtained based on dimensional grounds. Either of these two laws are very well substantiated in experiments and direct numerical simulations (Saddoughi and Veeravalli, 1994).

2.1.4 Higher-order statistics of turbulent flows

In the discussion above, we noted that the second-order structure function scales as $r^{2/3}$ while that of the third-order scales as r. This suggests that we can generalize the universality hypothesis. For large Re and for $\eta << r << \ell$, the probability density function (PDF) of the velocity increments $\delta u'/(r\langle\varepsilon\rangle)^{1/3}$ should have a universal form and be independent of ν. Further, as one considers only velocity differences, the

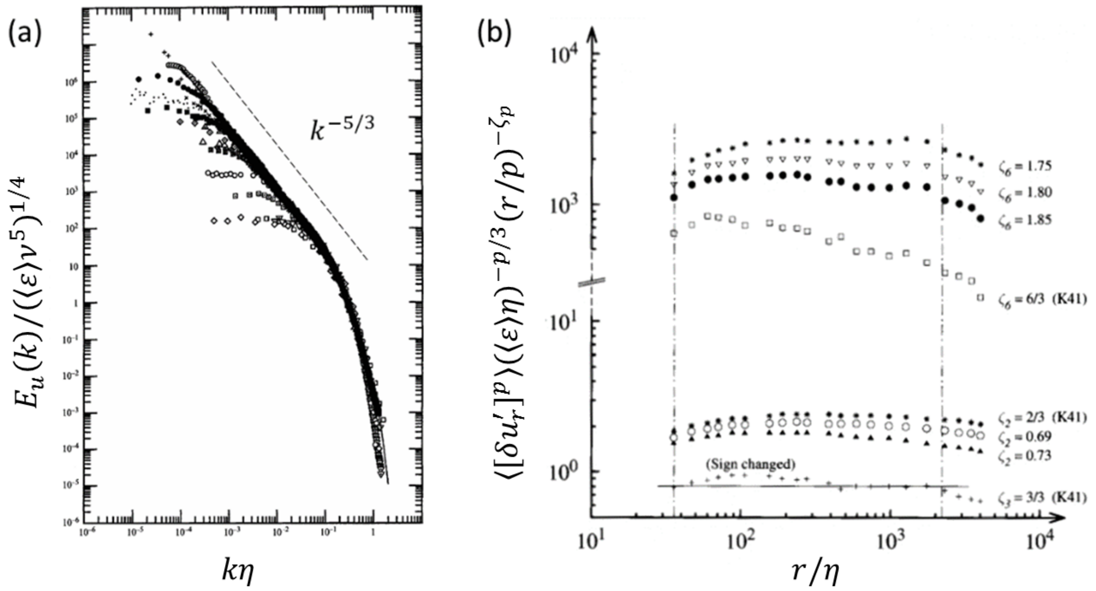

Figure 2.2: (a) Kolmogorov's $5/3^{\text{rd}}$ law observed empirically in a variety of turbulent flow datasets compiled by Saddoughi and Veeravalli (1994). The range over which $k^{-5/3}$ scaling is observed increases with an increase in Re. (b) Scaling of structure-function compensated with 'guessed' power-law exponents ζ_p for different values of p for wind tunnel data reported in Anselmet *et al.* (1984). Figures have been adapted with permission from Cambridge University Press.

statistics is expected to be applicable for any general turbulent flow. This implies that the statistics for any general order p follows:

$$\left\langle [\delta u'(r)]^p \right\rangle = \beta_p \varepsilon^{p/3} r^{p/3}, \qquad \forall \ \eta << r << \ell, \tag{2.20}$$

where, β_p are universal constants.

Nevertheless, numerous experimental and analytical studies have shown that the basis and predictions of K41 are inexact. In particular, there is a significant departure from the scaling exponent indicated by Eqn. (2.20) for $p \geq 3$. This departure can be observed in Fig. 2.2(b), where the structure-function compensated by the 'guessed' power-law exponent is plotted for wind tunnel data reported in Anselmet *et al.* (1984). Notice that

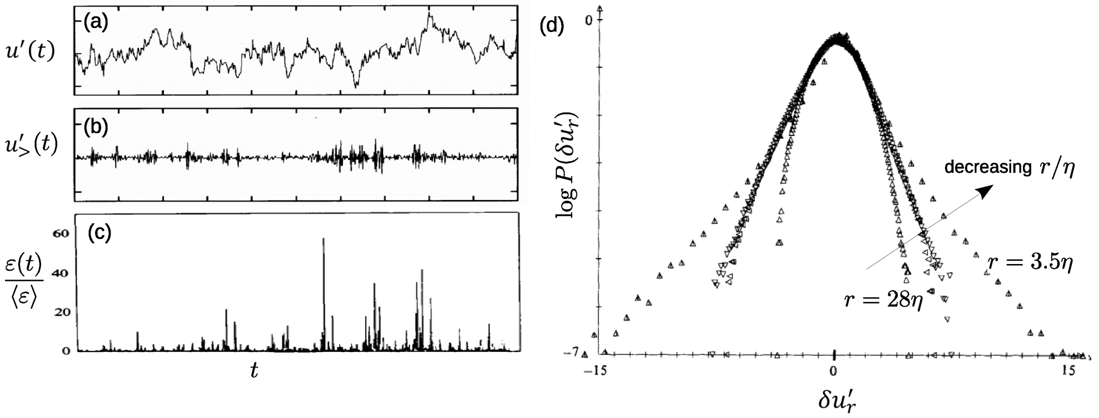

Figure 2.3: Typical time trace and properties of turbulent velocity fluctuations. Subfigure (a) shows $u'(t)$ for a turbulent jet and (b) shows the same signal after high-pass filtering (denoted as $u'(t)_{>}$) to highlight extreme fluctuations associated with small-scales (Gagne, 1980). (c) Time series of turbulent kinetic energy dissipation $\varepsilon \sim (du'/dt)^2$ obtained from atmospheric surface layer (Meneveau and Sreenivasan, 1991). (d) The PDF of velocity increments $\delta u'$ for different values of separation r/η (Anselmet *et al.*, 1984). Figures (c,d) have been adapted with permission from Cambridge University Press.

for $p = 1, 2$, the structure-function scales reasonably well according to K41. However, for $p = 6$, the structure-function does not scale with the exponent $p/3 = 2$, instead scales with a value less than $p/3$. The departure from $p/3$ widens with increase in the moment-order p (Fig. 2.4a). The PDF of velocity-increments also change continuously with a change in r (Fig. 2.3d), in contrast to the invariant form of PDF enshrined in K41. Similarly, the value of β_n has been found to vary for different flows. Finally, the skewness (third-moment) and flatness factor (fourth-moment) are found to be dependent on the Re of the flow, in contrast to what is expected according to K41.

The issue that underlies the departure from K41 universality is the strong spatio-temporal variability of energy dissipation. Indeed, we know from experimental measurements that ε displays extreme-fluctuations several order of magnitudes greater than variance (Fig. 2.3c). The strong variability arises due to two reasons. The first has to do with the large-scale anisotropy and inhomogeneity in turbulent flows, such as the active region of turbulence amidst quiescence during the transition. The large-scale clumpiness affects the local energy flux, which controls the local cascade of small-scale eddies. Since the local energy flux (averaged over scale of the order of ℓ) depends on the nature of the flow, the universality alluded through Eqn. 2.20, would no longer be universal. In other words, averaging over cascades resulting from large-scale unsteadiness would produce non-universal inertial-range statistics. This was first proposed by Landau and Lifshitz (1959). The second reason has to do with the multiplicative manner in which energy flux is distributed across smaller and smaller scales. This idea is discussed in more detail in the next section.

Consequently, the dynamics of small-scale eddies in a small region V_r of size r ($<< \ell$) should depend only on the flux of turbulent kinetic energy which is equal to the average dissipation rate in that local region V_r. Thus, based on the argument by Landau and Lifshitz (1959), Oboukhov (1962) suggested replacing the volume-averaged $\langle \varepsilon \rangle$ in K41 with locally averaged dissipation $\langle \varepsilon_r \rangle$, defined as

$$\langle \varepsilon_r \rangle = \frac{1}{V_r} \int_{V_r} \varepsilon dV, \tag{2.21}$$

where, $V_r = \mathcal{O}(r^3)$ and $r << \ell$. Since ε has extreme fluctuations through space and in time, $\langle \varepsilon_r \rangle$ itself varies. The variation in $\langle \varepsilon_r \rangle$ was presumed to be of the order of r/ℓ by Oboukhov (1962), accounting for the effect of large-scales on inertial-range statistics.

If the considerations of Oboukhov (1962) are correct, then the PDF of $\delta u'/(r\langle \varepsilon \rangle)^{1/3}$ would *not* be universal in the inertial range. However, we can still expect the moments of $\delta u'/(r\langle\varepsilon\rangle)^{1/3}$ to follow power-law scaling of the form:

$$\left\langle[\delta u'(r)]^p\right\rangle = \beta'_p \varepsilon^{p/3} r^{\zeta_p}, \qquad \forall\ \eta << r << \ell, \tag{2.22}$$

where, β'_p are non-universal and depend on the type of flow. However, the scaling exponent ζ_p, although disparate from $p/3$, can be assumed to be universal. Indeed, Kolmogorov (1962) considered these suggestions and proposed a *refined self-similarity* by considering the locally averaged dissipation, which results in

$$\left\langle[\delta u'(r)]^p\right\rangle = \beta'_p \langle\varepsilon^{p/3}\rangle r^{p/3}, \qquad \forall\ \eta << r << \ell. \tag{2.23}$$

In order to estimate the nature of the structure function, we make use of the empirically observed relation:

$$\langle\varepsilon_r^2\rangle/\varepsilon^2 = B(r/\ell)^{-\mu}, \qquad \forall \eta \leq r \leq \ell \tag{2.24}$$

where μ is referred to as the intermittency exponent. Further, assuming that ε_r follows log-normal statistics, and making use of the relation:

$$\langle\varepsilon_r^m\rangle/\varepsilon^m = \left[\langle\varepsilon_r^2\rangle/\varepsilon^2\right]^{m(m-1)/2}, \tag{2.25}$$

Kolmogorov (1962) obtained the log-normal model for the statistics of velocity increment as:

$$\left\langle[\delta u'(r)]^p\right\rangle = C_p(\varepsilon r)^{p/3}(\ell/r)^{\mu p(p-3)/18}, \qquad \forall\ \eta << r << \ell. \tag{2.26}$$

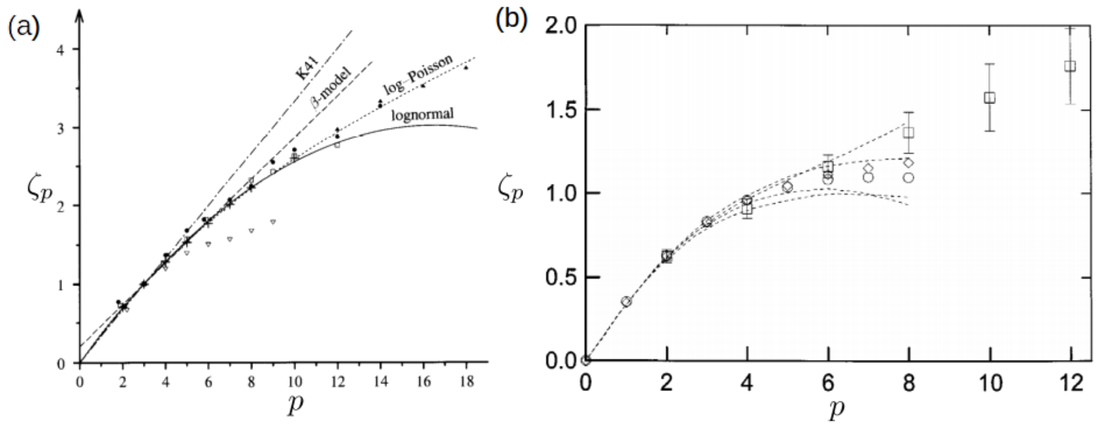

Figure 2.4: Anomalous scaling exponent ζ_p associated with structure-function based on (a) velocity increments ($\delta u'(r)$) and (b) scalar increments ($\delta c'(r)$). Various model predictions are shown in (a). Note the departure from $\zeta_p = p/3$ as predicted by K41 theory. Adapted from (a) Frisch (1995) with permission from Cambridge University Press and (b) Sreenivasan and Antonia (1997) with permission from Annual Reviews.

Here, $C_p = \beta_p B^{p(p-3)/18}$. The relation $(p-3)$ was introduced so as to fulfil the four-fifths law (Eqn. 2.19). Comparing with the generalized form in Eqn. (2.22), the power-law exponent for the log-normal model has the form:

$$\zeta_p = \frac{p}{3} + \frac{\mu}{18} p(p-3). \tag{2.27}$$

The log-normal model, thus, accounts for the impact of large-scale inhomogeneities in turbulence, on the inertial range statistics. The predictions of the log-normal model are shown in Fig. 2.4(a), and fares better than the $p/3$ limit of K41.

2.1.5 Small-scale intermittency in turbulent flows

In Fig. 2.3a, we notice that the velocity fluctuations are quite irregular. Upon filtering out the low-frequency components (depicted as $u'_{>}$ in Fig. 2.3a,b), we observe that the high-frequency components show fluctuations that are much larger than their mean value. These fluctuations are induced by the small-scale (or high frequency/wavenumber) motion of the velocity field. These extreme fluctuations lead to non-Gaussian and wide-tailed PDF of velocity increments $\delta u'_r$ (Fig. 2.3d). The PDF becomes increasingly non-Gaussian and wide-tailed as r is decreased (an operation akin to high-pass filtering) and approaches Kolmogorov microscale η, implying that extreme fluctuations occur with significantly higher probability and do not decay exponentially like in a Gaussian PDF.

Indeed, it is this behavior of extreme-value fluctuations and wide-tailed PDF that one wishes to capture using higher-moments of $\delta u'_r$. The universal theory of Kolmogorov (1941*a*) is an attempt at capturing this behavior of the turbulent velocity field through a rather simple and intuitive model. If the velocity field was not intermittent in the small scales, $\zeta_p = p/3$ would hold for any general turbulent flow. However, as the velocity field is intermittent, the scaling exponent ζ_p departs from $p/3$ for higher values of p (Fig. 2.4a). We also observed the refined self-similarity hypothesis (Eqn. 2.27), which accounted for the large-scale spottiness of turbulent flows and gave a better prediction for higher-order statistics.

Notwithstanding the large-scale spottiness of turbulent flows, there is a second more important contributor to the small-scale intermittency in turbulent flows. This contribution arises from the intuitive picture of cascade due to Richardson (1926). The central tenet of turbulence cascade is that large-scale turbulent eddies are progressively broken down into smaller eddies through the nonlinear term in the Navier-Stokes equation to small enough scales for viscosity to dissipate the energy of turbulent flows. Thus, there is a unidirectional transfer of turbulent kinetic energy from large scales (small wavenumber), which contain most of the energy, to small scales (large wavenumber), where energy is dissipated. Physically, this process takes place through the stretching of eddies which teases out vorticity into finer and finer elements. As vortex ribbons and tubes are teased out into finer structures, the vortex field becomes increasingly intermittent at smaller scales (Davidson, 2015). Consequently, dissipation ε also becomes spotty and intermittent at smaller scales. Thus, the small scales are inherently intermittent and arise through a multiplicative process where measures such as kinetic energy, enstrophy, scalar dissipation are distributed unevenly across various generations of the cascade process.

Thus, the non-trivial coupling between large-scales and small-scales and inherent spottiness of the velocity and vorticity field result in the intermittent statistics and cause the scaling exponent to deviate from $p/3$ of K41. The deviation from the $p/3$ limit is formally referred to as *anomalous scaling exponent*. The $\zeta_p - p$ curve is a convex and monotonic increasing function of p (Fig. 2.4). The convexity of the $\zeta_p - p$ curve follows from Hölder's inequality for central moments (Frisch, 1995). Let us consider the even order moments of increments in velocity fluctuations, which is indicated as: $S_{2p} \sim \langle (\delta u')^{2p} \rangle \sim r^{\zeta_{2p}}$, for $2p > 0$. Hölder's inequality for moments of random variable suggests that (Feller, 2008)

$$\left\langle (\delta u')^{2p_2} \right\rangle^{2p_3-2p_1} \leq \left\langle (\delta u')^{2p_1} \right\rangle^{2p_3-2p_2} \left\langle (\delta u')^{2p_3} \right\rangle^{2p_2-2p_1}, \tag{2.28}$$

for any positive integers $p_1 \leq p_2 \leq p_3$. Substituting $\langle (\delta u')^{2p} \rangle \sim r^{\zeta_{2p}}$ in the equation above, we obtain:

$$(p_3 - p_1)\zeta_{2p_2} \geq (p_3 - p_2)\zeta_{2p_1} + (p_2 - p_1)\zeta_{2p_3}. \tag{2.29}$$

It is easy to observe that the inequality above expresses the condition that ζ_p is a convex function of p.

2.1.6 Intermittent fields and multiplicative processes

Generally, intermittent fields are generated through the unequal distribution of measures of conserved quantities (Sreenivasan, 1991*a*). These conserved quantities include turbulent kinetic energy dissipation ε and enstrophy in fully-developed turbulent flows (Davidson, 2015), and scalar dissipation χ in the case of reacting turbulent flows (Peters, 2001). The division of conserved measures follows from the turbulent cascade, which entails the transfer of these quantities from large energy-containing scales to very small scales where these quantities are dissipated viscous mechanisms.

For sufficiently large Re, there is considerable scale separation between large energy-containing scales and dissipation scales. Thus, conserved quantities are unequally divided into succeedingly smaller scales. The division can be achieved in two manners:

equal measure distributed among unequal scales or unequal measures distributed among equal scales. However, the two procedures yield identical results for deterministic multifractals (Chhabra *et al.*, 1989). As the number of divisions increases, the measure in successive generations becomes more and more uneven. At any given generation, the measure is determined by the multipliers of all the previous generations, implying a multiplicative cascade process. The multipliers are fractions of measure transferred from one generation to the next. If the rule through which the measure is divided across generations is independent of the generation level, the statistical properties of the measure are expected to be self-similar across generations. Consequently, the statistical properties of the measure depict a power law with the scale of measurement. Thus, intermittent fields in turbulent flows arise from such multiplicative cascade processes (Mandelbrot, 1989). Such a description is quite well-substantiated in model predictions of turbulent flows (Sreenivasan, 1991*a*; Frisch, 1995).

2.1.7 The multifractal formalism

While small-scale intermittency is captured relatively well by the log-normal model (Eqn. 2.27), Mandelbrot (1972) showed that the use of log-normal model is theoretically suspect. This is because the formulation of the log-normal model crucially relies on the central-limit theorem, which cannot be used for describing extreme events which contribute to the wide-tails of PDFs of intermittent fields. Frisch *et al.* (1978) suggested the use of fractal or β-model for explaining small-scale intermittency. The model builds upon the assumption that space-filling large eddies are divided into successively smaller non-space filling eddies such that at any generation n of the cascade process, only a fraction β^n of the space is *active*. However, Meneveau and Sreenivasan (1991) showed that the β-model was inaccurate for higher-order moments.

A more rigorous treatment of intermittent fields in the form of multifractal formalism was first introduced in the context of turbulence to explain anomalous scaling associated with small-scale intermittency (Parisi and Frisch, 1985). Concurrently, Hentschel and Procaccia (1983) introduced a hierarchy of generalized dimension (D_q). Halsey *et al.* (1986) defined $f(\alpha)$ as the set of fractal dimension characterizing multifractals and christening the term ‘multifractals’.

The starting point of the multifractal formalism is the behavior of Navier-Stokes equations under scaling transformation. Under the scaling of t as $\lambda^{1-\alpha}t$, r as $\lambda\boldsymbol{r}$ and $\boldsymbol{u}$ as $\lambda^{\alpha}\boldsymbol{u}$ for some constant λ, all the terms in the Navier-Stokes equation (Eqn. 2.2) are multiplied by $\lambda^{2\alpha-1}$, except for the viscous term, which scales as $\lambda^{\alpha-2}$. Thus, for finite viscosity, only $\alpha = -1$ is permitted, which corresponds to the similarity principle in fluid dynamics. If on the other hand we the limit of $\nu \to 0$, the Navier-Stokes equations remain invariant under infinitely many groups of scaling transformation for $\alpha \in \Re$, where $\Re$ is the set of real number (Parisi and Frisch, 1985; Frisch, 1995). Thus, the key idea of the multifractal model is to relax the idea of a single global scaling exponent for the inertial range, where viscous effects are assumed to be negligible, as prescribed in Eqn. (2.20). Rather a weakened local scale invariance is considered where turbulence is presumed to posses a range of scaling exponents $I = (\alpha_{\min}, \alpha_{\max})$. Further, associated with each of these exponents α is a set $\mathcal{J}_\alpha \subset \mathbb{R}^3$, whose Hausdorff dimension is given by $f(\alpha)$. Then, in the limit of $r \to 0$, we have

$$\frac{\delta u'(r)}{\bar{v}} \sim \left(\frac{r}{\ell}\right)^{\alpha}, \qquad r \in \mathcal{J}_{\alpha}. \tag{2.30}$$

As there are many sets with varying α, we need to cover the turbulent field with boxes of size r and count the number of boxes for which the sets have the same value of α. The number of boxes thus, required is given by:

$$N(\alpha) \sim \left(\frac{r}{\ell}\right)^{-f(\alpha)} \tag{2.31}$$

Since the flow is three-dimensional, the volume of the set for which scaling has the value of α, is expressed as: $r^3 N(\alpha) \sim \ell^{-3}(r/\ell)^{3-f(\alpha)}$. Thus, the p order moment of $\delta u'$ can be expressed as an integral over the interval α and $\alpha + d\alpha$, such that

$$\begin{aligned} \frac{\langle[\delta u'(r)]^p\rangle}{\bar{v}^p} &\sim \ell^{-3} \int_{\alpha} \left(\frac{r}{\ell}\right)^{3-f(\alpha)} \left(\frac{r}{\ell}\right)^{p\alpha} d\alpha, \\ \frac{\langle[\delta u'(r)]^p\rangle}{\bar{v}^p} &\sim \ell^{-3} \int_{\alpha} \left(\frac{r}{\ell}\right)^{p\alpha+3-f(\alpha)} d\alpha. \end{aligned} \tag{2.32}$$

In the limit of $r \to 0$, the power-law is dominated by the smallest exponent in the integrand in Eqn. (2.32). Thus, Eqn. 2.32 can be solved through the method of steepest descent, which leads to

$$\zeta_p = \inf_{\alpha} \left[p\alpha + 3 - f(\alpha)\right]. \tag{2.33}$$

In writing the above, we made use of the relation $\langle[\delta u'(r)]^p\rangle \sim r^{\zeta_p}$ defined in Eqn. (2.22). Thus, if $f(\alpha) - \alpha$ spectrum is known, the ζ_p can be determined, and the higher-order statistics can be characterized appropriately.

The multifractal formalism has been quite successful in explaining the small-scale intermittency. In a series of papers, Sreenivasan and co-workers then characterized the intermittent nature of various fields (ε, χ, etc.) using the multifractal model in a self-consistent manner (Meneveau and Sreenivasan, 1987*b*; Prasad *et al.*, 1988; Chhabra *et al.*, 1989; Meneveau and Sreenivasan, 1991). Multifractal formalism remains one of the few statistical models which satisfactorily describe the extreme events and higher-order moments of intermittent fields adequately.

2.1.8 Scalar fields in turbulent flows

A related problem is the evolution of scalar fields in turbulent flows. The transport of scalar fields such as contaminants and temperature in turbulent flows through advection and diffusion are important for a wide range of phenomenon. Turbulent combustion also depends on the advection and diffusion of activated radicals and temperature across the reaction zone for sustaining the reaction. Thus, we briefly discuss the phenomenology of scalar fields in turbulent flows.

2.1.8.1 Scalar advection-diffusion equation

Scalar fields (C) in turbulent flows obey the advection-diffusion equation (Davidson, 2015):

$$\frac{\partial C}{\partial t} + (\boldsymbol{u} \cdot \nabla) C = \mathcal{D} \nabla^2 C, \tag{2.34}$$

where, $\mathcal{D}$ is the diffusivity of the scalar C. The transport dynamics is controlled by the non-dimensional Peclet number, $Pe = u'\ell/\mathcal{D}$. If Pe is large, then the scalar is advected by the velocity field and diffusion is negligible. In contrast, for $Pe \sim 1$, the scalar diffusion becomes singificant and competes with the advection due to the turbulent flow. Since the scalar evolves in the turbulent flow, the balance between kinematic viscosity (ν) and scalar diffusivity ($\mathcal{D}$) becomes important. This balance is parametrized using the Schmidt number, $Sc = \nu/\mathcal{D}$.

Depending upon the type of contaminant, contaminant microscale η_c can be defined. For scalar fields with $Sc > 1$, $\nu > \mathcal{D}$ implying that diffusion of C is less effective than the transport facilitated by vortices. Thus, one would expect that the fine structure of C will persist for $\eta_c < \eta$. In other words, the structure of contaminant will persists even for scales smaller than η. Thus, for higher Sc, contaminant sheets are formed, which encompass the entire flow field and sample vortical regions as small as η. The thickness of such sheets are of the order of $\eta_c \sim \mathcal{D}^{1/2}(u'_\eta/\eta)^{-1/2}$ (Batchelor, 1952). Since, at the Kolmogorov scale, $u'_\eta\eta/\nu \sim 1$, we can define the Batchelor scale as:

$$\eta_c \sim \left(\frac{\mathcal{D}}{\nu}\right)^{1/2}\eta, \qquad \nu > \mathcal{D}. \tag{2.35}$$

As $\eta_c < \eta$, the range of scale between η_c and η is referred to as *viscous-convective subrange*.

For scalar fields with $Sc < 1$ or $\nu < \mathcal{D}$, diffusion of scalar is more effective than that of the vorticity, and we have $\eta_c > \eta$, and the intermediate range is referred to as *inertial-diffusive subrange*. Turbulent velocity fluctuations steepen the scalar gradients at large scales. However, diffusion of scalar can compete with turbulent fluctuations at $Pe \sim 1$. Thus, at these scales advection is balanced by diffusion, we have: $u'_c \nu_c/\mathcal{D} \sim 1$. In the inertial subrange, the velocity of an eddy of scale r is given by $u'_r \sim (\varepsilon r)^{1/3}$. The velocity at the scale η_c, provided that it lies in the inertial subrange, is $u'_c \sim (\varepsilon \eta_c)^{1/3}$. Thus, we can define the Obukhov-Corrsin length scale as (Oboukhov, 1949; Corrsin, 1951):

$$\eta_c \sim \left(\frac{\mathcal{D}}{\nu}\right)^{3/4} \eta, \qquad \nu < \mathcal{D}. \tag{2.36}$$

The considerations of scalar advection and diffusion become evident in Chapter 6 where we measure the flux of scalar across the flame interface in order to determine the fractal dimension of highly turbulent premixed flames.

2.1.8.2 Scalar dissipation, higher-order statistics and intermittency

In general, one is concerned with the manner in which the variance of the scalar field $\langle C^2 \rangle$ evolves in a turbulent field where the scalar field C is assumed to be homogeneous and isotropic with a zero mean $\langle C \rangle$. Multiplying Eqn. (2.34) with C and taking an ensemble average leads to:

$$\frac{d\langle 1/2C^2 \rangle}{dt} = -\mathcal{D}\left\langle (\nabla C)^2 \right\rangle. \tag{2.37}$$

Thus, the fluctuations in the scalar field are destroyed at a rate proportional to:

$$\chi = -\mathcal{D}\left\langle (\nabla C)^2 \right\rangle, \tag{2.38}$$

where, χ is referred to as scalar dissipation. The scalar dissipation essentially represents the diffusion of scalar from positive to negative regions of C. While advection does not play a direct role in reducing scalar variance, it disperses the scalar into finer and finer filaments so that diffusion can act and destroy scalar variance through the term χ. As discussed above, the characteristic scale of scalar diffusion is η_c. Thus, scalar dissipation can be written as: $\chi = -\mathcal{D}[(\delta C)/\eta_c]^2$, where δC is the characteristic fluctuation in C over scale η_c. Thus, one is again concerned with the statistics of increment of scalar fluctuations C, which is written as:

$$\langle[\delta C(r)]^p\rangle = \langle[C(\boldsymbol{x}+\boldsymbol{r}) - C(\boldsymbol{x})]^p\rangle\,, \tag{2.39}$$

where, the statistics are assumed to follow from isotropy so that it only depends on $r = |\boldsymbol{r}|$ and not on $\boldsymbol{x}$, and p is order of the moment.

The phenomenology of scalar fields in turbulence can be considered in analogy with the phenomenology of the concomitant turbulent flow. Indeed, the statistical theory of scalar turbulence follows closely from the statistical theory of Kolmogorov (1941*b*, 1962) for the statistics of velocity increments. In the intermediate inertial-convective subrange ($\max[\eta_c, \eta] << r << \ell$), one would expect small-scale isotropy such that the statistics can be assumed to depend only on ε, χ and r, that is, $\langle[\delta C(r)]^p\rangle = f(\varepsilon, \chi, r)$. Dimensional arguments for $p = 2$, leads to the scalar equivalent of Kolmogorov's two-thirds law -

$$\left\langle[\delta C(r)]^2\right\rangle = \chi\varepsilon^{-1/3}r^{2/3}, \qquad \forall \;\; \max[\eta_c, \eta] << r << \ell. \tag{2.40}$$

Generalizing to arbitrary order p, we have

$$\langle [\delta C(r)]^p \rangle = \chi^{p/2} \varepsilon^{-p/6} r^{p/3}, \qquad \forall \;\; \max[\eta_c, \eta] << r << \ell. \tag{2.41}$$

The above was derived independently by Oboukhov (1949) and Corrsin (1951), and is therefore referred to as Kolmogorov-Obukhov-Corrsin (KOC) theory (Davidson, 2015). The theory has been quite useful in developing an intuitive understanding of the problem. However, experimental studies showed the limitation of the KOC theory. In particular, it was emphasized that the conditions of local isotropy are almost never achieved in laboratory relevant conditions (Sreenivasan, 1991*b*). The lack of local isotropy arises due to the persistence of mean scalar gradient at small scales, giving rise to ramp-cliff structures (Holzer and Siggia, 1994). Consequently, even in random Gaussian and ‘structure-less’ turbulent fields, statistics of scalar fluctuations are non-Gaussian and highly intermittent (Holzer and Siggia, 1994; Shraiman and Siggia, 2000). The structure of scalar fields arises from two concomitant contributions. The first is the kinematic contribution arising from Lagrangian chaos, while the other arises from the dynamic nature of Eulerian velocity fields (Shraiman and Siggia, 2000; Falkovich *et al.*, 2001; Tsinober, 2009). In fact, scalar fluctuations display a much stronger anomalous scaling exponent in comparison to the underlying velocity field (Frisch, 1995; Sreenivasan and Antonia, 1997), as can be seen from a comparison of the scaling exponents for the velocity and scalar fluctuations in Fig. 2.4(a) and 2.4(b), respectively.

Small-scale intermittency have important implications in a variety of fluid dynamical problems such as transition to turbulence (Goldenfeld, 2006), LES modeling of turbulent flows (Cerutti and Meneveau, 1998), atmospheric flows (Mahrt, 1989), Lagrangian dynamics (Picardo *et al.*, 2020), particle laden flows (Park *et al.*, 2017), wave turbulence (Newell *et al.*, 2001; Falcon *et al.*, 2007), solar winds (Bruno *et al.*, 2001), etc. Naturally, small-scale intermittency in turbulent flows have received considerable attention over the past decades (see Sreenivasan and Antonia, 1997; Shraiman and Siggia, 2000; Falkovich *et al.*, 2001; Dubrulle, 2019, for a comprehensive review on this topic).

2.2 TURBULENT COMBUSTION

In this section, we discuss the relevant concepts of premixed turbulent flames. We begin by discussing the balance between reaction and turbulence time scales and introduce the regime diagram for discerning various modes of combustion. We then discuss the evolution equation of premixed flames and discuss the spectral closure obtained by Peters (1992). We conclude our discussion on turbulent premixed flames with an overview of the local and global flame response to narrowband and broadband turbulent fluctuations.

2.2.1 Regimes of turbulent premixed flames

Premixed flames can either be laminar or turbulent. However, all turbulent flames cannot be grouped together. This is because depending upon the flow Re and turbulent intensity u', the interactions between turbulent and flame time scales change. The various modes of combustion can be delineated based on a comparison of turbulence

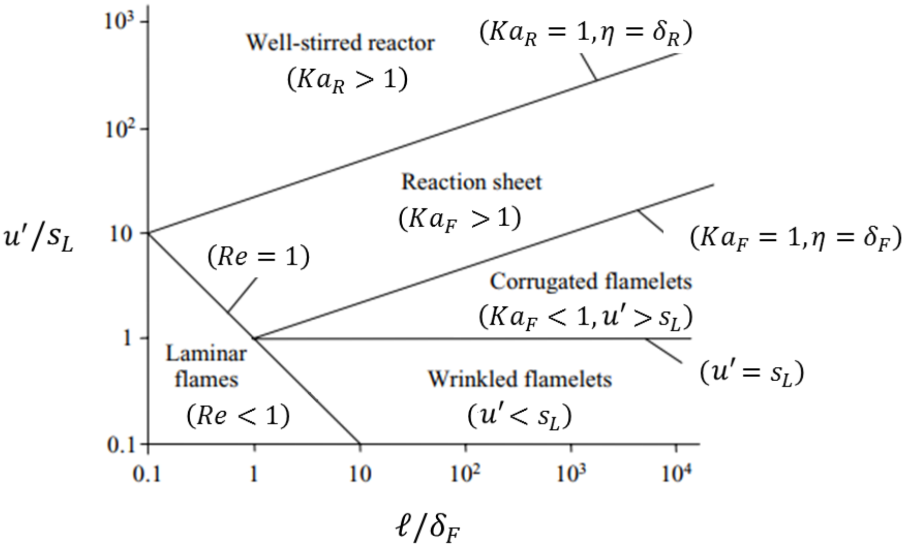
10^3
10^2
10
1
0.1
u'/s_L
0.1
1
10
10^2
10^3
10^4
ℓ/δ_F
Well-stirred reactor
$(Ka_R > 1)$
$(Ka_R = 1, \eta = \delta_R)$
Reaction sheet
$(Ka_F > 1)$
$(Ka_F = 1, \eta = \delta_F)$
$(Re = 1)$
Corrugated flamelets
$(Ka_F < 1, u' > s_L)$
Laminar
flames
$(Re < 1)$
Wrinkled flamelets
$(u' < s_L)$
$(u' = s_L)$

Figure 2.5: Regimes of turbulent combustion. Adapted from Law (2010) with permission from Cambridge University Press.

and flame time scales through the use of regime diagram referred to as Borghi diagram (Borghi, 1985; Peters, 1988), as shown in Fig. 2.5. The laminar flame speed is indicated as s_L, laminar flame thickness as δ_F, reaction zone thickness as δ_R. The integral scale and Kolmogorov scale are denoted as ℓ and η.

The laminar flame thickness is related to flame speed as $\delta_F = \nu/s_L$. The time scale of flame propagation is thus, $\tau_F = \delta_F/s_L = \nu/s_L^2$. The integral scale Reynolds number is related to laminar flame quantities through the relation:

$$Re = \frac{u'\ell}{\nu} = \frac{u'}{s_L}\frac{\ell}{\delta_F}. \tag{2.42}$$

Premixed flame can be sustained in a turbulent flow if the characteristic time of flame propagation is shorter than characteristic flow time. This balance defines the so called turbulent Karlovitz number $Ka_F = \tau_F/\tau_\eta$. The inverse of the Karlovitz number is referred to as the Damköhler number $Da = \tau_\eta/\tau_F$. Using the relation $\tau_\eta = \eta^2/\nu =$

$\nu/{u'_\eta}^2$ (Eqn. 2.10), we obtain:

$$Ka_F = \frac{\tau_F}{\tau_\eta} = \left(\frac{\delta_F}{\eta}\right)^2 = \left(\frac{u'_\eta}{s_L}\right)^2. \tag{2.43}$$

In the laminar flame regime ($Re < 1$), the flow is laminar, and turbulence intensity is very weak, and the flame undergoes minimal wrinkling. In the wrinkles flamelets regime ($Re > 1, Ka_F < 1, u' < s_L$), the flame thickness is much smaller than η such that turbulence fluctuations can only weakly wrinkle the flame surface. In the corrugated flamelets regime ($Re > 1, Ka_F < 1, u' > s_L$), the flame thickness is still much smaller than η. However, the turbulent intensity is appreciable such that the flame surface undergoes significant distortion while still maintaining its structure.

For the reaction sheet regime ($Re > 1, Ka_F > 1$), the Re and turbulent intensity is sufficiently high such that $\eta < \delta_F$. While the large-scale eddies only distort the flame surface, a range of eddies of size smaller than δ_F can penetrate the preheat zone and enhance the heat and mass transfer rates. Thus, the overall flame surface is broadened. Since the reaction zone thickness $\delta_R < \eta$, so the reaction zone is only wrinkled and remains unaffected by the motion of eddies.

In the well-stirred reaction regime ($Re > 1, Ka_R > 1$), the Karlovitz number based on the reaction thickness is greater than one, implying that $\delta_R > \eta$. Turbulent eddies penetrate the reactant zone and enhance diffusion from reactant to preheat zone, resulting in a significant drop in the temperature of the flame and consequently lead to flame extinction. The entire flow behaves like a well-stirred reactor devoid of any local structure.

While the regime diagram helps in delineating one combustion mode from another, it is often not useful in clarifying the dynamic nature of combustion. For instance, the role of kinematic restoration or the dynamic interaction between flame and turbulent fluctuations cannot be discerned from the turbulent regime diagram. Thus, it is necessary to analyse the evolution equation of scalar variables that approximates the flame surface, which is what we discuss in the next section.

2.2.2 Premixed flame formulation

We now discuss the dynamics of premixed flames in turbulent flows. Flame surfaces are scalar surfaces in turbulent flows capable of propagating with laminar flame speed s_L along the direction of local normal ($\boldsymbol{n}$). The flame surface can then be defined as an iso-surface of a scalar function $G(\boldsymbol{x}, t)$. The scalar function can be based on scalar variables such as reactant mass fraction, temperature, etc. The local flame speed is augmented by various effects of flame stretch and curvature induced by the local structure of the turbulent flow. Under these effects, the evolution equation of the scalar function $G(\boldsymbol{x}, t)$ can be written as (Peters, 1992):

$$\frac{\partial G(\boldsymbol{x}, t)}{\partial t} + \boldsymbol{u} \cdot \boldsymbol{\nabla} G(\boldsymbol{x}, t) = \left[s_L - s_L \eta_M \kappa + \eta_M \mathbf{n} \cdot \boldsymbol{\nabla} \boldsymbol{u} \cdot \boldsymbol{n}\right] |\nabla G|. \tag{2.44}$$

Here, $\boldsymbol{u}(\boldsymbol{x}, t)$ represents the velocity field. $\boldsymbol{n}$ is the local surface normal defined as $\hat{\boldsymbol{n}} = \nabla G / |\nabla G|$. Further, the flame curvature is defined as $\kappa = \nabla \cdot \boldsymbol{n}$. The evolution of flame surface is governed by a balance between heat and mass transport and needs to be taken into account explicitly. The balance between conductive heat transfer from the reaction zone to the reactants and diffusion of reactant species into the reaction zone is given by the Lewis number. The Lewis number is defined as $Le = \lambda/(\rho c_p s_L)$, where λ is the thermal conductivity, ρ is the density of the reactants, and c_p is the heat capacity. The Markstein length η_M is defined in such a manner so as to account for non-unity Lewis number effects such as increased flame speed as a result of enhanced heat transfer due to focusing around a concave flame surface, and so on (Pelce and Clavin, 1982; Clavin and Williams, 1982). Experimental measurement of η_M for various types of flames have been shown that η_M varies in the range of $2\delta_F - 6\delta_f$ (Searby and Quinard, 1990). We are concerned with the statistics of the scalar field $G(\boldsymbol{x}, t)$, and we will focus on the evolution equation of various moments of the scalar field next.

2.2.2.1 Equation for the mean and the variance of the G-equation

Let us suppose that the flame propagates in homogeneous and isotropic turbulence in the z-direction. The effects of large-scale variation due to propagation can be removed through the variable transformation: $G(\boldsymbol{x}, t) = z(t) + \xi(\boldsymbol{x}, t)$. We consider the case of a conical V-flame in Chapters 3, 4 and 5, and a similar transformation allows us to remove the effects of large scale orientation of the flame and focus on the fluctuations on the flame surface. We define the gradient of scalar as $\sigma(\boldsymbol{x}, t) = ||\nabla\xi(\boldsymbol{x}, t)||$, where $||\cdot||$ implies the magnitude of the vector $\nabla\xi(\boldsymbol{x}, t)$.

We can perform Reynolds decomposition and split the field of $\xi(\boldsymbol{x}, t)$ and $\boldsymbol{u}(\boldsymbol{x}, t)$ into mean and fluctuating components such that: $\xi(\boldsymbol{x},t) = \langle\xi(\boldsymbol{x})\rangle + \xi'(\boldsymbol{x},t)$, $\boldsymbol{u}(\boldsymbol{x},t) = \langle\boldsymbol{u}(\boldsymbol{x})\rangle + \boldsymbol{u}'(\boldsymbol{x},t)$ and $\sigma(\boldsymbol{x},t) = \langle\bar{\sigma}(\boldsymbol{x})\rangle + \sigma'(\boldsymbol{x},t)$. The time-average is defined as: $\langle\xi(\boldsymbol{x})\rangle = 1/T\int_T \xi(\boldsymbol{x},t)dt$, where T is sufficiently large to allow statistical convergence.

Following the above decomposition, we can obtain the evolution equation for the mean $\langle\xi(\boldsymbol{x})\rangle$ from Eqn. (2.44) as:

$$\begin{aligned}\left(\frac{\partial\langle\xi\rangle}{\partial t} + \langle u_i\rangle\frac{\partial\langle\xi\rangle}{\partial x_i}\right) &+ \frac{\partial\langle u_i'\xi'\rangle}{\partial x_i}\\ &= s_L\langle\sigma\rangle + s_L\eta_M\frac{\partial^2\langle\xi\rangle}{\partial x_i^2} - s_L\eta_M\left\langle\frac{\partial\ln\sigma}{\partial x_j}\frac{\partial\xi}{\partial x_j}\right\rangle + \eta_M\left\langle\frac{\partial u_i}{\partial x_j}\frac{\sigma_i\sigma_j}{\sigma}\right\rangle.\end{aligned} \tag{2.45}$$

We have used the index notation for expressing the summation of derivatives over $i, j = 1, 2, 3$. Similarly, the governing equation for fluctuations ξ' is obtained by subtracting Eqn. (2.45) from Eqn. (2.44):

$$\begin{aligned}\frac{\partial\xi'}{\partial t} + \langle u_i\rangle\frac{\partial\xi'}{\partial x_i} &+ \frac{\partial}{\partial x_i}\left(u_i'\langle\xi\rangle + u_i'\xi' - \langle u_i'\xi'\rangle\right)\\ &= s_L\sigma' + s_L\eta_M\frac{\partial^2\xi'}{\partial x_i^2} - s_L\eta_M\left(\frac{\partial\ln\sigma}{\partial x_j}\frac{\partial\xi}{\partial x_j}\right)' + \eta_M\left(\frac{\partial u_i}{\partial x_j}\frac{\sigma_i\sigma_j}{\sigma}\right)\end{aligned} \tag{2.46}$$

The equation for the variance of the scalar field $\langle\xi'^2\rangle$ can be derived by multiplying Eqn. (2.46) by $2\xi'$ and then taking the mean, which leads to (Peters, 1992):

$$\frac{\partial\langle\xi'^2\rangle}{\partial t} + \langle u_i\rangle\frac{\partial\langle\xi'^2\rangle}{\partial x_i} = S_1 + S_2 - S_3 - S_4 - S_5, \tag{2.47}$$

where,

$$
\begin{aligned}
S_1 &= -\frac{\partial}{\partial x_i}\left\langle u_i' \xi'^2 \right\rangle, \\
S_2 &= -2\left\langle u_i' \xi' \right\rangle \frac{\partial \langle \xi \rangle}{\partial x_i}, \\
S_3 &= -2 s_L \langle \xi' \sigma' \rangle, \\
S_4 &= -2 s_L \eta_M \left\langle \xi' \left(\frac{\partial^2 \xi}{\partial x_i^2} - \frac{\partial \ln \sigma}{\partial x_j} \frac{\partial \xi}{\partial x_j} \right)' \right\rangle, \\
S_5 &= -2 s_L \eta_M \left\langle \xi' \left(\frac{\partial u_i}{\partial x_j} \frac{\sigma_i \sigma_j}{\sigma} \right)' \right\rangle.
\end{aligned}
$$

The terms on the right-hand side of Eqn. (2.47) represent different balances that affect the variance of fluctuations of $\xi'(\boldsymbol{x}, t)$ and capture various underlying physical processes taking place in turbulent premixed combustion. These terms are:

S_1. Turbulent transport of the scalar variance.

S_2. Production of scalar variance by turbulent fluctuations.

S_3. This term quantifies the effect of the kinematic restoration. This term is given by the co-variance of the scalar fluctuations with its fluctuating gradient $\sigma' = |\boldsymbol{\nabla}\xi'|$. The co-variance $\langle \xi' \sigma' \rangle$ is, in general, negative, meaning that this term has a restorative effect on the variance of scalar (Peters, 1988). Thus, fluctuations induced by turbulent fluctuations are smoothed out by this term.

The effect of kinematic restoration becomes dominant at the Gibson scale. The Gibson scale ℓ_g can be derived through a kinematic balance between the laminar flame speed and the velocity of an eddy of size r in the inertial range. The velocity of an eddy in the inertial range is given by ${u_r'}^3 \sim \varepsilon r$. The Gibson length scale is the scale at which $s_L = u_r'$, and noting that $\varepsilon \sim u'^3 \ell$, we get

$$
\ell_g = \frac{s_L^3}{\varepsilon} = \left(\frac{s_L}{u'} \right)^3 \ell. \tag{2.48}
$$

For eddies of size $\ell > r > \ell_g$, the flame surface is perturbed, similar to how a passive surface would be perturbed in the inertial sub-range in non-reacting turbulent flows. In contrast, for eddies $r < \ell_g$, the velocity difference across the flame is smaller than the flame velocity s_L and cannot counterbalance flame propagation effects, and kinematic restoration becomes the dominant mechanism of dissipation of flame fluctuations.

S_4. This term represents the scalar dissipation. This term represents the co-variance of ξ' and the diffusive terms which appear in Eqn. (2.44). Among these terms, the most dominant term is the first term and is referred to as scalar dissipation. This term is dependent on the advection-diffusion balance of scalar variance.

This effect becomes dominant at the so-called Obhukov-Corrsin length scale based on the Markstein diffusivity, and is defined as (Peters, 2001):

$$\eta_c = \left(\frac{\mathcal{D}_M^3}{\varepsilon}\right)^{1/4} = \left(\frac{(s_L\eta_M)^3}{\varepsilon}\right)^{1/4}. \tag{2.49}$$

where, $\mathcal{D}_M = s_L\eta_M$ is the Markstein diffusivity. Recall, for a passive scalar surface, the equivalent Obhukov-Corrsin length scale was defined in Eqn. (2.36), where scalar diffusivity $\mathcal{D}$ was used instead of Markstein diffusivity $\mathcal{D}_M$.

Effects of scalar dissipation becomes dominant for scales below η_{OC}. In Chapter 6, we show that for $Da \sim \mathcal{O}(1)$ thickened flames are in the passive scalar limit, and η_c is utilized for determining the inner cut-off of fractal scaling for flames with finite thickness.

S_5. This term depicts the scalar-strain co-variance between ξ' and flow divergence induced flame stretch. This term is also restorative and smooths the flame surface by preferentially stretching the flame surface. This term comes into effect at the Markstein length η_M (Peters, 2001).

The terms S_3, S_4, and S_5 in Eqn. (2.47) for the variance of ξ' are unknown. Equation (2.47) cannot be solved without obtaining the closure of these terms. In our discussion of the unknown terms, we stressed the different range of scales at which these effects come into effect. Thus, we introduce the two-point correlation of ξ' as suggested by Peters (1992). The two-point correlation allows us to understand the nature of fluctuations in a scale-dependent manner and make considerations for the physical effects taking place at these scales.

2.2.2.2 Scalar two-point correlation and the spectrum function

The two-point auto-correlation of scalar fluctuations $\xi'(\boldsymbol{x},t)$ is defined as:

$$R_\xi(\boldsymbol{r},t) \equiv \langle \xi'(\boldsymbol{x}+\boldsymbol{r},t)\xi'(\boldsymbol{x},t)\rangle. \tag{2.50}$$

We assume that the conditions of isotropy and homogeneity are satisfied such that $R_\xi(\boldsymbol{r},t)$ is a function of $r = ||\boldsymbol{r}||$ only. Peters (1992) derived the evolution equation for the autocorrelation $R_\xi(\boldsymbol{x},t)$ assuming standard methods of homogeneous turbulence (see Batchelor, 1953):

$$\frac{\partial R_\xi}{\partial t} + 2\frac{\partial\langle u_i'(\boldsymbol{x}+\boldsymbol{r},t)\xi'(\boldsymbol{x},t)\xi'(\boldsymbol{x}+\boldsymbol{r},t)\rangle}{\partial r_i} + 2s_L S_3 + 2\mathcal{D}_M S_4 + 2\eta_M S_5 = 0, \tag{2.51}$$

where,

$$\begin{aligned}
S_3(\boldsymbol{r},t) &\equiv -\langle \xi'(\boldsymbol{x}+\boldsymbol{r},t)\sigma'(\boldsymbol{x},t)\rangle,\\
S_4(\boldsymbol{r},t) &\equiv -\left\langle \xi'(\boldsymbol{x}+\boldsymbol{r},t)\left(\frac{\partial^2\xi(\boldsymbol{x},t)}{\partial x_i^2} - \frac{\partial \ln\sigma(\boldsymbol{x},t)}{\partial x_j}\frac{\partial\xi(\boldsymbol{x},t)}{\partial x_j}\right)'\right\rangle,\\
S_5(\boldsymbol{r},t) &\equiv -\left\langle \xi'(\boldsymbol{x}+\boldsymbol{r},t)\left(\frac{\partial u_i(\boldsymbol{x},t)}{\partial x_j}\frac{\sigma_i(\boldsymbol{x},t)\sigma_j(\boldsymbol{x},t)}{\sigma(\boldsymbol{x},t)}\right)'\right\rangle.
\end{aligned}$$

Note that the terms S_3, S_4 and S_5 appearing in Eqn. (2.47) appear in Eqn. (2.51) as well in the form of two-point co-variance.

Introducing the Fourier transform of the auto-correlation $\hat{R}_\xi(\boldsymbol{k},t)$, we obtain

$$\hat{R}(\boldsymbol{k},t) = \frac{1}{(2\pi)^3}\int_{V(\boldsymbol{r})} R(\boldsymbol{r},t)e^{-i\boldsymbol{k}\cdot\boldsymbol{r}}d\boldsymbol{r},$$

where the integration is taken over the correlation space. The scalar spectrum function $\Gamma(k,t)$ is then defined as:

$$\Gamma(k,t) = k^2 \oint \hat{R}(\boldsymbol{k},t) d\Omega = 4\pi k^2 \hat{R}(k,t), \tag{2.52}$$

where, $d\Omega$ is the solid angle and $k = ||\boldsymbol{k}||$. Finally, Fourier transform of Eqn. (2.51) then leads to the evolution equation for the scalar spectrum function (Peters, 1992):

$$\frac{\partial \Gamma(k,t)}{\partial t} - T(k,t) + 4\pi k^2 \left[2 s_L \hat{S}_3(k,t) + 2 s_L \eta_M \hat{S}_2(k,t) + 2\eta_M \hat{S}_3(k,t) \right] = 0. \tag{2.53}$$

Here, $T(k,t)$ is the Fourier transform of the triple correlation $\langle u_i'(\boldsymbol{x}+\boldsymbol{r},t)\xi'(\boldsymbol{x},t)\xi'(\boldsymbol{x}+\boldsymbol{r},t)\rangle$ and indicates the transfer of scalar fluctuations from one wavenumber to another in the spectral space.

In order to obtain closure for $T(k,t)$, we use a gradient transport hypothesis introduced by Pao (1965, 1968), which is written as:

$$T(k,t) = -\frac{\partial W(k,t)}{\partial k}, \tag{2.54}$$

where,

$$W(k,t) = C_s^{-1} \epsilon^{1/3} k^{5/3} \Gamma(k,t). \tag{2.55}$$

Here, C_s is a constant for the scalar spectrum presumed to be universal. We note that above assumptions are dimensionally correct which can be verified by noting that the dimensions of the scalar spectrum function Γ is $[\xi^2]/\mathrm{s}$, dimensions of W is $[\xi^2]/\mathrm{ms}^2$ and for $T(k,t)$ is $[\xi^2]/\mathrm{s}^2$. In Eqn. (2.51), $S_3(\boldsymbol{r},t)$ and $S_4(\boldsymbol{r},t)$ contain derivative of ξ^2, their Fourier transform should be proportional to k and k^2 respectively. The term $S_5(\boldsymbol{r},t)$ contains gradient of velocity with dimension s^{-1}, which means its Fourier transform should contain term proportional to $\epsilon^{1/3}$. Simple dimensional argument suggests that the following relationship for the Fourier transform must hold:

$$\begin{aligned}
8\pi k^2 \hat{S}_3 &= c_3 C_s^{-1} k \Gamma(k,t) \\
8\pi k^2 \hat{S}_4 &= c_4 C_s^{-1} k^2 \Gamma(k,t) \\
8\pi k^2 \hat{S}_5 &= c_5 C_s^{-1} \varepsilon^{1/3} k^{5/3} \Gamma(k,t)
\end{aligned} \tag{2.56}$$

where, c_3, c_4 and c_5 are empirical constants. Thus, Eqn. (5.4) can be re-written as a linear differential equation:

$$C_s \frac{\partial \Gamma}{\partial t} + \varepsilon^{1/3}\left(\frac{5}{3}k^{2/3}\Gamma + k^{5/3}\frac{\partial \Gamma}{\partial k}\right) + c_3 s_L k \Gamma + c_4 s_L \eta_M k^2 \Gamma + c_5 \eta_M \varepsilon^{1/3} k^{5/3} \Gamma = 0. \tag{2.57}$$

Solving Eq. Eq15-SpectrumDiffEqn using the method of characteristics, we obtain (Peters, 1992):

$$\Gamma(k,t) = \mathcal{H}(k-k_\ell) k^{-5/3} \exp\left[-3c_3 (l_G k)^{1/3}\right] \exp\left[-\frac{3}{4} c_4 (l_c k)^{4/3}\right] \exp\left(-c_5 \eta_M k\right), \tag{2.58}$$

where, $\mathcal{H} = \mathcal{H}(k-k_\ell)$ is the Heaviside function such that $\mathcal{H} = 0$ if $k < k_\ell$ and $\mathcal{H} = 1$ if $k > k_\ell$. This is done to introduce a cut-off in the small-wavenumber range as there is no universal form for the small-wavenumber or the large scales in turbulent flows.

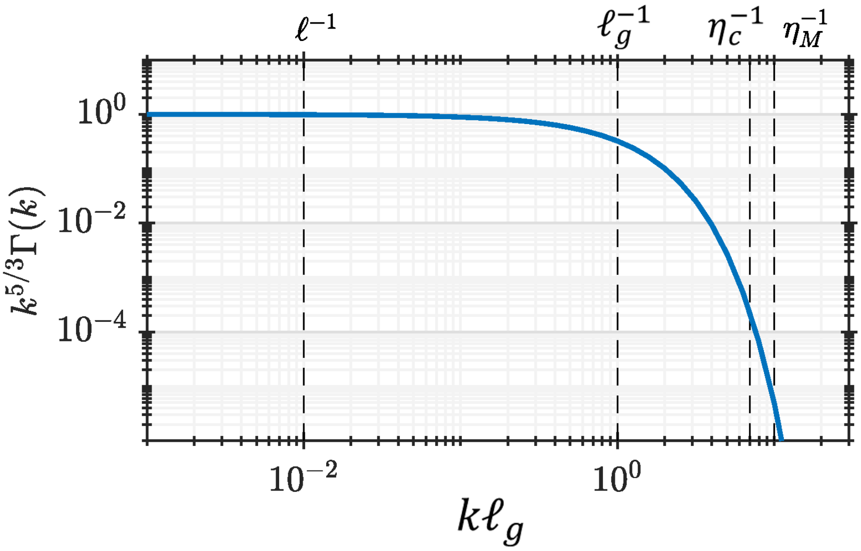

Figure 2.6: Schematic of the compensated spectrum function $k^{5/3}\Gamma(k)$ associated with flame fluctuations ξ' as a function of the non-dimensional wavenumber. We note that the spectrum decays exponentially through the additional term in Eqn. (5.5). The pertinent length scales are marked for clarity, where ℓ is the integral scale, ℓ_g is the Gibson scale, η_c the Corrsin scale and η_M the Markstein length.

The spectral closure of the terms S_3, S_4, and S_5 involving simple dimensional arguments, as discussed above, was first proposed by Peters (1992). The spectral closure has since then been well-substantiated and remains very influential in the combustion literature (Wirth and Peters, 1992; Collins, 1995; Chaudhuri *et al.*, 2011).

The specific form of the spectrum $\Gamma(k)$ has many interesting implications. First, the scaling of fluctuations at large scales ($r >> \ell$) depends on anisotropic effects such as mean shear in the flow, flame orientation, flame surface instabilities such as Darrieus-Landau instability, and so on. The scaling of the spectrum at large scales would be non-universal and depend on the specific configuration of the experiments.

Second, we observe that for scales smaller than integral scale and larger than Gibson scale ($\ell > l > \ell_g$), the spectrum function scales as $\Gamma(k) \sim k^{-5/3}$. This is the classical Kolmogorov scaling for the velocity field. In other words, for this intermediate range of scales, inertial range velocity fluctuations induce fluctuations on the flame surface, which depict Kolmogorov's scaling. The effect of turbulence is thus limited to perturbing the flame surface without affecting any of the physical balances inherent to the flame dynamics. The flame fluctuations are thus analogous to fluctuations induced on passive scalar surfaces in non-reacting turbulent flows in the inertial sub-range.

Third, for scales below the Gibson scale ($r < \ell_g$), the $k^{-5/3}$ scaling is no longer valid. This is a consequence of the restorative effect of flame propagation, which leads to a much steeper exponential decay in the spectra. The exponential decay becomes increasingly stronger as the effects of scalar dissipation and scalar-strain co-variance come into effect as smaller scales are approached.

2.2.2.3 Higher-order statistics and intermittency in turbulent premixed flames

Sreenivasan (2004) noted the limited attention afforded to the role of small-scale intermittency in the study of turbulent combustion. He further observed that in the very few studies on this matter, appropriate considerations were not made for differentiating between the effects of small-scale and large-scale intermittency. Large-scale intermittency arises due to flow unsteadiness in the transitional flows. Despite these gaps, dissipation-range intermittency has received some attention. For instance, it is quite well-known that the scalar dissipation rate conditioned on some scalar variables such as temperature, mass fraction show a considerable departure from a Gaussian behavior (Karpetis and Barlow, 2002; Hamlington *et al.*, 2012; Chaudhuri *et al.*, 2017).

Similarly, enstrophy and turbulent kinetic energy dissipation have also been shown to be intermittent, with their PDFs possessing wide-tails (Hamlington *et al.*, 2012). The deviation from Gaussianity of dissipation quantities in much of these studies was explained using the log-normal model (Hamlington *et al.*, 2012).

Till now, studies on turbulent premixed combustion have focussed mostly on intermittency in the dissipation range. So, very little is known regarding the small-scale intermittency, whose effects are most pronounced in the inertial sub-range. Further, the log-normal model is used quite often in explaining dissipation range intermittency and models on turbulent combustion in general (Poinsot and Veynante, 2005). However, the log-normal model is based on the central-limit theorem. Mandelbrot (1972) explained that the central-limit theorem can not describe extreme events, which determine the tails of the PDF of intermittent variables, and the associated higher-order moments.

Thus, there is a need for demarcation among large-scale, small-scale, and dissipation-range intermittency along with improved modelling approaches for studying intermittent statistics. Further, the exact nature of cross-over behavior from small-scale to dissipation range intermittency in turbulent premixed flames is another open question. Further, the effect of small-scale intermittency on flame-relevant quantities is of practical interest. Extreme fluctuations over small scales would evidently lead to extreme fluctuations in quantities that depend on the gradient of the fluctuations in the flame position, such as flame stretch, strain-rate, turbulent speed closures, etc. If not accounted for properly, these extreme fluctuations would dissuade any effort towards the development of theories associated with higher-order quantities.

Despite the lack of direct experimental confirmation, the effect of small-scale intermittency on premixed flames has been considered in some theoretical modelling studies. For instance, infinitely thin premixed flames ($Da \approx 10^2$) have been shown to possess fractal dimension of $\mathbb{D} = 7/3$ (Gouldin, 1987; Kerstein, 1988; Gülder *et al.*, 2000). Kerstein (1991) considered the effect of small-scale intermittency of turbulent kinetic energy dissipation on infinitely thin flames and derived correction to the limit of $\mathbb{D} = 7/3$. Gülder (2007) explicitly accounted for the effect of intermittency on scalar transport in the preheat zone of thickened flames and derived turbulent flame speed model. The flame speed model showed good experimental agreement. Similarly, the role of small-scale intermittency have been thought to affect the flame extinction and re-ignition probabilities (Meneveau and Poinsot, 1991; Kerstein, 2002) and contribute to deflagration-to-detonation transition (Pan *et al.*, 2008). However, the number of investigations till now is very limited.

Finally, a common way of characterizing intermittent fields and quantities is through the use of the multifractal model. Nevertheless, very few studies have adopted this approach in the study of turbulent combustion. Saha *et al.* (2014) characterized the intermittent nature of the flame-length ratio of an expanding flame through the multifractal spectrum. They noted that multifractal spectrum remained self-similar at different radii of propagation and concluded universality in the multiplicative process control the dynamics of the expanding flame. Raghunathan *et al.* (2020) determined the multifractal spectrum of partially premixed flame during the state of thermoacoustic instability. They depicted that the multifractal spectra oscillated periodically with the pressure oscillations, quantifying the effect of large-scale acoustic forcing on the multiplicative processes governing the flame evolution.

2.2.3 Large-scale flame response

The response of turbulent premixed flames is not always limited to the interaction between turbulent eddies and flame time scales. A number of large-scale (larger compared to turbulent time scales) processes can alter the flame response. Thus, the large-scale dynamics of the reacting flow field is controlled by the balance between various mean flow processes: the susceptibility of the background flow to flow instability (Rogers, 1956; Poinsot *et al.*, 1987; Schadow and Gutmark, 1992), alteration in the flow stability due to combustion (Lieuwen, 2012; Michalke, 1971; Monkewitz and Sohn, 1988; Yu and Monkewitz, 1990; Emerson and Lieuwen, 2015), manifestation of kinematic restoration over acoustic length scales (Peters, 1992, 1999; Shanbhogue *et al.*, 2009*a*; Hemchandra *et al.*, 2011), intrinsic flame instability such as Darrieus-Landau or Rayleigh-Taylor instability (Clanet and Searby, 1998; Creta *et al.*, 2011; Law and Sung, 2000) and thermoacoustic instability (Lieuwen, 2012; Sujith and Unni, 2020). As such, in the absence of flow instabilities, the balance between the characteristic scales (time and length) of the flow and the flame leads to various types of flame structures as indicated by the flame regimes in a Borghi diagram, discussed earlier (Borghi, 1985; Peters, 2001).

In turbulent combustion systems, flow instabilities play a crucial role in flame stabilization. So, flow instabilities are induced in practical combustors through flame holding mechanisms such as bluff body or dump plane, such that an unstable shear layer is created. The stability of the shear layer breaks down and leads to pronounced periodic vortex shedding through Bénard-von Kárman (BVK) instability. The periodic vortices create recirculation zones where combustion takes place. This process is thus responsible for fluctuations in the heat release rate response in such systems (Schadow and Gutmark, 1992; Poinsot *et al.*, 1987).

Many studies have shown that measuring the harmonic flame response can shed light on the effect that different large-scale flame-flow processes have on the overall flame response (Shanbhogue *et al.*, 2009*a*; Preetham *et al.*, 2007; Shin and Lieuwen, 2012, 2013; De Rosa *et al.*, 2016; Humphrey *et al.*, 2018). Similarly, the effect of turbulence on the large-scale flame response is also important. For bluff-body stabilized conical flames in the limit of corrugated flamelet and thin reaction regime, increase in turbulence intensity have shown to (1) increase the thickness of the preheat zone, (2) broaden the strain rate & curvature probability density functions, (3) increase the flame area ratio, and (4) increase & saturate the flame brush thickness (Chowdhury and Cetegen, 2017; Chowdhury *et al.*, 2017). Further, the average corrugated flame burning speed depends crucially on the turbulence intensity, with quadratic, 4/3 power law, and linear dependence at low, intermediate, and high turbulence levels, respectively (Aldredge and Williams, 1991; Aldredge, 2006, 2017). Kinematic restoration is strengthened with increasing turbulence, as is evidenced by the decrease in the ensemble-averaged flame fluctuations in numerical (Preetham *et al.*, 2007; Shin and Lieuwen, 2012, 2013) and experimental (Humphrey *et al.*, 2018; Humphrey and Lieuwen, 2017) studies. Figure 2.7(a) shows the increase in flame smoothing for a turbulent simulation (solid red line) and Fig. 2.7(b) shows the decrease in flame wrinkle amplitude, $|\langle\hat{\xi}(y, f_f)\rangle|$. The effect of kinematic restoration is indeed significant as it can alter the gain and phase of the flame transfer function considerably through leading order corrections in the asymptotic analysis of the heat release rate response (Hemchandra *et al.*, 2011).

The imposition of harmonic excitation, self-excited or external, on the flame-turbulence interaction brings in a characteristic acoustic length and time scale in addition to the range of length and time scales present due to the underlying flow turbulence. Consequently, the flame response to acoustic (Jones *et al.*, 2010; Bellows *et al.*, 2007; Durox *et al.*, 2009; Fleifil *et al.*, 1996) and vortical (Chaparro *et al.*, 2006; Balachandran *et al.*, 2005; Kaufmann *et al.*, 2002; Durox *et al.*, 2005) disturbances have been found to be highly nonlinear functions of the frequency and amplitude of the imposed disturbances. Further, the harmonic flame response is of practical importance because of the propensity of premixed flames to couple with acoustic fluctuations in confinement and leading to the state of thermoacoustic instability.

The harmonic flame response, measured at the amplitude and phase of the frequency of forcing or excitation $\hat{\xi}(f_f)$, also depends on the frequency (or wavelength) of the imposed acoustic disturbances (Hemchandra *et al.*, 2011). For instance, the kinematic restoration will cause the random fluctuation in the flame position to tend to the baseline imposed by the harmonic acoustic disturbances, as indicated by the dotted blue line in Fig. 2.7(c). Further, the baseline curvature can locally increase/decrease the turbulent flame consumption speed (Humphrey *et al.*, 2018). For bluff-body stabilized flames, Shanbhogue *et al.* (2009*a*) found that the harmonic flame response is a nonlinear

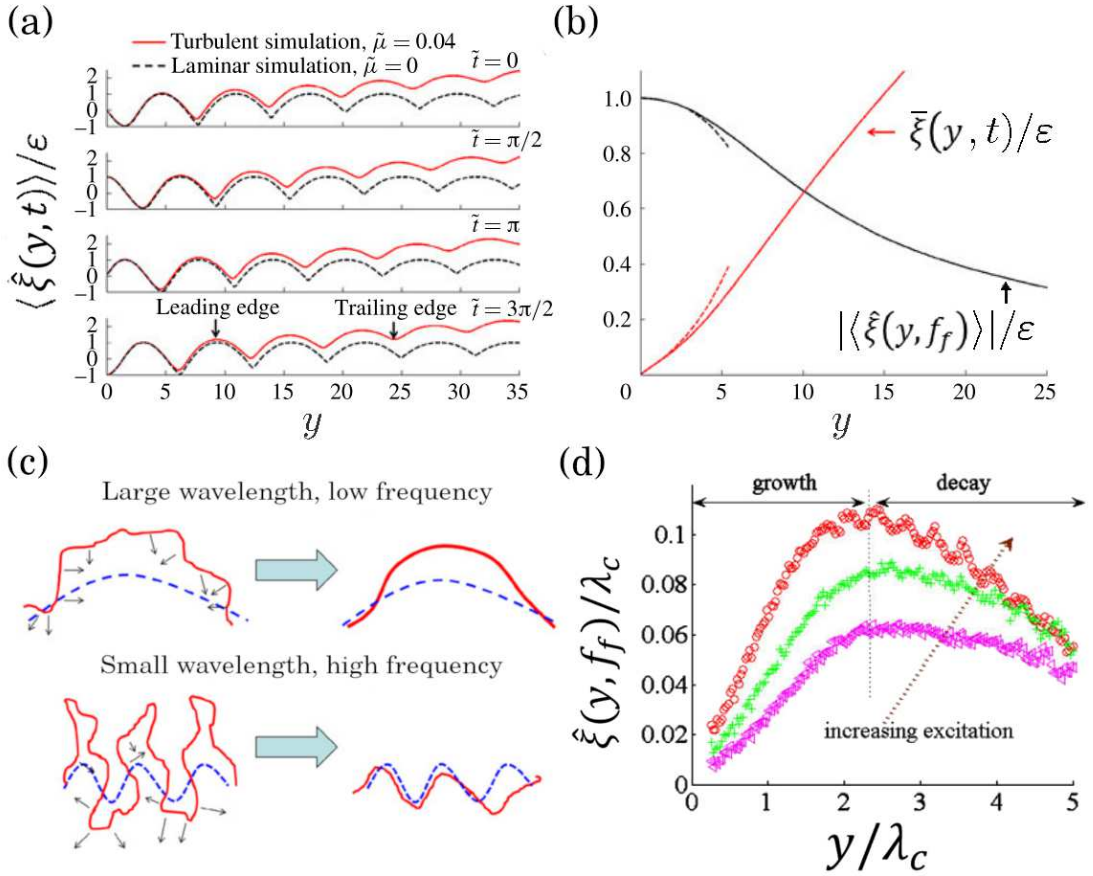

Figure 2.7: Effect of harmonic forcing and turbulence on the large-scale flame dynamics. (a) Flame sheet anchored on an oscillating bluff-body ensemble-averaged at different time instances. (b) Increase in the mean flame position, $\bar{\xi}(y,t)$, and decrease in the flame flame wrinkle amplitude $|\langle\hat{\xi}(y, f_0)\rangle|$, with downstream distance. (c) Cartoon depicting the effect of wavelength of harmonic disturbances on the mean flame response. (d) Typical response of a bluff-body stabilized flame. Adapted from (a, b) Shin and Lieuwen (2012), (c) Hemchandra *et al.* (2011) and (d) Shanbhogue *et al.* (2009*a*) with permission from Elsevier.

function of the downstream distance as illustrated in Fig. 2.7(d). The flame response in the vicinity of the bluff-body linearly increases with the downstream distance as flame holding mechanisms dominate the response. The flame response reaches its peak due to constructive interference between convection of vortical flow disturbances and propagation of coherent flame wrinkles along the flame front. Further downstream, in the absence of any disturbance generating mechanism, the flame response decays as the strength of vortical disturbances and coherent wrinkles diminish due to kinematic restoration and flame stretch effects (§2.2.2.1).

Thus, in Chapter 4, we probe the harmonic flame response of the V-flame at various experimental conditions and study the interaction of convecting disturbances on the flame surface, measure the local flame behavior, and quantify their effect on the large-scale harmonic heat release rate response.

2.3 THERMOACOUSTIC INSTABILITY

In this section, we briefly review the underlying mechanisms which lead to the phenomena of thermoacoustic instability. We also discuss the manner in which the transition takes place from a stable state of combustor operation to unstable limit cycle oscillations and how acoustic fluctuations affect the heat release rate response. Finally, we also discuss some control strategies for controlling limit cycle oscillations in unstable, turbulent combustors.

2.3.1 Wave equation and acoustic energy balance in reacting flows

In order to understand the coupling mechanisms between heat release rate and acoustic pressure oscillations, we need to understand the manner in which combustions alters the acoustic variables in combustors. For the present purposes, we consider a one-dimensional constant area, incompressible reacting flow system with very low mean flow velocity and negligible viscous stresses. Further, we assume that the fluctuations in

p', u' and $\dot{q}'$ are negligible in comparison to their mean values, indicated with $\bar{()}$. Under these assumptions, the momentum and energy equation can be written as (Poinsot and Veynante, 2005):

$$\frac{\partial u'}{\partial t} = -\frac{1}{\rho}\frac{\partial p'}{\partial x}, \tag{2.59}$$

$$\frac{1}{\gamma \bar{p}}\frac{\partial p'}{\partial t} + \frac{\partial u'}{\partial x} = \frac{\gamma - 1}{\gamma \bar{p}}\dot{q}'. \tag{2.60}$$

Here, ρ is the density of the medium and γ is the ratio of specific heat capacities. Partial differentiation of Eqn. (2.59) with respect to x and Eqn. (2.60) with respect to t leads to the nonlinear wave equation:

$$\frac{\partial^2 p'}{\partial x^2} - c_0^2 \frac{\partial^2 p'}{\partial x^2} = (\gamma - 1)\frac{\partial \dot{q}'}{\partial t}, \tag{2.61}$$

where, $c_0 = \sqrt{\gamma \bar{p}/\rho}$ is the adiabatic speed of sound. Thus, it is evident from Eqn. 2.61 that the presence of flames in confinement alters its acoustic field. In order to understand the manner in which acoustic disturbances grow, we consider the evolution of acoustic energy. The acoustic energy density is defined as: $e = \rho u'^2/2 + p'^2/2\rho c_0^2$. Multiplying Eqn. (2.60) with p' and Eqn. (2.59) with u' and adding the resulting equations lead to the evolution equation of the acoustic energy balance:

$$\frac{\partial}{\partial t}\left(\frac{1}{2}\rho u'^2 + \frac{p'^2}{2\rho c_0^2}\right) + \frac{\partial}{\partial x}\left(p'u'\right) = \frac{\gamma - 1}{\gamma \bar{p}} p'\dot{q}'. \tag{2.62}$$

This equation is known as the *acoustic energy corollary* as it is obtained as a consequence of the momentum and energy equation. The first term in the equation above implies the time evolution of acoustic energy based on a balance between the second term representing the acoustic flux and the third term, the acoustic source. In order to see whether acoustic energy will grow or decay over time, Eqn. (2.62) needs to be integrated over the combustor volume (V) and time. We have considered only one-dimensional flow. However, the formulation above can easily be extended over any general three-dimensional flow, given that the assumptions remain unchanged. For averaging over time, we consider the fluctuations to be harmonic with frequency f such that the time period is $T = 1/f$. Thus, the overall balance equation is expressed as:

$$\frac{d}{dt}\int_V\int_T\left(\frac{1}{2}\rho u'^2 + \frac{p'^2}{2\rho c_0^2}\right)dtdV + \int_A\int_T p'\boldsymbol{u}'dtdA = \frac{\gamma-1}{\gamma\bar{p}}\int_V\int_T p'\dot{q}'dtdV. \quad (2.63)$$

The second term indicates the acoustic flux losses from the boundary of the control volume. Thus, the equation above lays down the general condition for the growth or decay of acoustic energy for a reacting flow inside a combustion chamber based on the balance between the acoustic flux loss across the boundary and energy influx from the source term.

2.3.2 The Rayleigh criteria and its extensions

Rayleigh (1878) was the first to qualitatively state the condition for the growth of acoustic energy in reacting flows. He explained that if heat is added during local maximum or taken away during a local minimum of the pressure oscillations, acoustic energy will grow inside the duct. The acoustic energy will decay if the relations are reversed. The Rayleigh criteria allude to a positive correlation between heat release rate and pressure fluctuations as the source of thermoacoustic instability, which is expressed as:

$$\frac{\gamma - 1}{\gamma \bar{p}} \int_V \int_T p' \dot{q}' dt dV > 0. \tag{2.64}$$

The correlation expressed through $p'\dot{q}'$ is referred to as the Rayleigh index, and the condition is used extensively for providing bounds of thermoacoustic stability (see Lieuwen and Yang, 2005; Poinsot, 2017; Juniper and Sujith, 2018, for a review).

However, as can be observed from Eqn. 2.62, just a positive correlation between p' and $\dot{q}'$ is often not enough, and one needs to explicitly account for acoustic efflux across the boundary. Thus, an extended criteria implying the requirement for source term being greater than loss term for thermoacoustic instability, can be expressed as:

$$\frac{\gamma - 1}{\gamma \bar{p}} \int_V \int_T p' \dot{q}' dt dV > \int_A \int_T p' \boldsymbol{u}' dt dA. \tag{2.65}$$

Equation (2.65) is referred to as the extended Rayleigh criteria. Many studies have since then extended the criteria for thermoacoustic instability for more general cases such as combustion with a mean flow and entropy fluctuations (Chu, 1965; Myers, 1991; Karimi *et al.*, 2008) and for cases when the underlying eigenvalues of the system are non-orthogonal (Nagaraja *et al.*, 2009; Sujith *et al.*, 2016; Magri *et al.*, 2020).

2.3.3 Mechanisms of thermoacoustic instability

In general, thermoacoustic instability develops when acoustic fluctuations arising from heat release rate fluctuations (Eqn. 2.61) get reflected from combustor walls and perturb the flame surface to close the feedback loop. If the phase at which the reflected acoustic waves match the phase of fluctuations in the heat release rate and the losses are low (Eq-2.65), thermoacoustic instability develops. Such feedback usually results in periodic limit cycle oscillation of acoustic pressure and heat release rate at a frequency close to one of the acoustic eigenmodes of the combustor.

There are many different mechanisms through which laminar and turbulent flames are perturbed. These different mechanisms are often concomitant in laminar and turbulent combustors. These different mechanisms arise because the heat release rate fluctuations are related to the spatial structure of the laminar or turbulent flames. The overall heat release rate depends on the rate of burning of reactants and the area of the flame. The rate of burning can be expressed as $\dot{m} = \rho s_c$, where ρ is the density of reactants and s_c is the reaction consumption speed of the flame. Thus, the overall heat release rate can be defined as (Lieuwen, 2012):

$$\dot{q}(t) = \int_A \rho s_c h_R dA, \tag{2.66}$$

where h_R is the heat released per unit mass of reactants consumed.

It is evident that any factor causing fluctuations in any of these quantities in Eqn. (2.66) will cause fluctuations in the heat release rate. The heat release rate fluctuations can then couple with acoustic pressure fluctuations to lead to thermoacoustic instability. We briefly evaluate some of the mechanisms through which thermoacoustic instability develops in gas turbine relevant conditions.

Acoustic pressure coupling: Acoustic pressure and velocity perturbations directly affect the heat of reaction, density of unburned reactants, flame speed and lead directly to fluctuations in the heat release rate.

Velocity coupling: Reacting flows are often subjected to flow instabilities or intrinsic instabilities. Flow instabilities can be due to vortex shedding past a flame holder such as V-gutter in afterburners or at the point of sharp area expansion in dump combustors (Poinsot *et al.*, 1987; Schadow and Gutmark, 1992; George *et al.*, 2018) or helical instabilities in swirling flows (Bellows *et al.*, 2007; Candel *et al.*, 2014). Similarly, reacting flames also depict flame instabilities known as Darrieus-Landau instability due to flow dilatation and density gradients at the flame interface (Clanet and Searby, 1998; Creta *et al.*, 2011). In either of these cases, instabilities can lead to fluctuations in the burning area and flame speed, which drive heat release rate fluctuations. Often, this type of coupling is related to the mutual synchronization of the oscillatory reacting field with the acoustic field (Pawar *et al.*, 2017, 2019).

Equivalence ratio fluctuations: In partially premixed combustion, acoustic fluctuations can travel upstream along the fuel and air line. These acoustic fluctuations can then cause fluctuations in the equivalence ratio. These equivalence ratio fluctuations then cause fluctuations in the heat release rate and also flame speed oscillations (Lieuwen and Zinn, 1998; Lieuwen *et al.*, 1998; Shreekrishna *et al.*, 2010).

Intrinsic instability: In the mechanisms discussed above, thermoacoustic instability develops in a manner where feedback is established between heat release rate fluctuations and acoustic eigenmodes. In such a case, a clear causal relationship cannot be discerned. In contrast, Hoeijmakers *et al.* (2014) and Emmert *et al.* (2015) studied flame-acoustic in anechoic combustors and found that turbulent flames can depict *flame-intrinsic* feedback. The intrinsic feedback is established by a flame reacting to acoustic velocity fluctuations created by its own heat release rate fluctuations, implying that thermoacoustic instability can develop even when there are no acoustic reflections and very large acoustic losses.

It is quite difficult to pinpoint exact mechanisms responsible for thermoacoustic instability. What is, however, known is that the interactions between turbulence, combustion, and acoustic are highly nonlinear and complex. These complex interactions have been known to lead to highly nonlinear phenomena such as thermoacoustic intermittency, quasiperiodicity, chaos, and n-period oscillations (Sterling, 1993; Kabiraj and Sujith, 2012; Nair *et al.*, 2014; Juniper and Sujith, 2018). The highly nonlinear nature of the problem has necessitated the use of different approaches in making the problem tractable. These include the use of flame transfer and describing functions (Schuller *et al.*, 2020), non-normal and adjoint-based models (Sujith *et al.*, 2016; Magri, 2019), distributed time-lag models (Polifke, 2020) and complex systems approach (Sujith and Unni, 2020) in characterizing and controlling thermoacoustic oscillations.

2.3.4 Bifurcations and transition to thermoacoustic instability

In the previous sections, we discussed the various mechanisms which underlie the phenomenon of thermoacoustic instability. The means through which the state of instability is achieved is also of great practical relevance. The transition to the state of thermoacoustic instability is achieved when some control parameter is changed. For instance, thermoacoustic instability is observed in gas turbine combustors in power plants when the equivalence ratio or flow velocity is altered to deal with an increase or decrease in power demand. Thus, in general, one is concerned with the bifurcation from a stable state of combustor operation to a state of limit cycle oscillation.

2.3.4.1 Hopf bifurcations to limit cycle oscillations

Thermoacoustic instability is generally considered to be a result of Andronov-Hopf, or simply, Hopf bifurcation, where the system transitions from a steady state to limit cycle oscillations. This can take place in two ways. Depending upon the nonlinearity in the system, a change in a control parameter leads to the loss of linear stability of the steady-state, at which point, the system displays limit cycle oscillations, and the amplitude of oscillations gradually grows (Fig. 2.8a). A change in the parameter in the opposite direction leads to a stable state gradually becoming linearly stable, and the oscillations die down. This is referred to as *supercritical* Hopf bifurcation (Strogatz, 2018).

On the other hand, if there are significant nonlinearities in the system, a change in parameter can lead to the stable state becoming nonlinearly unstable such that there is an abrupt jump to a large amplitude limit cycle state at the Hopf point (Fig. 2.8b). A mere change in the parameter in the opposite direction is not enough to attain the steady-state, and the parameter requires to be changed significantly past the Hopf point to attain the steady-state. The point at which the state of limit cycle oscillations jump back to

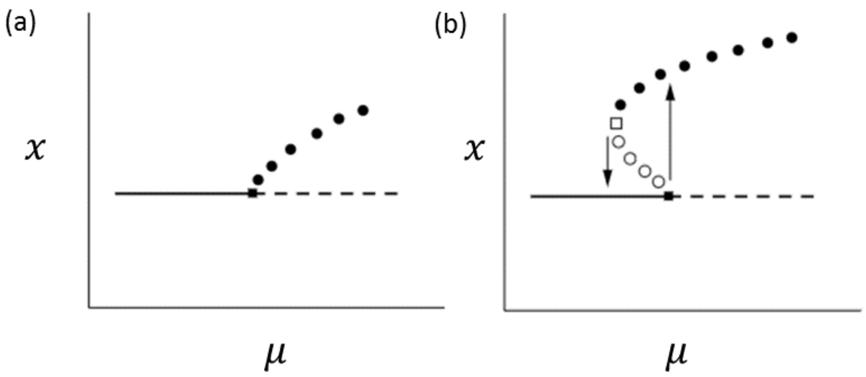

Figure 2.8: Normal form of (a) Supercritical and (b) subcritical Hopf bifurcation for a Van der Pol oscillators depicting the change in the amplitude of oscillations with a change in control parameter μ. Adapted from Ananthkrishnan *et al.* (1998) with permission from Elsevier.

a steady-state is known as the fold point (Fig. 2.8b). This entire scenario is referred to as *subcritical* Hopf bifurcation (Strogatz, 2018). Practical combustors often depict supercritical and subcritical Hopf bifurcation to limit cycle oscillations (Lieuwen, 2002; Campa and Juniper, 2012; Etikyala and Sujith, 2017; Roy *et al.*, 2021; Singh *et al.*, 2021).

2.3.4.2 Intermittency route to limit cycle oscillations

The paradigm of Hopf bifurcation is frequently invoked in experimental and modelling studies of laminar and turbulent combustors. However, there are inherent problems in its usage while discussing transitions in turbulent thermoacoustic systems.

The state of turbulent combustion system during stable combustor operation is never steady in reality. Turbulent flames generate sound through non-steady volumetric expansion and convective entropy modes (Strahle, 1971, 1978; Candel *et al.*, 2009). The radiated sound lacks any characteristic time scale, appears noisy, and possesses a

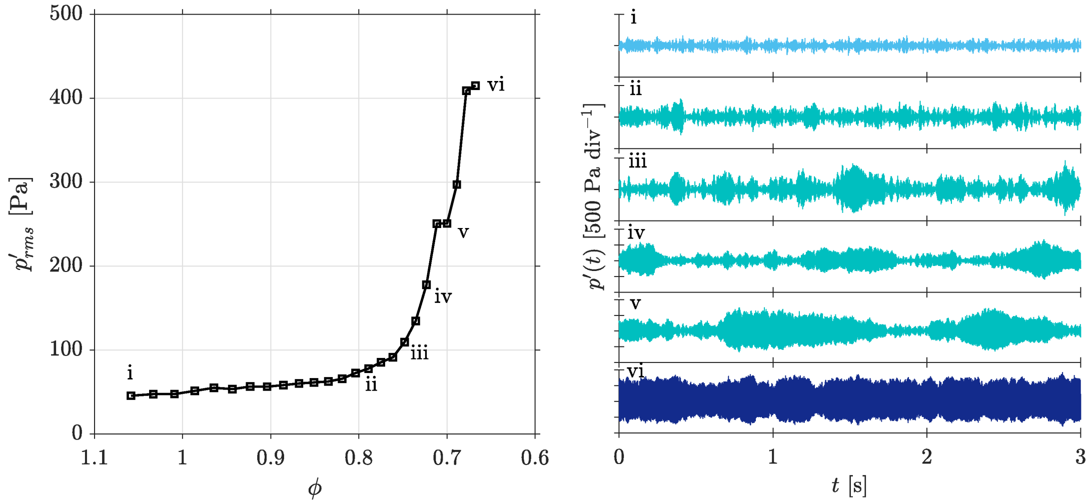

Figure 2.9: Typical bifurcation diagram showing amplitude p'_{rms} as a function of the equivalence ratio ϕ as observed in a bluff-body stabilized combustor. State (i) corresponds to the state of combustion noise, (ii-v) intermittency and (vi) thermoacoustic instability. Figure is adapted from George *et al.* (2018) with permission Cambridge University Press.

broadband signature (Fig. 2.9i). The sound generated during combustion is colloquially referred to as combustion noise (Candel *et al.*, 2009). However, later studies revealed that combustion noise displays scale invariance (Murugesan and Sujith, 2015) and possesses signatures of multifractality (Nair and Sujith, 2014). Nair *et al.* (2013) and Tony *et al.* (2015) showed that the pressure fluctuations during combustion noise are, in fact, deterministic, characterized with moderate to high dimensional chaotic fluctuations.

A continuous variation of control parameters such as equivalence ratio or Reynolds number leads to a transition from combustion noise to thermoacoustically unstable combustor operation. In contrast to the scenario of Hopf bifurcation, the transition is often associated with an intermediate state known as thermoacoustic intermittency (Nair *et al.*, 2014). Thermoacoustic intermittency comprises of a state where bursts of periodic oscillations appear interspersed with chaotic oscillations (Fig. 2.9ii-v). Note that the description of the state of thermoacoustic intermittency is perfectly consistent with the statistical definition of intermittency we have used in the previous sections. In the present case, the extreme fluctuations take the form of large-amplitude bursts of periodic oscillations. During the transition to thermoacoustic instability, there is a gradual loss in multifractality associated with the acoustic pressure and HRR oscillations (Nair and Sujith, 2014; Unni and Sujith, 2015). In other words, there is a transition from a state possessing multiple time scales to one possessing a single characteristic time scale.

2.3.5 Spatiotemporal behavior during intermittency route to thermoacoustic instability

The flow field also depicts many interesting characteristics when the combustor transitions to limit cycle oscillations through intermittency. Let us consider the case of a bluff-body stabilized turbulent combustor. During combustion noise and epochs of aperiodic oscillations during intermittency, small vortices are shed aperiodically, and the heat release rate field remains spatially incoherent (George *et al.*, 2018). In contrast, during thermoacoustic instability and periodic bursts during intermittency, vortices are shed periodically from the combustor's backward-facing step. These vortices carrying the air and fuel mixtures develop into large-scale coherent structures, which collide with the bluff-body and combustor walls. The collision results in intense mixing zones and leads to regions with intense heat release rate (George *et al.*, 2018; Premchand *et al.*, 2019*b*). Raghunathan *et al.* (2020) measured the multifractal spectrum from the spatial distribution of wrinkles on the flame surface at different states during the transition.

They showed that the span of the multifractal spectra increases during thermoacoustic instability, indicating the significant increase in the spatial scales over which HRR fluctuations occur (Raghunathan *et al.*, 2020).

2.3.6 Control of thermoacoustic instability

In the foregoing discussion, we highlighted the mechanisms through which thermoacoustic instability develops and characterized the states obtained during the transition to thermoacoustic instability. In this section, we briefly review some of the practical approaches utilized for abating thermoacoustic instability. The different approaches used for controlling thermoacoustic instability can broadly be classified into evasion/avoidance strategies, and passive and active control and evasion strategies.

The first strategy concerns the knowledge of the gas turbine stability margins and operates the combustor at parametric conditions, which guarantees stable operation. While simple in principle, knowing the stability of turbulent combustors is challenging due to many nonlinear effects arising in complex geometries of real-time combustors. A simpler way to evade thermoacoustic states in combustors is through the use of measures capable of providing a warning when the state of the combustor is about to change. This can be achieved by online monitoring of signals from the combustors, such as measurements of acoustic pressure, temperature, etc. These measurements can then be processed quickly using statistical tools for the prediction of thermoacoustic instability.

Nair *et al.* (2014) showed that the state of thermoacoustic intermittency often presages the state of full-blown thermoacoustic instability. Since the transition state shows a growing signature of periodicity (Fig. 2.9ii-v) as one approaches thermoacoustic instability, they were able to use statistical measures which can detect the decrease in fractal content of the signal. As the state of combustion noise has a multifractal signature, the moments of acoustic pressure signal do not converge and depict power-law with measurement scale (Nair and Sujith, 2014). As the periodic content of the signal increases during the transition, the multifractal signature is lost. As a result, Nair and Sujith (2014) were able to use the power-law exponent of the variance of the pressure signal, known as the Hurst exponent, to quantify the change from fractal to periodic nature of the signal. They found that the Hurst exponent decreased to zero well before the system transitioned to full-blown thermoacoustic instability. Thus, statistical measure of Hurst exponent was able to forewarn an impending thermoacoustic instability. Since then, a number of such measures have been found to be capable of forewarning the transition to thermoacoustic instability, such as recurrence rate, Shannon rate and trapping time of the signal (Nair *et al.*, 2014; Gotoda *et al.*, 2014), centrality measures of networks constructed from time series (Murugesan and Sujith, 2016; Gotoda *et al.*, 2017; Godavarthi *et al.*, 2017), symbolic logic of pressure signals (Unni *et al.*, 2015) and machine learning-based approaches (Kobayashi *et al.*, 2019; Sengupta *et al.*, 2021). The advances in the use of early warning systems have been reviewed very recently in Pavithran *et al.* (2021).

We intend to extend the use of the Hurst exponent measured from the velocity field in the combustor to optimize passive control strategies. So, we focus on approaches that are very easy to implement and can be used as a testing ground for devising measures based on statistical information from the flow field of the combustor.

In general, passive control strategies are implemented through a change in some aspect of the combustor (geometry, injector arrangement, dampers, etc.) independent of the operation of the combustor (Zhao and Li, 2015). Passive control strategies are widely implemented in practical combustion systems as they require low maintenance and are highly durable. In contrast, active control involves continuously monitoring the combustor and taking control measures based on the specific state of the system (Zhao *et al.*, 2018). These involve the use of actuators and tunable valves for modulating the primary air, secondary air, and fuel flow rates. Active control through modulation of flow rate has been successfully used for suppressing thermoacoustic instability (Langhorne *et al.*, 1990; McManus *et al.*, 1990; Uhm and Acharya, 2005; Hathout *et al.*, 2002). Modulation of secondary fuel or air relies on the response of high-speed actuators being robust. Ensuring fast response of actuators at frequencies where the combustor dynamics are most sensitive to forcing is a challenge. In addition, the durability of actuators operating in harsh environments of the combustor is another big factor that has limited the implementation of active control strategies in practical gas turbines.

Motivated by these limitations, Ghoniem and co-workers (Ghoniem *et al.*, 2005; Altay *et al.*, 2007, 2010) considered steady injection of secondary air for achieving control in a dump combustor. Ghoniem *et al.* (2005) found that the momentum-ratio of the jet to the main flow above unity leads to a compact flame structure that is less driven by the wake vortex. Later, Altay *et al.* (2010) compared the suppression observed during transverse and streamwise secondary air injection. For optimum transverse injection, a compact flame structure anchored upstream of the backward-facing step led to the suppression. On the other hand, optimum streamwise injection inhibited unsteady vortex formation at the backward-facing step, leading to suppression.

Next, we consider the importance of the location of secondary air injection. Although injecting secondary air near the location of flame anchoring leads to suppression, it also affects the flame stability. Consequently, Ghoniem *et al.* (2005) and Altay *et al.* (2010) used secondary H_2 injection to increase flame stability and prevent blow-out. However, injecting H_2 led to higher flame temperatures and increased NO_x levels considerably. Thus, Ghoniem *et al.* (2005) had to optimize the main flow after the injection of secondary air and H_2 to reduce the temperature inside the combustor and decrease the NO_x levels. Later, Oztarlik *et al.* (2020) showed that secondary H_2 injection in small fractions alone could suppress thermoacoustic instability.

To bypass the back and forth adjustments in the main and secondary airflow, prevent flame blow-out, and reduce the complexity involved in maintaining expensive H_2 plumbing, we consider steady and unmodulated injection of secondary air away from the region of flame anchoring. The optimal region for injection can be selected if we can identify local regions responsible for thermoacoustic instability. Uhm and Acharya (2005) considered the region of local maxima in HRR to be the optimum region. In contrast, Ghoniem and co-workers (Ghoniem *et al.*, 2005; Altay *et al.*, 2007, 2010) rationalized the optimum region as the region of flame anchoring, which led to flame stabilization problems. In a similar study, Tachibana *et al.* (2007) used a distribution of the Rayleigh index to optimize for the choice of the secondary fuel injector. Recently, Unni *et al.* (2018) used network centrality measures derived from the Pearson correlation coefficient to identify regions of critical importance during thermoacoustic instability for a bluff-body stabilized combustor. In a follow-up study, Krishnan *et al.* (2019*a*) demonstrated that targeting regions with large network measure values leads to the most effective control of thermoacoustic instability.

Thus, in Chapter 7, we extend the use of Hurst exponent from a one-dimensional system to the spatio-temporal field of the combustor for measuring statistics of the velocity field. Based on the difference in the scaling of statistics of the velocity field, we optimize for the location of secondary air injection for optimal control. We show how the predictive capability of the Hurst exponent can be better used for optimizing passive control.

2.4 INTERIM SUMMARY

In this chapter, we introduced the background on turbulence, turbulent combustion, and thermoacoustic instability. We emphasized the statistical theory of turbulence due to Kolmogorov and discussed the broad implications of global and local universality and the limitations due to the highly intermittent nature of small-scale structures in turbulent flows. We further clarified the motivation for studying the small-scale phenomenology of turbulent premixed flames with particular emphasis on the phenomenon of small-scale intermittency. We also discussed the large-scale response of turbulent flames and highlighted its importance in the context of thermoacoustic instability. We discussed elementary mechanisms responsible for thermoacoustic instability. We then clarified the motivation for extending statistical measures based on the flow field of the combustor for devising optimal passive control strategies.

In summary, we clarified the requirement for analyzing turbulent premixed combustion in a scale-dependent manner so as to understand small-scale dynamics related to elementary flame processes and large-scale dynamics related to thermoacoustic instability, and by extension, their use in devising practical control strategies. We introduce the experimental setups and diagnostic techniques in the next chapter.

CHAPTER 3

EXPERIMENTAL FACILITIES AND DIAGNOSTICS

In this chapter, we discuss the facilities used for carrying out experiments on turbulent premixed flame for studying the dynamics of premixed flames subjected to turbulence and harmonic forcing. We also describe the bluff-body stabilized combustor utilized for studying thermoacoustic instability and its passive control.

3.1 TURBULENT V-FLAME FACILITY

The experimental facility[1] consists of a combustor open to the atmosphere. The combustor is equipped to stabilize premixed methane (CH_4)-air flame on an oscillating flame holder. The experimental facility is shown in Fig. 3.1. The experimental configuration is designed to assess the effect of broadband forcing due to turbulence and narrowband forcing due to oscillating flame holder on the flame dynamics. The facility is based on past studies with similar research objectives (Petersen and Emmons, 1961; Kornilov *et al.*, 2007).

The setup consists of a turbulence generator, premixing chamber, seeder, settling chamber, flame holder coupled to a harmonic driver, and optically accessible combustion chamber. Air and fuel enter into the premixing chamber through a port at the bottom. Methane (CH_4) is used as the fuel. The premixing chamber is packed with ball bearings to facilitate thorough mixing of the fuel and air. Premixed air and

---

[1] We are thankful to Dr. Luke Humphrey for performing the experiments and Prof. Tim Lieuwen for graciously providing us with the dataset. The experiments were performed in Ben T. Zinn laboratory at Georgia Institute of Technology, USA.

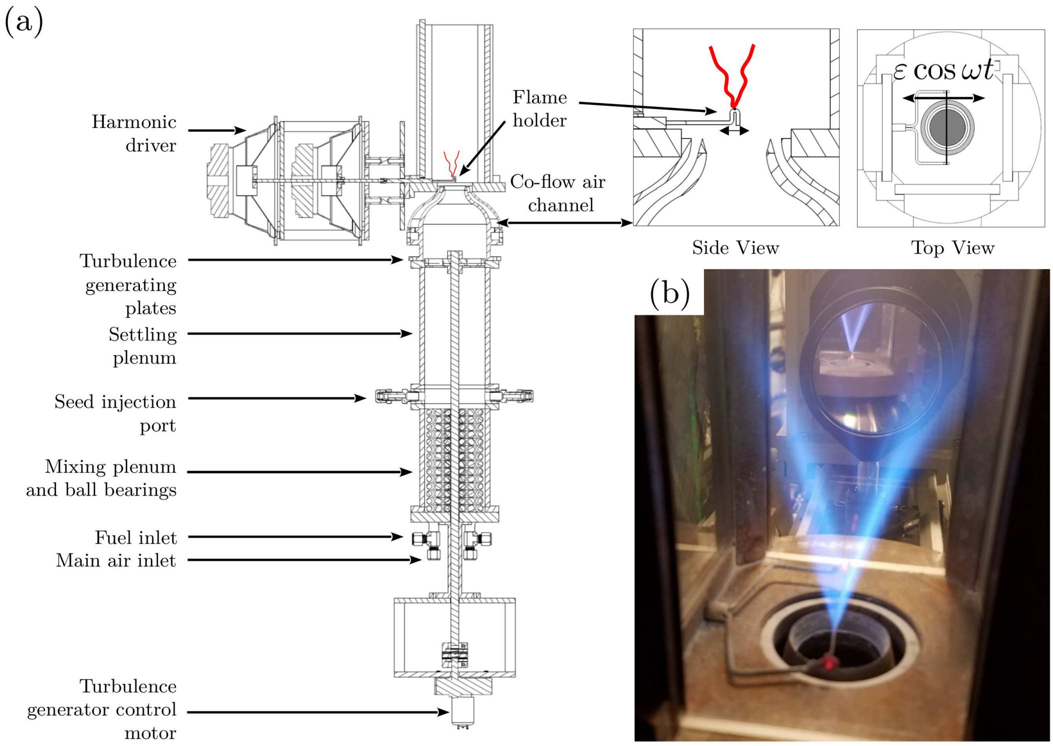
(a)
Harmonic driver
Flame holder
Co-flow air channel
Turbulence generating plates
Settling plenum
Seed injection port
Mixing plenum and ball bearings
Fuel inlet
Main air inlet
Turbulence generator control motor
$\varepsilon \cos \omega t$
Side View
Top View
(b)

Figure 3.1: Turbulent V-flame facility in Ben T Zinn lab in Georgia Tech. The large-scale and small-scale statistics of flame fluctuations measurement from this setup is reported in Chapter 4 and 5. Adapted from Humphrey *et al.* (2018) with permission from Cambridge University Press.

CH_4 enter the settling chamber and pass through a turbulence generator working on a stator-rotor mechanism and is then guided into the combustion chamber by a nozzle of exit diameter 36.3 mm. The entry into the combustion chamber is aided by a co-flow air injected through the co-flow air channel at the bottom of the nozzle. The co-flow is velocity matched to the main flow and ensues out of an annulus with an outer diameter of 36.3 mm. The main fuel and air flow rates are controlled using Aalborg GFC-67, $0 - 30$ m^3/min and Omega FMA-5428, $0 - 3$ m^3/min mass flow controller, respectively. Omega FMA-1843 gas flow and needle valve is used for controlling the air flow.

The flame is ignited by an electrically heated flame holder. The flame holder is a nichrome wire (0.81 mm, American Wire Gauge 20) and is heated by $6 - 12$ V alternating current. The flame holder is suspended 10 mm above the nozzle exit. The flame holder is coupled to speakers which drive the nichrome wire transverse to the oncoming jet flow. Two modified speakers (make - Goldwood 90 W) are connected in parallel and are utilized for oscillating the flame holder at different frequencies with different forcing amplitudes. The input signal to the speakers is generated using a function generator and amplified by two linear amplifiers.

The turbulence generator is made up of a fixed stator plate and a rotor plate. The rotor plate contains several pie shaped slots to modify the blockage ratio. The rotor plate can be rotated over a $28°$ range. By rotating the rotor, it is possible to change the blockage ratio from 69% to 97%. The change in the blockage ratio leads to a change in the turbulent intensity, measured as $u'/\bar{u}_y$, in the range of 8% to 36%. Here, $\bar{u}_y$ refers to the streamwise mean flow velocity and u' the turbulent velocity fluctuations. The uncertainty in measuring the angle of the top plate is $\pm 0.25°$. The turbulent generator can be controlled independently to change the mean flow velocity and turbulent intensity. For all the turbulence levels considered in our study, the flames correspond to either the corrugated flamelet or the thin reaction regime.

3.1.1 Optical diagnostics

Optical diagnostic was performed to determine the flame edges and velocity field. Titanium oxide (TiO_2) particles having a nominal diameter of 1 μm are used for seeding the flow. The seeding is achieved by a cyclone seeder through which a portion of the main air is diverted before the premixing plenum. The seeded flow enters upstream of

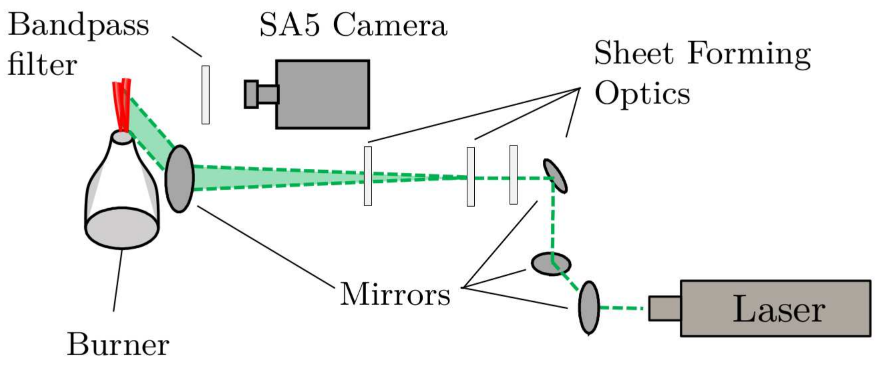

Figure 3.2: Arrangement of the optical diagnostic setup for measuring the flame surface and velocity field using TiO_2 Mie scattering and PIV. Adapted from Humphrey *et al.* (2018) with permission from Cambridge University Press.

the settling chamber as can be seen in Fig. 3.1. Only the main flow is seeded. Flame edge is detected using TiO_2 Mie scattering, and the velocity field is quantified through particle image velocimetry (PIV). Flame images are acquired using Photron Fastcam SAS high-speed video camera with a Nikon Micro-Nikkor $f = 55$m $f/2.8$ lens. For experiments conducted at $f_f = 200$ Hz and 750 Hz, the resolution was set at 768×848 pixels, and for those at $f_f = 1250$ Hz, it is set at 640×848 pixels. The camera and laser pulse are controlled together by a dual head and are triggered simultaneously. A frequency-doubled Litron Nd:YLF with a wavelength of 527 nm is used for producing the laser sheet. The laser, associated optics, and the camera arrangement are depicted in Fig. 3.2.

Experiments are conducted for three forcing frequencies $f_f = 200$ Hz, 750 Hz and 1250 Hz to understand the effect of forcing at low, moderate and higher forcing frequency. For understanding the effect of flow conditions, experiments are conducted at two nominal mean flow velocities: $\bar{U} = 5$ m/s and 8 m/s; and four turbulence levels varying in the range: $u'/\bar{u}_y \approx 8 - 35\%$. The experimental conditions were kept so as to avoid the formation of cellular instabilities in the flame. The choice of forcing frequency

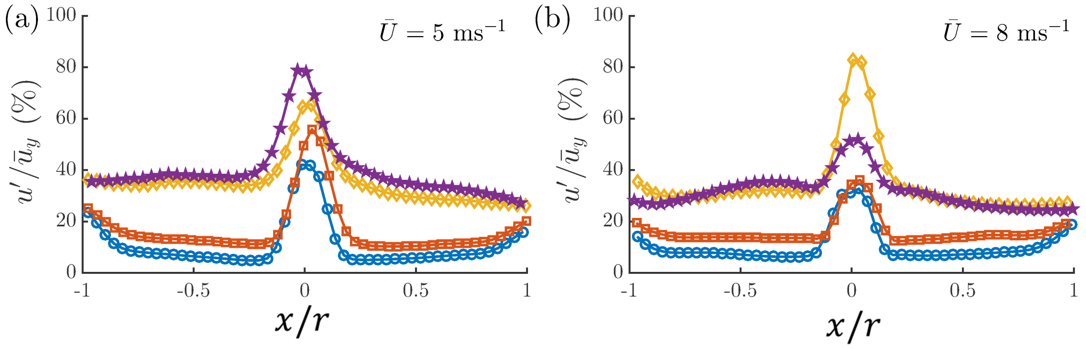

Figure 3.3: The turbulence intensity profile measured at a downstream distance of $y = 1.5$ mm above the flame holder for $f_f = 200$ Hz and for four different turbulence levels at a nominal velocity of (a) 5 m/s and (b) 8 m/s. Here r is the radius of the nozzle exit.

corresponds to the resonant frequency of the forcing system. At other frequencies, the amplitude of oscillations of the flame holder were not high enough to have a reasonable signal-to-noise ratio. The amplitude of forcing is determined by obtaining the time series of the flame holder position and evaluating its amplitude at the frequency of forcing. For $f_f = 200$, 750 and 1250 Hz, the average Fourier amplitudes measured over different mean flow and turbulent intensities are $\langle B(f_f) \rangle \approx 0.50$, 0.37 and 0.26 mm, respectively. For each of the forcing frequencies, images were acquired at a sampling frequency ten times the forcing frequency ($f_s = 10 f_f$) to eliminate spectral leakage and bias errors in spectral estimation.

LaVision DaVis PIV software (LaVision, 2006) is used to process the PIV data using an algorithm that uses multiple passages across the flame image. In the first passage, an interrogation window of size 48×48 pixel and 25% overlap is used. For resolving finer flow structure, smaller window of size 8×8 pixel and 25% overlap is used for later passage of the algorithm. This procedure yields a resolution of 13 pixels/mm between velocity vectors. For a description of uncertainty in the PIV measurements, please refer to Humphrey (2017) and Humphrey *et al.* (2018).

Figure 3.3 shows the profile of turbulence intensity ($u'/\bar{u}_y$) measured 1.5 mm from the flame holder when the forcing frequency is $f_f = 200$ Hz. Turbulence intensity at the centerline increases due to the turbulence generated by the oscillating flame holder. The intensity remains fairly constant on either side of the flame holder. The slight change in its behavior as $x/r \to \pm 1$ is due to the interaction of the main flow with the co-flow. Here $r = 13.7$ mm is the radius of the nozzle.

3.1.2 Flame edge identification and post-processing

Raw images are post-processed for improving clarity using LaVision DaVis PIV processing software. First, the images are de-wrapped using the default routine in the software to remove flame distortions due to the presence of the glass window. Figure 3.4(a) shows a representative flame image which has been cropped and processed. A weighted threshold algorithm proposed by Otsu (1979) is used to binarize the processed images to clearly visualize the flame edges. Figure 3.4(b) shows the resultant binarized image. We identify the flame front and extract only the primary flame edge, indicated in green in Fig. 3.4(b).

As all the flame-flow conditions remain in the limit of corrugated flamelets and thin reaction zone, the flame front remains continuous. We ignore flame holes and flame islands. Thus, we can extract the instantaneous flame edge $G(x, y, t)$. Note that the $G(x, y, t)$ can be multivalued, i.e., for a given x location, there are multiple values of G. We extract a single-valued flame position, $\xi(y, t)$ with respect to the y axis in the

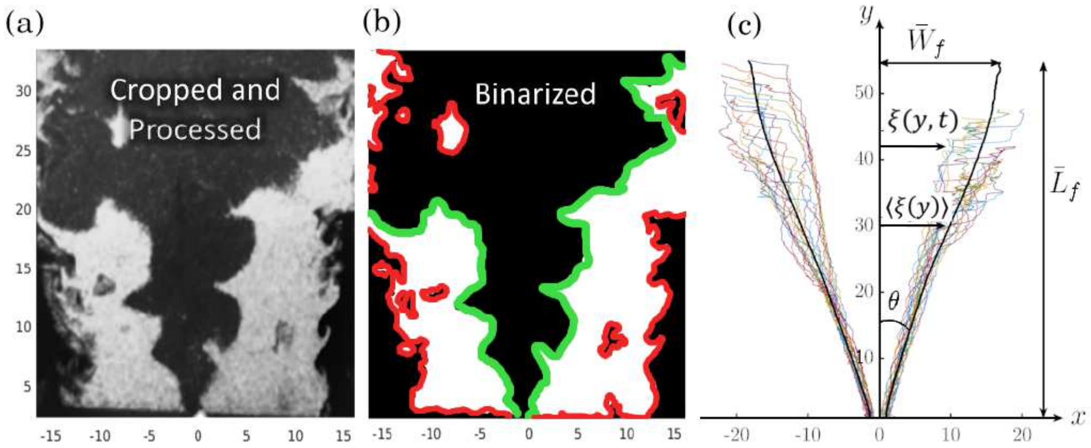

Figure 3.4: (a) Instantaneous Mie scattering image at at $\bar{u}_y = 4.2$ m/s, $u'/\bar{u}_y = 26.5$ and $f_0 = 750$ Hz. (b) The resulting binarized flame edge with the flame front identified in green. (c) Instantaneous flame edge, $\xi(x, y, t)$, indicated in color, and the mean flame edge, $\langle\xi(y)\rangle$, calculated using Eq. (3.1) and indicated in black for $\bar{u}_y = 4.87$ m/s, $u'/\bar{u}_y = 8.9\%$ and $f_0 = 200$ Hz. All dimensions are in mm. Reproduced from (a) (Humphrey *et al.*, 2018) with permission from Cambridge University Press.

following manner:

1. We calculate the average flame position as:

$$\langle\xi(y)\rangle = \frac{1}{N_t}\sum_t \frac{1}{N_x(t)}\sum_{x(t)} G(x, y, t), \tag{3.1}$$

   where, N_t refer to the number of images in the time series, and N_x refers to the number of multi-valued flame locations in the x direction for a given y location at a given instant of time. Thus, if the flame is not multivalued at a given time instant, $N_x = 1$.

2. The fluctuations of the flame edge above the mean is determined as $G'(x, y, t) = G(x, y, t) - \langle\xi(y)\rangle$.

3. We define a locally averaged flame edge, which is averaged over all the x-location at which the flame is multi-valued, as:

$$\xi'(y, t) = \frac{1}{N_x}\sum_x \{G'(x, y, t)\}. \tag{3.2}$$

4. We now define a *leading* and *trailing* flame edge as:

$$\xi'(y, t) = \begin{cases} \sup\{G'(x, y, t)\}, & \text{Leading Edge} \\ \inf\{G'(x, y, t)\}, & \text{Trailing Edge} \end{cases} \tag{3.3}$$

> where, $\sup$ and $\inf$ are the *supremum* and *infimum* of the set defined by $\{G'(x, y, t)\}$ for a given y. Thus, the leading and trailing flame edge are the farthest and closest points on the flame front from the y-axis at every streamwise location, respectively. Note that this procedure is the same variable transformation defined in §2.2.2.1 where the flame fluctuations are written with respect to the ordinate. For the single-valued flame front, all the three processed edges are the same. If the flame front remains single-valued, the locally x-averaged, leading, and trailing edge are the same as the instantaneous flame front. In the case of multi-valued edges, the leading edge propagates into the reactants before the locally averaged flame front does and is followed by the trailing edge (see inset of Fig. 3.5b).

The mean and instantaneous flame edges are shown in Fig. 3.4(c). The average flame length is $\bar{L}_f = \bar{\xi}\cos\theta$ and the width is $\bar{W}_f = \langle\xi\rangle\sin\theta$, where θ is the half-angle defined with respect to the mean flame edge $\langle\xi\rangle$. Figure 3.5(a) pictorially depicts the instantaneous (- black), locally x-averaged (- blue), leading (-. green) and trailing (- - red) flame edge.

We process 4000, 7500 and 12500 flame images, or roughly, a dataset consisting of 400, 750 and 1250 forcing cycles for $f_f = 200$ Hz, 750 Hz and 1250 Hz, respectively, and there are 10 data points every cycle. Finally, we decompose the time series of the fluctuating flame position $\xi'(y, t)$ into its spectral components through Fourier transform to obtain $\widehat{\xi}(y, f)$. The Fourier amplitude at the forcing frequency at a given downstream distance makes up the flame response. The frequency component of the signal is measured by using the standardized Fast Fourier Transform (FFT) routine (Frigo and Johnson, 1998). The sampling frequency is ten times the forcing frequency ($f_s = 10f_f$) and has a frequency resolution of 0.488, 0.915 and 0.763 Hz/bin for a total of 2048, 4096 and 8192 bins for $f_f = 200$, 750 and 1250 Hz cases, respectively.

Figure 3.5(b) shows the difference edges for $f_f = 750$ Hz, $\bar{u}_y = 4.12$ m/s and $u'/\bar{u}_y =$

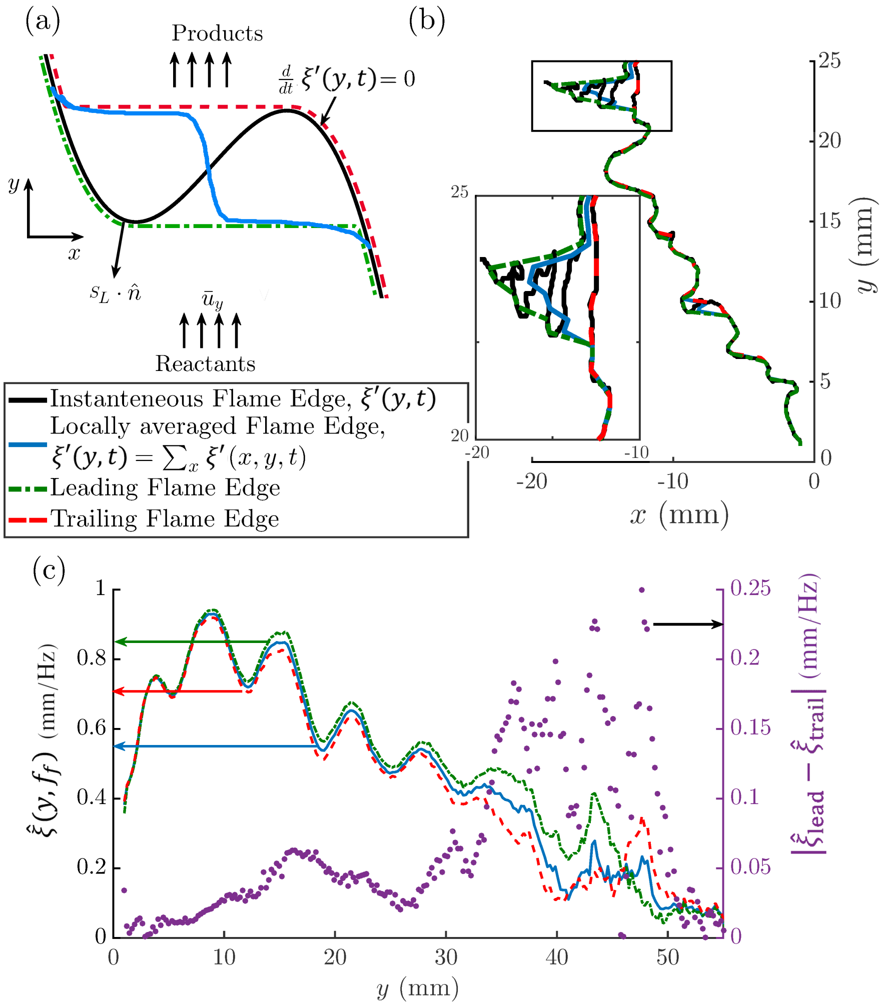

Figure 3.5: (a) Exaggerated pictorial depiction of converting multi-valued flame front into a locally averaged, leading and trailing flame edge, all of which are single-valued. (b) Representative left flame edge illustrating the difference between the leading, trailing and locally averaged flame edge. (c) Flame response of (-) locally averaged, (- -) trailing, (-.) leading flame edge as a function of the downstream distance. The difference between the response of leading and trailing edge (●) is plotted on the right axis. (b) and (c) are plotted for $f_f = 750$ Hz, $\bar{u}_y = 4.87$ m/s and $u'/\bar{u}_y = 8.9\%$.

29.5%. Figure 3.5(c) shows the flame sheet response, $\hat{\xi}(y, f_f)$, for a representative case with $f_0 = 750$ Hz, $\bar{u}_y = 4.12$ m/s and $u'/\bar{u}_y = 29.5\%$. It can be observed that the locally x-averaged, leading, and trailing flame edge lead to a very similar response. For shorter downstream distances, we notice that the response for all the three cases remains identical as the flame is single-valued. At larger distances, the flame front becomes more and more contorted, and we observe some differences in the response among these cases. However, the trend of the response visibly remains the same. The magnitude of the difference in the response of leading and trailing edge ($|\hat{\xi}_{\text{lead}} - \hat{\xi}_{\text{trail}}|$) depicts very small deviation close to the flame holder. The difference is more pronounced at larger distances where the flame fluctuations are much more aperiodic, and the chances of cusp and pocket formation are much larger (inset Fig. 3.5b). In any case, the present method is able to capture the harmonic response with very little dependence on the choice of edge used to process the results.

In Chapter 4, we use the flame fluctuations obtained from the leading edge to measure the harmonic flame response under different turbulent intensities. In Chapter 5, we measure the statistical properties for the cases where the fluctuations are visibly aperiodic and anharmonic. The results discussed in these two chapters remain the same when any of the leading, trailing, or locally averaged flame fluctuations are considered instead.

3.2 BLUFF-BODY STABILIZED COMBUSTOR

We also perform experiments on a bluff-body stabilized combustor for demonstrating passive control of thermoacoustic instability. The bluff-body combustor rig is depicted in Fig. 3.6(a). The cross-section of the combustor is 90×90 mm^2, and the length is 1100 mm. A stainless steel circular disk of 47 mm diameter and 10 mm thickness is used as the bluff-body for stabilizing the combustor. A hollow shaft of $d_s = 16$ mm diameter is used for supporting the bluff-body. For the experiments, the location of the bluff-body is fixed at 35 mm from the dump plane of the combustor (Fig. 3.6b). Air first passes through a settling chamber before being guided into the combustor through an inlet of diameter $d_i = 40$ mm. We use Liquified Petroleum Gas (LPG) as the fuel. LPG is made up of 60% butane and 40% propane by weight. The fuel is injected through holes of 1.7 mm diameter present on the hollow shaft, 110 mm upstream of the backward-facing step. The expansion ratio of the combustor is 6.45. The partially premixed fuel-air mixture is ignited using an electric spark plug mounted on the back wall of the combustion chamber. An 11 kV transformer is used for generating the spark. The combustion products are exhausted through a decoupling chamber (1000 mm $\times$ 500 mm $\times$ 500 mm) into the atmosphere.

Air and fuel flow rates are controlled using mass flow controllers manufactured by Alicat Scientific. The MCR series flow controllers have an uncertainty of $\pm 0.8\%$ of the reading and $\pm 0.2\%$ of full-scale measurements. In our experiments, the fuel flow rate is kept constant at 0.95 g/s while the air flow rate is varied from 9.80 g/s to 15.92 g/s such that the equivalence ratio (ϕ) varied in the range of 0.95 to 0.53. The nominal air velocity varies in the range of $v_a = 8.1$ m/s to 14 m/s. The air flow Reynolds number, calculated as $Re = v_a(d_i - d_s)/\nu$, varies from 12500 to 18000, where ν is the kinematic viscosity of air-fuel mixture measured according to Wilke (1950). The maximum uncertainty in the indicated value of ϕ, v_a, and Re are $\pm 1.6\%$, $\pm 0.8\%$ and $\pm 0.8\%$, respectively.

Secondary air injection ports of 5 mm diameter are present on either side of the centerline, as shown in Fig. 3.6(b). The injection port P1 is mounted on the dump

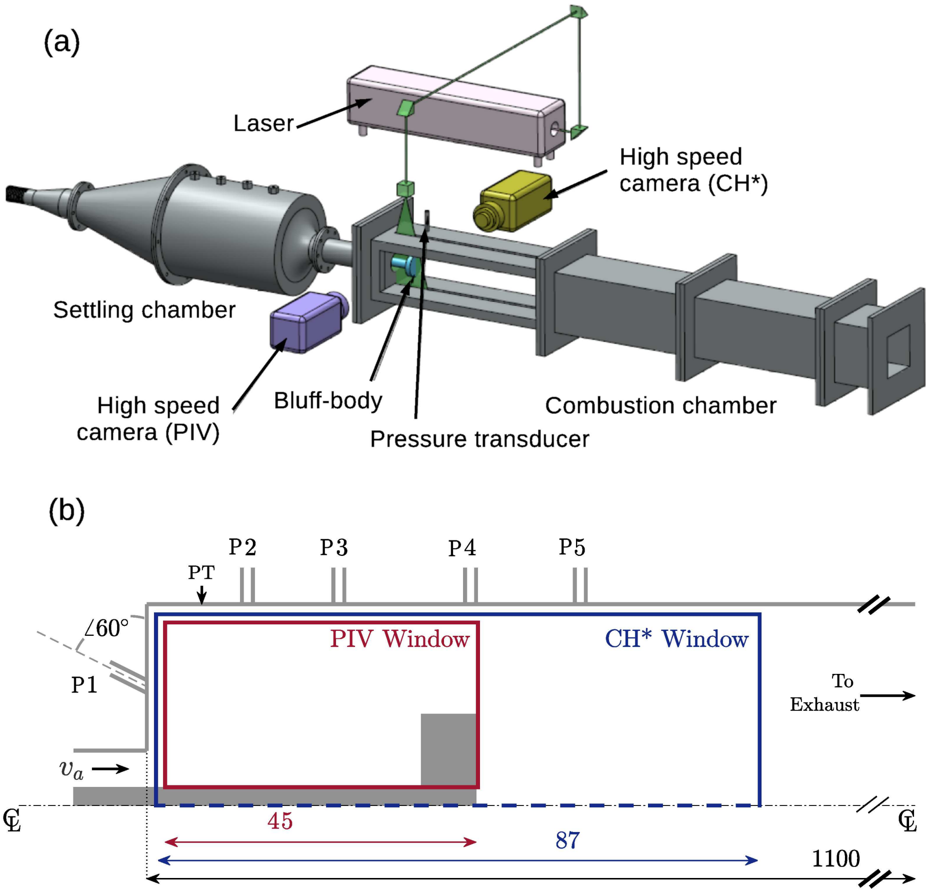
(a)
Laser
High speed
camera (CH*)
Settling chamber
High speed
camera (PIV)
Bluff-body
Pressure transducer
Combustion chamber
(b)
P2
P3
P4
P5
PT
∠60°
P1
PIV Window
CH* Window
To
Exhaust
v_a
℄
℄
45
87
1100

Figure 3.6: (a) The bluff-body stabilized turbulent combustor used for studying passive control of thermoacoustic instability in Chapter 7. (b) Schematic of the combustor cross-section indicating the PIV and CH* field of view. Secondary air injection ports (P1-P5) are present on either side of the centerline for the passive control study. PT indicates the location of the pressure transducer. All dimensions are in mm.

plane at a distance of 23.5 mm from the combustor centerline and is inclined at an angle of $45°$ with the horizontal axis. The four transversely mounted injection ports (P2-P5) are located at 15 mm, 25 mm, 45 mm, and 65 mm, respectively, from the dump plane. These ports target different regions of the flow field and are used for passive control. The secondary injection configuration was chosen to avoid flame anchoring and stability problems during control experiments, as discussed in §2.3.6. The secondary air is controlled through a separate mass flow controller. Secondary air is injected into the combustor during thermoacoustic instability in steps of 0.16 g/s until 1.90 g/s.

Piezoelectric transducers PCB103B02 are used for measuring the pressure inside the combustion chamber. The transducers have a sensitivity of 217 mV/kPa and uncertainty of ± 0.15 Pa. The pressure transducers are mounted on the combustor wall, 17 mm from the dump plane. Two-component two-dimensional high-speed PIV measurements are performed for acquiring the velocity field. The reactive flow field is seeded using 1 µm diameter TiO_2 particles. Mie scattering images were acquired with the aid of a Photron SA-4 CMOS high-speed camera. The procedure for determining the velocity field from Mie scattering images is detailed in (Krishnan *et al.*, 2019*b*). ZEISS 100 mm camera lens is used during the Mie scattering measurements. The lens is operated with $f/2$ aperture. A Phantom - V12.1 camera is used for acquiring chemiluminescence images. This camera is also outfitted with a ZEISS 50 mm camera lens. The light emitted by combustion is filtered using a bandpass filter centered around 435 ± 10 nm to capture the emissions from CH^* radicals from a region spanning 87×78 mm around the bluff-body (Fig. 3.6a). Due to limited sampling capability, only the flow-field spanning 45×40 mm from the dump plane to just beyond the bluff-body is imaged (Fig. 3.6b). The sampling frequencies for pressure, chemiluminescence, and PIV measurements are 20 kHz, 4 kHz, and 2 kHz, respectively.

We performed optical diagnostics at specific fuel and airflow rates corresponding to representative dynamical states of the combustion chamber, viz., combustion noise, thermoacoustic intermittency, and thermoacoustic instability. We also performed diagnostics during the control experiment to evaluate the effect of secondary jet on the flow and HRR characteristics. The results of the control experiments are discussed in Chapter 7.

CHAPTER 4

LARGE-SCALE HARMONIC RESPONSE OF TURBULENT PREMIXED FLAMES

In this chapter, we analyze the harmonic response of the V-flame subjected to broadband and narrowband forcing. The primary motivation of this chapter is to understand the large-scale harmonic flame response. Specifically, we focus on the nature of interaction among coherent and harmonic wrinkles induced by the oscillating flame holder on the flame and vortical disturbances induced by the flow on the flame. These local interactions of convecting disturbances affect the local and global heat release rate response. Quantifying the large-scale heat release rate response of turbulent flames is important from the consideration of thermoacoustic instability, as discussed in §2.3.

4.1 HARMONIC RESPONSE OF FLAME SURFACE FLUCTUATIONS

4.1.1 Ensemble averaged flame response

We begin by plotting the ensemble-averaged flame fluctuations ξ' at different phases of the forcing cycle in Fig. 4.1 for different values of f_f and nominal velocity of $\bar{U} = 5$ m/s. We also note the wavelength of $\langle \xi' \rangle$ decreases with an increase in f_f. Further, an increase in f_f leads to a decrease in the span in which coherent fluctuations travel. It is evident that the response of flame fluctuations depends on the forcing frequency.

The content of this chapter have been published in **A. Roy**, & R. I. Sujith (2019) Nonlinear flame response dependencies of a V-flame subjected to harmonic forcing and turbulence, *Combustion and Flame*, **207**, 101-119.

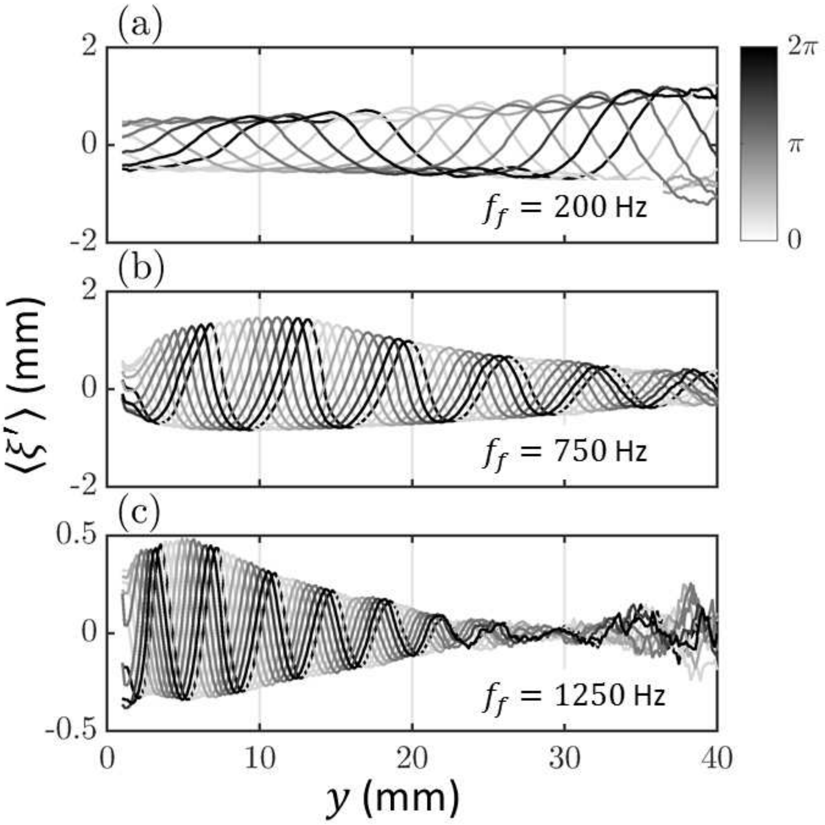

Figure 4.1: Ensemble-averaged flame fluctuations $\langle \xi' \rangle$ of the left flame edge plotted at different phases of the forcing cycle indicated by the legend. The experimental condition are: (a) $f_0 = 200$ Hz, $\bar{u}_y = 4.83$ m/s, $u'/\bar{u}_y = 8.4\%$, (b) $f_0 = 750$ Hz, $\bar{u}_y = 4.87$ m/s, $u'/\bar{u}_y = 8.9\%$, and (c) $f_0 = 1250$ Hz, $\bar{u}_y = 4.69$ m/s, $u'/\bar{u}_y = 7.6\%$.

The ensemble-averaged flame response shown in Fig. 4.1 also emphasizes the manner in which coherent wrinkles, induced by the oscillating flame holder, convect along the flame surface.

4.1.2 Amplitude spectrum of flame fluctuations

We plot the waterfall diagram depicting the amplitude spectrum at different turbulence levels in Figs. 4.2 and forcing frequencies. The left column indicates the response at a nominal flow velocity of $\bar{U} = 5$ m/s, and the right column is for $\bar{U} = 8$ m/s. The spectra were calculated from the time series of the fluctuations obtained at a representative downstream location of $y = 0.5\lambda_c$. Here, $\lambda_c = \bar{u}_y/f_f$ refers to the wavelength of the coherent wrinkles induced by the flame holder. For all the cases, the spectrum becomes increasingly more broadband with a marked decrease in the amplitude of the flame response at the forcing frequency. We also notice a dependence of the response on the forcing frequency as the peak flame response is much higher for $f_f = 750$ Hz and 1250 Hz, much larger than 200 Hz for almost all turbulence levels and nominal velocities. The inset in each sub-figure shows the peak response $\hat{\xi}(y, f_f)$ as a function of the turbulence intensity $u'/\bar{u}_y$. For nominal velocity of 5 m/s, there is a monotonic decrease in the peak flame response for most of the cases of harmonic forcing. In contrast, for 8 m/s, the peak response increases at intermediate turbulence levels and decreases at larger turbulent intensities. Finally, we also observe peaks at sub- or super-harmonic frequencies at certain conditions. These peaks probably appear due to a nonlinear transfer of energy.

4.1.3 Effect of turbulence on harmonic flame response

We now measure the harmonic response of the flame by determining the Fourier transformed amplitude of the flame front at the forcing frequency f and isolate the effects of changes in the mean flow velocity, turbulent intensity, and forcing frequency. In Fig. 4.3, we plot the amplitude of harmonic flame response as a function of the downstream distance at different forcing conditions. All the quantities, i.e., streamwise distances, y, or spectral amplitude, $\hat{\xi}(y, f)$, are normalized using the wavelength of the coherent wrinkles induced by the flame holder, calculated as, $\lambda_c = \bar{u}_y/f_f$.

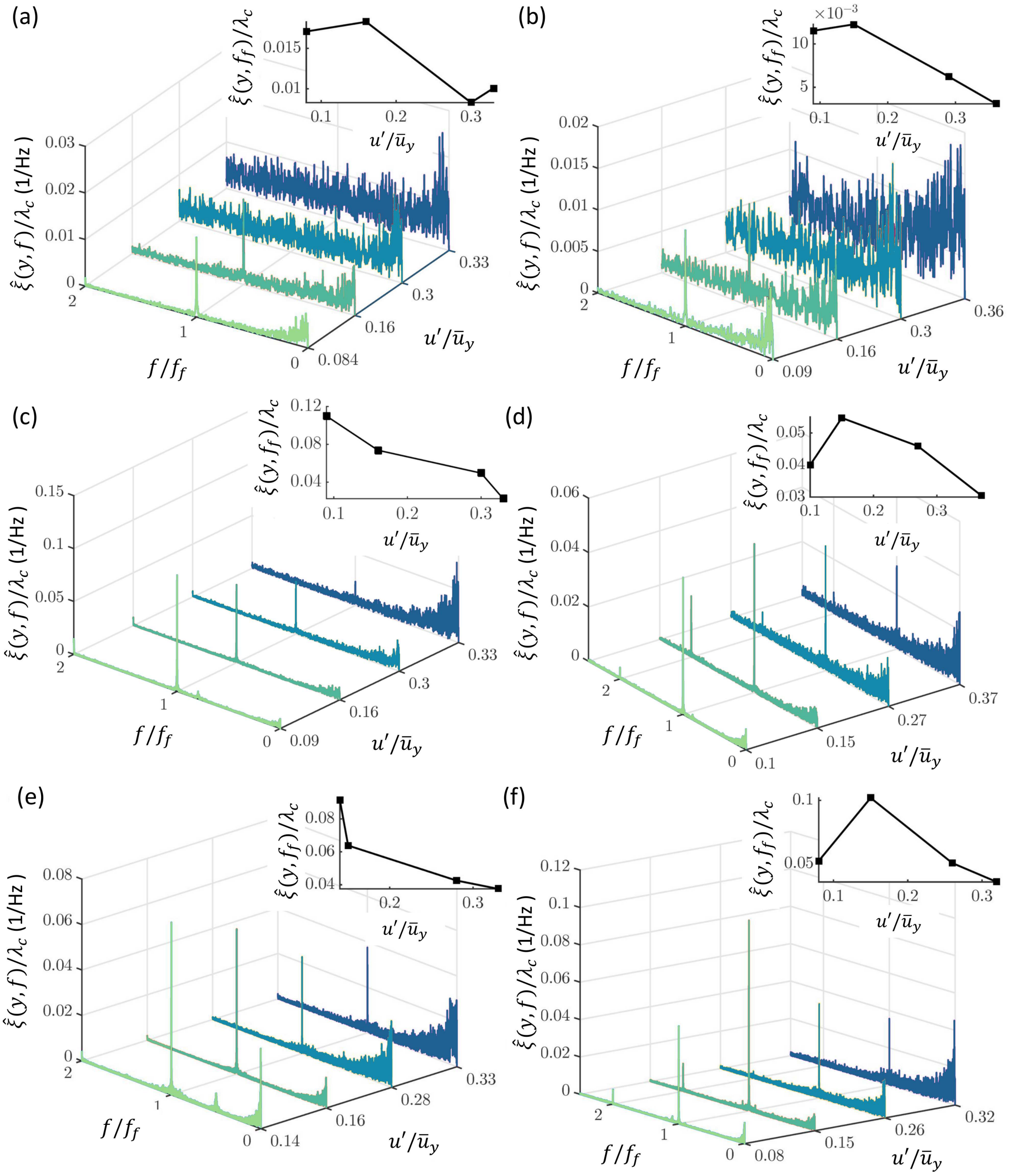

Figure 4.2: Amplitude spectrum of flame fluctuations $\hat{\xi}(y, f)$ plotted for different turbulence levels ($u'/\bar{u}_y$). Left column corresponds to a nominal velocity of 5 m/s and right to 8 m/s. The forcing frequency is (a,b) $f_f = 200$ Hz, (c,d) $f_f = 750$ Hz and (e,f) $f_f = 1250$ Hz. The fluctuations are measured at $y = 0.5\lambda_c$. The insets in each figure shows the variation in the strength of the peak at the forcing frequency as a function of the turbulence level.

Figure 4.3(a,b) depicts the response at $f_f = 200$ Hz for nominal velocity of $\bar{U} = 5$ m/s and 8 m/s, respectively. The effect of coherent wrinkles induced by the flame holder on the flame can be recognized by spatial oscillations in $\hat{\xi}(y, f_f)$ at integer multiples of

y/λ_c. For $\bar{U} = 5$ m/s, the oscillations have a wavelength close to half of the wavelength of the coherent wrinkles induced by the flame holder. However, a clear trend cannot be distinguished for these cases. For $\bar{U} = 8$ m/s, the spatial oscillations can be discerned till $y = \lambda_c$. At larger distances, the coherent wrinkles are indistinguishable as a result of anharmonic flame fluctuations (Figure 4.3b). The spatial oscillations with a wavelength of the order of $0.5\lambda_c$ are a result of the convection of coherent wrinkles induced by the oscillating flame holder along the flame edge.

Figures 4.3(c,d) shows the harmonic flame response at $f_f = 750$ Hz and Figs. 4.3(e,f) shows the harmonic response at $f_f = 1250$ Hz for two different nominal velocities. The flame response is markedly different at these higher forcing frequencies from that of $f_f = 200$ Hz. In Figs. 4.3(c-f), we observe two distinct length scales – short-wavelength undulation on top of a long wavelength. The short-wavelength oscillations clearly depict wavelength close to λ_c. Thus, the shorter wavelength oscillations are a result of the convection of coherent wrinkles induced by the flame holder. The response at the longer wavelength is possibly a result of fluctuations induced on the flame surface by vortical disturbances (Shanbhogue *et al.*, 2009*a*). These vortical disturbances act at much larger wavelengths as compared to the coherent wrinkles induced by the flame holder. Thus, the overall flame response we observe in Figs. 4.3(c-f) is a result of interference due to a mismatch in the phase speed of short wavelength coherent wrinkles and long-wavelength vortical disturbances.

In addition, for $f_f = 750$ Hz and 1250 Hz, the response changes significantly when nominal velocity is increased from $\bar{U} = 5$ m/s to 8 m/s. We can clearly observe

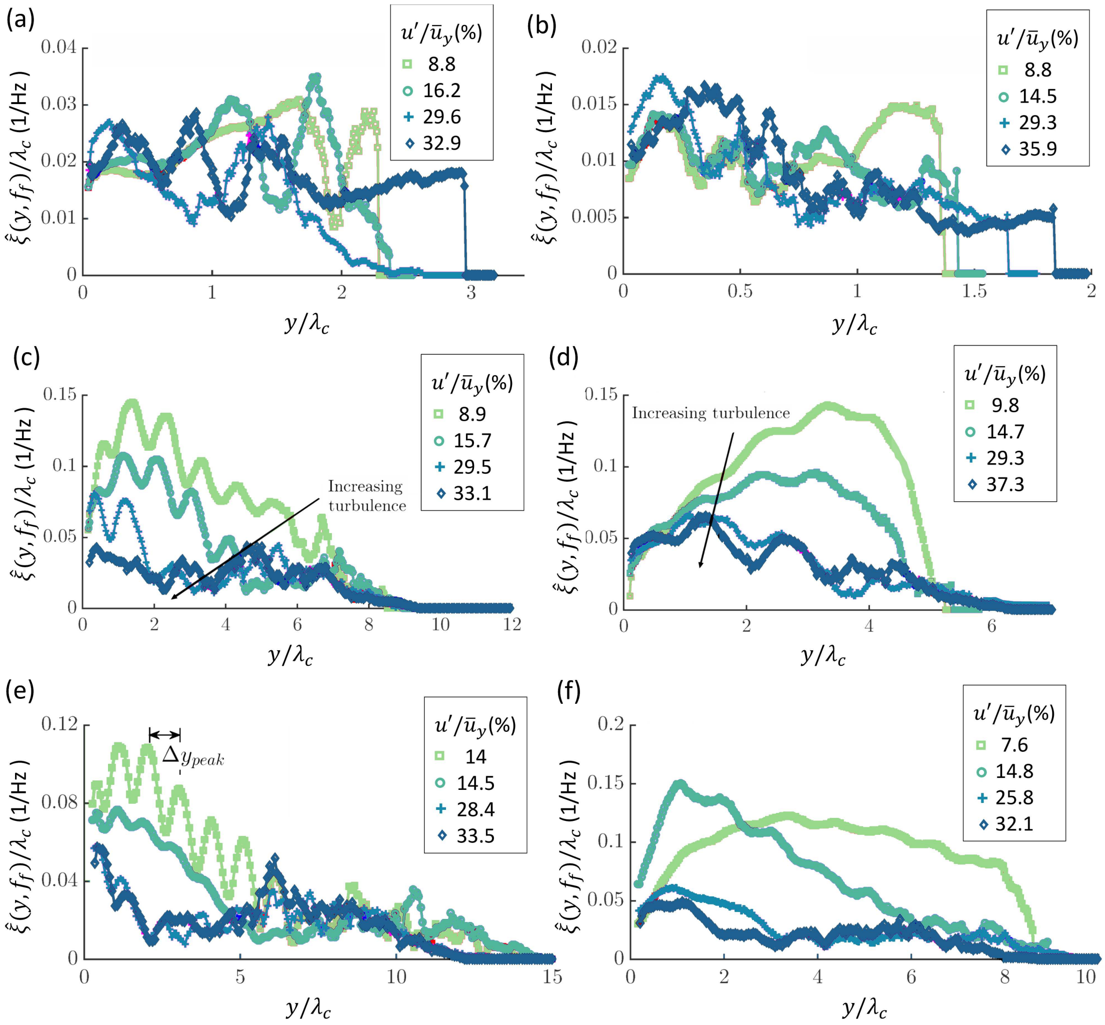

Figure 4.3: Amplitude of harmonic flame response $\hat{\xi}(y, f_f)$ as a function of downstream distance measured at (a,b) $f_f = 200$ Hz, (c,d) $f_f = 750$ Hz and (e,f) $f_f = 1250$ Hz. Each subfigure compares the harmonic flame response with increasing turbulence levels $u'/\bar{u}_y$. The response is measured for a nominal velocity of (left row) $\bar{U} = 5$ m/s and (right row) $\bar{U} = 8$ m/s.

a decrease in the amplitude of short wavelength coherent fluctuations. It is thus evident that for lower nominal velocity, the harmonic response of flame fluctuations is dominated by short-wavelength coherent disturbances induced by the flame holder. In contrast, at larger nominal velocity, the harmonic flame response is dominated by large-wavelength vortical disturbances.

Finally, we also notice that the peak of harmonic flame response shifts upstream with an increase in turbulent intensity in Figs. 4.3(c-f). For larger turbulence levels, the flame response attains maxima very close to the flame stabilization point and decays downstream. The shift in peak and decay in harmonic flame response at large turbulence levels are a consequence of the enhanced kinematic restoration of harmonic wrinkles at larger turbulence levels.

4.1.4 Interference of non-identical disturbances

The harmonic flame response observed in Fig. 4.3 implies the interference of disturbances induced on the flame surface. These disturbances are: (1) broadband convective disturbances propagating axially with velocity $\bar{u}_y$, whose amplitude decays downstream of the flame holder; (2) harmonic narrowband wrinkles induced by the oscillating flame holder propagating tangentially along the flame front with velocity $u_{ty,0}$; and (3) convective disturbances induced by the vortex shedding at the flame holder convecting with velocity $\bar{u}_y$ whose amplitude depends on the frequency of forcing. Out of these, we are interested in the interaction between coherent disturbances induced by the oscillating flame holder and vortical disturbances.

The pronounced low wavelength oscillations seen for $\bar{U} = 5$ m/s and $f_0 = 750$ Hz and 1250 Hz in Figs. 4.3(c,d) and 4.3(e,f) possibly arise because the forcing frequency matches the vortex shedding frequency of the cylindrical flame holder that holds the flame. The possibility of vortex shedding depends on the Strouhal number based on the diameter of the flame holder, which is defined as $St_d = f_f d/\bar{u}_y$. The Strouhal number for various cases is indicated in Table 4.1. The range of St_d indicated in

Table 4.1: The range of Strouhal numbers, St_d, based on the flame holder diameter (d), considered in our study. The italicized values of Strouhal number corresponds to the cases for which we expect vortex shedding by the flame holder due to BVK instability.

f_f (Hz)	$\bar{U}$ (m/s)	$\bar{u}_y\|_{max}$ (m/s)	$\bar{u}_y\|_{min}$ (m/s)	$St_d = f_f d/\bar{u}_y$ -
200	5	4.83	3.78	0.03 - 0.04
	8	8.14	6.06	0.02 - 0.03
750	5	4.87	3.76	*0.13 - 0.16*
	8	7.94	6.01	*0.08 - 0.10*
1250	5	4.69	3.70	*0.22 - 0.27*
	8	8.01	6.24	*0.13 - 0.16*

italics corresponds to the cases ($f_f = 750$ Hz and 1250 Hz) where the flame response depict interference pattern in the spatial oscillations. The italicized range of St_d is close to $St_d = 0.2$ for which Bénard-von Kármán (BVK) instability arises for flow past cylindrical bluff-bodies (Lieuwen, 2012; Cantwell and Coles, 1983). As these vortical disturbances are quite pronounced, the harmonic response shows the interference pattern between convecting vortical disturbances and the coherent wrinkles induced by the oscillating flame holder. Local peaks (troughs) in the response appear whenever there is constructive (destructive) interference between the two disturbances.

In general, the flame position is a function of the phase velocity of convective excitation, $\bar{u}_y$, and the flame wrinkle convection velocity, $u_{ty,0}$ (Lieuwen, 2012). These two disturbances propagate at the same phase speed when the phase speed parameter, $k_c = \bar{u}_y/u_{ty,0} = 1$. For other cases, the disturbances interfere and give rise to length scale, λ_{int}, defined as (Lieuwen, 2012):

$$\lambda_{\text{int}}/(\lambda_t \sin\theta) = \frac{1}{|1/k_c - 1|}, \tag{4.1}$$

where, θ is the half-angle of the averaged V-flame (as indicated in Fig. 3.4c), $\lambda_c = \bar{u}_y/f_f$ is the convection length scale of vortical disturbances, and $\lambda_t = u_{ty,0}/f_f$ is the length scale of wrinkles convecting tangentially along the flame front. The later can be experimentally evaluated as an axially averaged quantity in the domain $0 < y < 60$ mm through the relation (Emerson and Lieuwen, 2015):

$$\lambda_t = 2\pi \frac{\Delta y}{\Delta \angle \hat{\xi}}, \tag{4.2}$$

where, the phase of the flame edge response at a given axial location is calculated from the Fourier transform as:

$$\angle \hat{\xi}(y, f_f) = \tan^{-1} \frac{\Im\{\hat{\xi}(y, f_f)\}}{\Re\{\hat{\xi}(y, f_f)\}}. \tag{4.3}$$

Thus we can calculate all the relevant quantities. We can also compare the interference length scale calculated from Eqn. (4.1) which is indicated as $\lambda_{\text{int},1}$ with $\lambda_{\text{int},2}$ calculated from harmonic flame response obtained in Fig. 4.3. We can calculate the latter as: $\lambda_{\text{int},2} = \Delta y_{\text{peak}}/\cos\theta$, where Δy_{peak} is the peak to peak distance measured axially as indicated in Fig. 4.3(e). We note that $\lambda_{\text{int},2}$ cannot be calculated in many cases where the harmonic flame response do not show clear interference pattern. The comparison between $\lambda_{\text{int},1}$ and $\lambda_{\text{int},2}$ is tabulated in Table 4.2. As can be noted, the $\lambda_{\text{int},1}$ values matched with $\lambda_{\text{int},2}$ only for a few cases, viz., the case with highest turbulence level for $f_f = 200$ Hz and for $f_f = 750$ Hz.

Equation (4.1) shows that the presence of fast propagating long wavelength disturbance ($\bar{u}_y >> u_{ty,0}$ or $k_c >> 1$) will lead to shorter wavelength oscillations in the flame

Table 4.2: Comparison of the interference length scale $\lambda_{\text{int},1}$ calculated from Eqn. (4.1) and $\lambda_{\text{int},2}$ calculated from the harmonic flame response as $\lambda_{\text{int},2} = \Delta y_{\text{peak}}/\cos\theta$ (see Fig. 4.3e). Also tabulated are the convective (λ_c) and flame wrinkle (λ_t) length scales.

f_f	$\bar{u}_y$	$u'/\bar{u}_y$	λ_c	λ_t	k_c	$\lambda_{\text{int},1}/\lambda_c$	$\lambda_{\text{int},2}/\lambda_c$
(Hz)	(m/s)	(%)	(mm)	(mm)	-	-	-
200	4.83	8.50	24.14	16.14	1.50	15.47	0.61
	3.78	30.21	18.90	1.50	12.82	0.45	0.60
	8.14	8.60	4.71	69.47	0.58	22.40	-
	6.06	31.29	30.24	72.85	0.42	16.07	-
750	4.87	9.11	6.50	5.21	1.24	1.49	1.05
	4.67	15.11	6.23	4.51	1.38	0.98	0.94
	4.12	26.93	5.49	2.92	1.88	0.42	0.973
	3.76	29.75	5.02	33.75	0.15	0.39	-
	7.94	8.89	10.59	10.75	0.98	17.34	-
	6.01	32.33	8.01	16.75	0.48	0.63	-
1250	4.69	12.67	3.75	13.27	0.28	0.37	0.98
	3.70	27.73	2.95	3.61	0.82	2.21	-
	8.01	9.02	6.41	5.90	1.09	2.71	-
	6.24	28.23	4.99	13.08	0.38	0.57	-

response ($\lambda_{\text{int}} > 1$) (Lieuwen, 2012). For $f_f = 200$ Hz (refer to Table 4.2), oscillations are more pronounced only for higher turbulence levels (Fig. 4.3a,b). For the highest turbulence level, we find $k_c = 12.82$ and interference wavelength is $\lambda_{\text{int},1}/\lambda_c = 0.45$. The interference length scale, $\lambda_{\text{int},1}$, corresponds quite well with $\lambda_{\text{int},2}$ determined directly from the flame response (Fig. 4.3b). However, the mismatch for lower turbulence levels arises due to the fact that vortical disturbances are not very pronounced (Table 4.1), and only coherent disturbances due to the oscillating flame holder dominate the response. So, there are no visible interference pattern.

For higher forcing frequencies $f_f = 750$ Hz and 1250 Hz, the interference pattern is quite evident. We notice that for these cases, the phase speed parameter (k_c) remains order unity, i.e., flame wrinkles and vortical disturbances convect with similar phase speeds ($\bar{u}_y/u_{ty,0} \sim \mathcal{O}(1)$) and with similar wavelengths ($\lambda_c/\lambda_t \sim \mathcal{O}(1)$) and magnitudes. Further, these disturbances have a substantial impact on the overall response, indicating that the convecting velocity of these vortices is faster than the wrinkle convection speed ($\bar{u}_y > u_{ty,0}$), i.e., $k_c > 1$ as can be confirmed from Table 4.2. For cases where the magnitudes differ considerably, we obtain slight undulations on top of the long-wavelength disturbance (see Figs. 4.3d) and 4.3f). The long-wavelength disturbance is a result of vortical disturbances possessing a higher magnitude than the coherent flame wrinkle induced by the flame holder.

4.1.5 Frequency dependence of flame sheet response at comparable flow conditions

In this section, we isolate the effect of forcing frequency on the flame when the flow conditions are comparable. We plot the harmonic flame response at different forcing frequencies in Figs. 4.4 and 4.5 for $\bar{U} = 5$ m/s and 8m/s at comparable turbulent intensities, respectively.

We notice that for almost all the cases, the amplitude of the peak of the harmonic flame response normalized by λ_c rises from 200 Hz to 750 Hz, before decreasing at 1250 Hz. In the previous section, we observed that an increase in turbulence intensity led to a shift in the peak of the global flame response closer to the flame holder. We notice a similar behavior with increasing forcing frequency as well. For almost all the cases, the global peak shifts closer to the flame holder, as indicated by the arrows in Figs. 4.4 and 4.5. Thus, at high turbulence levels (Figs. 4.3) and frequencies (Figs. 4.4 and 4.5), the flame response is invariably maximum close to the flame holder and decays

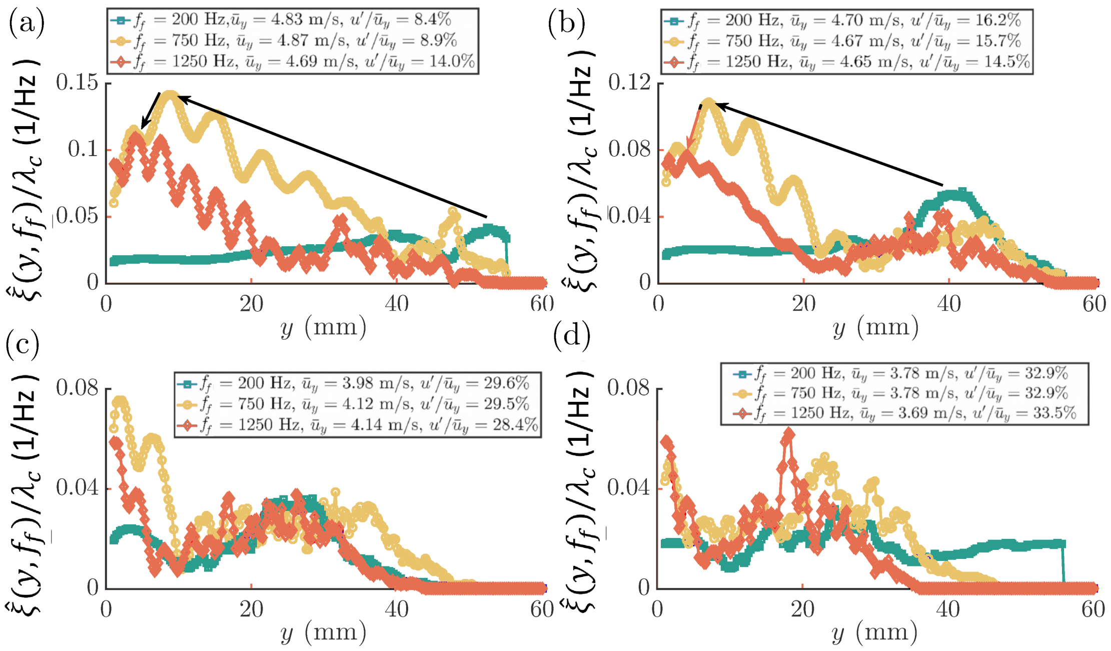

Figure 4.4: Flame sheet response, $\hat{\xi}(y, f_f)$, for increasing forcing frequencies at nominal velocity of $\bar{U} = 5$ m/s and comparable flow conditions. The mean velocity $\langle \bar{u}_y \rangle$ and turbulent intensity $\langle u'/\bar{u}_y \rangle$ are: (a) 4.8 m/s, 10.4%, (b) 4.7 m/s, 15.5%, (c) 4.1 m/s, 29.2%, and (d) 3.7 m/s, 33.2%, respectively. Here $\langle . \rangle$ indicates the average of the flow condition indicated in the legend of each sub-figure. The arrow in (a) and (b) indicates the shift in peak with increasing frequency.

downstream. Finally, at higher turbulence intensities, the flame response at f_f has oscillations that look seemingly random and anharmonic. Thus, turbulent fluctuations dominate harmonic response at higher forcing frequencies and turbulence levels.

4.2 HEAT RELEASE RATE RESPONSE

In §2.3.3, we observed that thermoacoustic instability develops through a coupling between narrowband acoustic pressure fluctuations and heat release rate fluctuations. The heat release rate fluctuations depend on the flame area fluctuations through leading order contributions (Fleifil *et al.*, 1996; Dowling, 1999; Schuller *et al.*, 2003; Lieuwen,

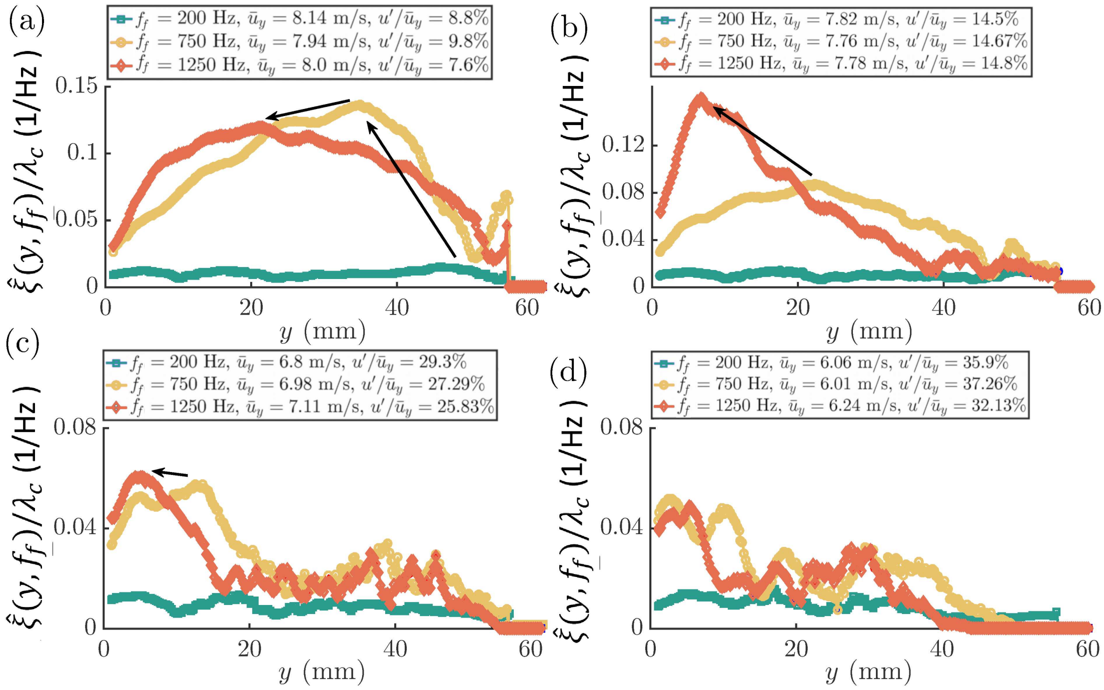

Figure 4.5: Flame sheet response, $\widehat{L}(y, f_0)$, for increasing forcing frequencies at nominal velocity of $\bar{U} = 8$ m/s and comparable flow conditions. The mean flow velocity $\langle \bar{u}_y \rangle$ and turbulence levels $\langle u'/\bar{u}_y \rangle$ are:(a) 8.0 m/s, 8.7%, (b) 7.8 m/s, 14.7%, (c) 7.0 m/s, 27.5% and (d) 6.1 m/s, 35.1%, respectively. Here $\langle . \rangle$ indicates the average of the flow condition indicated in the legend of each sub-figure. The arrow in (a)-(c) shows the shift in peak with increasing forcing frequency.

2012). In fact, the mean flame shape can preferentially suppress or promote the contribution of heat release rate fluctuations (Durox *et al.*, 2009). Here, we are interested in finding out the manner in which the harmonic flame fluctuations discussed in the earlier sections, affect the overall heat release rate fluctuations. This dependence was expressed in Eqn. 2.66, which upon linearization leads to: $\dot{q}'(y, t) \sim A'(y, t)$, where A' is the fluctuations in flame area.

In this section, we consider the effect of flame surface fluctuations on the area fluctuations and eventually on the local and global heat release rate fluctuations.

4.2.1 Flame asymmetry and cross-correlation

In order to determine the heat release rate response of the flame at different forcing frequencies and turbulence intensities, it is important to consider any asymmetry that may be present in the flame (Emerson and Lieuwen, 2015). The asymmetry in flame fluctuations is shown in Fig. 4.6. We can clearly see that the flame response is asymmetric for $f_f = 200$ Hz (Fig. 4.6a). For higher frequencies, the response is visibly symmetrical for $y < 40$ mm for $f_0 = 750$ Hz (Fig. 4.6b) and $y < 20$ mm for $f_f = 1250$ Hz (Fig. 4.6c). The span over which the flame retains symmetry is correlated to the height of the ensemble-averaged flame response shown in Fig. 4.1.

In order to ascertain the relative degree of symmetry, we determine the phase difference between the response of left and right flame edge. The relative phase is calculated as $\Delta\phi(y, f_f) = \angle\hat{\xi}_{\text{left}}(y, f_f) - \angle\hat{\xi}_{\text{right}}(y, f_f)$, where $\angle\hat{\xi}$ is determined according to Eqn. 4.3. We notice minor fluctuations in the phase difference $|\Delta\phi| < \pi$ whenever response of one edge leads the other (Fig. 4.6c). In other cases, large jumps in phase $|\Delta\phi| > \pi$ are visible in at large downstream distances. The phase jumps become quite random as the flame response becomes anharmonic and incoherent.

Next, we see that the magnitude of the left and the right flame edge are also quite different. This is due to slightly non-identical turbulence levels on the left and the right side as shown in Fig. 3.3. The $\langle . \rangle$ indicated in the caption of Fig. 4.6 shows the average of the turbulent intensity in the left and right side. In order to quantify symmetry, or the lack thereof, we calculate the cross-correlation coefficient of the left and right flame

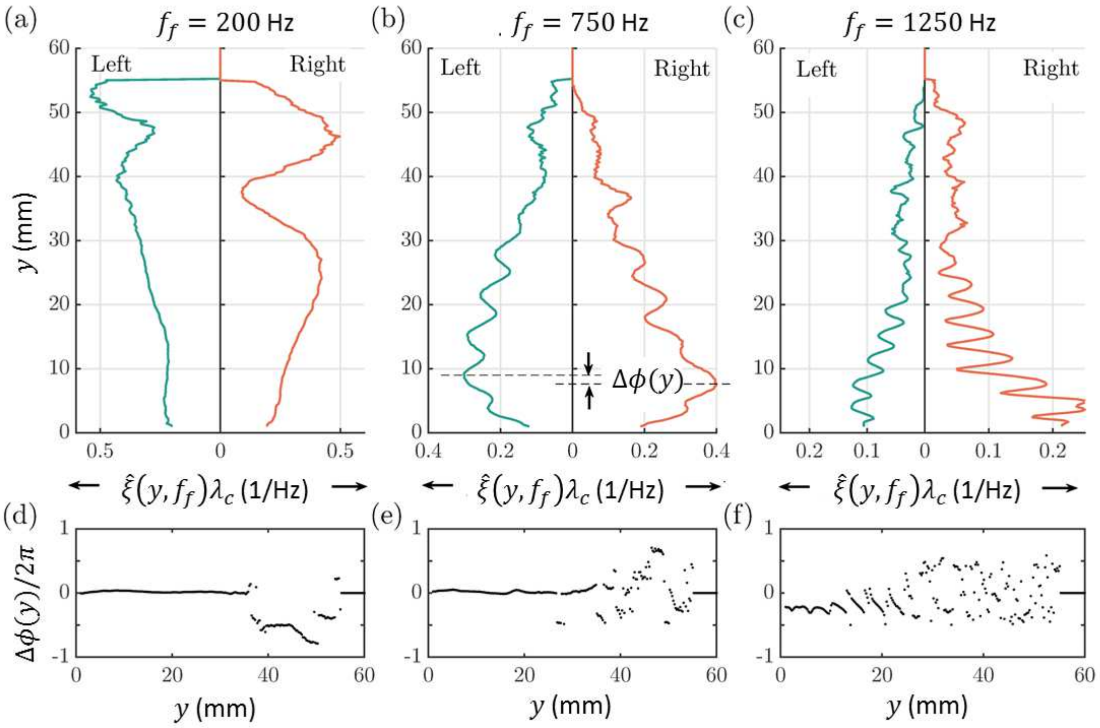

Figure 4.6: (a-c) Comparison of harmonic response of the left and right flame edge for representative forcing conditions for $\bar{U} = 5$ m/s. (d-f) Axial dependence of the phase difference, $\Delta\phi$ between the response of the two flame edges. The experimental conditions are: (a, d) $f_f = 200$ Hz; $\langle u'/\bar{u}_y \rangle \sim 8.5\%$; (b, e) $f_f = 750$ Hz; $\langle u'/\bar{u}_y \rangle \sim 9.1\%$; and (c, f) $f_f = 1250$ Hz, $\langle u'/\bar{u}_y \rangle \sim 12.7\%$.

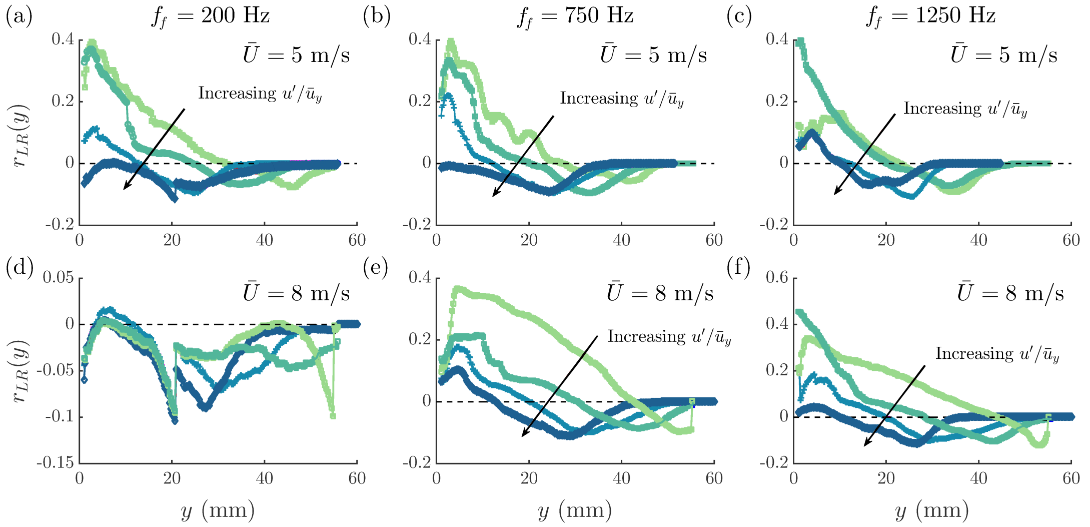

Figure 4.7: The correlation coefficient between left and right flame edge for: $\bar{U} =$ (a-c) 5 m/s and (d-f) 8 m/s, and (a,d) $f_f = 200$ Hz, (b,e) $f_f = 750$ Hz and (c,f) $f_f = 1250$ Hz for increasing turbulence levels. The markers are consistent with those in Figs 4.3.

edge:

$$r_{LR}(y) = \frac{\langle \xi'_{\text{left}}(y,t)\xi'_{\text{right}}(y,t)\rangle}{\sqrt{\langle \xi'_{\text{left}}(y,t)^2\rangle\langle \xi'_{\text{right}}(y,t)^2\rangle}}. \tag{4.4}$$

The correlation can only take values between $+1$ and -1. A value of $+1$ indicates symmetry in the left and the right flame edge, -1 indicates anti-symmetry, and 0 indicates the presence of uncorrelated and asymmetrical wrinkles. The variation of the cross-correlation coefficient with downstream distance is plotted in Fig. 4.7 for the different cases. We notice that the flame is symmetric just downstream of the flame holder and progressively becomes asymmetric as distance increases. At large downstream distances, the flame response of the two edges becomes uncorrelated. An increase in turbulence level leads to an increase in the degree of asymmetry in the flame response. Further, case-wise comparison of $\bar{U} = 8$ m/s with $\bar{U} = 5$ m/s indicates that $\bar{U} = 8$ m/s has a greater asymmetry in the flame response.

In Fig. 4.8 we plot the correlation coefficient measured at the downstream location where the flame sheet response has a global maximum. This correlation measured at the location of the peak in flame response can be used as a global descriptor of the flame asymmetry. We thus plot this correlation coefficient as a function of the turbulent intensity for different forcing frequencies and at different nominal flow velocities. We notice that the correlation value indicates symmetrically distributed wrinkles for $f_f = 750$ Hz and 1250 Hz for low and intermediate turbulence levels when $\bar{U} = 5$ m/s (Fig. 4.8a). For higher nominal velocity, only the case with $f_f = 1250$ Hz shows a relatively high value of the correlation coefficient (Fig. 4.8b). For either of the two nominal velocities and higher turbulence levels, the symmetric wrinkling disappears,

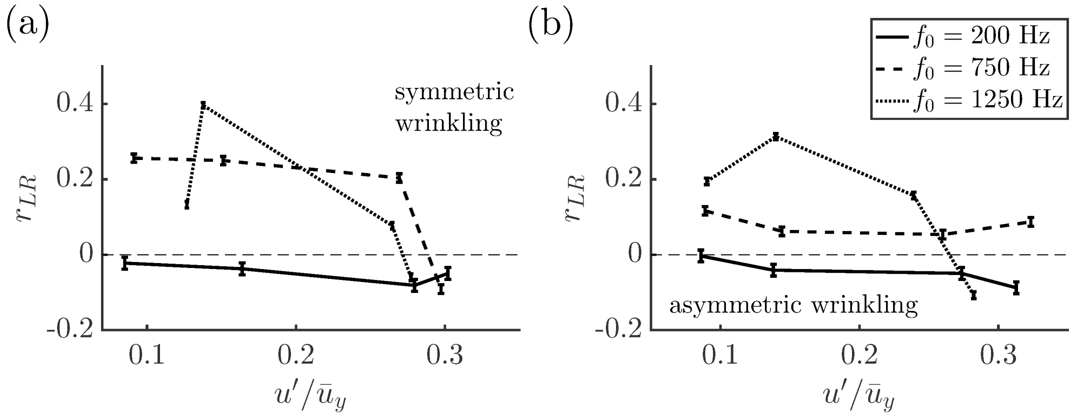

Figure 4.8: Flame peak correlation between the left and the right edge measured at the location of maxima in flame sheet response at nominal velocity (a) $\bar{U} = 5$ m/s and (b) $\bar{U} = 8$ m/s for different forcing frequencies.

and flame oscillations become asymmetrical and uncorrelated. For $f_f = 200$ Hz, the flame remains uncorrelated, regardless of the nominal flow velocity.

4.2.2 Local Heat Release Response

We calculate the local heat release response, and find its dependence on the forcing frequency and turbulent intensity. The local heat release rate fluctuation can be estimated as the mean of the contributions of two conical V-flames. Thus, we have:

$$q(y,t) = \int_0^y \dot{q}'(y,t)dy = \frac{1}{2}\left(\int_0^y \dot{q}'_{\text{left}}(y,t)dy + \int_0^y \dot{q}'_{\text{right}}(y,t)dy\right), \tag{4.5}$$

As we noted earlier, the heat release response is dependent on the area of the flame fluctuations. The area exclusively depends on the flame front (ξ') and the conical flame geometry. The instantaneous fluctuation in the flame area over a differential conical element dy is $dA' = 2\pi\xi'(y,t)dy$. Thus, the normal flame surface area fluctuations can be written as:

$$\frac{A'(y,t)}{\bar{A}} = \frac{2}{\bar{W}_f\sqrt{\bar{W}_f^2+\bar{L}_f^2}}\int_0^y \xi'(y,t)dy, \tag{4.6}$$

where, the normalization is obtained based on the mean curved surface area of the conical flame, which is expressed as:

$$\bar{A} = \pi\bar{W}_f\bar{L} = \pi\bar{W}_f\sqrt{\bar{W}_f^2+\bar{L}_f^2}, \tag{4.7}$$

the mean flame width, $\bar{W}_f = \bar{\xi}\sin\theta$, and mean flame length, $\bar{L}_f = \bar{\xi}\cos\theta$ (see Fig. 3.4c). Due to flame asymmetry, each quantity in Eqn. (4.6) need to be evaluated separately for the left and right flame branch. Similarly, $\bar{W}_f$ and $\bar{L}_f$ depends on the forcing frequency, mean flow velocity and turbulent intensity. So, each of these quantities have to be evaluated separately for every parametric case. Thus, the component of the net normalized HRR at the forcing frequency can be calculated from Eqns. (4.5) and (4.6) as:

$$\frac{\hat{\dot{q}}(y,f_f)}{\bar{\dot{q}}} = \frac{1}{2}\sum_{\text{left,right}}\frac{2}{\bar{W}_f\sqrt{\bar{W}_f^2+\bar{L}_f^2}}\int_0^y \hat{\xi}(y,f_f)\exp\Big(i\angle\hat{\xi}(y,f_f)\Big)dy. \tag{4.8}$$

Here, we have accounted for the phase of the flame response by including $\angle\hat{L}(y,f_f)$ in the integrand. The spatially integrated heat release rate response $|\hat{\dot{q}}(y,f_f)|$ evaluated in the spatial domain $0 < y < 60$ mm, is shown in Figs. 4.9 for $f_f = 200, 750$ and 1250 Hz, respectively. The markers and colors in each of these figures are consistent with the markers in Fig. 4.3, respectively. Equation (4.8) indicates that if the harmonic flame response is finite and dependent on the axial location, there would be an increase in $|\hat{q}(y, f_f)|$ with y. Similarly, if the phase of the flame response is finite and dependent on the axial location, $|\hat{q}(y, f_f)|$ will be oscillatory with nodes and anti-nodes present at integer multiple of λ_c.

Further, local increase or decrease in the HRR would be affected due to the phase difference in the response of the left and right flame edge. If the disturbances induced on the flame surface are sinuous such that the maximum displacement of the left edge corresponds to the minimum displacement of the right, i.e., the phase difference is 180°, the net increase in the area at one edge is cancelled by a decrease in the other. In contrast, if the disturbances induced on the flame surface are varicose, i.e., the flame response is symmetric with a negligible phase difference, the fluctuations would add up to effect an increase in the flame area fluctuations. Thus, the sinuous flame response would contribute to minimal heat release rate behavior due to the phase cancellation effect in the flame response, while varicose flame response would lead to a higher and more pronounced heat release rate.

In Fig. 4.9, we notice that the heat release rate response depicts the presence of a standing wave structure with nodes and anti-nodes and an increase or decrease in the mean heat release rate response arising from sinuous/varicose flame response. The nodes and anti-nodes are seen quite clearly in each of the cases plotted in Fig. 4.9. The effect of flame structure can similarly be observed. Varicose flame structure manifests in the net increase in the heat release rate response with a progressive increase in the magnitude at the nodal positions with increasing downstream distance for $\bar{U} = 5$ m/s cases (Figs. 4.9a,c,e). In contrast, we notice that for $\bar{U} = 8$ m/s (Figs. 4.9b,d,f), the

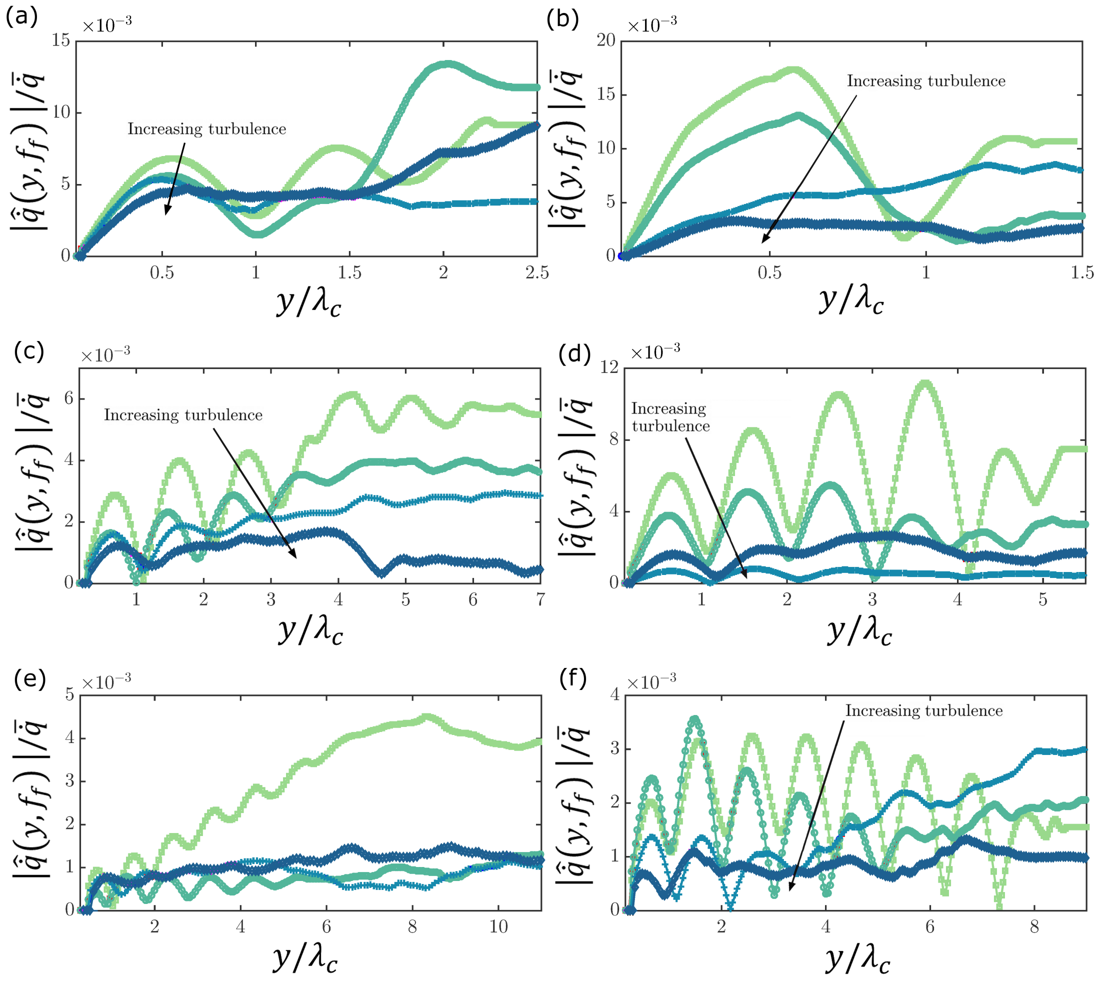

Figure 4.9: Normalized heat release response, $|\hat{Q}(y, f_f)|/\bar{Q}$ measured from the flame sheet response plotted as a function of the normalized downstream distance y/λ_c for (a) $\bar{U} = 5$ m/s and (b) $\bar{U} = 8$ m/s at $f_f = 200$ Hz. The markers are consistent with those used in Fig. 4.3.

heat release rate response tends to decrease following an initial increase. The increase is possible as a result of the flame response being symmetric downstream of the flame holder (varicose flame structure) and becoming progressively asymmetric (sinuous or uncorrelated flame structure) with increasing downstream distance. The slightly higher asymmetry in the flame structure for $\bar{U} = 8$ m/s as compared to $\bar{U} = 5$ m/s can be confirmed from Fig. 4.7 and 4.8. Thus, the flame asymmetry directly contributes to the spatial nature of the heat release rate response of the system.

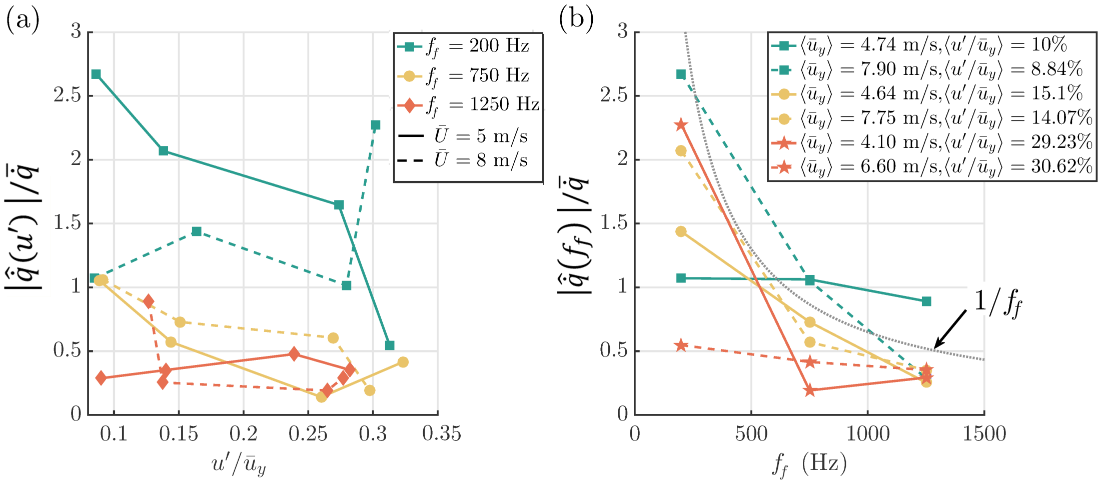

Figure 4.10: Spatially integrated heat release response measured from the harmonic flame response as a function of the (a) turbulence level, $u'/\bar{u}_y$, for different forcing frequencies and nominal velocities, and (b) forcing frequency, f_f, at different turbulence levels. The $1/f_f$ roll-off in the global heat release rate response with increase in forcing frequency has been indicated in (b)

4.2.3 Global heat release rate response

Finally, we consider the effect of forcing frequency and turbulent intensity on the global heat release rate response. The global heat release rate response can be obtained by taking the integral in Eqn. (4.8) from $y = 0$ to $y = \bar{L}_f$. We plot the dependence of the integrated response for increasing the turbulent intensity at a given frequency in Fig. 4.10(a) at different nominal flow conditions, and its dependence on the forcing frequency in Fig. 4.10 across different turbulence levels.

We notice that the heat release rate response at any given forcing frequency decreases with increasing turbulence levels for most of the cases. The decrease in heat release rate response is counter-intuitive as heat release rate response generally increases with an increase in turbulence intensity (Bellows *et al.*, 2007). As the heat release rate response is calculated solely based on the flame response, it will reflect the factors which affect the harmonic flame response. The flame response shows a sharp decrease downstream of the flame holder for higher turbulence levels due to enhanced kinematic restoration (see Fig. 4.3c,e). Thus, the globally integrated HRR response shows a decrease with increasing turbulence levels due to kinematic restoration.

The dependence of heat release rate response on the forcing frequency, however, is quite well captured. We notice a decrease with increasing forcing frequency at any given turbulence level. The decrease is reminiscent of the typical low-pass filter characteristic of turbulent flames (Fleifil *et al.*, 1996). The reduced response at higher turbulence levels stems from the fact that there is an increase in the phase variations of the heat release rate fluctuations with downstream distance, as can be confirmed from the variation of $\Delta\phi$ in Fig. 4.6(d-f). Further, the phase jumps become more prevalent at larger downstream distances for cases with higher forcing frequencies. Thus, if the flame response is integrated over space at any given instant of time, the net heat release rate will be minimal due to variation in the phase of the harmonic flame response. In other words, there would be a phase cancellation in the heat release response (Lieuwen, 2012). Such a response manifests in the $1/f$ decay generally seen in transfer function measurements at higher forcing frequencies (Jones *et al.*, 2010; Lieuwen, 2012). We notice a similar decay in heat release rate response at higher frequencies for almost all the cases (see Fig. 4.10b).

4.3 INTERIM SUMMARY

In this chapter, we evaluated the large-scale harmonic response of turbulent premixed V-flame at varying levels of turbulence intensity, nominal flow velocity, and forcing frequency. Coherent, convective disturbances are introduced in the flame through the flame holder, oscillating transverse to the streamwise direction, while a turbulence generator induces broadband forcing on the flame. We isolate the dependence of flame and heat release rate response on each of these effects.

We find that the amplitude spectrum broadens with the downstream distance, indicating a decay in harmonic flame response at large turbulence levels and forcing frequencies. We also observe that the amplitude of harmonic flame response depicts spatial oscillations arising from the interference of coherent wrinkles induced on the flame surface by the oscillating flame holder and fluctuations induced on the flame surface by vortical disturbances. We observed that for low nominal velocities, coherent wrinkles induced by the flame holder dominated the flame response. However, for higher nominal velocities, the response was dominated by long-wavelength vortical disturbances. We also observed that an increase in the forcing frequency and turbulence levels almost always shifts the response peak closer to the flame holder.

Finally, we characterize the asymmetry in flame response and show the relationship between the spatial flame response on the local and global heat release rate response. For lower flow velocities, the flame remains comparatively symmetric (varicose flame structure), resulting in flame area fluctuations which are more significant than higher flow velocities where the flame is asymmetric (sinuous or uncorrelated flame structure). Consequently, for lower flow velocities, there is a progressive increase in heat release rate response with increasing downstream distance. In contrast, for cases with higher turbulence levels and higher nominal velocity, an initial increase in heat release rate response is followed by a decrease at higher downstream distances. Finally, we find the globally integrated heat release rate response, which tends to roll off with increasing frequency ($1/f$ dependence), consistent with low-pass filter characteristics of flames in general. Similarly, there is a decay in the response with increasing turbulence levels, indicating the effect of kinematic restoration on the global flame response.

In this chapter, we have only focussed on the harmonic response of flame fluctuations. However, this approach is limited when characterizing the effect of fluctuations on the flame surface due to high levels of turbulence. At high turbulent intensities, the flame response is quite visibly anharmonic. In the next chapter, we introduce statistical analysis of these turbulent fluctuations and expound on the small-scale dynamics of flame fluctuations.

CHAPTER 5

SELF-SIMILARITY AND SMALL-SCALE INTERMITTENCY IN TURBULENT PREMIXED FLAMES

In the previous chapter, we measured the harmonic response of the flame when subject to large-scale effects such as variation in the mean flow velocities, turbulence levels, and narrowband forcing at different forcing frequencies. We observed strong nonlinear and anharmonic response at high turbulence levels. In fact, the flame response at high turbulence levels decayed at all forcing frequencies. Thus, quantifying only the harmonic response of the flame at high turbulence levels would yield an incomplete picture of the interaction between the premixed flame and the turbulent background flow.

Consequently, we consider the turbulence-flame interaction in greater detail. In particular, we consider the statistics of the flame fluctuations obtained at high turbulence levels and high forcing frequency. We begin by discussing the nature of the spectrum of the flame surface fluctuations. We show that the spectrum has a pronounced scaling behaviour, which we explain through heuristic arguments based on Kolmogorov's phenomenology of turbulent flows. We then quantify the higher-order moments of the flame surface fluctuations and discuss their implications. Through a scale-dependent analysis based on temporal two-point correlation of the flame fluctuations, we prove that the fluctuations display small-scale intermittency. We determine the anomalous scaling exponents associated with higher-order moments of the highly intermittent flame fluctuations. We also introduce the multifractal formalism and quantify the singularities of the underlying multiplicative processes, which give rise to small-scale intermittency. We close the chapter with a discussion on the implications of the above findings in the context of turbulent premixed flames.

5.1 SPECTRAL SCALING OF FLAME SURFACE FLUCTUATIONS

In this section, we quantify the spectrum of flame surface fluctuations. We focus on the experimental dataset which shows the most pronounced anharmonic response. We choose the highest forcing frequency and turbulence levels for two different mean flow velocity. We designate these two cases as Flame F1 and F2 for ease of reference. The experimental conditions for flame F1 are: $\bar{u}_y = 4.62$ m/s, $Re_d = 6.99 \times 10^3$, $u'/\bar{u}_y = 33.13\%$ and $u'/s_L = 4.20$. For the flame F2, $\bar{u}_y = 6.89$ m/s, $Re_d = \bar{u}_y d/\nu = 1.06^3$, $u'/\bar{u}_y = 32.13\%$ and $u'/s_L = 5.89$. The Damköhler number for the flames are $Da = 2.11$ and $Da = 5.23$, respectively. The nominal Reynolds number is defined as $Re_d = \bar{u}_y d/\nu$, where d is the diameter of the nozzle from which the flow ensues (see Fig. 2.2a). The control parameters for the two experiments are tabulated in Table 5.1.

5.1.1 Temporal power spectrum of flame fluctuations

In Fig. 5.1(b), we show a representative time series of the fluctuations ξ' for the two cases considered here. The fluctuations are measured at a location of $y/\lambda_c = 2$ downstream of the flame stabilization point. Here, $\lambda_c = \bar{u}/f_f$ is the wavelength of coherent, harmonic disturbances induced by the oscillating flame holder. The flame

Feature		**Flame F1**	**Flame F2**
Mean flow velocity	$\bar{u}_y$	4.62 m/s	6.89 m/s
Root mean square velocity	u'	0.53 m/s	1.04 m/s
Turbulent intensity	$u'/\bar{u}_y$	0.33	0.32
Equivalence ratio	ϕ	0.97	0.91
Kinematic viscosity	ν	1.81×10^{-5} m^2/s	1.81×10^{-5} m^2/s
Forcing frequency	f_f	1250 Hz	1250 Hz
Convective wavelength	$\lambda_c = \bar{u}_y/f_f$	3.7 mm	5.5 mm
Nominal Reynolds no.	$Re_d = \bar{u}_y d/\nu$	6.99×10^3	1.06×10^3
Integral length	ℓ	1.33 mm	7.1 mm
Integral Scale Reynolds no.	$Re_\ell = u'\ell/\nu$	38.81	408
Laminar flame speed	s_L	0.37 m/s	0.34 m/s
Laminar flame thickness	δ_F	0.44 mm	0.46 mm
Damköhler number	$Da = \ell s_L/\delta_F v'$	2.11	5.23
Kolmogorov length	$\eta = Re_\ell^{-3/4}\ell$	0.085 mm	0.078 mm
Gibson length	$l_g = (s_L/u')^3\ell$	0.452 mm	0.249 mm

Table 5.1: Relevant properties of the two turbulent premixed flames considered in this chapter. The convective wavelength is calculated as $\lambda_c = \bar{u}_y/f_f$. The quantities s_L and δ_F were obtained using CHEMKIN PREMIX calculation (see Humphrey, 2017).

fluctuations are quite visibly aperiodic.

Before moving ahead, let us define the auto-correlation function associated with ξ' as:

$$R_\xi(\tau) = \langle \xi'(t+\tau)\xi'(t) \rangle. \tag{5.1}$$

We have assumed that the conditions of homogeneity and isotropy are fulfilled such that R_ξ is only a function of the time delay τ. We can then define the power spectrum of the

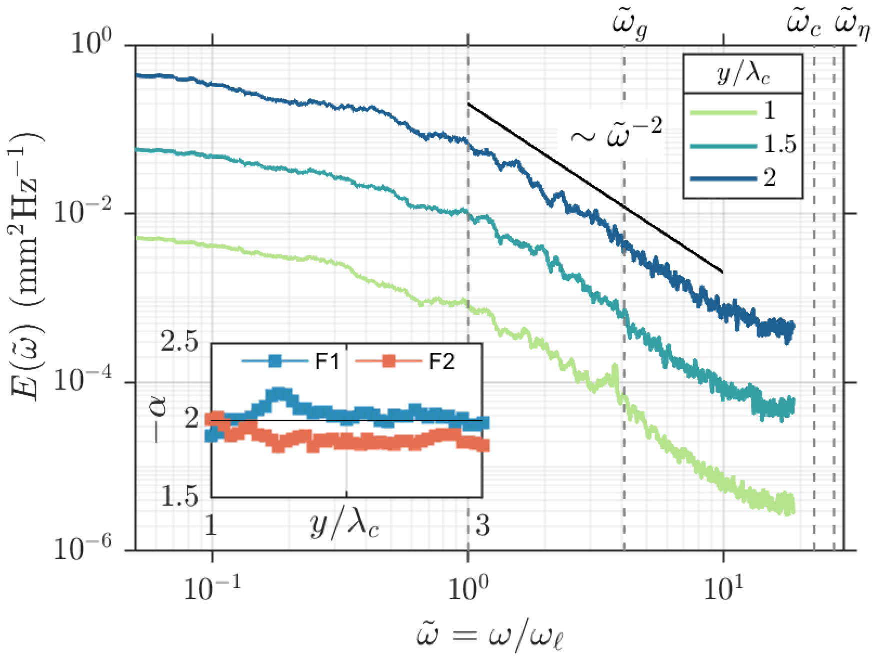

Figure 5.1: Temporal power spectral density $E(\tilde{\omega})$ measured at various axial locations y/λ_c, for flame F1. The power spectra varies as $E(\tilde{\omega}) \sim \tilde{\omega}^{-\alpha}$ over an intermediate range of frequencies. The estimated values of the exponent $-\alpha$ at various y/λ_c are shown in the inset for both flames F1 and F2. In both cases, the exponent is close to -2; the corresponding scaling behavior is depicted by the solid line in the main panel. The frequency corresponding to Gibson ($\tilde{\omega}_g$), Corrsin ($\tilde{\omega}_c$) and Kolmogorov ($\tilde{\omega}_\eta$) scales have been indicated by dashed lines.

flame fluctuations as:

$$E_\xi(\omega) = |\hat{\xi}(\omega)^2| = \int R_\xi(\tau) e^{i\omega\tau/2\pi} d\tau. \tag{5.2}$$

Here, the angular frequency is defined as: $\omega = 2\pi f$. The quantities $E_\xi(\omega)$ and $R_\xi(\tau)$ are the Fourier transform pairs.

The power spectra as a function of the normalized frequency corresponding to the two cases are shown in Fig. 5.1. A sliding-window averaging method was used to smooth out large variations in the spectra and obtain the underlying scaling behavior. The frequencies corresponding to eddy turnover times at various length scales have also been indicated. Here, τ_η corresponds to the turnover time of a Kolmogorov sized (η) eddy, τ_G is that of Gibson scale (ℓ_g) eddy and τ_c is for Corrsin scale (η_c) sized eddy.

The spectra for the two cases are quite evidently broadband. The small peak around 1250 Hz for flame F1 corresponds to the harmonic forcing of the flame stabilization point. We notice that the strength of harmonic forcing is very low compared to the broadband behavior of the spectrum induced by the turbulent flow. Such a peak is not visible for case F2 with a higher mean flow. The roll-off behavior of the two spectra is particularly interesting. We can clearly observe that the spectra have scale-invariant behavior and scales as:

$$|\hat{\xi}^2(\omega)| \sim \omega^{-\alpha}. \tag{5.3}$$

For flame F1, the spectrum scales with the scaling exponent $\alpha = 2.15$ while for flame F2, $\alpha = 1.79$ at $y/\lambda_c = 2$ in Fig. 5.1. We observe that the scaling persists for two decades of $f\tau_\eta \in (10^{-2}, 10^{-1})$. The broadband behavior of the spectra persists for fluctuations measured at different downstream locations. To better understand the overall behavior, the change in the scaling exponent α of the power spectrum of flame fluctuations as a function of the downstream distance y/λ_c from the flame stabilization point is plotted in the inset of Fig. 5.1. We observe that the value of the scaling exponent for either of the two flames remains close to 2 very close to the flame stabilization point and decays to lower values at larger downstream distances.

5.1.2 Kolmogorov's limit for temporal power spectrum

We now discuss the underlying phenomenology of turbulent flames which leads to the scale-invariant spectra depicting a power-law behavior. Peters (1992) derived the spectrum of turbulence-induced fluctuations of the scalar field $\xi'(\boldsymbol{x},t)$ from the scalar two-point correlation: $R_\xi(\boldsymbol{r},t) = \langle \xi'(\boldsymbol{x},t)\xi'(\boldsymbol{x}+\boldsymbol{r},t)\rangle$ (refer to discussion in §2.2.2.2). The spectrum function associated with scalar fluctuation ξ' is determined as,

$$\Gamma(k,t) = k^2 \oint \hat{R}_\xi(\boldsymbol{k},t)d\Omega = 4\pi k^2 \hat{R}_\xi(k,t), \tag{5.4}$$

where, $\hat{R}_\xi(\boldsymbol{k},t)$ is the Fourier transform of $R_\xi(\boldsymbol{r},t)$ and Ω is the solid angle over the Fourier $\boldsymbol{k}-$space. The spectrum of ξ' is then assumed to be related to the Eulerian velocity spectrum. Through a gradient diffusion hypothesis and dimensional analysis, Peters (1992) derived the form of the spectrum function associated with flame fluctuations, which is of the form:

$$\Gamma(k,t) = \mathcal{H}(k-k_\ell)k^{-5/3}\exp\left[-3c_3(\ell_g k)^{1/3}\right]\exp\left[-\frac{3}{4}c_4(\eta_c k)^{4/3}\right]\exp\left(-c_5\eta_M k\right). \tag{5.5}$$

It is evident that the spectrum of ξ' would scale according to the classical Kolmogorov's $k^{-5/3}$ scaling at scales smaller than the integral scale (ℓ) and much larger than scales where propagation (ℓ_g) and curvature (η_c, η_M) effects become relevant (see Fig. 1.5). However, as one approaches smaller scales, propagation and dissipation effects become dominant in smoothing out fluctuations in ξ', leading to the much steeper exponential decay of the spectrum. In Fig. 5.1 we have indicated the relevant time scales associated with the turnover times of eddies of integral (τ_ℓ), Gibson (τ_g) and Obukhov-Corrsin (τ_c) scale. Clearly, very high-frequency fluctuations are not sampled by Mie scattering measurements used for capturing flame edges. However, we observe that the measurements span intermediate-range above the Gibson scale till the integral scale ($\tau_\ell > t >> \tau_g$). More precisely, the flame fluctuations in ξ' are well-sampled for a range of scales unaffected by anisotropic effects at large scales and flame propagation effects at scales below Gibson scale. Thus, for this intermediate range, we observe self-similar scaling of the spectrum of ξ'. Thus, the spectrum function of ξ' simply reduces to,

$$\Gamma(k) \sim k^{-5/3}, \qquad \forall \ \ell > r > \ell_g. \tag{5.6}$$

In order to understand the scaling exponent, we need to consider the influence of turbulence on the temporal power spectrum. In the inertial-advective range, eddies of size (r) smaller than the integral scale ($r < \ell$) perturb the flame and contribute to the higher frequency range of the time spectrum. In addition, these eddies are randomly swept past due to random advection. The random advection of eddies would decorrelate the measurements, leading to spectral broadening, an effect analogous to Doppler's redshift (Tennekes, 1975). The frequency of such a random advection would be of the order of u'/ℓ, where u' is the root mean square of the fluctuations in the velocity field. Thus, the spectral broadening effect would be expected to occur below u'/ℓ, around the infrared range of the spectrum ($f < 1/\tau_\ell$), which is precisely what we observe in Fig. 5.1.

Thus, the spectral scaling behavior of ξ' would theoretically depend on eddies smaller than the integral scale $r < \ell$. Thus, the frequency of fluctuations induced on the flame surface is essentially due to eddy turnover in this range, which is of the order $\omega = 2\pi f \sim u'/r$. However, $1/r$ implies the wavenumber k of the eddy, implying that $\omega \sim u'k$. Further, in this range, the velocity spectrum scales according to Kolmogorov's theory ${u'}^2/k \sim k^{-5/3}$ (see Eqn. 2.18). In other words, velocity scales as: $u' \sim k^{-1/3}$. Thus, the frequency of fluctuations induced on the flame surface is related to the wavenumber of eddies through the simple scaling relation

$$\omega \sim u'k \sim k^{2/3}. \tag{5.7}$$

Finally, we note that at higher frequencies ($f > 1/\tau_\ell$), the dynamics would be unaffected by spectral broadening effects. Consequently, in the intermediate range of scales, the temporal power spectrum $E_\xi(\omega)$ of a flame fluctuation is essentially a re-arrangement of the spatial power spectrum $\Gamma(k)$, and the total integrated energy contained in either of the two spectrum should be equivalent (Tennekes and Lumley, 2018). Denoting with $E_\xi(\omega) \sim |\hat{\xi}^2(\omega)|$ the time spectrum of ξ', we have the following balance

$$\int E_\xi(\omega) d\omega \sim \int \Gamma(k) dk.$$

Using the fact that the wavenumber is a function of the frequency $k = k(\omega)$ according to Eqn. (5.7), and utilizing the form of spectrum function $\Gamma(k)$ in Eqn. (5.6) obtained for the intermediate range, we have

$$\begin{aligned}\int E_\xi(\omega)d\omega &\sim \int \Gamma(k(\omega))dk(\omega),\\ &\sim \int [k(\omega)]^{-5/3}\,\omega^{1/2}d\omega,\\ &\sim \int \left[\omega^{3/2}\right]^{-5/3}\omega^{1/2}d\omega,\\ &\sim \int \omega^{-2}d\omega. \end{aligned} \tag{5.8}$$

The correspondence between the left and right side of the equation implies that the time spectrum of ξ' must follow:

$$E_\xi(\omega) = |\hat{\xi}^2(\omega)| \sim \omega^{-2}. \tag{5.9}$$

This is Kolmogorov's limit of time spectrum associated with fluctuations on the flame surface induced by turbulence in the inertial sub-range.

In Fig. 5.1(a), we show the scaling of the spectra for the two flames. We observe that the scaling range starts around the frequency of integral scale turn over time and continues well past the frequency of a Gibson-scale eddy. In Fig. 5.1(c), we depict the variation in the scaling exponent $-\alpha$ with the fluctuations ξ' measured at several downstream locations. The scaling exponent varies around the limit of $\alpha = 2$ for the two flames. Thus, within experimental uncertainty, the scaling behavior of the time spectrum of ξ' follows directly from Kolmogorov's phenomenology of turbulent flows in the intermediate range. In this range, the flame fluctuations are neither affected by large-scale anisotropies nor does it depend on very short-scale (or high frequency) curvature and propagation effects. The flame behaves as a passive scalar in this range of scales, and the fluctuations induced on the flame surface simply reflect the signature of turbulent flows. Further, the scale-invariant nature of the spectra with a well-defined scaling exponent implies the cascade process through which the turbulence-induced flame fluctuations are transferred from small to large frequencies. The transfer of energy across scales in this range is self-similar. The cascade is essentially disrupted at scales below the Gibson scale as strong propagation effects cause exponential decay in the magnitude of fluctuations. However, as we have only limited data sampling capability, the high frequencies where the exponential decay starts is not captured, and the spectra appear to flatten at higher frequencies ($f > 1/\tau_g$). Thus, despite the lack of dissipation-scale resolution, we are able to delineate a clear self-similar power-law scaling, which evidently follows from Kolmogorov's arguments for passive scalars.

5.2 STATISTICS OF LARGE-SCALE FLAME FLUCTUATIONS

Now, we focus on the statistics of the flame fluctuations as a function of the distance from the flame stabilization point. As we saw earlier, the scaling of the spectra follows from Kolmogorov's theory at short distances from the flame stabilization point. At a larger distance, the scaling is quite different from $\alpha = -2$. The departure from Kolmogorov's limit is a consequence of increasing large-scale anisotropy at large downstream disturbances. Thus, the statistics are expected to reflect such a behavior.

In Fig. 5.2(a), we depict the change in the shape of the probability density function (PDF) of $\xi'(t)$ for increasing downstream distance. We observe that PDF changes from nearly Gaussian ($\mathcal{N}(0,1)$) at small y/λ_c to a stretched-exponential possessing significant tails. The PDF further becomes increasingly asymmetric and skewed. The flame length, i.e., the length of the flame front at any given instant of time along the flame fixed co-ordinate system, continuously varies in time due to the general large-scale unsteadiness of the flow. Thus, for a given $y-$location sufficiently downstream of the flame-holder, the flame front may or may not exist at a certain time instance. The probability of finding a flame front decreases as we move downstream of the flame-holder. Thus, we find large deviations from the mean flame locations for the instances when the flame propagates large downstream distances. These large deviations are responsible for the heavy-tails of the distribution. The peaks also sharpen, indicating the higher probability of the flame not to have propagated thus far downstream.

We measure the higher-order statistics, i.e., the skewness and the flatness factor of the PDF of fluctuations. The skewness and flatness factors (otherwise known as kurtosis) are given by the third and fourth moments of the PDF. Formally, it is written as:

$$S = \frac{\langle \xi'^3 \rangle}{\sigma_\xi^3}, \qquad F = \frac{\langle \xi'^4 \rangle}{\sigma_\xi^4}. \tag{5.10}$$

Here, the standard deviation is defined as $\sigma_\xi = \langle \xi'^2 \rangle^{1/2}$. The skewness indicates the asymmetry of the PDF, implying the relative propensity of fluctuations to be either positive or negative with respect to the mean value. The flatness factor quantifies the “tailedness" of the PDF and captures the significance of extreme value fluctuations in the PDF. The skewness of a zero-mean Gaussian distribution ($\mathcal{N}(0,1)$) is 0, and the flatness factor is 3.

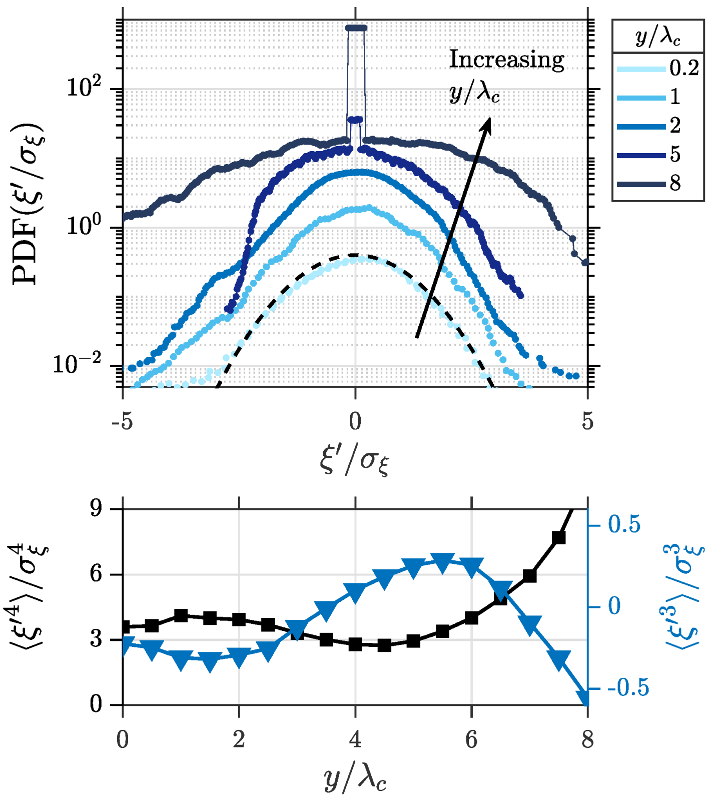

Figure 5.2: (a) Probability density function (PDF) of flame position fluctuations normalized by the standard deviation (σ_ξ) for increasing downstream distance from the flame holder ($y/\lambda_c = 0.2, 1, 2, 5, 8$). (b) Flatness factor ($\langle\xi'^4\rangle/\sigma_\xi^4$) and skewness ($\langle\xi'^3\rangle/\sigma_\xi^3$) of the PDF of $\xi'(t)$ as a function of the downstream distance. The data corresponds to flame F1. The PDFs have been shifted vertically for clarity.

In Fig. 5.2(b), we plot the variation of the skewness and the flatness factor of the PDF of ξ' as a function of the downstream distance. We observe that the skewness is non-zero, indicating that inward (negative) fluctuations are more likely than outward ones. In other words, the flame is slightly more likely to fluctuate towards the reactants with respect to the mean flame position $\langle\xi(y)\rangle$ than towards the products.

As noted earlier, the PDF becomes increasingly heavy-tailed at larger downstream distances. This is captured by the divergence of the flatness factor $\langle\xi'^4\rangle/\sigma_\xi^4$ from 3, for y far away from the flame-holder as a consequence of sporadic flame propagation to large distances. Thus, there is large-scale intermittency associated with flame propagation which is a direct result of large-scale unsteadiness in the evolution of flame fluctuations. On the other hand, near the flame stabilization point, there is no large-scale intermittency, as is indicated by the Gaussian PDF (Fig. 5.2) and the skewness and flatness factor following their respective Gaussian values. However, there can be intermittent fluctuations associated with the small-scale fluctuations induced by the turbulent flow. In the next section, we discuss the means of quantifying small-scale intermittency.

5.3 SMALL-SCALE INTERMITTENCY IN FLAME FLUCTUATIONS

5.3.1 Non-Gaussian statistics of increments in flame fluctuations

In the foregoing discussion, we noted that at smaller scales, Kolmogorov's phenomenology becomes inexact due to extreme fluctuations in dissipation-based quantities, which is referred to as small-scale intermittency. In order to determine whether fluctuations display small-scale intermittency, we need to focus on scale-dependent statistics. Thus, we compute the increments in the fluctuations of the flame surface:

$$\delta\xi'(y,\tau) \equiv \xi'(y,t+\tau) - \xi'(y,t). \tag{5.11}$$

Measuring the moments of the increment in the fluctuations $\delta\xi'(y,\tau)$ allows a scale dependent analysis of the statistics. Measurement of the statistics of increments over a range of time scales (τ) is tantamount to successive high-pass filtering

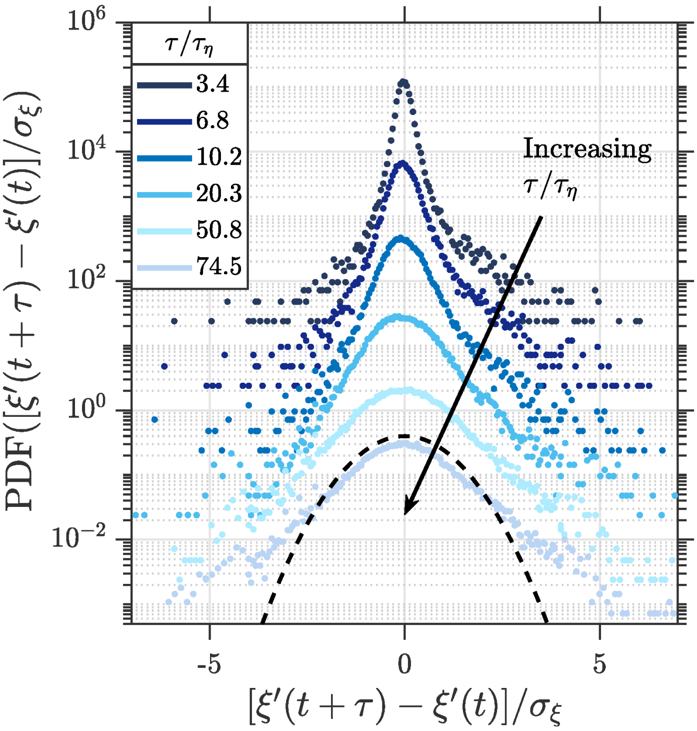

Figure 5.3: PDF of the normalized flame position increment ($\delta\xi'(\tau)/\sigma_\xi$) function for different values of normalized time lag τ/τ_η measured from $\xi'(t)$ at $y/\lambda_c = 0.5$ for flame F1. Each curve has been vertically shifted for clarity.

operation required to capture the extreme fluctuations appearing intermittently in the measurements. In fact, the moments of the increment in fluctuations are related to the auto-correlation defined in Eqn. (5.1). It is easy to observe that the second moment of the increment is related to the correlation through the relation:

$$\langle|\delta\xi'(y,\tau)|^2\rangle \equiv 2\langle\xi'^2\rangle \left(1 - \frac{R_\xi(y,\tau)}{\langle\xi'^2\rangle}\right). \tag{5.12}$$

Here, $\langle\xi'^2\rangle$ is the mean-squared fluctuations in ξ'.

We depict the PDF of the increments $\delta\xi'(\tau)$, measured at $y = 0.5\lambda_c$, for increasing values of τ for flame F1 in Fig. 5.3. For very large values of τ, the PDF approximately follows the Gaussian. This is due to the fact that at large values of τ, the two points in the time series become decorrelated, leading to the Gaussian distribution. However, as τ is decreased and approaches the turnover time of a Kolmogorov-sized eddy, the PDF becomes progressively sharp and possesses significantly wide tails. The PDF indicates the presence of intermittency at small scales.

In order to quantify the extent of intermittency, we define the structure-function associated with the increments for a generalized order p as:

$$S_p(y, \tau) \equiv \langle |\delta\xi'(y, \tau)|^p \rangle = \langle |\xi'(y, t + \tau) - \xi'(y, t)|^p \rangle. \tag{5.13}$$

We can therefore measure the skewness, and the flatness factor of the PDF indicated in Fig. 5.3. In terms of the generalized structure-function, the skewness is $S_3/S_2^{3/2}$, while the flatness factor is defined as S_4/S_2^2. We plot the skewness and flatness factor of the PDF of the increments in the flame fluctuations measured at a distance of $y/\lambda_c = 2$ in Fig. 5.4. We note that at large time delay τ, the flatness factor is very close to 3, implying Gaussian behavior, a fact we observed in Fig. 5.3 as well. The flatness factor increases monotonically as the time delay is lowered and approaches the turnover time of a Kolmogorov-sized eddy ($\tau \to \tau_\eta$). In fact, the flatness factor is close to 50 at very low values of τ, implying the unmistakable signature of small-scale intermittency.

The skewness of PDF also has similar behavior. At large values of τ, the skewness is close to 2. The PDF is near Gaussian with slight positive skewness. However, as we decrease the time delay, the skewness also increases monotonically. For time scales comparable to τ_η, the skewness is significant, implying the relatively higher propensity of the PDF of $\delta\xi'$ to have positive values in comparison to negative values.

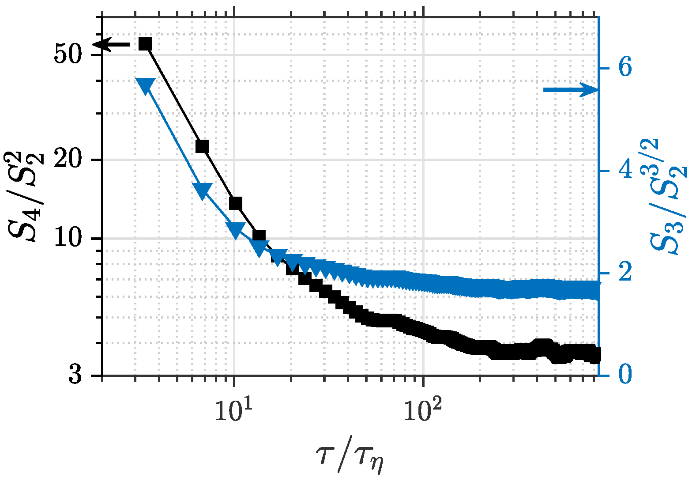

Figure 5.4: Flatness factor S_4/S_2^2 (■) and the skewness $S_3/S_2^{3/2}$ (▼) measured at $y = 2\lambda_c$ for flame F1. Note that the left axis for the flatness factor is in logarithms while right axis for the skewness is linear.

5.3.2 Power-law scaling of structure functions

For statistically stationary signals, the increments $\delta\xi'(y,\tau)$ and the structure function $S_p(y,\tau)$ depend only on the time lag τ. Further, for statistically intermittent signals, any general p^{th} order moment do not converge to a specific value, and displays power-law scaling with the measurement scale. We thus find that $S_p(y,\tau)$ depicts power-law scaling with the time lag τ with the scaling exponent $\zeta_p(y)$, such that:

$$S_p(y,\tau) \sim \tau^{\zeta_p(y)}. \tag{5.14}$$

In Fig. 5.5, we plot the structure-function up to the sixth order as a function of τ at $y = 0.5\lambda_c$. We notice that S_p scales non-trivially with τ across two decades. Further, the slope of the scaling increases as the order of the structure-function is increased. The scaling of the structure-function of different orders saturates, indicating the outer cut-off (τ_o). The outer cut-off is smaller but of the order of turnover time of eddy of the

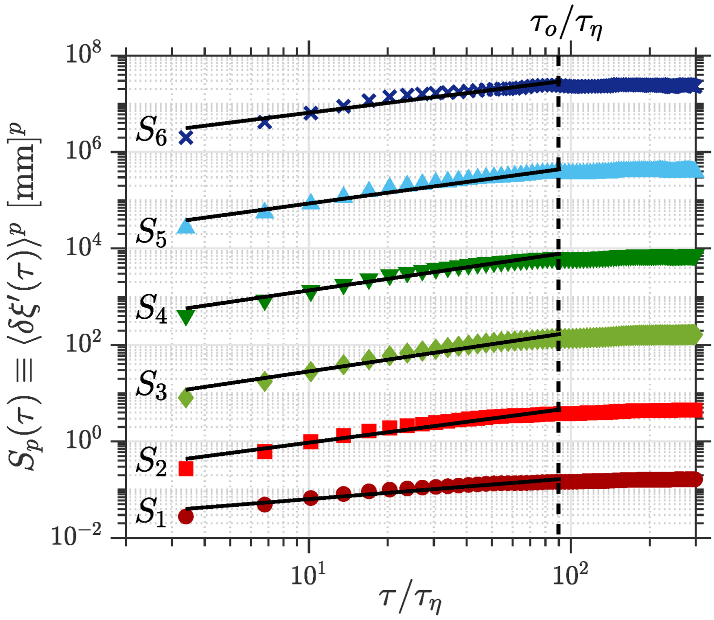

Figure 5.5: Structure function S_p with generalized order p is plotted as a function of the normalized time lag for flame position increments at $y/\lambda_c = 0.5$ for flame F1. Curves have been shifted vertically for clarity.

size of the integral scale ($\tau_o \lesssim \tau_\ell$). Above the outer cut-off ($\tau > \tau_o$) ξ' decorrelates and randomizes from its values at earlier times, essentially forgetting its past. The decorrelation leads to a Gaussian PDF as observed from Fig. 5.3 for large values of τ.

5.3.3 Kolmogorov's limit for structure-function scaling

The exact nature of scaling of the higher-order structure-function is quite important. If, for instance, we consider the signal to be non-intermittent and Gaussian, the scaling of the higher-order structure-function follows from the first two moments of the PDF. This allows one to unambiguously predict the behavior of the higher-order moments, and hence, quantify the tails containing the extreme fluctuations. For example, it is easy to deduce that any given odd moment of a Gaussian PDF should identically be equal to zero, as one would expect of the third moment, which is the skewness. This is precisely the case of K41 theory, which implicitly assumes homogeneous and isotropic turbulence, resulting in a Gaussian velocity field. Thus, the velocity structure function defined on the velocity increments ($\delta v_r \equiv v(x+r) - v(x)$), is expected to follow, for any p, the relation (see Eqn. 2.22):

$$\langle \delta v_r^p \rangle = \beta_p'(r\langle \varepsilon \rangle)^{\zeta_p}, \tag{5.15}$$

where β_p' are empirical constants and $\langle \varepsilon \rangle$ is the average turbulent kinetic energy dissipation. The scaling exponent assumes the form: $\zeta_p = p/3$. Two of these structure-function relations are quite important. The scaling of the second-order structure-function, is of the form: $\langle \delta v_r^2 \rangle \sim r^{2/3}\langle \varepsilon \rangle$. The equivalent spectral form leads to the $5/3^{\mathrm{rd}}$-law: $E_u(k) \sim \langle \varepsilon \rangle^{2/3} k^{-5/3}$. Although the $5/3$ scaling is empirically well substantiated (Fig. 2.2a), the scaling of the structure-function for $p = 2$ is based on dimensional arguments, and no exact relation is known. On the other hand, for $p = 3$, the relation is mathematically exact, and is known as the $4/5^{\mathrm{th}}$-law: $\langle v_r^3 \rangle = -4/5\langle \varepsilon \rangle r$. Thus, if the velocity field were to be Gaussian, the higher-order moments would follow exactly from Eqn. (5.15) and result in a non-intermittent velocity field. However, as it turns out, extensive experimental data show that the scaling exponents are fairly close to the predictions of K41 theory up to order $p = 3$ (Frisch, 1995; Sreenivasan and Antonia, 1997). However, for $p > 3$, there is a deviation from the $\zeta_p = p/3$ limit. The deviation in the scaling exponents from the $p/3$ dimensional limit is known as anomalous scaling exponents. The higher-order moments sample the tails of the PDF and quantify the extreme value fluctuations in the velocity field. Thus, the higher the deviation, the stronger the intermittency is, and the larger is the anomaly in the scaling exponent.

In §5.1.2, we observed that the spectrum of flame fluctuations follows $E_\xi(\omega) \sim \omega^{-2}$ for $\tau_\ell < \tau < \tau_g$. This would indicate that the second-order structure function should scale as: $\langle \delta\xi'(\tau)^2 \rangle / \omega \sim \omega^{-2}$. It is straightforward to observe that $\langle \delta\xi'(\tau)^2 \rangle \sim \tau$. Generalizing to any arbitrary order p, we have

$$S_p(\tau) = \langle \delta\xi'(\tau)^p \rangle \sim \tau^{p/2}. \tag{5.16}$$

In other words, the scaling of the exponents of the structure function of the increments in flame fluctuations should be:

$$\zeta_p = \frac{p}{2}. \tag{5.17}$$

We verify the exact behavior of the scaling exponents for the two flame data next.

5.3.4 Anomalous scaling exponents

The scaling of the structure function for various orders was shown in Fig. 5.5. We determine the scaling exponent for the power-law obtained for various orders as the slope of the resulting log-log plot, which is:

$$\zeta_p = \frac{\log\left(S_p(\tau)\right)}{\log \tau}, \qquad \forall\ \tau \in (\tau_\eta, \tau_o),\ \ p = 1, ..., 6. \tag{5.18}$$

In Fig. 5.7, we plot the dependence of the scaling exponent ζ_p as a function of the moment order p for fluctuations measured at $y/\lambda_c = 2$ for the two flames F1 and F2. Evidently, ζ_p does not scale according to $\zeta_p = p/2$ predicted based on Kolmogorov's dimensional limit and, in fact, shows a large deviation from the dimensional limit.

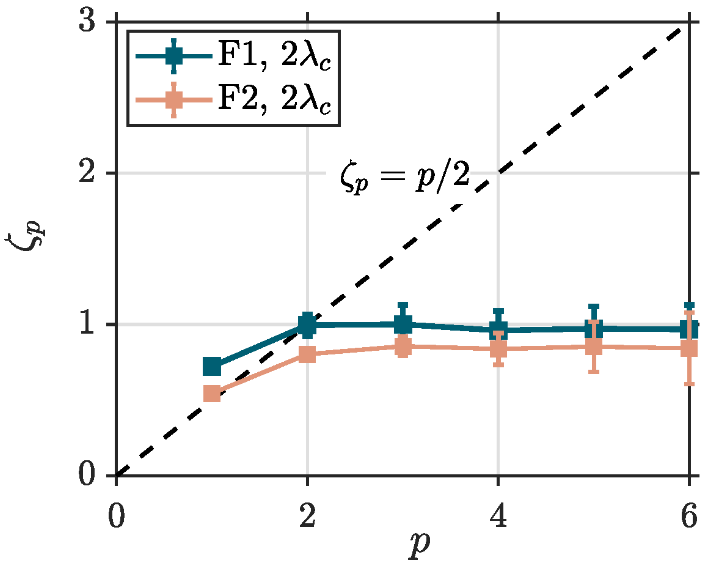

Figure 5.6: The variation of the scaling exponents ζ_p with the order p of the structure function, for both flames at $y/\lambda_c = 2$. The dashed line indicates the non-intermittent limit of $\zeta_p = p/2$. The strong deviation of ζ_p from this limit for $p > 2$, implies that the exponents scale anomalously and that the flame fluctuations are strongly intermittent. The error bars represent the standard deviation of the measured values obtained from different time series.

Further, the exact nature of the dependence of ζ_p on p is non-trivial. First, the monotonic increase in the value of ζ_p indicates that the higher-order moments of $\delta\xi'$ sufficiently capture the intermittent properties of ξ' even when its PDF of ξ' is Gaussian close to the flame stabilization point. Second, the concavity of $\zeta_p - p$ curve follows from Hölder's inequality (Eqn. 2.28). Finally, the deviation in ζ_p from $p/2$ becomes larger with increase in the order p. The deviation implies very strong intermittency at the smaller scales. A comparison with the typical plots of scaling exponents for velocity and passive scalars in turbulent flows (Fig. 2.4) indicates much stronger intermittency in the fluctuations of the flame surface (Fig. 5.6).

In our foregoing discussion, we noted that the structure functions are determined at various downstream locations. Thus, the scaling exponents would also depend upon the downstream location. Thus, in Fig. 5.7, we plot the variation in ζ_p as a function of

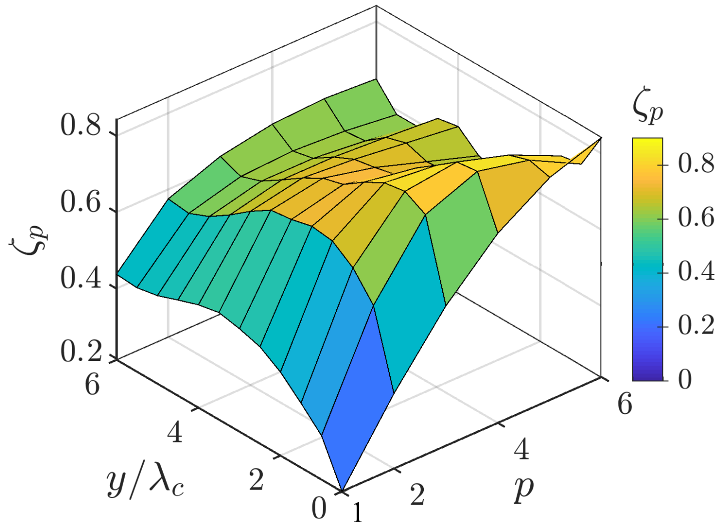

Figure 5.7: The moment order exponent ζ_p plotted as a function of the normalized downstream distance y/λ_c and order p.

moment order p and downstream location y/λ_c. We observe that the flame fluctuations depict small-scale intermittency at all downstream locations.

Having shown that the flame fluctuations depict small-scale intermittency, we use the statistical model of multifractality to capture intermittent statistics, explain the role of singularities, and extract important information about the nature of the fluctuations from the multifractal spectrum.

5.4 MULTIFRACTAL BEHAVIOR OF TURBULENT FLAMES

In this section, we explain the motivation for invoking the statistical model of multifractal formalism in characterizing the intermittent fluctuations in turbulent premixed flames and explain various important factors of the multiplicative process that leads to the observed small-scale intermittency.

5.4.1 Generalized dimension of flame fluctuations

As explained earlier, moments of intermittent quantities do not converge and are dependent on the measurement scale. Consequently, one obtains a power-law relation between the moment of a given order q and the scale of measurement (Halsey *et al.*, 1986). This is expressed as

$$\langle \delta\xi'^{q}_{\tau} \rangle \sim \langle \delta\xi' \rangle^{q} \left(\frac{\tau}{\tau_\ell} \right)^{\mu(q)} \qquad \forall \; q \in \mathbb{R}. \tag{5.19}$$

Here, we have used τ_ℓ as a normalizing scale and $\langle \delta\xi' \rangle$ is obtained by averaging over scale τ_ℓ.

The scaling exponent of the power-law scaling of the moments is referred to as the mass exponent and is denoted as $\mu(q) = (q-1)D_q$. The order q is essentially an amplifier that can be tuned to accentuate certain fluctuations over others. For $q > 0$, the major contribution to the value of the moment on the left-hand side of Eqn. (5.19) is from peaks in ξ' that gets larger as q is increased. While, for $q < 0$, the major contribution to the average is from peaks in ξ' of smaller and smaller intensities as q is decreased to larger negative values.

In Fig. 5.8, we depict the scaling of the moment of order q (Eqn. 5.19) as a function of the time delay τ. We have considered the fluctuations of flame F1 measured at $y = 0.5\lambda_c$ for exemplifying the nature of scaling. We notice that the general q-order moment of ξ' does not converge. Instead, we observe power-law scaling over a sizeable range of τ. This is a consequence of the fact that the fluctuations ξ' are generated as a

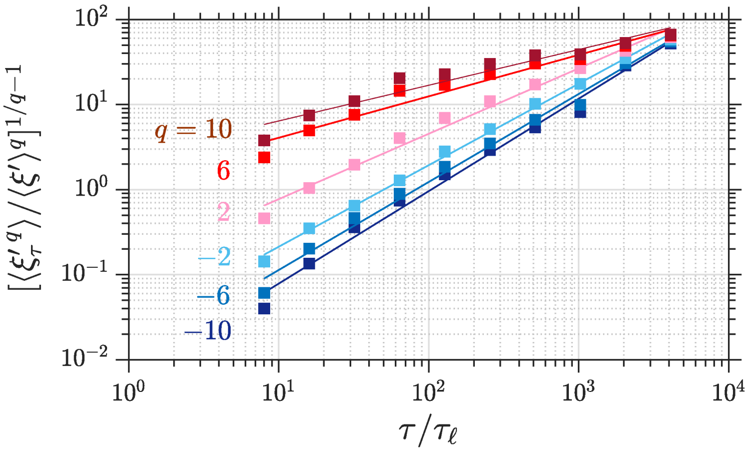

Figure 5.8: Scaling of the generalized moment (Eqn. 5.19) with time scales τ for various order q. The linear fits are also indicated for each case. The slope of the qth order moment with τ gives the mass exponent $\mu(q)$ and the generalized dimension D_q. The fluctuations $\xi'(t)$ corresponds to $y = 0.5\lambda$ for flame F1.

result of some underlying multiplicative process and, thus, have a fractal (multifractal) nature. Further, the scaling exponents are different for different q. We also observe that the scaling is much steeper for increasing larger negative values of q for which the contributions to the moments are only from small fluctuations in ξ'. In contrast, for larger positive values of q, only large fluctuations in ξ' contribute to the moments, and the slope becomes progressively shallower.

The generalized dimension is then defined as:

$$D_q = \mu(q)/(q-1). \tag{5.20}$$

D_q refers to the dimension of a set which, when used to intersect with the original measure, produces divergence of the moment of order q (Mandelbrot, 1989). Further, Hentschel and Procaccia (1983) showed that the D_0 corresponds to the fractal

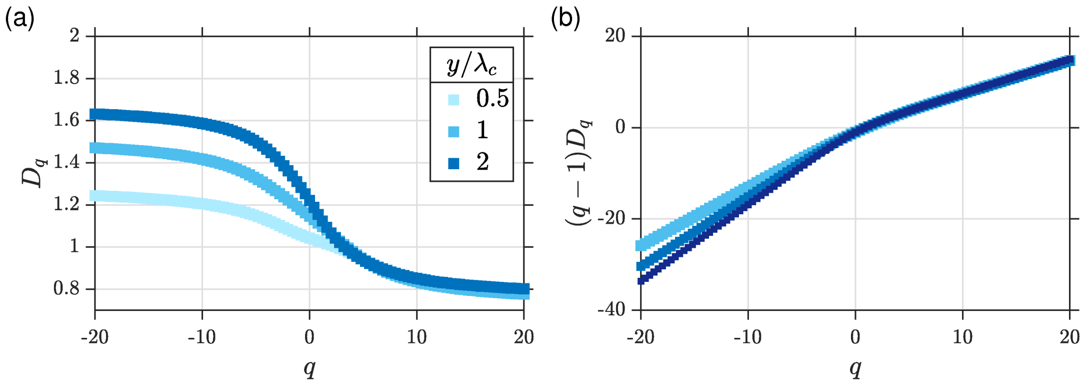

Figure 5.9: The variation of (a) the generalized dimension D_q, and (b) the mass exponent $\mu(q) = (q-1)D_q$ as a function of the generalized moment order q measured from ξ' at the indicated y/λ_c values for flame F1.

dimension of the support of the measure, D_1 the information dimension, and D_2 the correlation dimension. The information dimension is determined from the Shannon entropy in the signal (Hentschel and Procaccia, 1983). Essentially, D_1 quantifies the growth in the Shannon entropy as the time delay τ is varied. Finally, the correlation dimension is measured from the scaling of the correlation between the measure, which is the moment of ξ', among points separated by time duration τ.

The generalized dimension is measured from the slope of the linear fit of the logarithm of generalized moment, and is expressed as:

$$\frac{\mu(q)}{q-1} = D_q = \frac{\log\left[\left(\delta\langle \xi'^{q}_{\tau}\rangle / \langle \delta\xi'\rangle^{q}\right)^{1/q-1}\right]}{\log\left(\tau/\tau_\ell\right)}. \tag{5.21}$$

In Fig. 5.8, the linear fit on the log-log plot is indicated for scaling of each moment for different order q. The variation in the values of D_q and mass exponent $\mu(q)$ is further shown in Fig. 5.9 for ξ' measured at the indicated y/λ_c locations for flame F1. Since the fluctuations in ξ' arise out of multiplicative cascade, where the cascade is

Generalized dimension		$y/\lambda_c = 0.5$	$y/\lambda_c = 1$	$y/\lambda_c = 1.5$
Fractal dimension	D_0	1.10	1.14	1.21
Information dimension	D_1	1.02	1.10	1.12
Correlation dimension	D_2	1.00	1.06	1.08

Table 5.2: Generalized dimension of the fluctuations ξ' for flame F1 measured at the three locations.

embedded in $E-$dimensional space. The process of analyzing the data is essentially akin to obtaining the samples ξ' by taking a one-dimensional cut through a higher-dimensional multiplicative process. Thus, for the present case, we can do as well assuming $E = 2$, which results in intermittent fluctuations in time. We note that the condition of $\max D_q < E$ is followed (Mandelbrot, 1989). Further, we observe that the value of D_q decreases as a monotonic function of q, satisfying the criteria for generalized dimensions of the underlying attractor (Hentschel and Procaccia, 1983). The mass exponent $\mu(q)$, likewise, is a monotone decreasing function of q. Finally, The fractal dimension D_0 of ξ' for all the three downstream distances is greater than 1, implying a fractal behavior. The exact values of the fractal, information, and the correlation dimensions are tabulated in Table 5.2.

5.4.2 Singularities and the multifractal spectrum

As noted earlier, surfaces in turbulent flows are inherently fractal in nature and arise from the spatially hierarchical and temporally random structure of the velocity field (Sreenivasan, 1991*a*). Likewise, flames also depict fractal behavior and have been quite well studied in the past (Gouldin, 1987; Kerstein, 1988; Gülder *et al.*, 2000). Thus, we have a measure (moments of ξ') distributed on a fractal interface.

At this stage, it is important to delineate the meaning of measure and the support exactly. For instance, let us consider tossing two unbiased dice. The sum of outcomes of tossing two dice is the set of integers contained in $[2, 12]$. The probability of obtaining a number between 2 and 12 would be contained in $(0, 1)$. In other words, the probability measure is said to be supported by the set $[2, 12]$. In the context of turbulence, measure could refer to the moment of a flow variable such as velocity, kinetic energy, etc. A simple example of measure is an an iso-concentration contour of a scalar variable (concentration, temperature, etc.), which by definition, is the same everywhere. Thus, the measure is same as the support. This can be contrasted, for instance, with the actual distribution of scalar dissipation (defined as scalar increments) in real space. In which case, the support is the scalar concentration, and the measure is the spiky distribution of the scalar dissipation.

As discussed in §2.1.6, intermittent measures are generated by a multiplicative process where a conserved measure (e.g., the total energy of a flow) is divided unequally from one generation to next. As the number of unequal divisions increases, the measure becomes progressively uneven and intermittent. If the rule of division remains fixed from one to the next generation, the statistical properties of the measure depict a power-law (see Fig. 5.5 and Fig. 5.8).

Let us suppose that the measure of fluctuations ξ', as indicated in Fig. 5.1b, in the limit $[0, t]$ is $M([0, t])$. It is obvious that the measure is an increasing function of time such that the increments in the measure $M([0, t + dt]) - M([0, t])$ essentially gives the fluctuations ξ' at time t. If the fluctuations in ξ' were to be regular, the measure would have continuous density defined as $M(\Delta t)/\Delta t$. In the limit $\Delta t \to 0$, the density would tend to its true value. However, that would not be the case for the fluctuations shown in Fig. 5.1b, as the fluctuations are irregular and would remain so if one were to examine it on an even finer scale. A simpler test is to divide the fluctuations into two halves. It becomes quite clear that the measure would not be equally distributed among the two halves. If, on the other hand, we were to take the limit $t \to \infty$, the fluctuation would be even more 'wiggly' and uneven. Thus, it follows that the measure $M([0,t])$ is continuous and fails to have local density. In other words, the measure is not differentiable and is thus, *singular*. It is precisely this point that underlies the concept of multifractal distribution discussed in §2.1.7.

As the underlying measure giving rise to fluctuations in ξ' is singular, we define the singularity exponent α which relates the measure contained in a box of size τ with the scale of measurement through the relation:

$$\frac{\langle \delta\xi'_\tau \rangle}{\langle \xi' \rangle} \sim \left(\frac{\tau}{\tau_\ell}\right)^{\alpha-1}. \tag{5.22}$$

Here, $\langle \delta\xi'_\tau \rangle$ denotes the measure which is taken to be the moment of the increment in fluctuations, $\delta\xi'_\tau = \xi'(t+\tau) - \xi'(t)$, contained in the interval $[0,\tau]$.

The equation above is akin to performing a box-counting and determining the integrated measure contained in the box size. The singularity exponent α is the local singularity strength, which depends on the location of the box and its size. Equation 5.22 emphasizes that different values of α (for all $\alpha < 1$) are associated with regions of different singularity strengths. The smaller the value of α is, the larger is the strength of the fluctuations. In contrast, for $\alpha > 1$, the fluctuations are from regular regions where the measure is differentiable.

Since α is indicative of the local singularity strength and varies depending upon τ, the measure is evidently then distributed on an infinity of iso-α interfaces which are intertwined together. Thus, the number of boxes N of size τ which have the exponent α within a band of α and $\alpha + d\alpha$ is given by (Halsey *et al.*, 1986):

$$N(\alpha)d\alpha \sim \rho(\alpha)\left(\frac{\tau}{\tau_\ell}\right)^{-f(\alpha)} d\alpha. \tag{5.23}$$

Here, the scaling exponent $f(\alpha)$ can be interpreted as the fractal dimension associated with counting the number of boxes covering an iso-α set for $\alpha > 0$ and $f(\alpha) \geq 0$. The measures $f(\alpha) - \alpha$ and $D_q - q$ are analogous to each other. The need for the multifractal description using the relation between $f(\alpha) - \alpha$ allows us to understand the nature of the underlying multiplicative process, which leads to the singular distribution of the observed measure.

The measure $f(\alpha) - \alpha$ and $D_q - q$ are associated with each other by direct or inverse Legendre transform. This is obtained as (Halsey *et al.*, 1986):

$$f\left[\alpha(q)\right] = q\alpha(q) - (q-1)D_q, \tag{5.24}$$

$$\alpha(q) = \frac{d}{dq}\left[(q-1)D_q\right], \tag{5.25}$$

given that the following conditions are followed: $f'(\alpha) < 0$ and $\partial f(\alpha)/\partial\alpha = q$. Thus,

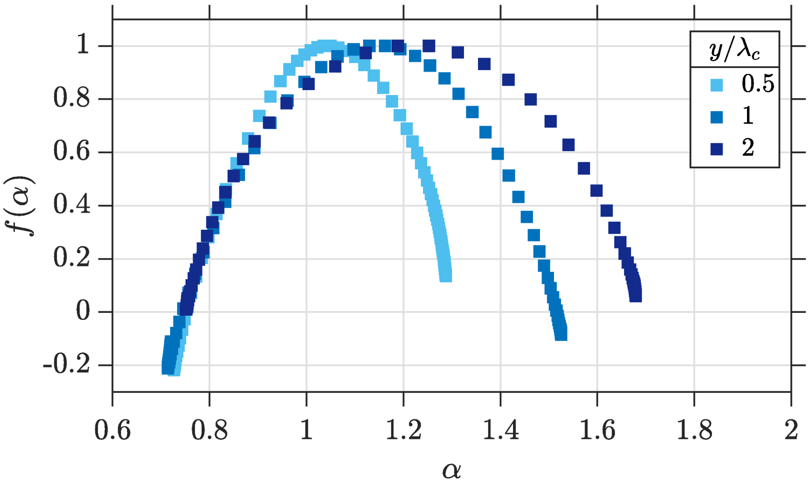

Figure 5.10: Multifractal spectrum $f(\alpha)$ as a function of the singularity spectrum (α) obtained from the Legendre transform of D_q and q.

given the $D_q - q$ curve, we can use the inverse Legendre transform to obtain $f(\alpha) - \alpha$. Thus, we use a central differencing scheme to obtain the derivative of $(q-1)D_q$ with respect to q. Using the Legendre transform relation above, we obtain α and $f(\alpha)$.

We plot the multifractal spectrum $f(\alpha)$ as a function of the singularity exponent in Fig. 5.10 for the fluctuations measured at the indicated y/λ_c locations for flame F1. First, we observe a number of salient features from the multifractal spectra. We note that the spectra for each case have a maximum ($\partial f/\partial\alpha = 0$) at $\alpha > 1$ where $f(\alpha) = 1$. The value $f(\alpha) = 1$ implies that the fluctuations in ξ' are supported on a set whose dimension is unity, which is the embedding space itself. Second, from Eq. 5.22, we note that $0 < \alpha < 1$ indicates singularities. Thus, the part of $f(\alpha) - \alpha$ spectra for $0 < \alpha < 1$ follows from the singularity in the fluctuations. The value α_{min} specifies the largest singularities in the dataset. Further, the singularities are distributed on a fractal set whose fractal dimension is given by $f(1)$, which is less than the dimension of the embedding space for all three cases. In contrast, $\alpha > 1$ signifies the contribution to the

Condition	$y/\lambda_c = 0.5$		$y/\lambda_c = 2$	
	α	$f(\alpha)$	α	$f(\alpha)$
α_{min}	0.73	-0.18	0.75	-0.03
α_{max}	1.40	0.092	1.73	-0.03
$w = \alpha_{\text{max}} - \alpha_{\text{min}}$	0.67	-	0.98	-
$\partial f/\partial\alpha = 0$	1.12	1.00	1.23	1.00
$f(1)$	1.00	0.89	1	0.85
$\partial f(\alpha)/\partial\alpha = 1$	1.05	0.97	1.04	0.92

Table 5.3: Comparison of the properties of the multifractal $f(\alpha)-\alpha$ spectrum for flame F1 at two locations.

spectrum from fluctuations that are non-singular, regular, and differentiable.

Finally, the special point where $\partial f(\alpha)/\partial\alpha = 1$ corresponds to the measure-theoretic support of the fluctuations. This point indicates the set of fluctuations that are quite prevalent. These fluctuations are weakly singular as f is quite close to unity. Thus, it follows that there are strong fluctuations with singularity strength α_{min} which are rarer. The majority of the fluctuations, however, correspond to weakly singular regions. For the fluctuations measured at the three locations, the fluctuations measured closest to the flame holder are the most singular as α_{min} is the lowest for the case closest to the flame holder. The fluctuations measured at larger distances contain more regular regions as the spectrum spans a greater region for $\alpha > 1$.

Next, we compare the multifractal behavior of the fluctuations measured for the two flames at the same location. We plot the $f(\alpha)-\alpha$ spectra for the cases in Fig. 5.11. The properties of the two spectra are depicted in Table 5.4. Much of our previous discussion remains valid for the observed spectra. We notice that the most singular regions have α_{min} values which are very similar. Further, fluctuations arising from regular regions

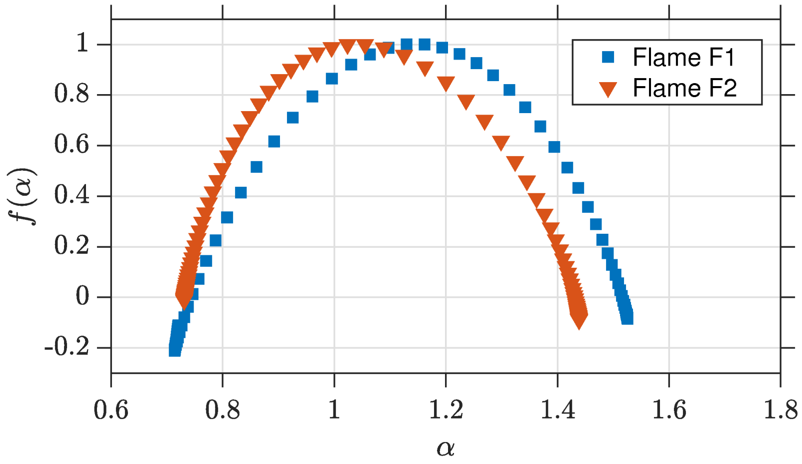

Figure 5.11: Comparison of multifractal spectrum $f(\alpha)$ as a function of the singularity spectrum (α) obtained from the Legendre transform of D_q and q for flame F1 and F2.

Condition	Flame F1		Flame F2	
	α	$f(\alpha)$	α	$f(\alpha)$
α_{min}	0.75	-0.03	0.73	-0.01
α_{max}	1.73	-0.03	1.44	-0.09
$w = \alpha_{\text{max}} - \alpha_{\text{min}}$	0.98	-	0.71	-
$\partial f/\partial\alpha = 0$	1.23	1.00	1.04	1.00
$f(1)$	1.00	0.85	1.00	0.98
$\partial f(\alpha)/\partial\alpha = 1$	1.04	0.92	0.97	0.97

Table 5.4: Comparison of the properties of the multifractal $f(\alpha)-\alpha$ spectrum measured at $y/\lambda_c = 2$ for flames F1 and F2.

are much more pronounced for the Flame F1 as the majority of the spectra lies in the range $\alpha > 1$.

Thus, in this section, we have depicted that intermittent fluctuations arise as a result of the underlying multiplicative process, which leads to a singular distribution of measures. We then showed that the quantification of the underlying singularities explains various features of the small-scale intermittency.

5.5 INTERIM SUMMARY

In this chapter, we reveal the presence of self-similarity and intermittency in the small-scale fluctuations of a turbulent premixed flame. From temporal measurements of the position of a methane-air V-flame, we find that the power spectrum has as a power-law dependence on frequency, over an intermediate range of time scales, with a scaling exponent close to -2. This exponent is explained as a consequence of the flame fluctuating passively in response to perturbations from inertial-range turbulent eddies.

We quantify the large-scale intermittency of the flame fluctuations, which arises from the general unsteadiness in the flow and leads to large variations in the flatness factor of the PDF of flame fluctuations at large downstream distances. Next, we calculate the moments of the temporal structure-function and find that they scale anomalously – a signature of small-scale intermittency – showing that higher frequency fluctuations have increasingly non-Gaussian, wide-tailed probability distributions. The anomalous scaling is confirmed by noting the deviation of the empirically determined scaling exponents from the exponents obtained from Kolmogorov's limit. Finally, we depicted that the intermittent fluctuations are much better represented through the multifractal spectrum.

Our results have important implications for modelling turbulent premixed flames while also showing how a flame reflects the characteristic features of the turbulent carrier flow. In the next chapter, we will analytically derive the effect of intermittent turbulent kinetic energy dissipation on the fractal dimension of turbulent flames.

CHAPTER 6

FRACTAL DIMENSION OF PREMIXED FLAMES IN INTERMITTENT TURBULENCE

In this chapter, we discuss the effects of small-scale intermittency in turbulent flows on the dynamics of turbulent premixed flames. We begin by introducing the formalisms of fractals and their relation to measures and embedding space. We then discuss the application of concepts of fractals in general turbulent flows and in turbulent premixed flames. We then derive the fractal dimension for thickened premixed flames with low Da values. We analytically show that the fractal dimension applicable for low Da flames needs to be appropriately corrected as small-scale intermittency leads to fluctuations in the inner cut-off of turbulent flames. We derive two corrections and discuss their implications.

6.1 FRACTALS, MEASURES AND DIMENSIONS

Let us begin with an explanation of fractal objects. Fractal objects are complex objects made up of reduced-size copies of the whole (Mandelbrot, 1982). We can measure the length, area, or volume of such objects by covering the entire object with square boxes of side r. The total number of boxes (N) required to cover such a surface obeys the power-law scaling (Mandelbrot, 1982):

$$N \sim \left(\frac{r}{r_o}\right)^{-\mathbb{D}}, \tag{6.1}$$

The content of this chapter have been published in **A. Roy** & R. I. Sujith (2021) Fractal dimension of premixed flames in intermittent turbulence. *Combustion and Flame*, **226**, 412-418.

where r_o is an outer cut-off scale and $\mathbb{D}$ is referred to as the fractal dimension of the complex object. Equation (6.1) can be verified by considering a square of size r_o. If we use smaller squares $r = r_o/2$ to cover the larger square, we will need $N = 4 = (r/r_o)^{-\mathbb{D}}$. It is evident that $\mathbb{D} = 2$ would be required to fulfil the equality. Thus, the concept of fractal dimension is a generalization of the usual Euclidean dimension. Since the square spans $\mathbb{R}^2$ space, we obtained $\mathbb{D} = 2$. Thus, we can easily extend this concept for quantifying the length, area, and volume of complex shapes and objects. A property of fractal objects which is quite important is that the fractal dimension ($\mathbb{D}$) is greater than or equal to the dimension of the embedding space $\mathbb{R}^d$, i.e., $\mathbb{D} \geq d$. For the example of the simple square, we considered, the fractal dimension is equal to the embedding dimension.

In general, one is interested in determining some measure associated with the complex fractal object. This is precisely what we tried to do when measuring the number of boxes required to cover the square. Equation (6.1) implies that the number of boxes, or more generally, the measure, changes with the measurement scale. An intuitive way of understanding this is by considering the challenge associated with measuring the length of the coast of a country. At the level of satellite imagery, the length of the coast would be quite small as smaller relief in the feature would be hidden in the image. However, as the resolution is increased, more features would be revealed, and the length of the coast would increase. This is exactly what is engendered in Eqn. (6.1), and is also evident from our earlier discussion on the distribution of multiplicative processes in §2.1.6. Another important aspect is the concept of cut-off in the range of fractal scaling. For computer-generated fractals, Eqn. (6.1) can be measured to arbitrarily large resolutions.

However, for practical objects, there is often an inner and outer cut-off beyond which the measure of an object no longer scales as a fractal. We discuss more about the inner and outer cut-off in §6.4.

In the case of surfaces in turbulent flows, the flux of important physical quantities such as species, mass, momentum, etc., depending on the length, area, or volume of these complex fluctuating surfaces. We can therefore find the area of a complex surface embedded in $\mathbb{R}^2$ space by multiplying the area of the smallest box used for counting. Thus, the total area is expressed as:

$$A_T = r^2 N = r_o^2 \left(\frac{r}{r_o}\right)^{2-\mathbb{D}}. \tag{6.2}$$

Here, the reference area is indicated by $A_0 = r_o^2$. We observe that the exponent in Eqn. 6.2 provides information of the dimension of the embedding space through the numerical value of 2 and fractal dimension $\mathbb{D}$. The difference between the embedding dimension and fractal dimension is referred to as co-dimension (Mandelbrot, 1982). The co-dimension quantifies the intersection of the fractal object of dimension $\mathbb{D}$ with the embedding space $\mathbb{R}^d$ of dimension d.

We utilize these concepts extensively for measuring the fractal dimension of turbulent flames in the next sections.

6.2 FRACTALS IN CLASSICAL TURBULENT FLOWS

The complex, intertwined motion of turbulent flows has led to the widespread use of fractals and related concepts to understand the phenomenology of turbulence (Mandelbrot, 1982; Sreenivasan, 1991*a*). Most notably, scalar iso-surfaces in homogeneous, isotropic turbulence have been shown to have fractal behavior where the area is independent of the measurement scale and depends only upon the scaling exponent, known as the fractal dimension (Sreenivasan, 1991*a*). These predictions have been tested and validated in controlled experiments (Sreenivasan and Meneveau, 1986; Sreenivasan *et al.*, 1989). The most renowned example of the fractal behavior of scalar surfaces in turbulence is the fractal dimension of clouds which was shown to be $\mathbb{D} = 7/3$ by Lovejoy (1982). Later studies predicted the limit of $\mathbb{D} = 7/3$ through considerations of particle-pair diffusion (Hentschel and Procaccia, 1984) and scaling arguments related to the estimate of flux of passive scalar in entraining turbulent flows with sharp interfaces separating the turbulent from quiescent regions(Sreenivasan *et al.*, 1989).

For scalar surfaces in well-developed turbulence, Constantin *et al.* (1991) derived the estimate of the area of an iso-scalar surface contained within a ball (of radius r) using the co-area formula of geometric measure theory. They showed that for scales below the inner cut-off, the scalar diffusion dominates the advection and smears out the scalar gradient, leading to a smooth area. Consequently, the iso-surface only appears as a fractal above some inner cut-off dependent on the local Reynolds number. The fractal dimension was then shown to be $\mathbb{D} = 8/3$ after assuming that the velocity estimate follows Kolmogorov's phenomenology. Further, the fractal dimension of $\mathbb{D} = 8/3$ was also suggested by Mandelbrot (1975) for scalars in Gaussian random fields and Kolmogorov spectra.

Small-scale intermittency plays a crucial role in determining the dynamics of passive scalar surfaces. As explained, small-scale intermittency refers to the increasing non-Gaussian behavior in dissipation quantities when one approaches scales close to Kolmogorov's length scale. The small-scale intermittency is tied to the multifractality in the dissipation field, leading to extreme-value fluctuations in dissipation quantities, localized non-uniformly and intermittently throughout space (Sreenivasan and Antonia, 1997). Sreenivasan *et al.* (1989) showed that intermittent dissipation of turbulent kinetic energy significantly affects the lower cut-off estimate and leads to corrections to the estimate of the fractal dimension of scalar iso-surfaces in entraining flows. The correction was a result of the fact that for spatially intermittent dissipation, the moment of dissipation taken over a box size of a given scale depends on the scale itself. Thus, the inner cut-off defined on the averaged dissipation will vary if the scale over which the averaging is performed depends on the measurement scale. Hentschel and Procaccia (1983) and Halsey *et al.* (1986) introduced the multifractal formalism for describing intermittent fields, which was then adopted by Meneveau and Sreenivasan (1990) for characterizing the intermittent nature of dissipation. They presented a more refined analysis by explicitly performing an integration over boxes along the interface and derived the correction to the fractal dimension.

6.3 FRACTALS IN PREMIXED TURBULENT FLAMES

A closely related problem to the statistical description of scalar surfaces in turbulence is the description of propagating interfaces in turbulence. Propagating interfaces are frequently encountered in the study of premixed combustion and are of practical importance. In the limit where flow time scales are much larger compared to combustion time scales (i.e., Damköhler number, $Da = \tau_\eta/\tau_F = (\eta/\delta_F)^2 >> 1$), one can unambiguously define a flame surface by considering an iso-temperature or iso-concentration surface (Borghi, 1985; Peters, 2001). In other words, internal flame processes are not affected by turbulent fluctuations, and the effect of turbulence is restricted only to wrinkles on the flame surface. Such flames are referred to as corrugated flamelets (see §2.2.1). Here, τ_η indicates the time scale with respect to a Kolmogorov scale (η) vortex, and τ_F is the flame time scale, and δ_F is the laminar flame thickness. In contrast, for low Da flames, a range of eddies have turnover times comparable to the reaction time scale. These eddies can penetrate and disrupt the preheat zone. The scalar transport (heat and reactants) are enhanced due to turbulence, leading to a thickening of the preheat zone (Law, 2010). These flames are appropriately referred to as thickened flames. In the present chapter, we consider flames in the thickened flame limit ($Da \simeq 0.1 - 10$) where the turbulence can only affect the preheat zone and not the reaction zone. Further, we consider high turbulence levels, such that cellular instabilities do not cause any cut-off in the fractal scaling range (Chaudhuri *et al.*, 2011).

Early studies on the application of fractals in combustion considered the limit of

$Da >> 1$ and assumed the flame surface to be a passive interface with a fractal dimension 7/3 (Gouldin, 1987; Kerstein, 1988). However, Kerstein (Kerstein, 1988) showed that the similarity in the estimate of fractal dimension to that of passive scalars in turbulence is only coincidental. It was shown that a dynamical balance between wrinkling due to turbulent convection and smoothing effects due to flame propagation is established at all length scales in the scaling range. The fractal dimension of 7/3 was recovered naturally by considering the balance between characteristic burning time governed by turbulent burning velocity and eddy turnover time. Since then, the fractal dimension of $\mathbb{D} = 7/3$ has been well-validated in experiments since then (Mantzaras *et al.*, 1989; North and Santavicca, 1990; Thiesset *et al.*, 2016), although the exact value has been noted to depend on the measurement approach, as summarized in Gülder *et al.* (2000). Later, Kerstein (1991) considered the effect of intermittency in turbulent kinetic energy dissipation and arrived at a corrected value of the fractal dimension, which was quite similar to the correction obtained by Meneveau and Sreenivasan (1990). However, the two approaches were quite different and implied the possibility of geometrical equivalence of different surfaces in turbulent flows.

Application of concepts of fractals in the description of turbulent flames, however, has remained confined to combustion in the corrugated flamelet regime ($Da >> 1$). This has led to the development of various combustion models (Gouldin, 1987; Gouldin *et al.*, 1989; Mantzaras *et al.*, 1989; Gülder, 1991; Gülder and Smallwood, 1995; North and Santavicca, 1990; Gülder *et al.*, 2000). In particular, researchers have been quite successful in obtaining closure for the unresolved flame area in Large Eddy Simulation (LES) models (Lindstedt and Vaos, 1999; Knikker *et al.*, 2002; Charlette *et al.*, 2002;

Fureby, 2005; Hawkes *et al.*, 2012). However, the success has not translated nearly as well while modeling low Da flames, with some exception (Chatakonda *et al.*, 2010; Hawkes *et al.*, 2012; Keppeler *et al.*, 2014). As mentioned earlier, for low Da flames, a range of turbulent eddies can penetrate and disrupt the preheat zone. Nonetheless, the fractal framework is still applicable as the burning rate of the flame depends on the flux of fuel across the iso-concentration surface, which is being entrained by the eddies in the preheat zone, provided that there are no local extinctions. Thus, even for the case of low Da flames, one can define the flame surface as an iso-surface of progress variable based on fuel mass fraction and extract statistical properties of the fractal iso-surface (Chatakonda *et al.*, 2013). Thus, the fractal properties of low Da flame surfaces are expected to differ from that of corrugated flamelets (Chatakonda *et al.*, 2010, 2013).

For low Da thickened flames ($Da = 0.44 - 4.22$), Chatakonda *et al.* (2013) considered a balance between flame stretch rates at the smallest scales of wrinkling. A balance of the tangential flame strain and the effects of curvature and flame propagation leads to a modified inner cut-off scale known as the Obhukhov-Corrsin length scale (η_c). The effect of this modified inner cut-off scale then leads to a modified prediction in the fractal dimension of low Da flames, which is equal to $\mathbb{D} = 8/3$. This prediction was then verified through direct numerical simulation of hydrogen-air flame and thermonuclear flames in type 1a supernovae (Chatakonda *et al.*, 2013).

6.4 ESTIMATE OF FRACTAL DIMENSION OF THICKENED FLAMES

We define the flame surface as an iso-concentration surface of a progress variable based on fuel mass fraction. This allows us to define a flame surface even for low Da flames where turbulent eddies penetrate the preheat zone, as the net burning rate depends upon the flux of reactants across the fuel iso-concentration surface. We assume that the flame is devoid of any local extinction. We consider a flame surface, defined in this manner, propagating freely into a volume containing a combustible mixture where the flow is homogeneous and isotropic. The flame surface divides the region of reactants and products. We focus on the wrinkles on the flame surface induced by turbulent fluctuations in the inertial range such that the flame does not experience any anisotropic effects due to the directional nature of flame propagation and mean shear in the flow. Then, it follows that the fluctuations on the flame surface are locally isotropic, and the wrinkles follow dynamic self-similarity.

We assume that the Reynolds number is sufficiently high such that there is a significant scale separation. The outer cut-off can then be conveniently defined as the integral length scale ℓ, as done previously (Gouldin, 1987; Gülder, 1991). Thus, the true area of the flame surface, A_T, can be written from Eqn. (6.2) as

$$A_T(r) = A_0 \left(\frac{r}{\ell}\right)^{2-\mathbb{D}}, \tag{6.3}$$

where $A_0 = \ell^2$ and $\mathbb{D}$ is the fractal dimension of the flame. In order to get the true area of the flame correctly, it is important to estimate the inner cut-off below which the flame surface is no longer a fractal. Here, we present the formulation given in Chatakonda *et al.* (2013) for determining the inner cut-off. A more detailed derivation is given in Hawkes *et al.* (2012).

For a stable and well-maintained flame surface in a turbulent flow field, turbulence-induced tangential flame strain at the lowest length scales are balanced by the effects of curvature and flame propagation (Hawkes *et al.*, 2012). The tangential flame strain rate due to an eddy of size r is $a_T = u'/r$, where u' is the velocity characteristic of eddies of size r. Further, following Kolmogorov's phenomenology (Eqn. 2.17), we have $u' \sim (\langle\varepsilon\rangle r)^{1/3}$, where $\langle\varepsilon\rangle$ is the rate of turbulent kinetic energy dissipation averaged over the volume ℓ^3. Thus, the tangential flame strain rate can be re-written as $a_T \sim (\langle\varepsilon\rangle r)^{1/3}/r$.

The effect of flame propagation in balancing the tangential flame stretch is negligible for low Da flames, and is well-supported by theory (Peters, 1999) and DNS results (Hawkes and Chen, 2005). In such a case, the equilibrium on the flame surface is maintained by the effect of curvature alone (Hawkes *et al.*, 2012). Curvature is quantified by the divergence of the surface normal $\nabla \cdot \boldsymbol{n}$. The balance between the curvature and the tangential flame strain is, thus, $\mathcal{D}\langle(\nabla \cdot \boldsymbol{n})^2\rangle_s \sim \langle a_T\rangle_s$, where $\mathcal{D}$ is the diffusivity and $\langle\rangle_s$ indicates average weighted by the surface area of the flame surface (Chatakonda *et al.*, 2013). The balance then leads to

$$\langle(\nabla \cdot \boldsymbol{n})^2\rangle_s \sim \frac{1}{r^2}\frac{r^2}{\mathcal{D}}\frac{(\varepsilon r)^{1/3}}{r}. \tag{6.4}$$

We can then define the Obhukhov-Corrsin length scale (η_c) based on the balance above as (Chatakonda *et al.*, 2013)

$$\eta_c \sim \left(\mathcal{D}^3/\langle\varepsilon\rangle\right)^{1/4} \sim Sc^{-3/4}\eta, \tag{6.5}$$

where the Schmidt number (Sc) is defined as the ratio of the kinematic viscosity (ν) and the diffusivity ($\mathcal{D}$), i.e., $Sc = \nu/\mathcal{D}$. Note that η_c in Eqn. (6.5) was introduce in the context of scalar turbulence (Eqn. 2.36). Here, η is the Kolmogorov length scale and is related to the kinematic viscosity and mean turbulent kinetic energy dissipation as $\eta = (\nu^3/\langle\varepsilon\rangle)^{1/4}$. For premixed flames, Sc is generally less than 1, such that we get the following hierarchy of spatial scales: $\eta < \eta_c < r < \ell$.

We note that the inner cut-off scale (η_c) makes physical sense if we consider an advection-diffusion balance at the inner cut-off. The scalar evolution is governed by the advection-diffusion equation (Eqn. 2.34), where diffusion of the scalar competes with advection of scalar for Peclet number $Pe \sim u'r/\mathcal{D} \sim 1$. For $Sc < 1$ or $\nu < \mathcal{D}$, diffusion of the scalar is more effective than the diffusion by vorticity. Consequently, the scalar gradient induced by advecting eddies below the inner cut-off will be smoothed by diffusion, leading to a smooth surface. The surface will then appear fractal only above an inner cut-off where the gradients induced by the eddies dominate diffusive effects, leading to a fractal surface. Thus, η_c demarcates the length scale below which the surface appears smooth and above which the surface appears fractal.

We assume local isotropy such that KOC phenomenology (cf. §2.1.8) is followed. Thus, at the inner cut-off ($r \sim \eta_c$), the scalar gradient is given by $\delta C_{\eta_c}/\eta_c$, where δC_{η_c} is the difference in scalar concentration associated with length scale η_c. Thus, according to

KOC phenomenology (cf. Eqn. 2.40), we have

$$\delta C_{\eta_c} \sim (\eta_c/\ell)^{1/3} C. \tag{6.6}$$

where, C is characteristic scalar fluctuation at the integral scale.

Thus, the total scalar flux across the flame interface is proportional to the total area (A_T), the diffusivity ($\mathcal{D}$), and the scalar gradient ($\delta c_{\eta_c}/\eta_c$), which is

$$F \sim A_T \mathcal{D}\big(\delta C_{\eta_c}/\eta_c\big) \tag{6.7}$$

$$\sim A_0 \mathcal{D} C \big(\eta_c/\ell\big)^{2-\mathbb{D}} \big(\eta_c/\ell\big)^{1/3} (1/\eta_c) \tag{6.8}$$

Using the definition of η_c from Eqn. (6.5) and the scaling relation in the universal inertial subrange, $\eta/\ell \sim (Re)^{-3/4}$ where, $Re = u'\ell/\nu$, we obtain:

$$F \sim A_0 c u' (Sc)^{3/4(\mathbb{D}-8/3)} (Re)^{3/4(\mathbb{D}-8/3)} \sim A_0 c u' (Pe)^{3/4(\mathbb{D}-8/3)}. \tag{6.9}$$

Thus, we express the scalar flux in terms of only the Peclet number ($Pe = ScRe = u'\ell/\mathcal{D}$). In the above estimate of scalar flux, we assumed that the gradient follows from a cascade of the scalar fluctuations, which is halted as the scales approach $r \sim \eta_c$. Thus, the scalar cascade, by analogy with the cascade of the accompanying turbulent eddies, is expected to be independent of the details of diffusivity ($\mathcal{D}$) and depends only on the scalar properties associated with the largest scales. Consequently, the scalar flux determined in Eqn. (6.9) must be independent of the Peclet number. Thus, for Pe independence, the fractal dimension must be $\mathbb{D} = 8/3 = 2.67$.

A clarification regarding the physical mechanism leading to the two limits of fractal dimension – $\mathbb{D} = 7/3$ and $8/3$ – for both the reacting and non-reacting flow is in order. The fractal dimension is $\mathbb{D} = 7/3$ for iso-surfaces in entraining flows (Sreenivasan *et al.*, 1989) and high Da flamelet combustion (Gouldin, 1987; Kerstein, 1988). In this case, the scalar gradient depends only on the difference in the concentration value across the iso-surface in entraining flow and the thin reaction zone separating the reactants and products in flamlets. In other words, turbulence only facilitates scalar flux by inducing fractal characteristics to the flame interface, thereby increasing the total area of the interface according to Eqn. (6.3), without affecting the scalar gradient and the transport process. We re-emphasize Kerstein's viewpoint (Kerstein, 1988) that the value of $\mathbb{D} = 7/3$ for flamelet combustion, although the same as the dimension of iso-scalar surfaces in entraining non-reacting flows, is purely coincidental and should not be taken as an equivalence between them.

In contrast, the fractal dimension is $\mathbb{D} = 8/3$ for iso-scalar surfaces in well-developed turbulence (Constantin *et al.*, 1991) and low Da flames (Chatakonda *et al.*, 2013). In both of these surfaces, the inner cut-off plays a very important role. The inner cut-off is determined by the scale at which scalar advection due to turbulent eddies balances the scalar diffusion. Below this inner cut-off, diffusion smears out any fluctuations on the interface, making it smooth and regular. Thus, the interface only appears a fractal above this inner cut-off. Further, we derive the net scalar flux (Eqn. 6.8) by considering that the characteristic scalar difference (δc_{η_c}) is dependent on the inner cut-off through the relation: $\delta c_{\eta_c} \sim \eta_c^{1/3}$. The scalar gradient then scales as: $\delta c_{\eta_c}/\eta_c \sim \eta_c^{-2/3}$. Thus, turbulence not only increases the surface area of the flame iso-surface through the fractal scaling but also aids the transport of reactants by actively altering the scalar gradients. Thus, the increase in the estimate of $\mathbb{D}$ for low Da flames is reflective of the higher degree of flame-turbulence interaction as a result of enhanced transport in the preheat zone.

6.5 INFLUENCE OF INTERMITTENCY ON THE FRACTAL DIMENSION OF THE FLAME

6.5.1 A coarse-grained estimate based on the moments of the intermittent dissipation field

So far, we have considered an averaged dissipation $\langle\varepsilon\rangle$ over volume ℓ^3. The volume-averaged dissipation controls the inner cut-off scales η and η_c. However, the formulation here also suffers from the same setbacks that Kolmogorov (1941*b*,*a*) suffered from, and that has to do with the averaging procedure. Any spottiness in the large scales of the flow would affect the local cascade of energy flux, which, when averaged, would lead to departure from universal statistics (cf. §2.1.4). Instead, a locally averaged dissipation $\langle\varepsilon_{\eta_c}\rangle$ over volume η_c^3 should be considered (cf. Eqn. 2.21). This locally averaged dissipation $\langle\varepsilon_{\eta_c}\rangle$ varies strongly in space. Fluctuations in dissipation will lead to fluctuations in the inner cut-off η_c through Eqn. (6.5). Thus, we can obtain the correction by spatially averaging the flux after replacing averaged η and η_c with their corresponding locally fluctuating value. The fluctuations in the inner cut-off will also affect the scalar difference and the gradients.

The local dissipation can be related to the averaged dissipation by generalizing the empirical power-law relation given in Eqn. (2.24). We re-write this in terms of general order q and generalized dimension D_q, such that we have (Sreenivasan *et al.*, 1989):

$$\langle \varepsilon_{\eta_c}^q \rangle = \langle \varepsilon \rangle^q (\eta_c/\ell)^{(q-1)(D_q-1)}, \tag{6.10}$$

where, D_q indicates the generalized dimension of order q where q is any real number and $\langle \varepsilon \rangle$ is the averaged dissipation in box of size ℓ^3. For $q = 2$, we get the variance of dissipation: $\langle \varepsilon_{\eta_c}^2 \rangle = \langle \varepsilon \rangle^2 (\eta_c/\ell)^{-\mu}$, where $\mu = 1 - D_2$ is the well-known intermittency exponent expressed in Eqn. (2.24).

We note that Eqn. (6.10) is a restatement of the fact that any general q order moment of intermittent quantity depends upon the scale itself through a power-law relation characterized by the scaling exponent $(q-1)D_q$. The moment order q is used to focus on fluctuations associated with a given scale r. For $q > 0$, the major contributions on the left-hand side of Eqn. (6.10) are from local maxima in ε_r, while for $q < 0$, contributions are from fluctuations of smaller intensities.

We are interested in measuring the flux across the interface allowing for the variability in quantities which are defined on the value of dissipation ε_r such as η and η_c. Thus, instead of calculating the flux based on η and η_c defined by average dissipation rate $\langle \varepsilon \rangle$, we measure the spatial average of flux based on η and η_c defined by the unaveraged dissipation rate ε_r. This is essentially equivalent to replacing $\langle \varepsilon \rangle^{1/4}$ with $\langle \varepsilon^{1/4} \rangle$ in the defintion of η and η_c. Thus, we replace $q = 1/4$ in Eqn. (6.10) and find that:

$$\langle \varepsilon^{1/4} \rangle \sim \langle \varepsilon_{\eta_c}^{1/4} \rangle = \langle \varepsilon \rangle^{1/4} (\eta_c/\ell)^{3/4(1-D_{1/4})}. \tag{6.11}$$

Further, we can re-write Eqn. (6.5) as:

$$\eta_c \sim (\mathcal{D}^3/\varepsilon_{\eta_c})^{1/4}. \tag{6.12}$$

Substituting Eqn. (6.11) in Eqn.(6.12), we find:

$$\frac{\eta_c}{\ell} \sim \frac{1}{\ell}\left(\frac{\mathcal{D}^3}{\varepsilon_{\eta_c}}\right)^{1/4} \sim (ScRe)^X, \tag{6.13}$$

where, $X = -(3/4)/\big[1 + 3/4(1 - D_{1/4})\big]$. Substituting Eqn. (6.13) in Eqn. (6.5) and carrying out the algebra, it is straightforward to see that the flux becomes:

$$F \sim A_0 c u'(ScRe)^Y,$$

where,

$$Y = \frac{3/4\big[\mathbb{D} - 8/3 - 3/4\big(1 - D_{1/4}\big)\big]}{1 + 3/4(1 - D_{1/4})}.$$

The Peclet number ($Pe = ScRe$) independence stipulates that $B = 0$, from which we obtain:

$$\mathbb{D} = \frac{8}{3} + \frac{3}{4}\big(1 - D_{1/4}\big). \tag{6.14}$$

Equation (6.14) makes up our first result. We emphasize that although the fluctuations in the dissipation rate are quite strong, the inner cut-off scale has a quarter power dependence on the dissipation rate so that the strong variability in dissipation rate does not exactly translate to comparable fluctuations in the cut-off scale. Hence, we expect the corrections to be small.

6.5.2 A fine-scaled estimate based on the multifractal formalism

As mentioned above, the intermittent nature of dissipation leads to fluctuations in the inner cut-off η_c (Eqn. 6.12). Intermittent quantities are conveniently analyzed through multifractal formalism, and we adopt the same in this section.

To find the corrections, we find the total flux by integrating boxes along the flame interface in the manner detailed in Meneveau and Sreenivasan (1990). We assume that the flame is contained in a domain of size ℓ^3. We cover the entire domain in cubic boxes of size η_c^i, which is the inner cut-off scale for our problem. Thus, the total flux is due to the sum of contributions of each of these boxes along the entire interface. The contributions of each box again depends on the area of the element $((\eta_c^i)^2)$, the diffusivity ($\mathcal{D}$), and the scalar gradient $(\delta C_{\eta_c}/\eta_c^i)$. Thus, the total flux after substituting the appropriate scalings associated with the gradient becomes:

$$F \sim \sum_i \eta_c^i \mathcal{D} \delta C_{\eta_c}^i \sim c u' \ell^2 (ScRe)^{-1} \sum_i (\eta_c^i/\ell)^{4/3}. \tag{6.15}$$

Locally, for a domain of length scale η_c^i, the dissipation depends on the local singularity strength α_i through the relation (Sreenivasan, 1991*a*):

$$\varepsilon_{\eta_c} \sim \langle \varepsilon \rangle \left(\frac{\eta_c^i}{\ell} \right)^{\alpha_i - 3}. \tag{6.16}$$

The value of α_i quantifies the strength of singularity in the dissipation field. For values of $\alpha_i < 3$, $\eta_c \to 0$ leads to $\varepsilon_{\eta_c} \to \infty$, implying that smaller values of α_i correspond to stronger peaks in ε_{η_c}. In contrast, $\alpha_i > 3$ corresponds to regular region with smooth variation in ε_{η_c}. We can then express the inner cut-off η_c^i in terms of singularity exponent α_i alone by substituting Eqn. (6.16) into Eqn. (6.12) to obtain:

$$\eta_c^i/\ell \sim \left(\frac{\eta}{\ell}\right)^{4/(\alpha_i+1)} (Sc)^{-3/(\alpha_i+1)}. \tag{6.17}$$

Now, we calculate the number of cubic boxes of size η_c^i having local singularity exponent $\alpha = \alpha_i$. The total number of boxes containing singularity exponent α_i in the box ℓ^3 is defined by the scaling relation (cf. Eqn. 2.31):

$$N(\alpha_i) \sim \left(\frac{\eta_c^i}{\ell}\right)^{-f(\alpha_i)}. \tag{6.18}$$

Here, $f(\alpha_i)$ is the distribution of the fractal dimension of each iso-α_i set for $f(\alpha_i) \geq 0$. Interpretation for $f(\alpha_i) < 0$ is more nuanced, and can be found in Mandelbrot (1989). For the present purposes, we can assume that the bound $f(\alpha_i) \geq 0$ holds without any loss in generality. Substituting Eqn. (6.17) in Eqn. (6.18), we obtain

$$N(\alpha_i) \sim \left(\frac{\eta}{\ell}\right)^{-4f(\alpha_i)/(\alpha_i+1)} (Sc)^{3f(\alpha_i)/(\alpha_i+1)}. \tag{6.19}$$

In order to make further progress, we need to determine the total number of boxes of size η_{OC}^i and singularity exponent α_i *only along the flame interface*. Let $\mathcal{S}_1$ and $\mathcal{S}_2$ indicate the set containing the fractal flame element of dimension $\mathbb{D}$ and singularity α_i of dimension $f(\alpha_i)$ in 3-dimensional space $\mathbb{R}^3$, respectively. We are interested in the intersection of the sets $\mathcal{S}_1$ and $\mathcal{S}_2$. Physically, this translates to intersection of the space where dissipation is intermittent and the space of the fractal surface of the flame. The condition of intersection of objects in the embedding space is mathematically expressed in terms of the co-dimension. The co-dimension of $\mathcal{S}_1$ and $\mathcal{S}_2$ in $\mathbb{R}^3$ is $3 - \mathbb{D}$ and $3 - f(\alpha_i)$. The additive property of sets $\mathcal{S}_1$ and $\mathcal{S}_2$ stipulates:

$$\text{co-dim}(\mathcal{S}_1) + \text{co-dim}(\mathcal{S}_2) < \text{dim}(\mathbb{R}^d), \tag{6.20}$$

which is the condition of intersection of sets $\mathcal{S}_1$ and $\mathcal{S}_2$ in a d-dimensional space (Mandelbrot, 1982). Thus, we have:

$$[3 - f(\alpha_i)] + [3 - \mathbb{D}] < 3 \Rightarrow f(\alpha_i) + \mathbb{D} > 3. \tag{6.21}$$

The dimension of the intersection of $\mathcal{S}_1$ and $\mathcal{S}_2$, i.e., the set of singularities α_i *only along the* fractal flame interface, follows from the above equation as: $\mathscr{D} = f(\alpha_i) + \mathbb{D} - 3$. Thus, the total number of boxes where $\alpha = \alpha_i$ along the interface is given by the dimension of the intersection of the sets $\mathcal{S}_1$ and $\mathcal{S}_2$ so that Eqn. (6.19) gets modified to

$$N(\alpha_i) \sim \left(\frac{\eta}{\ell}\right)^{-4\mathscr{D}/(\alpha_i+1)} (Sc)^{3\mathscr{D}/(\alpha_i+1)}. \tag{6.22}$$

Note that we have cast the contribution of each box of size η_c^i to the total flux in terms of the distribution of singularity only along the interface. Thus, the summation in the contribution of all the individual boxes, defined in Eqn. (6.15), can be replaced with an integral over the entire spectrum of singularity exponent α. The flux can then be calculated as

$$F \sim Cu'\ell^2(ScRe)^{-1}\int N(\alpha)(\eta_c(\alpha)/\ell)^{4/3}d\alpha. \tag{6.23}$$

Substituting the expression for $N(\alpha)$ from Eqn. (6.22) and η_c from Eqn. (6.17) in Eqn. (6.23), we obtain

$$F \sim Cu'\ell^2(ScRe)^{-1}\int \left(\frac{\eta}{\ell}Sc^{-3/4}\right)^X d\alpha, \tag{6.24}$$

where, $X = -4(\mathscr{D} - 4/3)/(\alpha + 1) = -4[f(\alpha) - 13/3 + \mathbb{D}]/(\alpha + 1)$. The power law in Eqn. (6.24) is dominated by the smallest exponent in the integrand. Thus, Eqn. (6.24) can be solved using the method of steepest descent in the limit of small $\eta << \ell$. The saddle point is determined from $\partial X/\partial\alpha = 0$, which leads to:

$$\frac{df}{d\alpha} = \frac{f(\alpha) - 13/3 + \mathbb{D}}{\alpha + 1}. \tag{6.25}$$

Now, we know that $q = df/d\alpha$ which relates the order of the generalized dimension q and the singularity specturm $f(\alpha)$. Further, the generalized dimension D_q is related to the $f(\alpha)$ through the following relation (Halsey *et al.*, 1986):

$$D_q = \frac{1}{(q-1)}[q\alpha - f(\alpha)]. \tag{6.26}$$

Now, whenenver Eqn. (6.25) is satisified for a given q, we assign it the value Q such that

$$\frac{df}{d\alpha} = \frac{f(\alpha) - 13/3 + \mathbb{D}}{\alpha + 1} = Q = -X/4. \tag{6.27}$$

From here, we can work out the relation for $f(\alpha)$, which is

$$f(\alpha) = Q(\alpha + 1) + 13/3 - \mathbb{D}. \tag{6.28}$$

The integral in Eqn. (6.24) is evaluated at the saddle point where, in the power of the integrand, we substitute $X = -4Q$. In such a case, the total flux across the flame surface can be re-written, after substituting $\eta/\ell \sim Re^{-3/4}$, as:

$$F \sim Cu'\ell^2 (ScRe)^{-1+3Q}. \tag{6.29}$$

Further, from Eqns. (6.26), (6.27) and (6.28) we get

$$D_Q = \frac{Q\alpha - f(\alpha)}{Q - 1},$$

which after substituting Eqn. (6.28) leads to

$$\mathbb{D} = 13/3 + Q + (Q - 1)D_Q. \tag{6.30}$$

As mentioned earlier, the flux should be independent of the Peclet number ($Pe = ScRe$), which upon enforcing in Eqn. (6.29) we obtain $-1 + 3Q = 0$, which yields $Q = 1/3$. Consequently, we find from Eqn. (6.30) the correction in the fractal dimension of the flame front as:

$$\mathbb{D} = \frac{8}{3} + \frac{2}{3}(3 - D_{1/3}). \tag{6.31}$$

Equation (6.31) makes up the second result of our paper and is a direct result of the fluctuations in the area of low Da flames due to small-scale intermittency.

6.6 DISCUSSION

As mentioned earlier, Kerstein's (Kerstein, 1988) result of $\mathbb{D} = 7/3$ corresponds to the fractal dimension associated with Damköhler's large-scale limit. The dynamics of such flames are dominated by strong propagation effects. The limit $\mathbb{D} = 7/3$ is numerically comparable to the large-scale limit of $\mathbb{D} = 7/3$ in a superlayer of entraining turbulent flow as found by Sreenivasan *et al.* (1989). Later, Kerstein (1991) derived the corrections to the fractal dimension due to dissipation-scale intermittency and observed the same numerical correction as obtained for entraining turbulent flow by Meneveau and Sreenivasan (1990). On the other hand, the limit of $\mathbb{D} = 8/3$ was derived by Chatakonda *et al.* (2013) by accounting for Damköhler's small-scale limit, which is similar to the dimension of the interface due to small-scale fluctuations inside the core of a turbulent jet (Constantin *et al.*, 1991). The equivalence in the value of $\mathbb{D}$ for low Da flames with that seen for an interface in turbulence indicates the passive scalar limit of the flame. The flame dynamics are controlled by the turbulent flux of scalar concentration (reactants, temperature, etc.) across the reaction zone analogous to the transport of passive scalar in fully-developed turbulence.

Equations (6.14) and (6.31), which quantify the effect of dissipation-scale intermittency on the fractal dimension of the interface associated with Damköhler's small-scale limit, make up the main result of this chapter. We arrive at the two results through two key considerations. The first result is a consequence of spatially averaging the scalar flux across the interface after accounting for the variability in the inner cut-off due to dissipation-range intermittency, instead of calculating the average flux by considering an inner cut-off based on the average dissipation rate. The second result follows from a more fine-scale analysis based on multifractal formalism. The multifractal formalism accounts for the underlying multiplicative process, which leads to small-scale intermittency. Thus, we have accounted for either of the two processes which cause small-scale intermittency. The first is related to the coupling between large-scale spottiness of turbulence (cf. §2.1.4) and its effect on the averaging procedure, while the second arises due to the multiplicative cascade process (cf. §S2.1.5-Small-scale intermittency).

The particular form in which the correction to the fractal dimension of low Da flames has been expressed in Eqn. (6.14) and (6.31) allows us to also correlate the fractal dimension with the velocity structure function. We know that the moment of velocity difference ($\Delta \mathbf{v}_r$) between two points separated by distance r follows a power-law of the form (Eqn. 2.22):

$$\langle \delta \boldsymbol{u}_r^p \rangle \sim \langle [\boldsymbol{u}(\boldsymbol{x}+\boldsymbol{r}) - \boldsymbol{v}(\boldsymbol{x})]^p \rangle \sim r^{\zeta_p}, \tag{6.32}$$

where ζ_p is the scaling exponent associated with order p. For homogeneous isotropic turbulence, the scaling exponent is $\zeta_p = p/3$, and follows directly follows from Kolmogorov's work (Kolmogorov, 1941*b*). Intermittent nature of dissipation rate manifest in the scaling exponent deviating from $\zeta_p = p/3$ at $p > 3$. Following Meneveau and Sreenivasan (Meneveau and Sreenivasan, 1987*a*, 1990), we find for intermittent turbulence that the scaling exponent for $p = 1$ is related to the moment exponent through the relation:

$$\zeta = \frac{1}{3} + \frac{2}{3}\left(3 - D_{1/3}\right) \tag{6.33}$$

Comparing this with Eqn. (6.31), we observe that

$$\mathbb{D} = \frac{7}{3} + \zeta. \tag{6.34}$$

Thus, the second correction in Eqn. (6.31) shows that the fractal dimension of low Da flames is also related to the scaling exponent of the velocity structure-function.

Experimentally measuring the multifractal spectrum of turbulent kinetic energy dissipation in turbulent reacting flows is a significant challenge as it involves the determination of two-point velocity and scalar concentration correlations. The generalized dimension D_Q, which appears in Eqs. (6.14) and (6.31), can then only be measured from high fidelity turbulent DNS data.

We believe that the corrections to the value of the fractal dimension of low Da premixed turbulent flame would be relatively small. Nonetheless, the considerations made above are still important. To the best of our knowledge, we did not find any study on turbulent combustion which have measured these dissipation quantities (D_Q, $f(\alpha)$, α, etc.). So, we do not know the exact extent of variation in the estimate of $\mathbb{D}$. The determination of $f(\alpha) - \alpha$ and $D_q - q$ from DNS data appears worthwhile as it has the potential to lead to better closure models for low Da flames used in LES and a better understanding of the effects of dissipation-range intermittency on the flame dynamics.

6.7 INTERIM SUMMARY

In this chapter, we derive corrections to the fractal dimension of premixed flames in the limit of $Da \sim \mathcal{O}(1)$. We consider the flame surface to be defined by an iso-concentration surface based on the progress variable of the fuel mass fraction. For low Da flames, we obtain the so-called Obhukov-Corrsin length scale after considering a dynamical balance on the flame surface at the smallest scales. Upon considering the net flux across the flame surface, we obtain the upper limit for the fractal dimension of low Da flames as $\mathbb{D} = 8/3$. However, such a consideration does not account for the intermittent nature of turbulent kinetic energy dissipation, which leads to strong fluctuations in the dissipation field. Such fluctuations lead to significant variability in the inner cut-off and consequently to the scalar flux and total area of the flame interface. We account for these effects by adopting a coarse-grained approach based on the moments of the dissipation field and a fine-scale analysis through the use of multifractal formalism. We obtain two corrections in the estimate of the fractal dimension of low Da flames (Eqs. 6.14 and 6.31). We show that the correction is intimately tied to the scaling exponent of the velocity structure-function (Eqn. 6.34). Thus, we analytically quantify the effect of intermittent turbulent dissipation upon low Da premixed combustion.

CHAPTER 7

CRITICAL REGION AND SMART PASSIVE CONTROL IN A TURBULENT THERMOACOUSTIC SYSTEM

In our discussion regarding thermoacoustic instability in Chapter 2, we highlighted the importance of quantifying the spatiotemporal behavior of the reacting flow field during the transition to the state of thermoacoustic instability (TAI). The dynamics of a thermoacoustic system are controlled by the spatiotemporal evolution of the interaction between three subsystems – turbulent flow field, combustion, and acoustic field of the combustor. Quantifying this spatiotemporal evolution using the right mathematical tool is crucial in forewarning an impending thermoacoustic instability. Nair *et al.* (2014) found that the scaling of the acoustic pressure fluctuations (quantified by the Hurst exponent, H) during combustion noise and intermittency fares better than corresponding measures based on tracking the amplitude of the pressure oscillations when predicting thermoacoustic instability. Nonetheless, such single-point acoustic measurements cannot be used to predict the changes required in the combustor to control thermoacoustic instability in advance. Thus, there is a need for extending such an analysis in the spatial domain.

We also emphasized the challenges in developing even a relatively simple passive control strategy involving an unmodulated secondary air. Thus, the key objectives of this chapter are to optimize for secondary air-injection location targeting the *critical*

The content of this chapter have been published in **A. Roy**, C. Premchand, M. Raghunathan, A. Krishnan, V. Nair & R. I. Sujith (2021) Critical region in the spatiotemporal dynamics of a turbulent thermoacoustic system and smart passive control. *Combustion and Flame*, **226**, 274-284.

region in the combustor without hampering the flame stability. Such a critical region is determined from spatiotemporal quantities such as the amplitude of velocity fluctuations, mean vorticity, Rayleigh index, and averaged heat release rate (HRR) field. Further, we wish to extend the analysis using the Hurst exponent (H) in the spatial domain. As mentioned earlier, H measured from single-point pressure measurements is invaluable in predicting impending instability. A spatial analysis using H may provide useful insights in optimizing secondary air injection location during the states leading up to TAI. Consequently, the advantages of optimized passive control can be complemented by the predictive capability of the Hurst exponent, resulting in a smart passive control strategy.

7.1 CHARACTERIZING THE TURBULENT COMBUSTOR

The bluff-body stabilized combustor used for control experiments was detailed in §3.2. Experiments were performed by varying the air flow rate to obtain the state of thermoacoustic instability. Acoustic pressure (p'), heat release rate ($\dot{q}$) and velocity field ($u(x, y, t)$) of the combustor were measured. The details of the diagnostic techniques are provided in §3.2.

Figure 7.1 depicts the transition of the turbulent combustor from the state of combustion noise (CN) to thermoacoustic instability (TAI) through the state of intermittency (INT). In Fig. 7.1(a), we show the change in p'_{rms} as a function of the nominal velocity v_a of air (bottom axis) and equivalence ratio ϕ (top axis). Markers ‘A’, ‘B’, and ‘C’ correspond to three points representative of the states of CN, INT, and TAI, used for

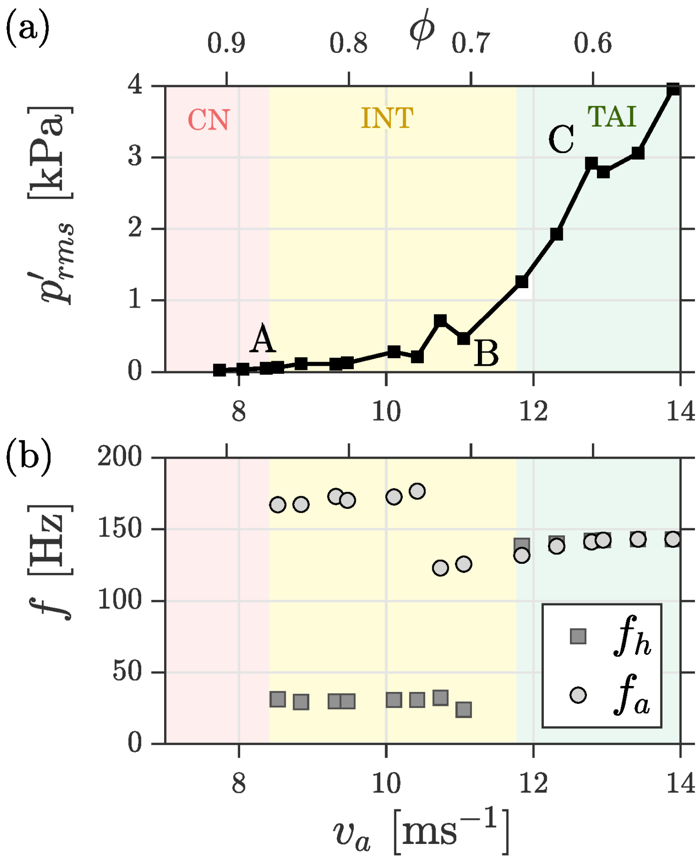

Figure 7.1: Intermittency route to thermoacoustic instability observed in the turbulent combustor. Variation of (a) p'_{rms} and (b) the frequency corresponding to the acoustic (f_a) and hydrodynamic mode (f_h) as a function of nominal velocity of air v_a (bottom axis) and equivalence ratio ϕ (top axis). Adapted from (a) (George *et al.*, 2018) with permission from Cambridge Unversity Press, and (b) (Premchand *et al.*, 2019*b*) with permission from AIP Publishing.

the subsequent spatiotemporal analysis. The state of thermoacoustic intermittency is characterized by bursts of periodic oscillations appearing apparently randomly among aperiodic oscillations (cf. Fig. 2.9ii-v). Note that this state fits the statistical definition of intermittency, which we have used in the preceding chapters. Here, the extreme fluctuations during thermoacoustic intermittency (INT) take the form of large amplitude bursts of periodic oscillations.

Figure 7.1(b) shows the change in the dominant frequency of the pressure fluctuations and spatially-averaged velocity time series during the transition to thermoacoustic instability. We can observe the two separate time scales – acoustic ($1/f_a$) and hydrodynamic ($1/f_h$) – during intermittency (Premchand *et al.*, 2019*b*). At the onset of thermoacoustic instability, the frequency of vortex shedding matches with the acoustic mode of the combustor. This process is associated with the mutual synchronization of the acoustic, hydrodynamic, and HRR field of the combustor (Pawar *et al.*, 2017; Premchand *et al.*, 2019*b*). In §7.3, we discuss the spatiotemporal dynamics from the perspective of optimization for the location of secondary injection. A more thorough discussion on the spatiotemporal dynamics of bluff-body stabilized combustors can be found in George *et al.* (2018) Premchand *et al.* (2019*b*).

7.2 NONLINEAR TIME SERIES ANALYSIS: THE HURST EXPONENT

The time-series of velocity fluctuations obtained from different locations in the combustor during CN and INT are intermittent, and hence, central moments diverge over time (Nair *et al.*, 2014). The fluctuations during the state of TAI are periodic. It is instructive to calculate the scaling of the moments with respect to the change in measurement time scale. The transition from CN to TAI can, thus, be expressed in terms of the change in the nature of scaling of velocity fluctuations.

The scaling exponent of the second moment, or the variance, is called the Hurst exponent. The scaling is a measure of long-term memory in the system. Historically, the Hurst exponent was utilized to determine the optimum dam size for the Nile river based on long-term flood and drought data (Hurst, 1951). The Hurst exponent was later connected to the geometry of fractals by Mandelbrot (1982). We measure the Hurst exponent using Multifractal Detrended Fluctuation Analysis (MFDFA) (Kantelhardt *et al.*, 2002), which we briefly discuss below.

We first perform Reynolds decomposition and calculate the fluctuations in x and y velocity component (u'_x, u'_y) by subtracting the respective time-averaged values ($\bar{u}_x$, $\bar{u}_y$) at all points in the velocity field obtained from PIV measurements. We then determine the total magnitude of velocity fluctuations as:

$$u_T(x, y, t) = \sqrt{[(u'_x(x, y, t)]^2 + [u'_y(x, y, t)]^2}. \tag{7.1}$$

Finally, we detrend the time series by subtracting the mean to obtain the fluctuations of the resultant velocity: $u'_T = u_T - \bar{u}_T$, where $\bar{u}_T$ is the time-averaged resultant velocity. Note that u'_T is essentially the same as turbulent velocity fluctuations defined as the root mean square of the fluctuating velocity components. We plot the representative turbulent velocity fluctuations, measured at a representative point inside the combustor as indicated in the inset. The turbulent velocity fluctuations are plotted during the three states of combustor operation in Figs. 7.2(a-c). We can clearly observe an increase in periodic content of the velocity fluctuations during the transition to TAI. We aim to quantify the change in the nature of the signal with the Hurst exponent.

We then calculate the cumulative deviate series:

$$y_k = \sum_{t=1}^{k} u'_T(t) = \sum_{t=1}^{k} [u_T(t) - \bar{u}_T]. \tag{7.2}$$

where, $k = 1, 2, ..., N$ with N being the length of the signal. The deviate series

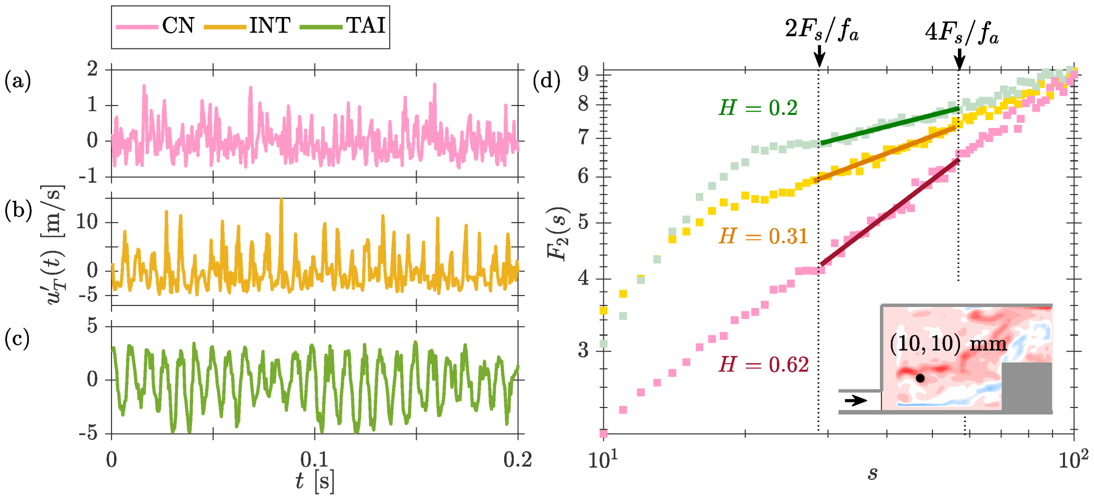

Figure 7.2: (a-c) Time series of turbulent velocity fluctuations (u'_T) during combustion noise, intermittency and thermoacoustic instability at a representative point inside the combustor shown in the inset in (b). The three states correspond to point A, B and C indicated in Fig. 7.1. (d) The variation of the second-order structure function $F_2(s)$ measured from u'_T with the scale s for the three states.

is divided into n_s non-overlapping segments ($y_i(t)$, $i = 1, 2..., n_s$) of equal span s. Local trends are removed by a local polynomial fit $\bar{y}_i$ onto the deviate series y_i. Local fluctuations are obtained by subtracting the fit from the deviate series. The computation time of the Hurst exponent is approximately proportional to the polynomial order used for local detrending. Hence, we consider a local linear fit for detrending as it is computationally faster and produces reliable results. The q^{th} order structure-function, F_q can be obtained from the local fluctuations as (Kantelhardt *et al.*, 2002):

$$F_q(s) = \left[\frac{1}{n_s} \sum_{i=1}^{n_s} \left(\frac{1}{s} \sum_{t=1}^{s} [y_i(t) - \bar{y}_i]^2 \right)^{q/2} \right]^{1/q} \forall q \neq 0. \tag{7.3}$$

The second-order structure function scales as $F_2(s) \sim s^H$ within the bounds set by the minimum and maximum window size. The Hurst exponent H is then determined as:

$$H = \frac{\log F_2(s)}{\log s} \;\; \forall \;\; s \in [2/f_a, 4/f_a]. \tag{7.4}$$

The Hurst exponent, H, measures the correlation and persistence in a time series. If a large (small) value is more likely to be followed by another large (small) value, the signal is said to be persistent and long-range correlated. Such signals have $H > 0.5$. If a large (small) value is more likely to be followed by a small (large) value, the signal is anti-persistent. For such signals, $H < 0.5$ and only short-range correlations exist (Nair and Sujith, 2014). $H = 0$ indicates a purely periodic signal, while $H = 0.5$ indicates white noise. Thus, the spatial distribution of H indicates the persistence and correlation in the velocity fluctuations over the flow-field.

We plot the second-order structure function F_2 as a function of the scale s measured from the time series of turbulent velocity fluctuations $u'_T(t)$ at a representative point in the flow field for the three states of combustor operation in Fig. 7.2(d). We observe that the Hurst exponent is $H = 0.62$ during combustion noise. The signal shown in Fig.7.2(a) is thus persistent and possesses long-range correlations. In fact, the signal is fractal in nature. In contrast, during intermittency and thermoacoustic instability, $H = 0.31$ and $H = 0.2$, which are much lower. The representative signal shown in Figs. 7.2(b,c) suggests anti-persistent and periodic behavior. The decreasing value of H during the transition to thermoacoustic instability is an indicator of the increasing periodic content in the system dynamics. We repeat this process over the entire flow field and obtain the spatial distribution of H over the entire flow field.

We chose the scaling of the structure-function within the bounds $s \in [2/f_a, 4/f_a]$ for two key reasons. First, $s \in [2/f_a, 4/f_a]$ ensures that the segment size is not too low to be within a periodic cycle and not too large as to become completely uncorrelated (Kerres *et al.*, 2016). Such behavior is also evident from Fig. 7.2, where we observe that F_2 is relatively flat for low values of s ($< 2/f_a$), indicating the high correlation between the segments by them being in the same periodic cycle. Similarly, for large s ($> 4/f_a$), F_2 shows oscillations, indicating contributions from decorrelated segments. Second, the acoustics of the combustor impose a characteristic length and time scale on the turbulent flow. Consequently, one only needs to be concerned with the scaling of the structure-function of turbulent velocity fluctuations in the range of time scales comparable to the acoustic time scale. The onset of thermoacoustic instability is captured by the gradual disappearance of the scaling of the structure-function in the bounded range of s.

7.3 SPATIOTEMPORAL BEHAVIOR DURING THE TRANSITION TO THERMOACOUSTIC INSTABILITY

We start by analyzing the spatiotemporal dynamics during the transition from CN to TAI. As already discussed, we acquire simultaneous data associated with velocity, CH* chemiluminescence, and pressure fluctuations. In Fig. 7.3, we plot the Fourier amplitude of the resultant velocity fluctuations (u_T) at the acoustic frequency f_a i.e., $|\hat{u}_T(f_a)|$, the time-averaged vorticity ($\bar{\omega}_z(x, y)$), and the time-averaged heat release rate field ($\bar{q}(x, y)$) during combustion noise, intermittency and thermoacoustic instability at parametric points A, B and C indicated in Fig. 7.1(a). We also plot the Rayleigh index,

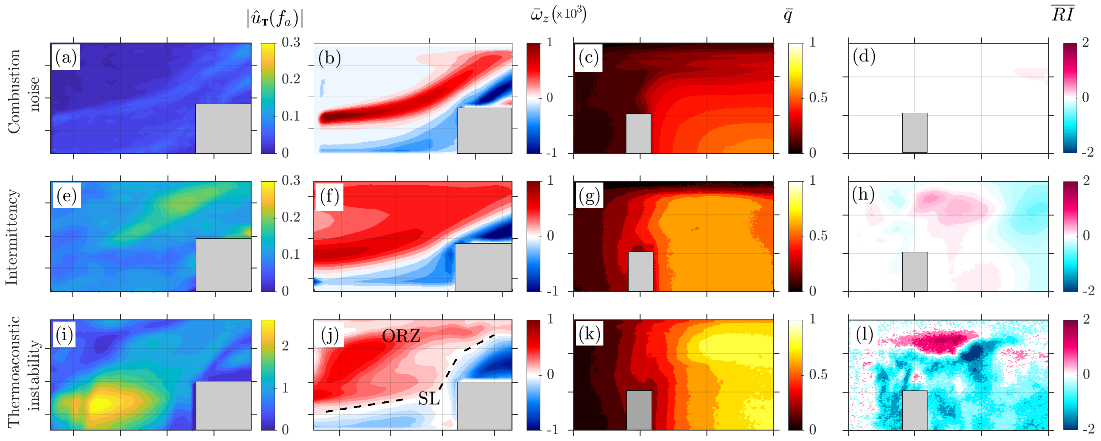

Figure 7.3: Comparison of the Fourier amplitude of turbulent velocity fluctuations $|\hat{u}_T(f_a)|$ (m/s), time-averaged vorticity $\bar{\omega}_z$ ($\times 10^3$, s^{-1}), time-averaged heat release field $\bar{q}$ (a.u.) and time-average Rayleigh index $\overline{RI}$ (a.u.) during the states of (a-d) combustion noise, (e-h) intermittency and (i-l) thermoacoustic instability. The flow conditions are indicated in Fig. 7.1. The span of the ordinate and abcissa are indicated in Fig. 3.6b. The gray region indicates the position of the bluff-body.

which is defined as:

$$\overline{RI}(x, y) = \frac{1}{NT} \int_0^{NT} p'(t)\dot{q}'(x, y, t)dt, \tag{7.5}$$

as discussed in §2.3.2. Here, $N(= 686)$ denotes the total number of cycles, and $T(= 1/f_a)$ denotes the time period of oscillations. The spatial distribution of the Rayleigh index quantifies the strength of acoustic power sources and sinks depending upon positive or negative feedback between pressure and heat release rate oscillations, respectively.

During the state of combustion noise at $\phi = 0.86$ and $v_a = 8.1$ m/s, flow fluctuations show broadband characteristics. The Fourier transformed amplitude $|\hat{u}_T(f)|$ at the acoustic mode $f = f_a$ is very low (Fig. 7.3a). Notice that the scale only extends until 0.1 m/s, which is very low. The time-averaged vorticity field shown in Fig. 7.3(b) indicates that the vortices evolve only along the shear layer (SL). The transverse span of vorticity contour indicates that the size of vortices is very small. We also notice the absence of the outer recirculation zone (ORZ). The time-averaged heat release rate field also shows very low values (Fig. 7.3c). Likewise, the Rayleigh index shows very low values throughout the combustor (Fig. 7.3d).

During the state of intermittency at $\phi = 0.66$ and $v_a = 11.1$ m/s, $|\hat{u}_T(f_a)|$ shows higher values above the shear layer as compared to the state of combustion noise due to intermittent periodic oscillations of turbulent velocity induced by intermittent acoustic pressure oscillations (fig. 7.3e). During epochs of periodic oscillations, larger vortices are shed, leading to the flow recirculating at the dump plane. This can be seen from the rather large distribution of $\bar{\omega}_z$ in Fig. 7.3(f). The maximum of $\bar{\omega}_z$ along the shear layer indicates that most of the vortices are shed along the shear layer but only recirculate intermittently. The time-averaged heat release rate field (Fig. 7.3g) and Rayleigh index (Fig. 7.3b) also show higher values when compared with that during combustion noise.

There is a significant change in the spatiotemporal behaviour during the state of TAI at $\phi = 0.63$ and $v_a = 12.3$ m/s (Figs. 7.3i-l). Thermoacoustic instability in bluff-body stabilized combustors is associated with the phenomenon of vortex-acoustic lock-on wherein the frequency of vortex shedding matches the acoustic frequency $f_h = f_a$ (as shown in Fig. 7.1b) and is central to the establishment of the thermoacoustic feedback in the combustor (Poinsot *et al.*, 1987; Chakravarthy *et al.*, 2007; Pawar *et al.*, 2017). Accordingly, we observe a clearly defined region with a very high value of $|\hat{u}_T(f_a)|$ (Fig. 7.3i). The periodically shed vortices from the dump plane and the tip of the bluff-

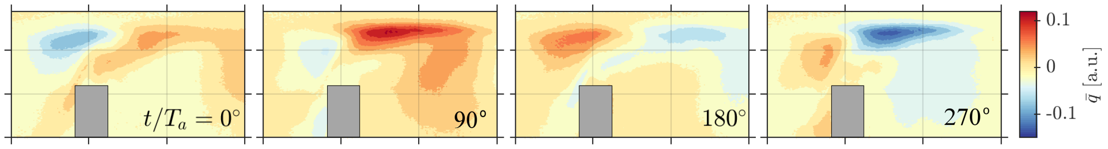

Figure 7.4: Phase-averaged heat release rate field at the indicated phases of the acoustic cycle during the state of thermoacoustic instability. The gray mask indicates the position of the bluff-body.

body develop into large coherent structures which recirculate into the outer recirculation zone (ORZ) and can be observed from the high value of $\bar{\omega}_z$ (Fig. 7.3j).

The large coherent structures carrying unburnt reactants impinge on the bluff-body and the combustor walls and lead to intense heat release. The time-averaged heat release rate field in Fig. 7.3(k) shows maxima in the HRR fluctuations downstream of the bluff-body. To better understand the HRR dynamics, we show the phase-averaged value of HRR from the mean-subtracted chemiluminescence images at $0°, 90°, 180°$, and $270°$ of the acoustic cycle in Fig. 7.4. The phase-averaged HRR field is indicative of the evolution of the flame structure at different points of the acoustic cycle. In the phase-averaged CH* field, we observe very intense regions in the heat release rate above the bluff-body. The intensity increases from moderate to high positive/negative values as one moves closer to maxima ($90°$) and minima ($270°$) of the pressure fluctuations. At pressure maxima ($90°$), we observe large positive heat release rate fluctuations occupying considerable space above the bluff-body. During pressure minima ($270°$), negative fluctuations dominate the field. This behavior is consistent with the Rayleigh criteria (§2.3.2), where large positive fluctuations in the HRR field appear at pressure maxima and vice versa. The relation between pressure and HRR fluctuations is better understood from the plot of the local Rayleigh index in Fig. 7.3(l). We observe very high and positive values of the local Rayleigh index in the region above the bluff-body. These are the primary acoustic power sources that drive thermoacoustic instability.

As we mention earlier, precursor-based methods are great for predicting impending thermoacoustic instability. However, such methods do not provide any information required for implementing passive control measures. Passive control requires knowledge about the relative importance of different regions in the flow field. Based on the considerations made above, we find different regions of interest from different measures. For instance, the region between the dump plane and the bluff-body appears significant based on the large amplitude of $|\hat{u}_T(f_a)|$ during thermoacoustic instability (Fig. 7.3i). Similarly, the maxima in $\bar{\omega}_z$ during thermoacoustic instability (Fig. 7.3j) emphasizes the importance of the outer recirculation zone. Likewise, $\bar{q}(x, y)$ points towards the region after the bluff-body (Fig. 7.3k), while phase-averaged heat release field (Fig. 7.4) and Rayleigh index (Fig. 7.3l) highlights the importance of the region above the bluff-body. We test the efficacy of passive control when these “critical” regions are selectively targeted with secondary air injection. Finally, as with the precursor, we would like to determine whether it is possible to predict such critical regions inside the combustor during the state of intermittency itself.

7.4 PASSIVE CONTROL OF THERMOACOUSTIC INSTABILITY

7.4.1 Suppression of thermoacoustic instability

We now attempt passive control of thermoacoustic instability using secondary air injection from various ports mounted on the combustor side-walls (see Fig. 3.6b). Figure 7.5(a) shows the amplitude of pressure oscillations (p'_{rms}) as a function of the ratio of momentum of the injected air to that of the primary air, $(\upsilon_{inj}/\upsilon_a)^2$ (bottom axis) and the ratio of mass flow rate, $\dot{m}_{inj}/\dot{m}_a$ (top axis). The plot essentially depicts the effectiveness of targeting various regions of the flow field in getting suppression. We notice that targeting the region between the dump plane and bluff-body through either port P1 or combined injection through P2 and P3 leads to a significant decrease in p'_{rms}. There is a decrease from 1.75 kPa to 0.22 kPa, which amounts to an 87.4% reduction in the amplitude of limit cycle oscillations. During the state of control, the amplitude levels are similar to those observed during the state of combustion noise and low-amplitude intermittency. Individually injecting from P2 and P3 does not lead to any reduction. Further, targeting the region above the bluff-body through port P4 or the region after the bluff-body through port P5 does not lead to any reduction in p'_{rms}, and in fact, lead to a slight increase in the amplitude of the limit cycle oscillations.

We also plot the time series and the sound pressure level (SPL) in Figs. 7.5(b) and 7.5(c) at representative points I and II indicated in Fig. 7.5(a) . We observe a shift in the dynamics from the thermoacoustic limit cycle at point I to fluctuations resembling the state of intermittency during suppression at point II. The maximum amplitude during

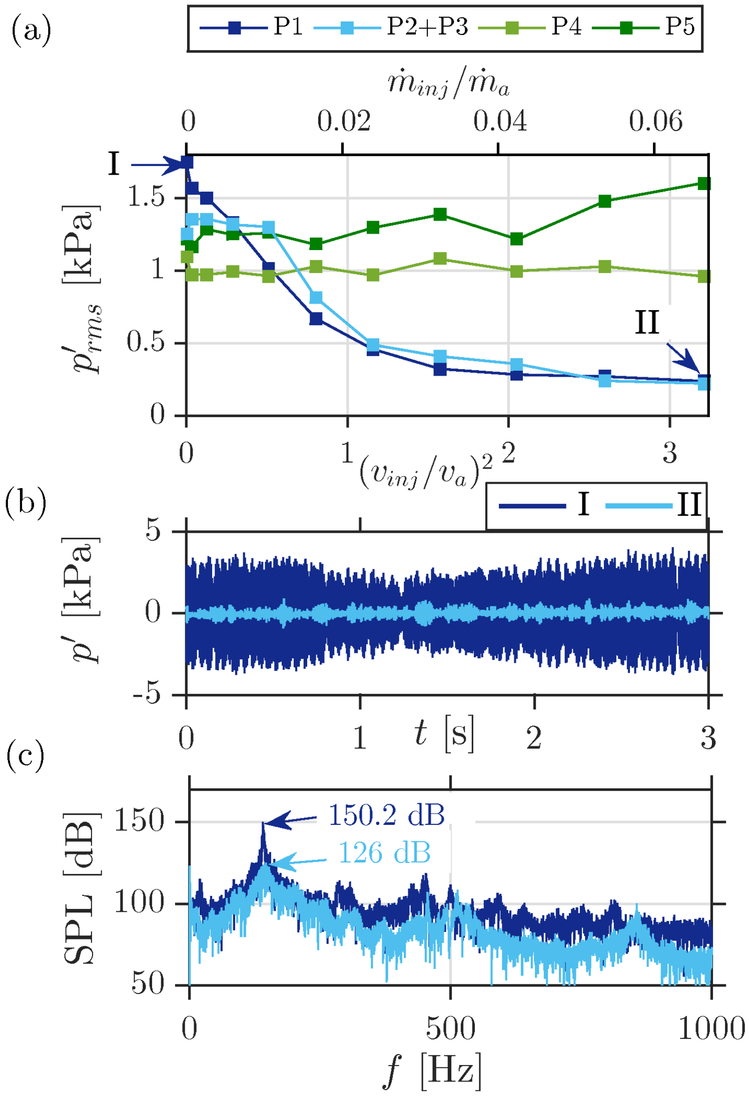

Figure 7.5: Illustration of control of thermoacoustic instability through secondary air injection targeting different regions of the combustor. (a) Amplitude of pressure fluctuations, p'_{rms}, as functions of the momentum ratio, $(v_{inj}/v_a)^2$, and mass flow ratio, $\dot{m}_{inj}/\dot{m}_a$. Representative (b) time series and (c) sound pressure level (SPL) observed during thermoacoustic instability, point I in (a), and subsequent control, point II in (a). Subfigure (a) adapted from (Krishnan *et al.*, 2019*b*) with permission from IOP Publishing.

suppression is of the order of 100 Pa. We further observe a 24.2 dB drop in the sound pressure level from 150.2 dB during thermoacoustic instability to 126 dB after suppression (Fig. 7.5c).

The above exercise shows us the relative importance of different regions of the flow field as far as passive control is concerned. The region between the dump plane and bluff-body, as identified by the amplitude of turbulent velocity fluctuations $|\hat{u}_T(f_a)|$ in Fig. 7.3(i), is “critical" to the spatiotemporal dynamics of thermoacoustic instability. Thus, targeting the critical region through P1 and P2+P3 leads to effective control. Other regions such as the top of the bluff-body or region downstream of the bluff-body identified respectively from the Rayleigh index (Fig. 7.3l) and averaged HRR (Fig. 7.3k) are not as crucial and, hence, cannot be used for optimizing the location of secondary injection. This is in direct contrast to Tachibana *et al.* (2007), who observed the most significant control when secondary micro-jet of air targeted the region of the largest Rayleigh index in their swirl-stabilized combustor. We surmise that the Rayleigh index identifies the region of the most significant acoustic driving; however, it does not always identify the region most sensitive to control. Thus, we cannot always use the local Rayleigh index or average HRR for determining the critical region.

7.4.2 Spatiotemporal behavior during suppression

Next, we analyze the effect of secondary air injection on different measures. Figure 7.6 depicts the spatial dynamics associated with the state of suppression (point II indicated in Fig. 7.5a). We notice many differences in the dynamics during thermoacoustic instability. The maxima of $|\hat{u}_T(f_a)|$ is much lower during the state of control and moves from the region between the dump plane and the bluff-body (Fig. 7.3i) to the top of the bluff-body (Fig. 7.6a). The time-averaged vorticity field $\bar{\omega}_z$ shows vortices concentrated along a small region along the shear layer, indicating the suppression of the large coherent structures formed during thermoacoustic instability (Fig. 7.3a). We further

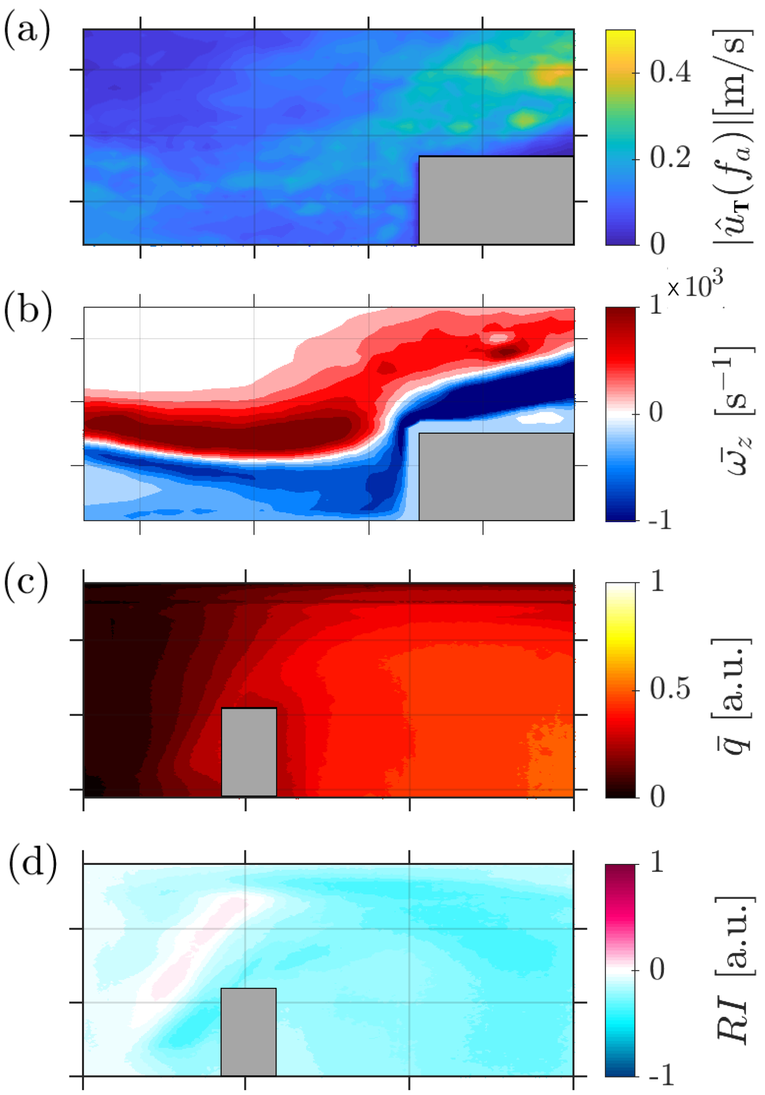

Figure 7.6: (a) Amplitude of velocity fluctuations $|\hat{u}_T(f_a)|$, (b) time-averaged vorticity $\bar{\omega}_z$, (c) time-averaged HRR $\bar{q}$ and (d) Rayligh index $\overline{RI}$ during suppressed state corresponding to point II in Fig. 7.5(a) attained after inject secondary air from port P1.

notice that the mean flame structure (Fig. 7.6c) is no longer as concentrated downstream of the bluff-body, as was the case during thermoacoustic instability (Figs. 7.3k). In fact, the HRR gets more distributed and extends far downstream. Accordingly, the Rayleigh index is very low value throughout the combustor, indicating the reduction in the strength of acoustic power sources inside the combustor due to secondary injection.

During the state of suppression, the pressure fluctuations show intermittent

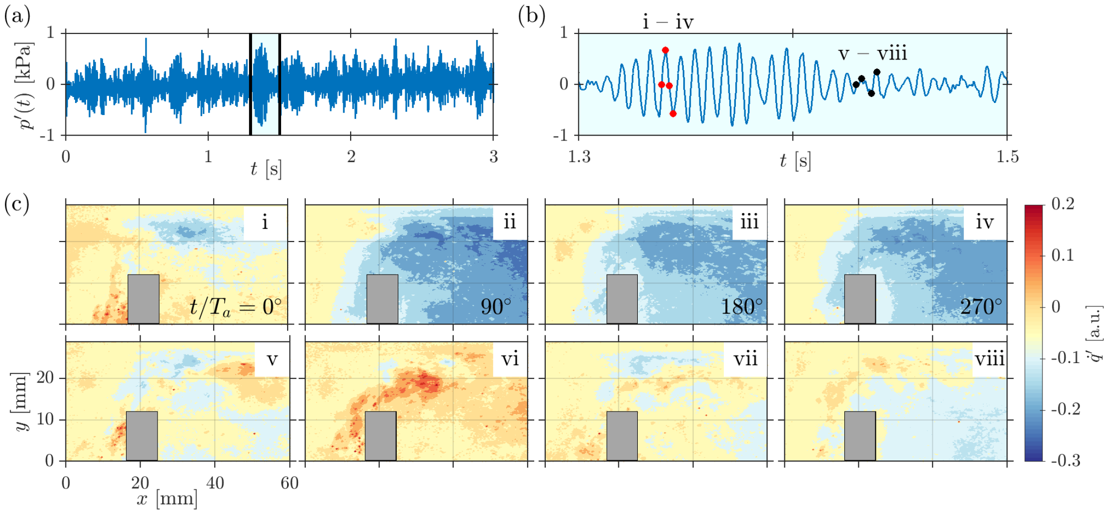

Figure 7.7: Heat release rate field during the state of suppression of thermoacoustic instability for point II indicated in Fig. 7.5a. (a) Intermittent acoustic pressure fluctuations during suppression and (b) an enlarged portion showing alternate cycles of periodic and aperiodic fluctuations. (c) Points i-iv correspond to $\dot{q}'(x, y)$ at four points of the periodic cycle indicated in (b). Points v-viii correspond to $\dot{q}'(x, y)$ at the indicated points during aperiodic oscillations as indicated in (b).

characteristics (Fig. 7.7a,b). We plot the instantaneous mean-subtracted HRR field $\dot{q}'(x, y)$ at four points during the epoch of periodic oscillations in Figs. 7.7(ci-iv) and aperiodic oscillations in Fig. 7.7(cv-viii). We can observe that the flame is anchored along the shear layer after the bluff-body and extends downstream. During periodic oscillations, the instantaneous HRR field shows no concentrated spots in the HRR field as were present during thermoacoustic instability (Fig. 7.4). The entire field is distributed with moderate levels of HRR fluctuations. During aperiodic oscillations, the HRR field is incoherent. Finally, the instantaneous HRR field does not show any visible correlation with pressure fluctuations either during periodic or aperiodic oscillations, leading to very low values of the Rayleigh index (Fig. 7.6d).

7.4.3 Mechanism of suppression

The suppression of thermoacoustic instability depends upon the underlying mechanism and the effect of micro-jet injection on it. In the present combustor, thermoacoustic instability develops when the reactive field mutually synchronizes with the acoustic field (Pawar *et al.*, 2017). Vortices from the unstable shear layer are shed at the acoustic frequency and develop into large coherent structures in the region between the dump plane and the bluff-body (George *et al.*, 2018; Premchand *et al.*, 2019*b*). These large-scale vortices carry unburnt reactants, which upon collision with the bluff-body and the combustor walls, release large amounts of heat (Fig. 7.4). Consequently, the heat release rate and Rayleigh index are, thus, largest above and beyond the dump plane (Fig. 7.3k,l). However, the source of such a large heat release rate can still be traced back to the unstable shear layer developing at the dump plane (Premchand *et al.*, 2019*a*).

Secondary injection from port P1 suppresses perturbations in the shear layer from amplifying, thereby hindering the formation of large coherent structures and, eventually, thermoacoustic instability. On the other hand, injection ports P2 and P3 are further downstream of the dump plane and at a larger distance from the shear layer than P1. Thus, injection from P2 and P3 alone are not enough to control the shear layer and require combined injection for control. On the other hand, injection ports P4 and P5 are much further downstream and cannot impede the unstable shear layer from developing into large coherent structures. Thus, they are ineffective in attaining control.

7.5 OPTIMIZED PASSIVE CONTROL USING HURST EXPONENT

We have established that effective passive control of thermoacoustic instability depends crucially on the region targeted using secondary air injection. Determination of the critical region is non-trivial as different physical measures point to different regions. Of these, we observed that amplitude of turbulent velocity fluctuations $|\hat{u}_T(x, y, f_a)|$ correctly identifies the critical region, targeting which led to the suppression of thermoacoustic instability. The critical region is also identified from network-based measures, as shown in Krishnan *et al.* (2019*a*). However, neither $|\hat{u}_T(x, y, f_a)|$ nor the network-based measures in (Krishnan *et al.*, 2019*a*) are able to distinguish the critical region during the state of intermittency. We remedy this by implementing the spatiotemporal analysis using Hurst exponent calculated from the turbulent velocity fluctuations (u_T), as discussed in §7.2.

During the state of combustion noise at $\phi = 0.86$ and $v_a = 8.1$ m/s, H values in the range $(0.5, 1.2)$ are distributed throughout the combustor (Fig. 7.8a). The regions with different H indicate the difference in the nature of the turbulent velocity fluctuations. The presence of values of $H > 0.5$ indicates that the dynamics of velocity fluctuations are persistent, i.e., a large (small) value is more likely to be followed by another large (small) value. In fact, the velocity fluctuations in regions with $0.5 < H < 1$ have fractal characteristics and possess long-range correlations typically associated with fully-developed turbulent flows (Mordant *et al.*, 2002). Thus, the aperiodically shed small-scale vortices during combustion noise have persistent and fractal behavior.

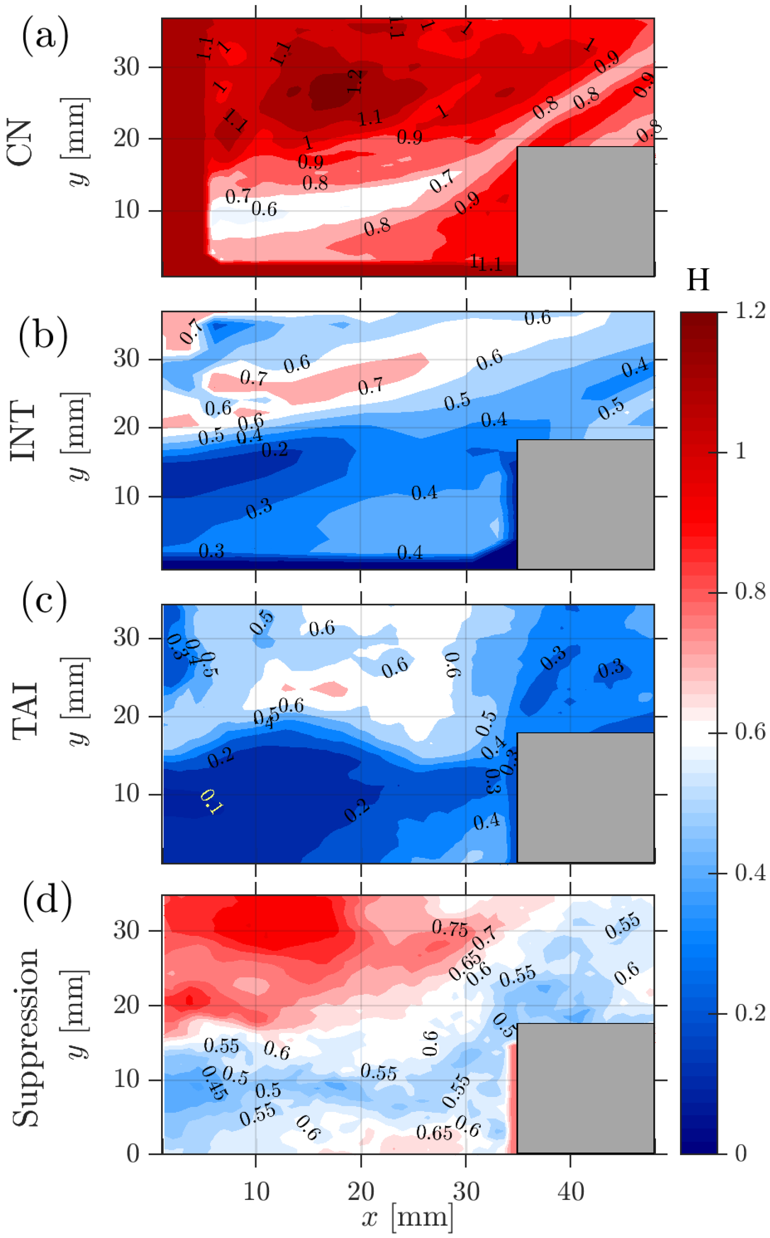

Figure 7.8: Field of Hurst exponent (H) calculated from the intensity of velocity fluctuations during (a) combustion noise, (b) intermittency and (c) thermoacoustic instability. The experimental conditions for (a-c) correspond to the points A, B and C in Fig. 7.1, and (d) corresponds to point II in Fig. 7.5.

Figure 7.8(b) shows the distribution of H during the state of intermittency at $\phi = 0.66$ and $v_a = 11.1$ m/s. We observe large-amplitude periodic bursts embedded randomly amidst the low amplitude aperiodic fluctuations in the measured pressure signal. We notice that the H values in the range of $(0.2, 0.7)$ are distributed across the flow field.

Regions with $H < 0.5$ indicate anti-persistent behavior in that large (small) values associated with velocity fluctuations are more likely to be followed by a small (large) fluctuation. For H close to 0 indicates anti-persistent and periodic behavior. This indicates that the velocity field exhibits periodicity temporally. The region with H close to 0.2 indicates the region over which spatial coherence is maximum in the field.

During thermoacoustic instability at $\phi = 0.63$ and $v_a = 12.3$ m/s (Fig. 7.8c), we observe that the field has H values predominantly lesser than 0.5. We can observe that the H values in the region immediately after the dump plane are very low ($H \approx 0.1$). Signals with H values near-zero imply the absence of scaling of the structure-function. In other words, the fluctuations are bounded. As a consequence, the signal displays a strong anti-persistent behavior, characteristic of periodic signals. Thus, in the region with $H < 0.3$, the temporal dynamics of velocity fluctuations are nearly periodic, and much of the spatial region displays coherence.

We plot the histogram of H values observed during the three different states in Fig. 7.9. We can observe that the histogram shifts to lower H values during the transition from combustion noise to thermoacoustic instability. This shift clearly indicates that the dynamics of velocity fluctuations are predominantly periodic and anti-persistent during thermoacoustic instability. In contrast, during combustion noise, the dynamics show persistent behavior possessing long-range temporal correlations.

Figure 7.8d shows the distribution of H when control using secondary jets from injection port P1 is successfully implemented. The experimental condition corresponds to point II in Fig. 7.5a. We observe that the expansive region with H close to 0 during

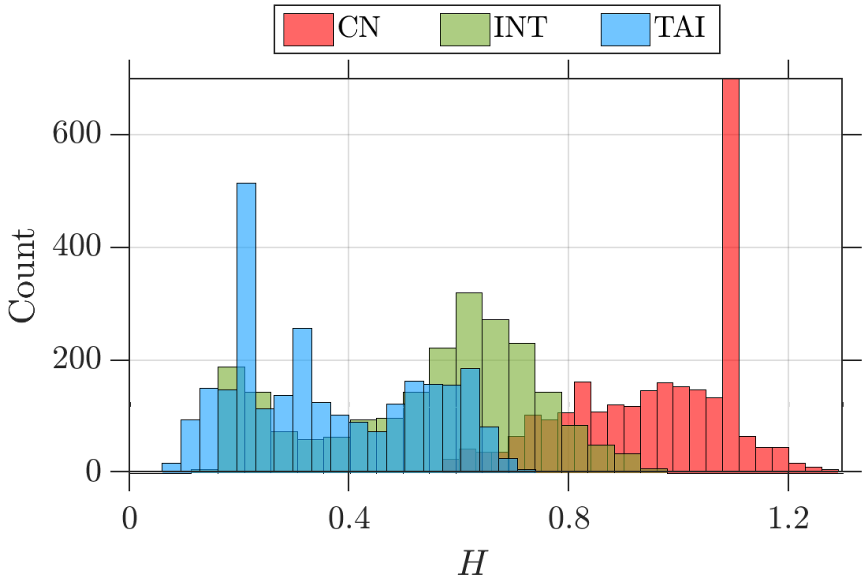

Figure 7.9: Histogram showing the distribution of the Hurst exponent (H) during the states of combustion noise (CN), intermittency (INT), and thermoacoustic instability (TAI).

the state of thermoacoustic instability, located between the backward-facing step and the bluff-body, is no longer present. In other words, secondary injection disrupted the region with coherence in spatiotemporal dynamics. The resultant flow field has a distribution of H values ranging from 0.5 to 1, which has persistent behavior similar to that observed during the state of combustion noise (Fig. 7.8a).

Thus, we see that the Hurst exponent correctly identifies the critical region in the flow field, as was also done by Fourier transformed velocity amplitude $|\hat{u}_T(f_a)|$ (Fig. 7.3i). As noted earlier, $|\hat{u}_T(f_a)|$ identified the critical region only during thermoacoustic instability. Similarly, network-based measures also identified the critical region during thermoacoustic instability (Krishnan *et al.*, 2019*a*). In contrast, we observe that H can capture the critical region even during the state of intermittency (Fig. 7.8b), which is something we do not observe from the field of $|\hat{u}_T(f_a)|$ during the state of intermittency (Fig. 7.3e). Hence, it is possible to predict the critical region from the velocity field obtained during the state of intermittency. To the best of our knowledge, prediction of the critical region for targeted passive control during the states leading up to thermoacoustic instability has not been achieved until now. Thus, the Hurst exponent proves to be a very robust measure in analyzing the temporal and spatiotemporal dynamics of thermoacoustic systems.

A literature review suggests that the intermediate state of intermittency is observed in almost all types of combustion systems (Nair *et al.*, 2014; Gotoda *et al.*, 2014; Pawar *et al.*, 2016; Ebi *et al.*, 2018; Kheirkhah *et al.*, 2017). Such an intermittent state is also associated with corresponding intermittent states in the spatio-temporal dynamics, such as intermittent vortex shedding (George *et al.*, 2018; Kheirkhah *et al.*, 2017) and chimera-like states where spatial patches of order develop amidst disorder (Mondal *et al.*, 2017). Thus, the Hurst exponent can be used to analyze spatial data such as PIV and distinguish spatial regions displaying distinct dynamics. For our purpose, the Hurst exponent was able to predict the critical region where the dynamics are periodic and most sensitive to passive control. We thus believe that the present methodology is generalizable to arbitrary combustor geometries and other intermittent states observed in the combustion dynamics literature.

7.6 INTERIM SUMMARY

In the present chapter, we develop a smart passive control strategy for combating thermoacoustic instability in a bluff-body stabilized turbulent combustor. We analyze the transition from combustion noise to thermoacoustic instability through the state of intermittency. We use several measures, such as the Fourier amplitude of turbulent velocity fluctuations, time-averaged vorticity, averaged heat release rate (HRR), and Rayleigh index to quantify the spatiotemporal dynamics of the combustor. We optimize the secondary air injection location based on the location of the maxima of these physical measures. We find that secondary injection targeting the region of maxima in the amplitude of turbulent velocity fluctuations leads to the highest suppression. We observe a 20 dB drop in the sound pressure level. More importantly, we found that targeting local regions identified from maxima in the Rayleigh index and averaged HRR did not lead to any significant suppression compared to the past study. The Rayleigh index identifies the most significant acoustic power sources; however, it does not identify the most suitable region for control.

It has been found that the Hurst exponent is a much more robust measure than the velocity amplitude for predicting thermoacoustic instability (Nair *et al.*, 2014). We extend this into the spatiotemporal domain to combine the predictive abilities of the Hurst exponent with the idea of optimizing the location of secondary air injection. Using the spatial distribution of the Hurst exponent during the state of thermoacoustic instability, we are able to correctly identify the critical region recognized by the amplitude of turbulent velocity fluctuations, thus validating our approach. We then find that the spatial distribution of the Hurst exponent can predict the critical region during the state of intermittency, in contrast to the other physical measures. The capability of the Hurst exponent in predicting the critical region during the state of intermittency constitutes the most important finding of our study.

In closing, we note that the present methodology has the potential for broad application in combustors. First, it can be used to determine critical regions most suited for aiming control strategies without infringing upon the stability of the flame. Second, the distribution of Hurst exponent can be used to predict critical region if the flow-field is known during the states before full-blown thermoacoustic instability. Thus, for already commissioned combustors, critical regions can be obtained from LES simulations and used to determine the right combination of secondary air-injection ports for efficient control of thermoacoustic instability. Such control can expand the operational regime of combustors leading to reduced costs and energy saving in gas turbine combustors. Finally, we believe that the present methodology can be extended to any turbulent combustion systems displaying intermittent states.

CHAPTER 8
CONCLUSION AND OUTLOOK

Turbulent premixed combustion is a multi-scale phenomenon replete with interactions taking place at small and large scales. These scale-dependent interactions give rise to a rich phenomenology. At large scales, the interaction of heat release rate response of premixed flames can couple with acoustic oscillations and drive destructive thermoacoustic instability. While at the small scales, extreme fluctuations of the premixed flames can alter flame properties, cause intense fluctuations in quantities such as turbulent flame speed, flame strain rate, etc., and in severe cases, can promote flame quenching. Thus, understanding the scale-dependent response of premixed flames is of paramount importance. This thesis deals with both of these aspects.

We explain the effects of nonlinear interference on the harmonic flame response and characterize the large-scale heat release rate response of turbulent flames. At very high turbulence levels, the harmonic response only reflects a part of the picture of the overall flame dynamics. Consequently, we quantify the statistics of turbulent flame fluctuations. We show that the power spectrum of turbulent flame fluctuations depicts a well-defined power-law behavior with a scaling exponent of -2 over an intermediate range of scales. The exponent of power-law scaling is explained as a response of flame surface fluctuating passively to the turbulent flow. We calculate the higher-order moments of the turbulent flame fluctuations and find that they scale anomalously – a signature of small-scale intermittency. We then quantify the multifractal spectrum of the multiplicative cascade process, which is responsible for the phenomenon of small-scale intermittency.

Turbulent flame surfaces depict pronounced fractal scaling, another consequence of dynamic self-similarity arising due to cascades in turbulent flows. We analytically consider the effect of small-scale intermittency on the fractal behavior of the thickened premixed flames and derive corrections to the fractal dimension. The corrections are a result of extreme fluctuations in dissipation quantities which cause strong variability in the inner cut-off of fractal scaling and lead to a change in the fractal dimension.

Finally, we study the practical aspect of control of thermoacoustic instability in turbulent combustors. The transition to unstable combustor operation is associated with a change from a steady-state where system dynamics show fluctuations possessing fractal signature, which is progressively lost as the system moves closer to thermoacoustic instability. We determine the spatial distribution of Hurst exponent from the velocity field, which captures the loss in the fractal signature from different regions and predicts critical region which, when targeted, leads to optimal control.

Thus, in this thesis, we have comprehensively demonstrated the statistical aspect of turbulent premixed combustion, differentiated between the scale-dependent response, discovered signatures of small-scale intermittency, accounted for the effect of small-scale intermittency of flames, and contrived a novel statistical method of controlling thermoacoustic instability.

8.1 FUTURE DIRECTIONS

The present thesis promises exciting new directions for future work. Small-scale intermittency has not been studied in turbulent combustion research till now and raises important questions. Flame fluctuations are central to quantities of long-standing practical interest such as turbulent flame speed, heat release rate, flame curvature, etc. For instance, turbulent flame speed (s_T) is related to flame fluctuations to the leading order through the relation (Chaudhuri *et al.*, 2012): $s_T/s_L \sim \langle [1 + (\partial_x \xi)^2]^{1/2} \rangle$. Small-scale intermittency in ξ' would lead to extreme fluctuations in the gradient $\partial_x \xi$ as well as s_T. Thus, it will be interesting to study the effect of small-scale intermittency on the behavior of these quantities as a follow-up to the present investigations.

A related question is the prediction of higher-order moments of flame fluctuations in turbulent combustion. The concept of multiplicative processes and multifractals underlies the phenomenon of small-scale intermittency. Thus, it would be interesting to investigate the effect of multifractal scalar dissipation on the prediction of anomalous scaling exponents of higher-order moments of turbulent flame fluctuations. This will not only clarify the mechanism of small-scale intermittency but also prove useful in the statistical modelling of turbulent premixed flames, which often relies on the use of log-normal statistics.

We also underscored the importance of the fractal nature of flame surfaces in the study of premixed turbulent combustion. In our analysis, we observed that quantities such as burning rate and heat releaser rate depend on the flux of reactants across the fractal flame interface. We also observed that the sound radiated during turbulent combustion possesses unmistakable fractal signatures (Nair and Sujith, 2014). Turbulence essentially imprints various signatures of dynamic self-similarity on the flame surface and the radiated sound. Hence, it would be fascinating to analytically model the turbulent combustion using fractal formalism and discern their effects on combustion noise. Recently, Raghunathan *et al.* (2020) observed that the fractal dimension of turbulent premixed flames increases during the occurrence of thermoacoustic instability from their corresponding value during combustion noise. Thus, it would be a challenge to unify the concomitant fractal behavior of the premixed flame and the loss of multifractality during the transition to thermoacoustic instability through a self-consistent statistical model.

REFERENCES

1. **Al-Ghussain, L.** (2019). Global warming: review on driving forces and mitigation. *Environmental Progress & Sustainable Energy*, **38**(1), 13–21. 4

2. **Aldredge, R.** (2006). The speed of isothermal-front propagation in isotropic, weakly turbulent flows. *Combustion Science and Technology*, **178**(7), 1201–1215. 64

3. **Aldredge, R.** and **F. Williams** (1991). Influence of wrinkled premixed-flame dynamics on large-scale, low-intensity turbulent flow. *Journal of Fluid Mechanics*, **228**, 487–511. 64

4. **Aldredge, R. C.** (2017). Flame propagation in multiscale transient periodic flow. *Combustion and Flame*, **183**, 166–180. 64

5. **Altay, H. M.**, **D. E. Hudgins**, **R. L. Speth**, **A. M. Annaswamy**, and **A. F. Ghoniem** (2010). Mitigation of thermoacoustic instability utilizing steady air injection near the flame anchoring zone. *Combustion and Flame*, **157**(4), 686–700. 80, 81

6. **Altay, M.**, **R. Speth**, **D. Snarheim**, **D. Hudgins**, **A. Ghoniem**, and **A. Annaswamy**, Impact on microjet actuation on stability of a backward-facing step combustor. *In 45th AIAA Aerospace Sciences Meeting and Exhibit*. 2007. 80, 81

7. **Amato, A.**, **J. Seitzman**, and **T. Lieuwen**, Emissions from oxyfueled or highexhaust gas recirculation turbines. *In* **T. Lieuwen** and **V. Yang** (eds.), *Gas Turbine Emissions*. Cambridge University Place, New York, 2013. 12

8. **Ananthkrishnan, N.**, **K. Sudhakar**, **S. Sudershan**, and **A. Agarwal** (1998). Application of secondary bifurcations to large-amplitude limit cycles in mechanical systems. *Journal of Sound and Vibration*, **215**(1), 183–188. xvi, 75

9. **Anselmet, F.**, **Y. l. Gagne**, **E. J. Hopfinger**, and **R. A. Antonia** (1984). High-order velocity structure functions in turbulent shear flows. *Journal of Fluid Mechanics*, **140**, 63–89. xv, xvi, 32, 33

10. **ASME** (2007). The world's first industrial gas turbine set – GT neuchâtel: A historical mechanical engineering landmark. `https://www.asme.org/wwwasmeorg/media/resourcefiles/aboutasme/who%20we%20are/engineering%20history/landmarks/135-neuchatel-gas-turbine.pdf`. Retrieved on July 3, 2021. 2

11. **Augustin, L.**, **C. Barbante**, **P. R. Barnes**, **J. M. Barnola**, **M. Bigler**, **E. Castellano**, **O. Cattani**, **J. Chappellaz**, **D. Dahl-Jensen**, **B. Delmonte**, *et al.* (2004). Eight glacial cycles from an antarctic ice core. *Nature*, **429**, 623–628. xv, 4

12. **Balachandran, R.**, **B. Ayoola**, **C. Kaminski**, **A. Dowling**, and **E. Mastorakos** (2005). Experimental investigation of the nonlinear response of turbulent premixed flames to imposed inlet velocity oscillations. *Combustion and Flame*, **143**(1-2), 37–55. 65

13. **Batchelor, G.**, Diffusion in a field of homogeneous turbulence: Ii. the relative motion of particles. *In Mathematical Proceedings of the Cambridge Philosophical Society*, volume 48. Cambridge University Press, 1952. 44

14. **Batchelor, G. K.**, *The theory of homogeneous turbulence*. Cambridge university press, 1953. 29, 56

15. **Bellows, B. D.**, **M. K. Bobba**, **A. Forte**, **J. M. Seitzman**, and **T. Lieuwen** (2007). Flame transfer function saturation mechanisms in a swirl-stabilized combustor. *Proceedings of the Combustion Institute*, **31**(2), 3181–3188. 65, 72, 117

16. **Borghi, R.**, On the structure and morphology of turbulent premixed flames. *In Recent advances in the Aerospace Sciences*. Springer, 1985, 117–138. 49, 63, 158

17. **Bothien, M. R.**, **A. Ciani**, **J. P. Wood**, and **G. Fruechtel**, Sequential combustion in gas turbines: The key technology for burning high hydrogen contents with low emissions. *In ASME Turbo Expo*. ASME, 2019. 12

18. **Bradshaw, P.**, **D. H. Ferriss**, and **R. F. Johnson** (1964). Turbulence in the noise-producing region of a circular jet. *Journal of Fluid Mechanics*, **19**, 591–624. xv, 28

19. **Brinley, T.**, *The industrial revolution and the Atlantic economy: selected essays*. Routledge, 1993. 1

20. **Bruno, R.**, **V. Carbone**, **P. Veltri**, **E. Pietropaolo**, and **B. Bavassano** (2001). Identifying intermittency events in the solar wind. *Planetary and Space Science*, **49**(12), 1201–1210. 48

21. **Burnett, R.**, **H. Chen**, **M. Szyszkowicz**, **N. Fann**, **B. Hubbell**, **C. A. Pope**, **J. S. Apte**, **M. Brauer**, **A. Cohen**, **S. Weichenthal**, *et al.* (2018). Global estimates of mortality associated with long-term exposure to outdoor fine particulate matter. *Proceedings of the National Academy of Sciences*, **115**(38), 9592–9597. 3

22. **Campa, G.** and **M. P. Juniper**, Obtaining bifurcation diagrams with a thermoacoustic network model. *In ASME Turbo Expo*, volume 44687. ASME, 2012. 75

23. **Candel, S.**, **D. Durox**, **S. Ducruix**, **A.-L. Birbaud**, **N. Noiray**, and **T. Schuller** (2009). Flame dynamics and combustion noise: progress and challenges. *International Journal of Aeroacoustics*, **8**(1), 1–56. 75, 76

24. **Candel, S.**, **D. Durox**, **T. Schuller**, **J.-F. Bourgouin**, and **J. P. Moeck** (2014). Dynamics of swirling flames. *Annual Reviews of Fluid Mechanics*, **46**, 147–173. 72

25. **Cantwell, B.** and **D. Coles** (1983). An experimental study of entrainment and transport in the turbulent near wake of a circular cylinder. *Journal of Fluid Mechanics*, **136**, 321–374. 104

26. **Carlson, J. A.**, **A. Jaffe**, and **A. Wiles**, *The millennium prize problems*. Citeseer, 2006.

27. **Cerutti, S.** and **C. Meneveau** (1998). Intermittency and relative scaling of subgrid-scale energy dissipation in isotropic turbulence. *Physics of Fluids*, **10**(4), 928–937. 48

28. **Chakravarthy, S.**, **R. Sivakumar**, and **O. Shreenivasan** (2007). Vortex-acoustic lock-on in bluff-body and backward-facing step combustors. *Sadhana*, **32**(1), 145–154. 187

29. **Chaloulakou, A.**, **I. Mavroidis**, and **I. Gavriil** (2008). Compliance with the annual NO_2 air quality standard in athens. required NOx levels and expected health implications. *Atmospheric Environment*, **42**(3), 454–465. 8

30. **Chaparro, A.**, **E. Landry**, and **B. M. Cetegen** (2006). Transfer function characteristics of bluff-body stabilized, conical v-shaped premixed turbulent propane–air flames. *Combustion and Flame*, **145**(1-2), 290–299. 65

31. **Charlette, F.**, **C. Meneveau**, and **D. Veynante** (2002). A power-law flame wrinkling model for les of premixed turbulent combustion part i: non-dynamic formulation and initial tests. *Combustion and Flame*, **131**(1-2), 159–180. 159

32. **Chatakonda, O.**, **E. Hawkes**, **M. Brear**, **J. Chen**, **E. Knudsen**, and **H. Pitsch**, Modeling of the wrinkling of premixed turbulent flames in the thin reaction zones regime for large eddy simulation. *In Proceedings of the Summer Program*. 2010. 160

33. **Chatakonda, O.**, **E. R. Hawkes**, **A. J. Aspden**, **A. R. Kerstein**, **H. Kolla**, and **J. H. Chen** (2013). On the fractal characteristics of low damköhler number flames. *Combustion and Flame*, **160**(11), 2422–2433. 160, 162, 163, 165, 174

34. **Chaudhuri, S.**, **V. Akkerman**, and **C. K. Law** (2011). Spectral formulation of turbulent flame speed with consideration of hydrodynamic instability. *Physical Review E*, **84**(2), 026322. 15, 59, 158

35. **Chaudhuri, S.**, **H. Kolla**, **H. L. Dave**, **E. R. Hawkes**, **J. H. Chen**, and **C. K. Law** (2017). Flame thickness and conditional scalar dissipation rate in a premixed temporal turbulent reacting jet. *Combustion and Flame*, **184**, 273–285. 60

36. **Chaudhuri, S.**, **S. Kostka**, **M. W. Renfro**, and **B. M. Cetegen** (2010). Blowoff dynamics of bluff body stabilized turbulent premixed flames. *Combustion and Flame*, **157**(4), 790–802. 15

37. **Chaudhuri, S.**, **F. Wu**, **D. Zhu**, and **C. K. Law** (2012). Flame speed and self-similar propagation of expanding turbulent premixed flames. *Physical review letters*, **108**(4), 044503. 205

38. **Chhabra, A. B.**, **C. Meneveau**, **R. V. Jensen**, and **K. R. Sreenivasan** (1989). Direct determination of the $f(\alpha)$ singularity spectrum and its application to fully developed turbulence. *Physical Review A*, **40**(9), 5284. 40, 43

39. **Choi, C.** (2012). History of fire milestone, one million years old, discovered in homo erectus' wonderwerk cave. `https://www.huffpost.com/entry/history-fire-million-homo-erectus_n_1397810`. 1

40. **Chowdhury, B. R.** and **B. M. Cetegen** (2017). Experimental study of the effects of free stream turbulence on characteristics and flame structure of bluff-body stabilized conical lean premixed flames. *Combustion and Flame*, **178**, 311–328. 64

41. **Chowdhury, B. R.**, **J. A. Wagner**, and **B. M. Cetegen** (2017). Experimental study of the effect of turbulence on the structure and dynamics of a bluff-body stabilized lean premixed flame. *Proceedings of the Combustion Institute*, **36**(2), 1853–1859. 64

42. **Chu, B.-T.** (1965). On the energy transfer to small disturbances in fluid flow (part i). *Acta Mechanica*, **1**(3), 215–234. 17, 70

43. **Clanet, C.** and **G. Searby** (1998). First experimental study of the Darrieus-Landau instability. *Physical Review Letters*, **80**(17), 3867. 63, 72

44. **Clavin, P.** and **F. Williams** (1982). Effects of molecular diffusion and of thermal expansion on the structure and dynamics of premixed flames in turbulent flows of large scale and low intensity. *Journal of Fluid Mechanics*, **116**, 251–282. 52

45. **Collins, L. R.** (1995). Spectral analysis of a simulated premixed flame surface in two dimensions. *Computers & Fluids*, **24**(6), 663–683. 59

46. **Constantin, P.**, **I. Procaccia**, and **K. Sreenivasan** (1991). Fractal geometry of isoscalar surfaces in turbulence: theory and experiments. *Physical Review Letters*, **67**(13), 1739. 156, 165, 174

47. **Cook, A. F.** (2003). John barber - the inventor of the gas turbine: A potted history. *Nuneaton and North Warwickshire Family History Society*. 2

48. **Corrsin, S.** (1951). On the spectrum of isotropic temperature fluctuations in an isotropic turbulence. *Journal of Applied Physics*, **22**(4), 469–473. 45, 47

49. **Creta, F.**, **N. Fogla**, and **M. Matalon** (2011). Turbulent propagation of premixed flames in the presence of darrieus–landau instability. *Combustion Theory and Modelling*, **15**(2), 267–298. 63, 72

50. **Culick, F.** and **P. Kuentzmann** (2006). Unsteady motions in combustion chambers for propulsion systems. Technical report, Nato Research and Technology Organization Neuilly-Sur-Seine (France). 16

51. **Davidson, P. A.**, *Turbulence: an introduction for scientists and engineers*. Oxford University Press, 2015. 30, 38, 39, 43, 47

52. **Davis, L. B.** and **S. H. Black**, Dry low NOx combustion systems for ge heavy-duty gas turbines. *In Powergen Conference*. Penwell Conferences & Exhibitions, 1995. 12

53. **De Rosa, A. J.**, **J. Samarasinghe**, **S. J. Peluso**, **B. D. Quay**, and **D. A. Santavicca** (2016). Flame area fluctuation measurements in velocity-forced premixed gas turbine flames. *Journal of Engineering for Gas Turbines and Power*, **138**(4), 041507. 64

54. **Dowling, A. P.** (1999). A kinematic model of a ducted flame. *Journal of Fluid Mechanics*, **394**, 51–72. 108

55. **Driscoll, J. F.** (2008). Turbulent premixed combustion: Flamelet structure and its effect on turbulent burning velocities. *Progress in Energy and Combustion Science*, **34**(1), 91–134. 15

56. **Dubrulle, B.** (2019). Beyond kolmogorov cascades. *Journal of Fluid Mechanics*, **867**. 48

57. **Durox, D.**, **T. Schuller**, and **S. Candel** (2005). Combustion dynamics of inverted conical flames. *Proceedings of the Combustion Institute*, **30**(2), 1717–1724. 65

58. **Durox, D.**, **T. Schuller**, **N. Noiray**, and **S. Candel** (2009). Experimental analysis of nonlinear flame transfer functions for different flame geometries. *Proceedings of the Combustion Institute*, **32**(1), 1391–1398. 65, 109

59. **Ebi, D.**, **A. Denisov**, **G. Bonciolini**, **E. Boujo**, and **N. Noiray** (2018). Flame dynamics intermittency in the bistable region near a subcritical hopf bifurcation. *Journal of Engineering for Gas Turbine and Power*, **140**(6). 200

60. **Emerson, B.** and **T. Lieuwen** (2015). Dynamics of harmonically excited, reacting bluff body wakes near the global hydrodynamic stability boundary. *Journal of Fluid Mechanics*, **779**, 716–750. 63, 105, 110

61. **Emmert, T.**, **S. Bomberg**, and **W. Polifke** (2015). Intrinsic thermoacoustic instability of premixed flames. *Combustion and Flame*, **162**(1), 75–85. 73

62. **Etikyala, S.** and **R. Sujith** (2017). Change of criticality in a prototypical thermoacoustic system. *Chaos*, **27**(2), 023106. 75

63. **Falcon, E.**, **S. Fauve**, and **C. Laroche** (2007). Observation of intermittency in wave turbulence. *Physical Review Letters*, **98**(15), 154501. 48

64. **Falkovich, G.**, **K. Gawędzki**, and **M. Vergassola** (2001). Particles and fields in fluid turbulence. *Reviews of Modern Physics*, **73**(4), 913. 47, 48

65. **Feller, W.**, *An introduction to probability theory and its applications, vol 2*. John Wiley & Sons, 2008. 39

66. **Fleifil, M.**, **A. M. Annaswamy**, **Z. Ghoneim**, and **A. F. Ghoniem** (1996). Response of a laminar premixed flame to flow oscillations: A kinematic model and thermoacoustic instability results. *Combustion and Flame*, **106**(4), 487–510. 65, 108, 118

67. **Freeman, S.**, **D. S. Lee**, **L. L. Lim**, **A. Skowron**, and **R. R. De León** (2018). Trading off aircraft fuel burn and no x emissions for optimal climate policy. *Environmental Science & Technology*, **52**(5), 2498–2505. 13

68. **Frigo, M.** and **S. G. Johnson**, Fftw: An adaptive software architecture for the fft. *In Proceedings of the 1998 IEEE International Conference on Acoustics, Speech and Signal Processing, ICASSP'98 (Cat. No. 98CH36181)*, volume 3. IEEE, 1998. 91

69. **Frisch, U.**, *Turbulence: The Legacy of A. N. Kolmogorov*. Cambridge University Press, 1995. xv, xvi, 28, 36, 38, 40, 41, 47, 138

70. **Frisch, U.**, **P.-L. Sulem**, and **M. Nelkin** (1978). A simple dynamical model of intermittent fully developed turbulence. *Journal of Fluid Mechanics*, **87**(4), 719–736. 40

71. **Fureby, C.** (2005). A fractal flame-wrinkling large eddy simulation model for premixed turbulent combustion. *Proceedings of the Combustion Institute*, **30**(1), 593–601. 160

72. **Gagne, Y.** (1980). *Contribution à l'étude expérimentale de l'intermittence de la turbulence à petite échelle*. Ph.D. thesis, Université de Grenoble. xvi, 33

73. **George, N. B.**, **V. R. Unni**, **M. Raghunathan**, and **R. Sujith** (2018). Pattern formation during transition from combustion noise to thermoacoustic instability via intermittency. *Journal of Fluid Mechanics*, **849**, 615–644. xvii, xx, 72, 76, 77, 180, 181, 195, 200

74. **Ghoniem, A. F.**, **A. Annaswamy**, **S. Park**, and **Z. C. Sobhani** (2005). Stability and emissions control using air injection and H_2 addition in premixed combustion. *Proceedings of the Combustion Institute*, **30**(2), 1765–1773. 80, 81

75. **Godavarthi, V.**, **V. Unni**, **E. Gopalakrishnan**, and **R. Sujith** (2017). Recurrence networks to study dynamical transitions in a turbulent combustor. *Chaos*, **27**(6), 063113. 79

76. **Gokulakrishnan, P.** and **M. S. Klassen**, NOx and CO formation and control. *In* **T. Lieuwen** and **V. Yang** (eds.), *Gas Turbine Emissions*. Cambridge University Place, New York, 2013. xv, 8, 9, 10, 11

77. **Gokulakrishnan, P.**, **M. Ramotowski**, **G. Gaines**, **C. Fuller**, **R. Joklik**, **L. Eskin**, **M. Klassen**, and **R. Roby** (2008). A novel low nox lean, premixed, and prevaporized combustion system for liquid fuels. *Journal of Engineering for Gas Turbines and Power*, **130**(5). 13

78. **Goldenfeld, N.** (2006). Roughness-induced critical phenomena in a turbulent flow. *Physical Review Letters*, **96**(4), 044503. 47

79. **Gotoda, H.**, **H. Kinugawa**, **R. Tsujimoto**, **S. Domen**, and **Y. Okuno** (2017). Characterization of combustion dynamics, detection, and prevention of an unstable combustion state based on a complex-network theory. *Physical Review Applied*, **7**(4), 044027. 79

80. **Gotoda, H.**, **Y. Shinoda**, **M. Kobayashi**, **Y. Okuno**, and **S. Tachibana** (2014). Detection and control of combustion instability based on the concept of dynamical system theory. *Physical Review E*, **89**(2), 022910. 79, 200

81. **Gouldin, F.**, **K. Bray**, and **J.-Y. Chen** (1989). Chemical closure model for fractal flamelets. *Combustion and Flame*, **77**(3-4), 241–259. 159

82. **Gouldin, F. C.** (1987). An application of fractals to modeling premixed turbulent flames. *Combustion and flame*, **68**(3), 249–266. 62, 145, 159, 161, 165

83. **Gülder, Ö. L.**, Turbulent premixed combustion modelling using fractal geometry. *In Symposium (International) on Combustion*, volume 23. Elsevier, 1991. 159, 161

84. **Gülder, Ö. L.** (2007). Contribution of small scale turbulence to burning velocity of flamelets in the thin reaction zone regime. *Proceedings of the Combustion Institute*, **31**(1), 1369–1375. 62

85. **Gülder, Ö. L.** and **G. J. Smallwood** (1995). Inner cutoff scale of flame surface wrinkling in turbulent premixed flames. *Combustion and Flame*, **103**(1-2), 107–114. 159

86. **Gülder, Ö. L.**, **G. J. Smallwood**, **R. Wong**, **D. R. Snelling**, **R. Smith**, **B. M. Deschamps**, and **J.-C. Sautet** (2000). Flame front surface characteristics in turbulent premixed propane/air combustion. *Combustion and Flame*, **120**(4), 407–416. 62, 145, 159

87. **Halsey, T. C.**, **M. H. Jensen**, **L. P. Kadanoff**, **I. Procaccia**, and **B. I. Shraiman** (1986). Fractal measures and their singularities: The characterization of strange sets. *Physical Review A*, **33**(2), 1141. 41, 142, 148, 157, 172

88. **Hamlington, P. E.**, **A. Y. Poludnenko**, and **E. S. Oran** (2012). Intermittency in premixed turbulent reacting flows. *Physics of Fluids*, **24**(7), 075111. 60, 61

89. **Hansen, J.**, **M. Sato**, **R. Ruedy**, **K. Lo**, **D. W. Lea**, and **M. Medina-Elizade** (2006). Global temperature change. *Proceedings of the National Academy of Sciences*, **103**(39), 14288–14293. 4

90. **Harari, Y. N.**, *Sapiens: A brief history of humankind*. Random House, 2014. 1

91. **Hassa, C.**, Partially premixed and premixed aero combustors, in gas turbine emissions. *In* **T. Lieuwen** and **V. Yang** (eds.), *Gas Turbine Emissions*. Cambridge University Place, New York, 2013. 14

92. **Hathout, J.**, **M. Fleifil**, **A. Annaswamy**, and **A. F. Ghoniem** (2002). Combustion instability active control using periodic fuel injection. *Journal of Propulsion and Power*, **18**(2), 390–399. 80

93. **Hawkes, E. R.**, **O. Chatakonda**, **H. Kolla**, **A. R. Kerstein**, and **J. H. Chen** (2012). A petascale direct numerical simulation study of the modelling of flame wrinkling for large-eddy simulations in intense turbulence. *Combustion and Flame*, **159**(8), 2690–2703. 160, 162

94. **Hawkes, E. R.** and **J. H. Chen** (2005). Evaluation of models for flame stretch due to curvature in the thin reaction zones regime. *Proceedings of the Combustion Institute*, **30**(1), 647–655. 162

95. **Hemchandra, S.**, **N. Peters**, and **T. Lieuwen** (2011). Heat release response of acoustically forced turbulent premixed flames – role of kinematic restoration. *Proceedings of Combustion Institute*, **33**(1), 1609–1617. xvi, 63, 65, 66

96. **Hentschel, H.** and **I. Procaccia** (1984). Relative diffusion in turbulent media: the fractal dimension of clouds. *Physical Review A*, **29**(3), 1461. 156

97. **Hentschel, H. G. E.** and **I. Procaccia** (1983). The infinite number of generalized dimensions of fractals and strange attractors. *Physica D*, **8**(3), 435–444. 41, 143, 144, 145, 157

98. **Hoeijmakers, M.**, **V. Kornilov**, **I. L. Arteaga**, **P. de Goey**, and **H. Nijmeijer** (2014). Intrinsic instability of flame–acoustic coupling. *Combustion and Flame*, **161**(11), 2860–2867. 73

99. **Holzer, M.** and **E. D. Siggia** (1994). Turbulent mixing of a passive scalar. *Physics of Fluids*, **6**(5), 1820–1837. 47

100. **Humphrey, L.** (2017). *Ensemble-averaged dynamics of premixed, turbulent, harmonically excited flames*. Ph.D. thesis, Georgia Institute of Technology. xiv, 89, 123

101. **Humphrey, L.** and **T. C. Lieuwen**, Experimental investigation of the ensemble-averaged turbulent displacement speed. *In 55th AIAA Aerospace Sciences Meeting, Grapevine, Texas*. 2017. 64

102. **Humphrey, L. J.**, **B. Emerson**, and **T. C. Lieuwen** (2018). Premixed turbulent flame speed in an oscillating disturbance field. *Journal of Fluid Mechanics*, **835**, 102–130. xvii, 64, 65, 85, 87, 89, 90

103. **Hurst, H. E.** (1951). Long-term storage capacity of reservoirs. *Transactions of American Society of Civil Engineers*, **116**, 770–799. 181

104. **IEA** (2021). Global energy review. `https://iea.blob.core.windows.net/assets/d0031107-401d-4a2f-a48b-9eed19457335/GlobalEnergyReview2021.pdf`. Retrieved on July 3, 2021. xv, 3, 6, 7

105. **Jones, B.**, **J. G. Lee**, **B. D. Quay**, **D. A. Santavicca**, **K. Kim**, and **S. Srinivasan**, Flame response mechanisms due to velocity perturbations in a lean premixed gas turbine combustor. *In ASME Turbo Expo*. 2010. 65, 118

106. **Juniper, M. P.** and **R. I. Sujith** (2018). Sensitivity and nonlinearity of thermoacoustic oscillations. *Annual Reviews of Fluid Mechanics*, **50**, 661–689. 16, 17, 70, 73

107. **Kabiraj, L.** and **R. Sujith** (2012). Nonlinear self-excited thermoacoustic oscillations: intermittency and flame blowout. *Journal of Fluid Mechanics*, **713**, 376–397. 73

108. **Kantelhardt, J. W.**, **S. A. Zschiegner**, **E. Koscielny-Bunde**, **S. Havlin**, **A. Bunde**, and **H. E. Stanley** (2002). Multifractal detrended fluctuation analysis of nonstationary time series. *Physica A*, **316**(1-4), 87–114. 182, 183

109. **Karimi, N.**, **M. J. Brear**, and **W. H. Moase** (2008). Acoustic and disturbance energy analysis of a flow with heat communication. *Journal of Fluid Mechanics*, **597**, 67–89. 70

110. **Karman, T.** and **L. Howarth** (1938). On the statistical theory of isotropic turbulence. *Proceedings of the Royal Society of London*, **164**(917), 192–215. 31

111. **Karpetis, A.** and **R. Barlow** (2002). Measurements of scalar dissipation in a turbulent piloted methane/air jet flame. *Proceedings of the Combustion Institute*, **29**(2), 1929 – 1936. 60

112. **Kaufmann, A.**, **F. Nicoud**, and **T. Poinsot** (2002). Flow forcing techniques for numerical simulation of combustion instabilities. *Combustion and Flame*, **131**(4), 371–385. 65

113. **Keppeler, R.**, **E. Tangermann**, **U. Allaudin**, and **M. Pfitzner** (2014). Les of low to high turbulent combustion in an elevated pressure environment. *Flow Turbulence and Combustion*, **92**(3), 767–802. 160

114. **Kerres, B.**, **V. Nair**, **A. Cronhjort**, and **M. Mihaescu** (2016). Analysis of the turbocharger compressor surge margin using a hurst-exponent-based criterion. *SAE International Journal of Engines*, **9**(3), 1795–1806. 185

115. **Kerstein, A. R.** (1988). Fractal dimension of turbulent premixed flames. *Combustion Science and Technology*, **60**(4-6), 441–445. 62, 145, 159, 165, 174

116. **Kerstein, A. R.** (1991). Fractal dimension of propagating interfaces in turbulence. *Physical Review A*, **44**(6), 3633. 62, 159, 174

117. **Kerstein, A. R.** (2002). Turbulence in combustion processes: Modeling challenges. *Proceedings of the Combustion Institute*, **29**(2), 1763–1773. 62

118. **Kheirkhah, S.**, **J. M. Cirtwill**, **P. Saini**, **K. Venkatesan**, and **A. M. Steinberg** (2017). Dynamics and mechanisms of pressure, heat release rate, and fuel spray coupling during intermittent thermoacoustic oscillations in a model aeronautical combustor at elevated pressure. *Combustion and Flame*, **185**, 319–334. 200

119. **Knikker, R.**, **D. Veynante**, and **C. Meneveau** (2002). A priori testing of a similarity model for large eddysimulations of turbulent premixed combustion. *Proceedings of the Combustion Institute*, **29**(2), 2105–2111. 159

120. **Kobayashi, T.**, **S. Murayama**, **T. Hachijo**, and **H. Gotoda** (2019). Early detection of thermoacoustic combustion instability using a methodology combining complex networks and machine learning. *Physical Review Applied*, **11**(6), 064034. 79

121. **Kolmogorov, A. N.** (1941*a*). Dissipation of energy in locally isotropic turbulence. **32**, 16. xxiii, 19, 22, 29, 31, 37, 166

122. **Kolmogorov, A. N.** (1941*b*). The local structure of turbulence in incompressible viscous fluid for very large reynolds numbers. *Doklady Akademii Nauk SSSR*, **30**(4), 301–305. xxiii, 19, 29, 46, 166, 175

123. **Kolmogorov, A. N.** (1962). A refinement of previous hypotheses concerning the local structure of turbulence in a viscous incompressible fluid at high reynolds number. *Journal of Fluid Mechanics*, **13**(1), 82–85. 35, 46

124. **Kornilov, V.**, **K. Schreel**, and **L. De Goey** (2007). Experimental assessment of the acoustic response of laminar premixed bunsen flames. *Proceedings of the Combustion Institute*, **31**(1), 1239–1246. 84

125. **Krishnan, A.**, **R. Manikandan**, **P. Midhun**, **K. Reeja**, **V. Unni**, **R. Sujith**, **N. Marwan**, and **J. Kurths** (2019*a*). Mitigation of oscillatory instability in turbulent reactive flows: A novel approach using complex networks. *European Physical Letters*, **128**(1), 14003. 82, 196, 199

126. **Krishnan, A.**, **R. Sujith**, **N. Marwan**, and **J. Kurths** (2019*b*). On the emergence of large clusters of acoustic power sources at the onset of thermoacoustic instability in a turbulent combustor. *Journal of Fluid Mechanics*, **874**, 455–482. xxi, 96, 191

127. **Landau, L. D.** and **E. M. Lifshitz**, *Fluid Mechanics, Second Edition: Volume 6 (Course of Theoretical Physics)*. Course of theoretical physics / by L. D. Landau and E. M. Lifshitz, Vol. 6. Pergamon Press, 1959. 34

128. **Langhorne, P.**, **A. Dowling**, and **N. Hooper** (1990). Practical active control system for combustion oscillations. *Journal of Propulsion and Power*, **6**(3), 324–333. 80

129. **LaVision** (2006). Flowmaster PIV/PTV - systems. `http://www.lavision.de/en/products/flowmaster/index.php`. 88

130. **Law, C.** and **C. Sung** (2000). Structure, aerodynamics, and geometry of premixed flamelets. *Progress Energy and Combustion Science*, **26**(4-6), 459–505. 63

131. **Law, C. K.**, *Combustion physics*. Cambridge university press, 2010. xvi, 15, 18, 49, 158

132. **Lee, D. S.**, **D. Fahey**, **A. Skowron**, **M. Allen**, **U. Burkhardt**, **Q. Chen**, **S. Doherty**, **S. Freeman**, **P. Forster**, **J. Fuglestvedt**, *et al.* (2021). The contribution of global aviation to anthropogenic climate forcing for 2000 to 2018. *Atmospheric Environment*, **244**, 117834. 6

133. **Lefebvre, A. H.** (1977). Lean premixed/prevaporized combustion. *NASA CP-2016*. 13

134. **Lieuwen, T.** (2003). Modeling premixed combustion-acoustic wave interactions: A review. *Journal of Propulsion and Power*, **19**(5), 765–781. 17

135. **Lieuwen, T.**, **V. McDonell**, **E. Petersen**, and **D. Santavicca** (2008). Fuel flexibility influences on premixed combustor blowout, flashback, autoignition, and stability. *Journal of Engineering for Gas Turbines and Power*, **130**(1). 14

136. **Lieuwen, T.** and **K. McManus** (2003). Introduction: Combustion dynamics in lean-premixed prevaporized (lpp) gas turbines. *Journal of Propulsion and Power*, **19**(5), 721–721. 13, 14

137. **Lieuwen, T.**, **Y. Neumeier**, and **B. T. Zinn** (1998). The role of unmixedness and chemical kinetics in driving combustion instabilities in lean premixed combustors. *Combustion Science and Technology*, **135**(1-6), 193–211. 72

138. **Lieuwen, T.** and **B. T. Zinn**, The role of equivalence ratio oscillations in driving combustion instabilities in low NOx gas turbines. *In Symposium (International) on Combustion*, volume 27. Elsevier, 1998. 72

139. **Lieuwen, T. C.** (2002). Experimental investigation of limit-cycle oscillations in an unstable gas turbine combustor. *Journal of Propulsion and Power*, **18**(1), 61–67. 75

140. **Lieuwen, T. C.**, *Unsteady combustor physics*. Cambridge University Press, 2012. 18, 63, 71, 104, 106, 108, 118

141. **Lieuwen, T. C.** and **V. Yang**, *Combustion instabilities in gas turbine engines: operational experience, fundamental mechanisms, and modeling*. American Institute of Aeronautics and Astronautics, 2005. 7, 16, 70

142. **Lindstedt, R.** and **E. Vaos** (1999). Modeling of premixed turbulent flames with second moment methods. *Combustion and Flame*, **116**(4), 461–485. 159

143. **Lovejoy, S.** (1982). Area-perimeter relation for rain and cloud areas. *Science*, **216**(4542), 185–187. 156

144. **Maghon, H.**, **A. Kreutzer**, and **H. Termuehlen**, The v84 gas turbine designed for base-load and peaking duty. *In Proceedings of the American Power Conference*, volume 50. 1988. xv, 10

145. **Magri, L.** (2019). Adjoint methods as design tools in thermoacoustics. *Applied Mechanics Review*, **71**(2). 73

146. **Magri, L.**, **M. P. Juniper**, and **J. P. Moeck** (2020). Sensitivity of the rayleigh criterion in thermoacoustics. *Journal of Fluid Mechanics*, **882**. 70

147. **Mahrt, L.** (1989). Intermittency of atmospheric turbulence. *Journal of Atmospheric Sciences*, **46**(1), 79–95. 48

148. **Mandelbrot, B. B.**, Possible refinement of the lognormal hypothesis concerning the distribution of energy dissipation in intermittent turbulence. *In Statistical models and turbulence*. Springer, 1972, 333–351. 40, 61

149. **Mandelbrot, B. B.** (1975). On the geometry of homogeneous turbulence, with stress on the fractal dimension of the iso-surfaces of scalars. *Journal of Fluid Mechanics*, **72**(3), 401–416. 157

150. **Mandelbrot, B. B.**, *The fractal geometry of nature*, volume 1. WH freeman New York, 1982. 153, 155, 156, 171, 181

151. **Mandelbrot, B. B.**, Multifractal measures, especially for the geophysicist. *In Fractals in geophysics*. Springer, 1989, 5–42. 40, 143, 145, 170

152. **Mantzaras, J.**, **P. Felton**, and **F. Bracco** (1989). Fractals and turbulent premixed engine flames. *Combustion and Flame*, **77**(3-4), 295–310. 159

153. **Mcdonell, V.** and **M. Klein**, Ground-based gas turbine combustion: Metrics, constraints, and system interactions. *In* **T. Lieuwen** and **V. Yang** (eds.), *Gas Turbine Emissions*. Cambridge University Place, New York, 2013. 12

154. **McKinney, M. L.** and **J. L. Lockwood** (1999). Biotic homogenization: a few winners replacing many losers in the next mass extinction. *Trends in ecology & evolution*, **14**(11), 450–453. 5

155. **McManus, K.**, **U. Vandsburger**, and **C. Bowman** (1990). Combustor performance enhancement through direct shear layer excitation. *Combustion and Flame*, **82**(1), 75–92. 80

156. **Meneveau, C.** and **T. Poinsot** (1991). Stretching and quenching of flamelets in premixed turbulent combustion. *Combustion and Flame*, **86**(4), 311–332. 62

157. **Meneveau, C.** and **K. Sreenivasan** (1990). Interface dimension in intermittent turbulence. *Physical Review A*, **41**(4), 2246. 157, 159, 169, 174, 175

158. **Meneveau, C.** and **K. Sreenivasan** (1991). The multifractal nature of turbulent energy dissipation. *Journal of Fluid Mechanics*, **224**, 429–484. xvi, 33, 41, 43

159. **Meneveau, C.** and **K. R. Sreenivasan** (1987*a*). The multifractal spectrum of the dissipation field in turbulent flows. *Nuclear Physics B*, **2**, 49–76. 175

160. **Meneveau, C.** and **K. R. Sreenivasan** (1987*b*). Simple multifractal cascade model for fully developed turbulence. *Physical Review Letters*, **59**(13), 1424. 43

161. **Michalke, A.** (1971). Instability of a compressible round free-radial understanding the influence of the strain-layer thickness. Technical report, German Research and Examination Center for Air and Space EV Berlin, West Germany. 63

162. **Mondal, S.**, **V. R. Unni**, and **R. I. Sujith** (2017). Onset of thermoacoustic instability in turbulent combustors: an emergence of synchronized periodicity through formation of chimera-like states. *Journal of Fluid Mechanics*, **811**, 659–681. 200

163. **Monkewitz, P. A.** and **K. Sohn** (1988). Absolute instability in hot jets. *AIAA Journal*, **26**(8), 911–916. 63

164. **Morales, A. J.**, **I. M. Lasky**, **M. K. Geikie**, **C. A. Engelmann**, and **K. A. Ahmed** (2019). Mechanisms of flame extinction and lean blowout of bluff body stabilized flames. *Combustion and Flame*, **203**, 31–45. 15

165. **Mordant, N.**, **J. Delour**, **E. Léveque**, **A. Arnéodo**, and **J.-F. Pinton** (2002). Long time correlations in lagrangian dynamics: a key to intermittency in turbulence. *Physicl Review Letters*, **89**(25), 254502. 196

166. **Murugesan, M.** and **R. Sujith** (2015). Combustion noise is scale-free: transition from scale-free to order at the onset of thermoacoustic instability. *Journal of Fluid Mechanics*, **772**, 225–245. 76

167. **Murugesan, M.** and **R. Sujith** (2016). Detecting the onset of an impending thermoacoustic instability using complex networks. *Journal of Propulsion and Power*, **32**(3), 707–712. 79

168. **Myers, M. K.** (1991). Transport of energy by disturbances in arbitrary steady flows. *Journal of Fluid Mechanics*, **226**, 383–400. 70

169. **Myerson, A. L.**, The reduction of nitric oxide in simulated combustion effluents by hydrocarbon-oxygen mixtures. *In Symposium (International) on Combustion*, volume 15. Elsevier, 1975. 11

170. **Nagaraja, S.**, **K. Kedia**, and **R. Sujith** (2009). Characterizing energy growth during combustion instabilities: Singularvalues or eigenvalues? *Proceedings of the Combustion Institute*, **32**(2), 2933–2940. 70

171. **Nair, V.** and **R. Sujith** (2014). Multifractality in combustion noise: predicting an impending combustion instability. *Journal of Fluid Mechanics*, **747**, 635–655. 76, 77, 79, 184, 206

172. **Nair, V.**, **G. Thampi**, **S. Karuppusamy**, **S. Gopalan**, and **R. Sujith** (2013). Loss of chaos in combustion noise as a precursor of impending combustion instability. *International Journal of Spray and Combustion dynamics*, **5**(4), 273–290. 76

173. **Nair, V.**, **G. Thampi**, and **R. Sujith** (2014). Intermittency route to thermoacoustic instability in turbulent combustors. *Journal of Fluid Mechanics*, **756**, 470–487. 73, 76, 78, 79, 178, 181, 200, 201

174. **NASA** (2021). Global climate change: Evidence. `https://climate.nasa.gov/vital-signs/carbon-dioxide/`. Retrieved on July 5, 2021. xv, 3, 4, 5

175. **Newell, A. C.**, **S. Nazarenko**, and **L. Biven** (2001). Wave turbulence and intermittency. *Physica D*, **152**, 520–550. 48

176. **North, G.** and **D. Santavicca** (1990). The fractal nature of premixed turbulent flames. *Combustion Science and Technology*, **72**(4-6), 215–232. 159

177. **Oboukhov, A.** (1949). Structure of the temperature field in turbulent flows. *Isv. Geogr. Geophys. Ser.*, **13**, 58–69. 45, 47

178. **Oboukhov, A. M.** (1962). Some specific features of atmospheric tubulence. *Journal of Fluid Mechanics*, **13**(1), 77–81. 34

179. **Oefelein, J. C.** and **V. Yang** (1993). Comprehensive review of liquid-propellant combustion instabilities in f-1 engines. *Journal of Propulsion and Power*, **9**(5), 657–677. 16

180. **Otsu, N.** (1979). A threshold selection method from gray-level histograms. *IEEE Transactions on Systems, Man, and Cybernatics*, **9**(1), 62–66. 89

181. **Oztarlik, G.**, **L. Selle**, **T. Poinsot**, and **T. Schuller** (2020). Suppression of instabilities of swirled premixed flames with minimal secondary hydrogen injection. *Combustion and Flame*, **214**, 266–276. 81

182. **Pan, L.**, **J. C. Wheeler**, and **J. Scalo** (2008). The effect of turbulent intermittency on the deflagration to detonation transition in supernova ia explosions. *The Astrophysical Journal*, **681**(1), 470. 62

183. **Pao, Y.-H.** (1965). Structure of turbulent velocity and scalar fields at large wavenumbers. *Physics of Fluids*, **8**(6), 1063–1075. 57

184. **Pao, Y.-H.** (1968). Transfer of turbulent energy and scalar quantities at large wavenumbers. *Physics of Fluids*, **11**(6), 1371–1372. 57

185. **Parisi, G.** and **U. Frisch**, On the singularity structure of fully developed turbulence. *In* **G. P. M. Ghil, R. Benzi** (ed.), *Turbulence and Predictability in Geophysical Fluid Dynamics*. North Holland, Amsterdam, 1985. 41

186. **Park, G. I.**, **M. Bassenne**, **J. Urzay**, and **P. Moin** (2017). A simple dynamic subgrid-scale model for LES of particle-laden turbulence. *Physical Review Fluids*, **2**(4), 044301. 48

187. **Pavithran, I.**, **V. R. Unni**, and **R. Sujith** (2021). Critical transitions and their early warning signals in thermoacoustic systems. *The European Physical Journal Special Topics*, 1–22. 79

188. **Pawar, S. A.**, **S. Mondal**, **N. B. George**, and **R. Sujith** (2019). Temporal and spatiotemporal analyses of synchronization transition in a swirl-stabilized combustor. *AIAA Journal*, **57**(2), 836–847. 72

189. **Pawar, S. A.**, **A. Seshadri**, **V. R. Unni**, and **R. I. Sujith** (2017). Thermoacoustic instability as mutual synchronization between the acoustic field of the confinement and turbulent reactive flow. *Journal of Fluid Mechanics*, **827**, 664–693. 72, 181, 187, 195

190. **Pawar, S. A.**, **R. Vishnu**, **M. Vadivukkarasan**, **M. Panchagnula**, and **R. Sujith** (2016). Intermittency route to combustion instability in a laboratory spray combustor. *Journal of Engineering for Gas Turbine and Power*, **138**(4). 200

191. **Pelce, P.** and **P. Clavin** (1982). Influence of hydrodynamics and diffusion upon the stability limits of laminar premixed flames. *Journal of Fluid Mechanics*, **124**, 219–237. 52

192. **Peters, N.**, Laminar flamelet concepts in turbulent combustion. *In Symposium (International) on Combustion*, volume 21. Elsevier, 1988. 49, 54

193. **Peters, N.** (1992). A spectral closure for premixed turbulent combustion in the flamelet regime. *Journal of Fluid Mechanics*, **242**, 611–629. 19, 22, 48, 51, 53, 55, 56, 57, 58, 59, 63, 126

194. **Peters, N.** (1999). The turbulent burning velocity for large-scale and small-scale turbulence. *Jounral of Fluid Mechanics*, **384**, 107–132. 63, 162

195. **Peters, N.**, *Turbulent combustion*. IOP Publishing, 2001. 15, 18, 39, 55, 63, 158

196. **Petersen, R. E.** and **H. W. Emmons** (1961). Stability of laminar flames. *Physics of Fluids*, **4**(4), 456–464. 84

197. **Picardo, J. R.**, **A. Bhatnagar**, and **S. S. Ray** (2020). Lagrangian irreversibility and eulerian dissipation in fully developed turbulence. *Physical Review Fluids*, **5**(4), 042601. 48

198. **Poinsot, T.** (2017). Prediction and control of combustion instabilities in real engines. *Proceedings of the Combustion Institute*, **36**(1), 1–28. 17, 70

199. **Poinsot, T.** and **D. Veynante**, *Theoretical and numerical combustion*. RT Edwards, Inc., 2005. 15, 61, 68

200. **Poinsot, T. J.**, **A. C. Trouve**, **D. P. Veynante**, **S. M. Candel**, and **E. J. Esposito** (1987). Vortex-driven acoustically coupled combustion instabilities. *Journal of Fluid Mechanics*, **177**, 265–292. 63, 64, 72, 187

201. **Polifke, W.** (2020). Modeling and analysis of premixed flame dynamics by means of distributed time delays. *Progress in Energy and Combustion Science*, **79**, 100845. 73

202. **Prasad, R. R.**, **C. Meneveau**, and **K. R. Sreenivasan** (1988). Multifractal nature of the dissipation field of passive scalars in fully turbulent flows. *Physical Review Letters*, **61**(1), 74. 43

203. **Prather, M. J.**, **J. Hsu**, **N. M. DeLuca**, **C. H. Jackman**, **L. D. Oman**, **A. R. Douglass**, **E. L. Fleming**, **S. E. Strahan**, **S. D. Steenrod**, **O. A. Søvde**, *et al.* (2015). Measuring and modeling the lifetime of nitrous oxide including its variability. *Journal of Geophysical Research: Atmospheres*, **120**(11), 5693–5705. 9

204. **Preetham**, **S. Hemchandra**, and **T. C. Lieuwen** (2007). Response of turbulent premixed flames to harmonic acoustic forcing. *Proceedings of the Combustion Institute*, **31**(1), 1427–1434. 64

205. **Premchand, C. P.**, **N. B. George**, **M. Raghunathan**, **V. R. Unni**, **P. R. Sujith**, and **V. Nair** (2019*a*). Lagrangian analysis of flame dynamics in the flow-field of a bluff-body stabilized combustor. *Journal of Engineering for Gas Turbine and Power*. 195

206. **Premchand, C. P.**, **N. B. George**, **M. Raghunathan**, **V. R. Unni**, **R. I. Sujith**, and **V. Nair** (2019*b*). Lagrangian analysis of intermittent sound sources in the flow-field of a bluff-body stabilized combustor. *Physics of Fluids*, **31**(2), 025115. xx, 77, 180, 181, 195

207. **Raghunathan, M.**, **N. B. George**, **V. R. Unni**, **P. R. Midhun**, **K. V. Reeja**, and **R. I. Sujith** (2020). Multifractal analysis of flame dynamics during transition to thermoacoustic instability in a turbulent combustor. *Journal of Fluid Mechanics*, **888**. 62, 77, 78, 206

208. **Ralph, M.**, **P. Kuentzmann**, **L. Maurice**, and **J. Tilston** (2009). Report of the independent experts to CAEP 8 on the second NOx review & long term technology goals. *London, March*. 14

209. **Rayleigh, J. W. S.** (1878). The explanation of certain acoustical phenomena. *Nature*, **18**(455), 319–321. 16, 17, 69

210. **Richardson, L. F.** (1926). Atmospheric diffusion shown on a distance-neighbour graph. *Proceedings of the Royal Society of London*, **110**(756), 709–737. 38

211. **Ritchie, H.** (2020). Climate change and flying: what share of global CO_2 emissions come from aviation? `https://ourworldindata.org/co2-emissions-from-aviation`. 6

212. **Rogers, D. E.** (1956). A mechanism for high-frequency oscillation in ramjet combustors and afterburners. *Journal of Jet Propulsion*, **26**(6), 456–462. 63

213. **Roy, A.**, **S. Singh**, **A. Nair**, **S. Chaudhuri**, and **R. Sujith** (2021). Flame dynamics during intermittency and secondary bifurcation to longitudinal thermoacoustic instability in a swirl-stabilized annular combustor. *Proceedings of the Combustion Institute*, **38**(4), 6221–6230. 75

214. **Saddoughi, S. G.** and **S. V. Veeravalli** (1994). Local isotropy in turbulent boundary layers at high reynolds number. *Journal of Fluid Mechanics*, **268**, 333–372. xv, 31, 32

215. **Saha, A.**, **S. Chaudhuri**, and **C. K. Law** (2014). Flame surface statistics of constant-pressure turbulent expanding premixed flames. *Physics of Fluids*, **26**(4), 045109. 62

216. **Schadow, K.** and **E. Gutmark** (1992). Combustion instability related to vortex shedding in dump combustors and their passive control. *Progress in Energy and Combustion Science*, **18**(2), 117–132. 63, 64, 72

217. **Schuller, T.**, **D. Durox**, and **S. Candel** (2003). A unified model for the prediction of laminar flame transfer functions: comparisons between conical and v-flame dynamics. *Combustion and Flame*, **134**(1-2), 21–34. 108

218. **Schuller, T.**, **T. Poinsot**, and **S. Candel** (2020). Dynamics and control of premixed combustion systems based on flame transfer and describing functions. *Journal of Fluid Mechanics*, **894**. 73

219. **Searby, G.** and **J. Quinard** (1990). Direct and indirect measurements of markstein numbers of premixed flames. *Combustion and Flame*, **82**(3-4), 298–311. 52

220. **Sengupta, U.**, **C. E. Rasmussen**, and **M. P. Juniper** (2021). Bayesian machine learning for the prognosis of combustion instabilities from noise. *Journal of Engineering for Gas Turbines and Power*, **143**(7), 071001. 79

221. **Shanbhogue, S.**, **D. H. Shin**, **S. Hemchandra**, **D. Plaks**, and **T. Lieuwen** (2009*a*). Flame-sheet dynamics of bluff-body stabilized flames during longitudinal acoustic forcing. *Proceedings of Combustion Institute*, **32**(2), 1787–1794. xvi, 63, 64, 65, 66, 101

222. **Shanbhogue, S. J.**, **S. Husain**, and **T. Lieuwen** (2009*b*). Lean blowoff of bluff body stabilized flames: Scaling and dynamics. *Progress in Energy and Combustion Science*, **35**(1), 98–120. 14, 15

223. **Shin, D. H.** and **T. Lieuwen** (2012). Flame wrinkle destruction processes in harmonically forced, laminar premixed flames. *Combustion and Flame*, **159**(11), 3312–3322. xvi, 64, 66

224. **Shin, D. H.** and **T. Lieuwen** (2013). Flame wrinkle destruction processes in harmonically forced, turbulent premixed flames. *Journal of Fluid Mechanics*, **721**, 484–513. 64

225. **Shraiman, B. I.** and **E. D. Siggia** (2000). Scalar turbulence. *Nature*, **405**(6787), 639. 47, 48

226. **Shreekrishna**, **S. Hemchandra**, and **T. Lieuwen** (2010). Premixed flame response to equivalence ratio perturbations. *Combustion Theory and Modelling*, **14**(5), 681–714. 72

227. **Singh, S.**, **A. Roy**, **R. KV**, **A. Nair**, **S. Chaudhuri**, and **R. Sujith** (2021). Intermittency, secondary bifurcation and mixed-mode oscillations in a swirl-stabilized annular combustor: Experiments and modeling. *Journal of Engineering for Gas Turbines and Power*, **143**(5), 051028. 75

228. **Skalska, K.**, **J. S. Miller**, and **S. Ledakowicz** (2010). Trends in NOx abatement: A review. *Science of the total environment*, **408**(19), 3976–3989. 8, 9, 11, 12

229. **Sreenivasan, K.** (2004). Possible effects of small-scale intermittency in turbulent reacting flows. *Flow, Turbulence and Combustion*, **72**(2-4), 115–131. 60

230. **Sreenivasan, K.** and **C. Meneveau** (1986). The fractal facets of turbulence. *Journal of Fluid Mechanics*, **173**, 357–386. 156

231. **Sreenivasan, K.**, **R. Ramshankar**, and **C. Meneveau** (1989). Mixing, entrainment and fractal dimensions of surfaces in turbulent flows. *Proceedings of the Royal Society of London A*, **421**(1860), 79–108. 156, 157, 165, 167, 174

232. **Sreenivasan, K. R.** (1991*a*). Fractals and multifractals in fluid turbulence. *Annual Reviews of Fluid Mechanics*, **23**(1), 539–604. 39, 40, 145, 156, 169

233. **Sreenivasan, K. R.** (1991*b*). On local isotropy of passive scalars in turbulent shear flows. *Proceedings of the Royal Society of London*, **434**(1890), 165–182. 47

234. **Sreenivasan, K. R.** (1995). On the universality of the kolmogorov constant. *Physics of Fluids*, **7**(11), 2778–2784. 30

235. **Sreenivasan, K. R.** and **R. Antonia** (1997). The phenomenology of small-scale turbulence. *Annual Reviews Fluid Mechanics*, **29**(1), 435–472. xvi, 36, 47, 48, 138, 157

236. **Sterling, J. D.** (1993). Nonlinear analysis and modelling of combustion instabilities in a laboratory combustor. *Combustion Science and Technology*, **89**(1-4), 167–179. 73

237. **Stone, R.** (2002). Counting the cost of London's killer smog. *Science*, **298**, 2106–2107. 3

238. **Strahle, W. C.** (1971). On combustion generated noise. *Journal of Fluid Mechanics*, **49**(2), 399–414. 75

239. **Strahle, W. C.** (1978). Combustion noise. *Progress in Energy and Combustion Science*, **4**(3), 157–176. 75

240. **Strogatz, S. H.**, *Nonlinear dynamics and chaos with student solutions manual: With applications to physics, biology, chemistry, and engineering*. CRC press, 2018. 74, 75

241. **Sujith, R.**, **M. Juniper**, and **P. Schmid** (2016). Non-normality and nonlinearity in thermoacoustic instabilities. *International Journal of Spray and Combustion Dynamics*, **8**(2), 119–146. 70, 73

242. **Sujith, R.** and **V. R. Unni** (2020). Complex system approach to investigate and mitigate thermoacoustic instability in turbulent combustors. *Physics of Fluids*, **32**(6), 061401. 17, 63, 73

243. **Tachibana, S.**, **L. Zimmer**, **Y. Kurosawa**, and **K. Suzuki** (2007). Active control of combustion oscillations in a lean premixed combustor by secondary fuel injection coupling with chemiluminescence imaging technique. *Proceedings of the Combustion Institute*, **31**(2), 3225–3233. 81, 192

244. **Temme, J. E.**, **P. M. Allison**, and **J. F. Driscoll** (2014). Combustion instability of a lean premixed prevaporized gas turbine combustor studied using phase-averaged piv. *Combustion and Flame*, **161**(4), 958–970. 13

245. **Tennekes, H.** (1975). Eulerian and lagrangian time microscales in isotropic turbulence. *Journal of Fluid Mechanics*, **67**(3), 561–567. 127

246. **Tennekes, H.** and **J. L. Lumley**, *A first course in turbulence*. MIT press, 2018. 27, 128

247. **Thiesset, F.**, **G. Maurice**, **F. Halter**, **N. Mazellier**, **C. Chauveau**, and **I. Gökalp** (2016). Modelling of the subgrid scale wrinkling factor for large eddy simulation of turbulent premixed combustion. *Combustion Theory and Modelling*, **20**(3), 393–409. 159

248. **Tian, H.**, **R. Xu**, **J. G. Canadell**, **R. L. Thompson**, **W. Winiwarter**, **P. Suntharalingam**, **E. A. Davidson**, **P. Ciais**, **R. B. Jackson**, **G. Janssens-Maenhout**, *et al.* (2020). A comprehensive quantification of global nitrous oxide sources and sinks. *Nature*, **586**(7828), 248–256. 9

249. **Tony, J.**, **E. Gopalakrishnan**, **E. Sreelekha**, and **R. Sujith** (2015). Detecting deterministic nature of pressure measurements from a turbulent combustor. *Physical Review E*, **92**(6), 062902. 76

250. **Tsinober, A.**, *An informal conceptual introduction to turbulence*, volume 483. Springer, 2009. 47

251. **Turns, S. R.**, *Introduction to combustion*, volume 287. McGraw-Hill Companies, 1996. 2

252. **Tylecote, R. F.** (1977). A history of metallurgy. *British Corrosion Journal*, **12**(3), 137–140. 1

253. **Uhm, J. H.** and **S. Acharya** (2005). Low-bandwidth open-loop control of combustion instability. *Combustion and Flame*, **142**(4), 348–363. 80, 81

254. **UNCC** (2016). United nations climate change: The paris agreement. `https://unfccc.int/process-and-meetings/the-paris-agreement/the-paris-agreement`. 5

255. **Unni, V. R.**, **A. Krishnan**, **R. Manikandan**, **N. B. George**, **R. Sujith**, **N. Marwan**, and **J. Kurths** (2018). On the emergence of critical regions at the onset of thermoacoustic instability in a turbulent combustor. *Chaos*, **28**(6), 063125. 82

256. **Unni, V. R.**, **A. Mukhopadhyay**, and **R. Sujith** (2015). Online detection of impending instability in a combustion system using tools from symbolic time series analysis. *International Journal of Spray and Combustion Dynamics*, **7**(3), 243–255. 79

257. **Unni, V. R.** and **R. Sujith** (2015). Multifractal characteristics of combustor dynamics close to lean blowout. *Journal of Fluid Mechanics*, **784**, 30–50. 77

258. **Vohra, K.**, **A. Vodonos**, **J. Schwartz**, **E. A. Marais**, **M. P. Sulprizio**, and **L. J. Mickley** (2021). Global mortality from outdoor fine particle pollution generated by fossil fuel combustion: Results from GEOS-Chem. *Environmental Research*, **195**, 110754. 3

259. **Wake, D. B.** and **V. T. Vredenburg** (2008). Are we in the midst of the sixth mass extinction? A view from the world of amphibians. *Proceedings of the National Academy of Sciences*, **105**(1), 11466–11473. 5

260. **WHO** (2018). Ambient air pollution. `https://www.who.int/data/gho/data/themes/topics/topic-details/GHO/ambient-air-pollution`. 3

261. **Wilke, C.** (1950). A viscosity equation for gas mixtures. *The Journal of Chemical Physics*, **18**(4), 517–519. 94

262. **Winkler, D.**, **W. Geng**, **G. Engelbrecht**, **P. Stuber**, **K. Knapp**, and **T. Griffin** (2017). Staged combustion concept for gas turbines. *Journal of the Global Power and Propulsion Society*, **1**, 184–194. 12

263. **Wirth, M.** and **N. Peters**, Turbulent premixed combustion: A flamelet formulation and spectral analysis in theory and ic-engine experiments. *In Symposium (International) on Combustion*, volume 24. Elsevier, 1992. 59

264. **Woodrow, P.** (1997). Nitric oxide: some nursing implications. *Intensive and Critical Care Nursing*, **13**(2), 87–92. 8

265. **Yu, M. H.** and **P. A. Monkewitz** (1990). The effect of nonuniform density on the absolute instability of two-dimensional inertial jets and wakes. *Physics of Fluids A: Fluid Dynamics*, **2**(7), 1175–1181. 63

266. **Zhao, D.** and **X. Li** (2015). A review of acoustic dampers applied to combustion chambers in aerospace industry. *Progress in Aerospace Science*, **74**, 114–130. 80

267. **Zhao, D.**, **Z. Lu**, **H. Zhao**, **X. Li**, **B. Wang**, and **P. Liu** (2018). A review of active control approaches in stabilizing combustion systems in aerospace industry. *Progress in Aerospace Science*, **97**, 35–60. 80

CURRICULUM VITAE

1. **NAME** : Amitesh Roy
2. **DATE OF BIRTH** : 10 April, 1994
3. **EDUCATIONAL QUALIFICATION**

2012 **Bachelor of Technology (B.Tech.)**

Institution : Vellore Institute of Technology, Vellore, Tamil Nadu

Specialization : Mechanical Engineering

2021 **Doctor of Philosophy (Ph.D.)**

Institution : Indian Institute of Technology Madras, Chennai

Specialization : Aerospace Engineering

Registration date : 12 July, 2016

DOCTORAL COMMITTEE

CHAIRPERSON: Dr. H. S. N. Murthy

Professor and Head

Department of Aerospace Engineering

GUIDE: Dr. R. I. Sujith

Professor

Department of Aerospace Engineering

MEMBERS: Dr. Sunetra Sarkar

Professor

Department of Aerospace Engineering

Dr. P. A. Ramakrishnan

Professor

Department of Aerospace Engineering

Dr. Niket Kaisare

Associate Professor

Department of Mechanical Engineering